

UNCLASSIFIED

AD NUMBER

AD916429

LIMITATION CHANGES

TO:

Approved for public release; distribution is unlimited.

FROM:

Distribution authorized to U.S. Gov't. agencies only; Test and Evaluation; 08 AUG 1973. Other requests shall be referred to Defense Nuclear Agency, Washington, DC 20305.

AUTHORITY

DNA ltr, 30 Aug 1974

THIS PAGE IS UNCLASSIFIED

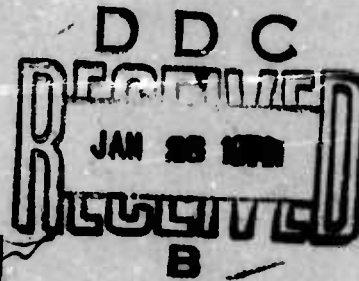
L
AD916429**CONSTITUTIVE MODELS AND COMPUTER TECHNIQUES
FOR GROUND MOTION PREDICTIONS**

T. D. Riney
G. A. Frazier
S. K. Garg
A. J. Good
R. G. Herrmann
L. W. Morland
J. W. Pritchett
M. H. Rice
J. Sweet

Systems, Science and Software
P. O. Box 1620
La Jolla, California 92037

30 March 1973

Final Report

Contract No. DASA 01-69-C-0159 (~~P0004~~)

Distribution limited to U. S. Government agencies only; test and evaluation; 8 August 1973.
Other requests for this document must be referred to Director, Defense Nuclear Agency, Wash-
ington, D. C. 20305

This work was supported by the Defense Nuclear
Agency under Subtask ZL438-01.

AD No. _____
DDC FILE COPY

Prepared for

Director
Defense Advanced Research Projects Agency
Arlington, Virginia 22209

ACCESSION FOR	
NTIS	White Section <input type="checkbox"/>
DGC	Gulf Section <input checked="" type="checkbox"/>
UNANNOUNCED	<input checked="" type="checkbox"/>
JUSTIFICATION	
BY	
DISTRIBUTION/AVAILABILITY CODES	
Dist.	AVAIL. and/or SPECIAL
B	

Destroy this report when it is no longer needed.
Do not return to sender.

UNCLASSIFIED

SECURITY CLASSIFICATION OF THIS PAGE (When Data Entered)

19 REPORT DOCUMENTATION PAGE		READ INSTRUCTIONS BEFORE COMPLETING FORM	
1. REPORT NUMBER (18) DNA 3180F	2. GOVT ACCESSION NO.	3. RECIPIENT'S CATALOG NUMBER	
4. TITLE (and Subtitle) (6) CONSTITUTIVE MODELS AND COMPUTER TECHNIQUES FOR GROUND MOTION PREDICTIONS.		5. TYPE OF REPORT & PERIOD COVERED (9) Final Report	
7. AUTHOR(S) (10) T. D. Riney, G. A. Frazier, S. K. Garg, A. J. Good, R. G. Herrmann, L. W. Morland, J. W. Pritchett, M. H. Rice, J. Sweet		6. PERFORMING ORG. REPORT NUMBER (14) SSS-R-73-1494	
9. PERFORMING ORGANIZATION NAME AND ADDRESS Systems, Science and Software P. O. Box 1620 La Jolla, California 92037		8. CONTRACT OR GRANT NUMBER(S) (5) Contract No. DASA 01-69-C-0159	
11. CONTROLLING OFFICE NAME AND ADDRESS Director, Defense Advanced Research Projects Agency, 1400 Wilson Boulevard, Arlington, Virginia 22209		10. PROGRAM ELEMENT, PROJECT, TASK AREA & WORK UNIT NUMBERS (12) ARPA Order -1438 Task No. ZL438 Work Unit No. 1	
14. MONITORING AGENCY NAME & ADDRESS (if different from Controlling Office)		12. REPORT DATE (11) 30 Mar 1973	
		13. NUMBER OF PAGES 357 (12) 349 p.	
		15. SECURITY CLASSIFICATION (of this report) Unclassified	
		15a. DECLASSIFICATION/DOWNGRADING SCHEDULE	
16. DISTRIBUTION STATEMENT (of this Report) Distribution limited to U. S. Government agencies only; test and evaluation; 8 August 1973. Other requests for this document must be referred to Director, Defense Nuclear Agency, Washington, D. C. 20305.			
17. DISTRIBUTION STATEMENT (of the abstract entered in Block 20, if different from Report) (16) DNA-ARPA-ZL-438, SSS-119 DN 388 507 ✓			
18. SUPPLEMENTARY NOTES This work was supported by the Defense Nuclear Agency under Subtask ZL438-01.			
19. KEY WORDS (Continue on reverse side if necessary and identify by block number) Ground Motion Calculations, Rock and Soil Models, Composite Materials, Mine Dust HE Test, Waste Injection Wells, Stress Waves in Geologic Media, Equations of State, Jointed Rock Masses.			
20. ABSTRACT (Continue on reverse side if necessary and identify by block number) The general subroutine (TAMEOS) for generating thermodynamic equations of state for rock-water-void mixes has been used in the 1D SKIPPER code to predict the spherically symmetric ground motion for the Mine Dust HE test in partially saturated tuff. The pre-test calculations are in good agreement with the measured in situ stress and velocity time histories. Planar TAMEOS/SKIPPER parameter calculations are presented which demonstrate the need for explicit treatment of water vaporization in evaluating near			

DD FORM 1 JAN 73 1473

EDITION OF 1 NOV 55 IS OBSOLETE

UNCLASSIFIED

SECURITY CLASSIFICATION OF THIS PAGE (When Data Entered)

Next page

Cont-
UNCLASSIFIED

SECURITY CLASSIFICATION OF THIS PAGE(When Data Entered)

surface ground motion effects. An equation of state for granite is developed which includes the coesite-stishovite phase change. Planar and spherical SKIPPER parameter calculations demonstrate that the two-phase equation of state should be used when stresses greater than 70 kbar are involved. The cap model and the Mohr-Coulomb model with kinematic work hardening are generalized to two space dimensions and incorporated into the 2D CRAM code for treating rocks with high shear strength. A continuum model for a regularly jointed rock mass is formulated in terms of the block spacing and the frictional forces on the planes of weakness. Although the blocks are considered elastic, block slippage and interlock produces a formulation analogous to an elastic-plastic model. An improved version of the 1D POROUS code has been developed to treat ground motion problems within the framework of the Theory of Interacting Continua (TINC). Comparison calculations using the spherical POROUS and SKIPPER codes are presented. The 2D FRI finite element code for solving the linearized TINC equations is applied to study the rock-fluid mechanical interactions in the vicinity of a fluid injection well.

UNCLASSIFIED

SECURITY CLASSIFICATION OF THIS PAGE(When Data Entered)

FOREWORD

This formal technical report entitled "Constitutive Models and Computer Techniques for Ground Motion Predictions," is submitted by Systems, Science and Software (S³) to the Advanced Research Projects Agency (ARPA) and to the Defense Nuclear Agency (DNA). The report presents the results of the fourth phase of an effort to develop reliable material models and computer techniques for predicting the motion of inhomogeneous and porous geologic media. This work, in support of the PRIME ARGUS and MILITARY GEOPHYSICS programs, was accomplished under Contract No. DASA 01-69-C-0159(P00004), which was funded by ARPA and monitored by DNA. Dr. Stanley Ruby was the ARPA Program Manager and Mr. Clifton B. McFarland was the DNA Project Scientist.

Dr. T. David Riney was the S³ Project Manager for the study. The technical results presented in this report represent the work of a number of S³ staff members in addition to the authors. It is appropriate to list here the contributors to technical Sections II through VII.

Section II: T. D. Riney, J. T. Cherry, A. J. Good,
M. H. Rice

Section III: M. H. Rice, J. W. Kirsch, C. M. Archuleta

Section IV: J. Sweet, J. K. Dienes

Section V: S. K. Garg, R. G. Herrmann, J. W. Pritchett

Section VI: L. W. Morland, M. M. Baligh

Section VII: G. A. Frazier, R. J. Archuleta, M. M. Baligh

The authors would like to extend their sincere appreciation and gratitude for the ingenuity, understanding and support of Ms. Darlene A. Roddy in the preparation of this report.

The contractor report number assigned to this document is SSS-R-73-1490; the project number is 119.

TABLE OF CONTENTS

	Page
FOREWORD.	1
I. INTRODUCTION AND SUMMARY	7
2.1 ROCK-WATER-VOID MIXTURE MODELS.	15
2.2 MINE DUST HE PREDICTIONS.	20
2.2.1 Background	20
2.2.2 Test Site Medium	20
2.2.3 Isotropic Response Model for Medium.	27
2.2.4 Deviatoric Response Model for Medium	31
2.2.5 H.E. Source Equation of State.	39
2.2.6 Comparison of Predictions with Measurement.	40
2.3 SURFACE LOADING PARAMETER STUDY	70
III. A TWO-PHASE EQUATION OF STATE MODEL FOR GRANITE.	81
3.1 TWO-PHASE MODEL	81
3.2 INCORPORATION OF THE MODEL INTO THE SKIPPER CODE.	89
3.2.1 Interpolated-Pressure Method	89
3.2.2 Pressure-Temperature Equilibrium Method	91
3.2.3 Numerical solution for V_1 and V_2	94
3.3 EXPLORATORY CALCULATIONS WITH PLANAR SKIPPER	100

TABLE OF CONTENTS (Continued)		Page
	3.4 THE TRANSITION RATE	109
	3.5 CALCULATIONS WITH SPHERICAL SKIPPER	113
IV.	GENERALIZED PLASTICITY MODELS IN 2D CPAM	121
	4.1 BACKGROUND AND INTRODUCTION	121
	4.2 DEVELOPMENT OF MATHEMATICAL MODEL	127
	4.2.1 The Equation of State.	127
	4.2.2 Elastic and Plastic Strains.	128
	4.2.3 Matrix Volume Governing Equation	130
	4.3 KINEMATIC WORK HARDENING MODEL.	135
	4.4 WEIDLINGER CAP MODEL.	138
	4.5 SUMMARY	141
V.	TINC DEVELOPMENT AND THE POROUS CODE	145
	5.1 INTRODUCTION.	145
	5.2 CONSTITUTIVE LAWS	146
	5.2.1 Saturated Media.	150
	5.2.2 Unsaturated Case	156
	5.2.3 Data Fit for $\frac{\partial n^{(1)}}{\partial (p_c - p_p)}$	158
	5.3 THE POROUS CODE	165
	5.3.1 Boundary Conditions.	166
	5.3.2 Interaction Terms.	167
	5.3.3 Constitutive Relations	168
	5.3.4 Low Amplitude Finite-Difference Equations.	170

TABLE OF CONTENTS (Continued)		Page
	5.4 NUMERICAL CALCULATIONS.	174
VI.	CONTINUUM MODEL OF REGULARLY JOINTED MEDIA	207
	6.1 ROCK MASSES IN SITU	208
	6.2 FRACTURE AND FAILURE CRITERIA	213
	6.3 TESTS AND DEDUCTIONS.	222
	6.4 BLOCK STRUCTURE AND MOTION.	234
	6.5 CONTINUUM APPROXIMATION	246
	6.6 BI-AXIAL LOADING.	252
VII.	FLUID-ROCK INTERACTION NEAR AN INJECTION WELL. . .	267
	7.1 INTRODUCTION.	267
	7.1.1 Hydraulically Induced Tensile Cracks	267
	7.1.2 Hydraulically Triggered Shear Failure.	268
	7.1.3 Consolidation Theory	270
	7.2 QUASISTATIC THEORY OF FLUID-ROCK COMPOSITE. .	272
	7.2.1 Simplifying Assumptions.	272
	7.2.2 TINC Notation.	272
	7.2.3 Constitutive Equations	275
	7.2.4 Conservation of Momentum	282
	7.2.5 Finite Element Formulation	285
	7.3 NUMERICAL RESULTS	290
	7.3.1 Test Calculations.	290
	7.3.2 Spherically Symmetric Injection Cavity	291
	7.3.3 Shallow Injection Well	296

TABLE OF CONTENTS (Continued)	Page
7.4 SUMMARY AND CONCLUSIONS	339
VIII. DISCUSSION	341
IX. REFERENCES	345
DISTRIBUTION LIST	353

I. INTRODUCTION AND SUMMARY

A deterministic model to predict the radiated signature from a buried nuclear explosion is concerned with the characterization of the stress wave propagated from the vicinity of the source to remote locations. The stress level in the earth may be many megabars near the source, but at distant detection stations the signal has attenuated to a value which is small compared to the elastic strength of earth media. Adequate geologic material response models and associated computer techniques are required to treat the complex nonlinear physical processes that occur near the source and to carry the calculations out to the point where the medium responds in a linear manner. It is then possible to obtain an equivalent elastic source function which propagates a signal into the far field elastic region that is the same as that produced by the real explosive source. This equivalent explosive source function can be used as input data in seismic code calculations which propagate the signal to teleseismic distances through an appropriate elastic earth structure.

The results to be presented in this report are focused on the development and verification of realistic material models and associated computer techniques for treating the nonlinear region near the explosion. The work is a continuation of that performed in earlier phases of this contract, described in 3SR-267, [1] 3SR-648 [2] and 3SR-1071. [3] By constructing material models of increasing sophistication it has been possible to include such complex nonlinear physical processes as irreversible compaction, heterogeneity, pore water pressure and diffusion, yield and fracture phenomena, dilatancy, water and rock interactions, material phase changes, and dependence of strength parameters on the stress history and thermodynamic state.

In a companion program at S³ the improved ground motion methods developed under this contract are used in a systematic analysis of the nonlinear processes near the source which affect the signature radiation to teleseismic distances.^[4] To accomplish this, the nonlinear shock code techniques for determining the equivalent explosive source function were merged with seismic code calculations of the stress wave propagation through an appropriate elastic earth structure to remote sites.

A typical geologic medium consists of a rock or soil matrix containing cracks or pores that may be partially filled with water. Even if the matrix material is unchanged, the porosity and the water content will vary with depth and with surface distance and the stress propagation characteristics of the medium will vary accordingly. For teleseismic calculations it is impossible to know the porosities and degrees of saturation at inaccessible nuclear test sites. Even when local geological conditions and the water table location have been established by field logging tests, as would be possible in evaluating the vulnerability of underground structures, it is economically impractical to perform laboratory material properties tests on all the porosities and degrees of saturation that occur. Consequently, it is desirable to construct the material models in such a fashion that the response of the medium can be predicted as these quantities are varied.

The early modeling effort centered on Nevada Test Site (NTS) tuffs as representative of partially saturated porous geologic media.^[1,2] A computer routine was developed which calculates the isotropic thermodynamic states of rock-water-void mixtures, including a description of irreversible collapse of the air filled pores (void volume). The routine (TAMEOS) calculates the response of the composite

in terms of the behavior of the isolated rock and water components and may be readily used in standard ground motion computer codes. It includes several options for the crushup response and the partition of energy between the rock and water components. The routine was incorporated into the Lagrangian 1D SKIPPER code and a series of spherical calculations made for a representative tuff with varied degrees of water saturation of the pore space.^[3]

The recent Mine Dust HE test provided an excellent opportunity to test the validity of TAMEOS for partially saturated media with relatively low shear strength. This 1000-lb nitromethane shot in tuff was conducted in Area 16 at NTS. As part of this test program, other contractors generated static test data on core samples from the site, and fielded radial stress and velocity gages to provide a description of the stress wave at various radial distances from the spherically symmetric source. Section II of this report presents the results of pretest predictions of the ground motion calculated using 1D SKIPPER with the TAMEOS equation of state routine and a Mohr-Coulomb plasticity model fitted to strength data from the core samples. The predicted time resolved histories at the various gage locations are in very good agreement with the corresponding measured time histories.

The Mine Dust HE results reinforce our confidence that realistic ground motion predictions can be made at least for relatively weak rocks such as tuff.* Parameter calculations illustrating the effect of water vaporization at a free surface are also presented in Section II. The planar mode of SKIPPER was used to compare the stress pulses calculated

*A version of TAMEOS has subsequently been incorporated into a computer code used at S³ for ground motion calculations concerned with the stemming and containment of underground nuclear tests.

using the TAMEOS routine with the calculations using an analytic form of the equation of state which does not treat water vaporization. In all cases the rate of pressure decay of a function of depth is significantly less in the calculations with the TAMEOS scheme. The backward momentum of the vaporized material is offset by an increase in the forward momentum carried by the stress pulse. The importance of this effect on ground motion and crater formation from near surface nuclear burst is apparent.

Realistic ground motion calculations for geologic materials with high shear strength (e.g. granite) require plasticity models more sophisticated than a Mohr-Coulomb model. Generalized plasticity models that fair the complex deviatoric strength properties of hard rocks observed in laboratory tests with a high pressure equation of state were presented in an earlier report.^[3] Major emphasis was placed on a generalized Mohr-Coulomb model with kinematic work hardening and a generalized Weidlinger cap model to treat the required range of pressure and strain. The 1D SKIPPER code was then applied to compare the Hard Hat and Pile Driver ground motion measurements with the calculations using these two models. It was found that the inclusion of the Bauschinger effect (kinematic hardening) stretched out the pulse over a longer time at a fixed station resulting in reasonable agreement with the field measurements. Moreover, it was necessary to greatly scale down the rock strength from that measured on competent laboratory specimens.^[3]

A major uncertainty in the model for granite used in these earlier code calculations is the possibility of a phase change at high pressures. Consequently, a two-phase equation of state model for granite was developed which is based on laboratory shock wave data and the assumption that some time is required for mixtures of the two phases to reach equilibrium. The model is presented in Section III along with a series of 1D

SKIPPER planar and spherical code calculations to investigate the effects of the phase change. The difference between the stress profiles and attenuation rates for the two-phase model and a single-phase model is pronounced. The attenuation rate is greater for the two-phase model and the stress profiles are stretched out. These comparisons indicate that a realistic treatment of ground motion should include explicitly any possible phase changes.

Section IV presents the two-dimensional formulation of the kinematic work hardening and Weidlinger cap models and describes the manner in which they have been incorporated into the Lagrangian 2D CRAM computer code as options. This code treats two-dimensional continua in either plane or rotationally symmetric geometry. The single-phase analytic equation of state used is the same as that employed in the earlier SKIPPER calculations for the Hard Hat and Pile Driver comparisons, but the coding has been arranged to facilitate future changes. For example, either the two-phase model for granite or TAMEOS can be readily adopted.

Standard ground motion computer codes, such as SKIPPER and CRAM, treat a geologic medium as a single continuum in that each computational zone has associated a single value of pressure, velocity, etc. Homogenized mixture equations of state (e.g. TAMEOS) cannot treat relative motion of the pore water with respect to the matrix material. For soils and rock aggregates the relative motion may be an important effect in some applications. In rock media the pressure of the pore water will differ from the stress carried by the matrix material and the strength properties of the rock are strongly affected by this difference. In recognition of these limitations of standard methods of analysis, the Theory of Interacting Continua (TINC) was adopted to provide a framework general enough to allow explicit treatment of these physical effects. Each volume is considered to contain both

rock and water components with provisions for momentum and energy exchange between the two components by inclusion of interaction terms in their respective governing equations.

The early TINC modeling effort was restricted to a mechanical theory. [1,2] The formulation was subsequently extended to include thermodynamic effects, irreversible crushup, and an improved model for the deviatoric strength response of the rock matrix component. [3] In Section V additional improvements in the theory are described together with the numerical procedures used in the associated 1D POROUS code for solving the governing system of equations. POROUS treats both planar and spherical geometries. A series of parameter runs in the latter configuration is also presented.*

Section VI presents the results of a study which has the objective of deriving a rational basis for scaling relations between laboratory and field strength data. The analysis considers the in situ geologic medium to contain regularly spaced planes of weakness (e.g., joints or faults). Each block is considered to deform elastically but relative slippage between blocks is permitted. A continuum model is formulated which is analogous to an elastic plastic model where the shear strength is determined by the joint spacing and the frictional properties of the fault planes. As a consequence of this analogy, it appears that the model could be incorporated into a continuum mechanics code such as CRAM once sufficient data to define slippage and block interlock are available.

* The TINC framework has been successfully used at S^3 in a study of stress wave effects in reinforced composite materials. [5,6] The regular geometry and interfacial bond permit the required interaction terms to be calculated in terms of the dimensions, properties and geometries of the reinforcements.

Section VII is not concerned with ground shocks. It presents the results of a study of the mechanical interaction of a pore fluid with a saturated rock matrix as the fluid is driven through the medium under a hydraulic gradient. A quasistatic formulation of the process within the linearized TINC equation was given earlier.^[3] A 2D fluid-rock interaction code (FRI) for treating the coupled elastic and diffusive processes has been developed. Calculations of the perturbations of the stress field in the rock mass surrounding a fluid injection well are presented.

In Section VIII, the status of the work is summarized and suggestions are made for its application to a number of current problems.

II. HOMOGENIZED WET TUFF CALCULATIONS

2.1 ROCK-WATER-VOID MIXTURE MODELS

In modeling porous geologic media, it was recognized from the outset that rock-water-void (air) volume fractions would vary from one test site to another and that the material response would vary accordingly.^[1] Consequently, the models were constructed in such a fashion that the response of the medium can be predicted as the volume fractions of the rock, water and air (void) are varied:

$$\begin{array}{ccc} (1) & (2) & (3) \\ n \text{ (Rock)}, & n \text{ (Water)}, & n \text{ (Void)} \end{array}$$

The geologic medium is considered as a composite and a description of its wave propagation characteristics has been sought in terms of the behavior of the isolated rock matrix and water components. The Theory of Interacting Continua (TINC) was adopted to provide a framework general enough to allow explicit treatment of pore pressure effects and relative motion between the rock and water components (see Section V). However, since practical 2D calculations are currently performed using computer codes that treat a medium as a single continuum, the bulk of the material response modeling effort has been conducted under the additional homogenizing assumption of no relative motion between the rock and water.

One may derive various mixture equations of state on the basis of a number of assumed equilibrium conditions achieved behind a shockwave.^[2] A unique set of shock states is achieved only when a constraint is prescribed for the partitioning of internal energy between the rock and the water. Such a set of states can be obtained if the pressure and temperature of the constituents are equal (PTEQ model). If there is insufficient time for thermal equilibration, but the components are homogenized to the extent that they are in pressure equilibrium, other energy partitions may

attain, such as in the PEQ and P*EQ models. In the PEQ model each component is assumed to independently attain the mutual equilibrium by a single shock process and no heat transfer between components is permitted. The P*EQ model is based on an intermediate partition of the shock energy based on the multiple shock sequence whereby the pore water and rock matrix materials eventually attain their equilibrium pressure. Again, no heat transfer is permitted between the rock and water components.

Although the predicted Hugoniot p-V and u-U curves are very nearly the same for all three models, the Hugoniot temperatures are very different. In Fig. 2.1 shock temperature in the water and tuff components predicted from the PEQ, P*EQ and PTEQ models are shown for saturated wet tuff (mass fraction $M_w = 15\%$). The lower temperature of the water component for the PTEQ and P*EQ models imply that it may undergo a phase transformation to Ice VII, whereas this would not occur in the PEQ model, Fig. 2.1. Both Water-Ice VI and Water-Ice VII phase changes have often been found in static tests but only recently has such a transformation been observed under shock loading conditions. Gaffney^[7] observed the Water-Ice VII transformation between 20 and 26 kbars in gas gun experiments with nearly saturated clay and shale specimens from the Middle Gust site. Since thermal equilibrium is not attained under the test conditions, these results appear to support the P*EQ model.

For a given model and shock pressure, the shock temperatures depend on the volume fractions of rock/water/void. The residual energy in the components of the shock processed mixture also depend on the relative volume fractions. This is illustrated in Fig. 2.2 by the release adiabats calculated for a PTEQ model of wet tuff. The increased shock heating for the mixtures with higher air-filled porosity produces vaporization of the water at a higher pressure during the release process.

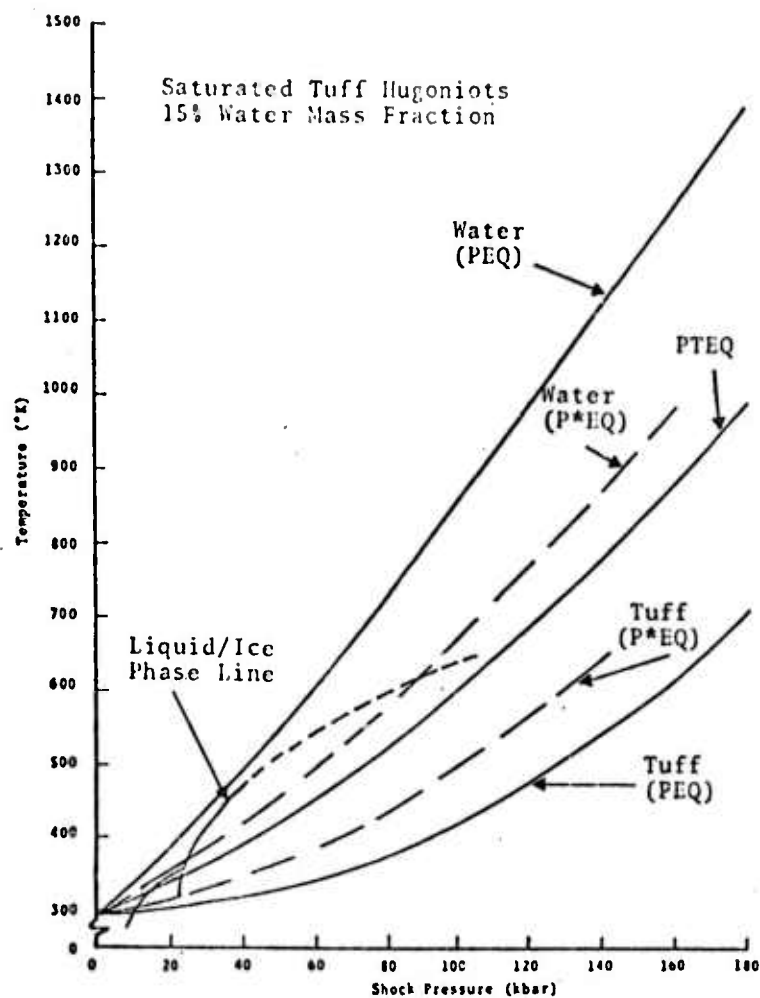


Fig. 2.1--Shock temperatures calculated from the PTEQ, PEQ and P*EQ models for saturated NTS wet tuff with $M_w = 15\%$. The Water-ICE VII phase line is based on static test data (see Ref. [2]).

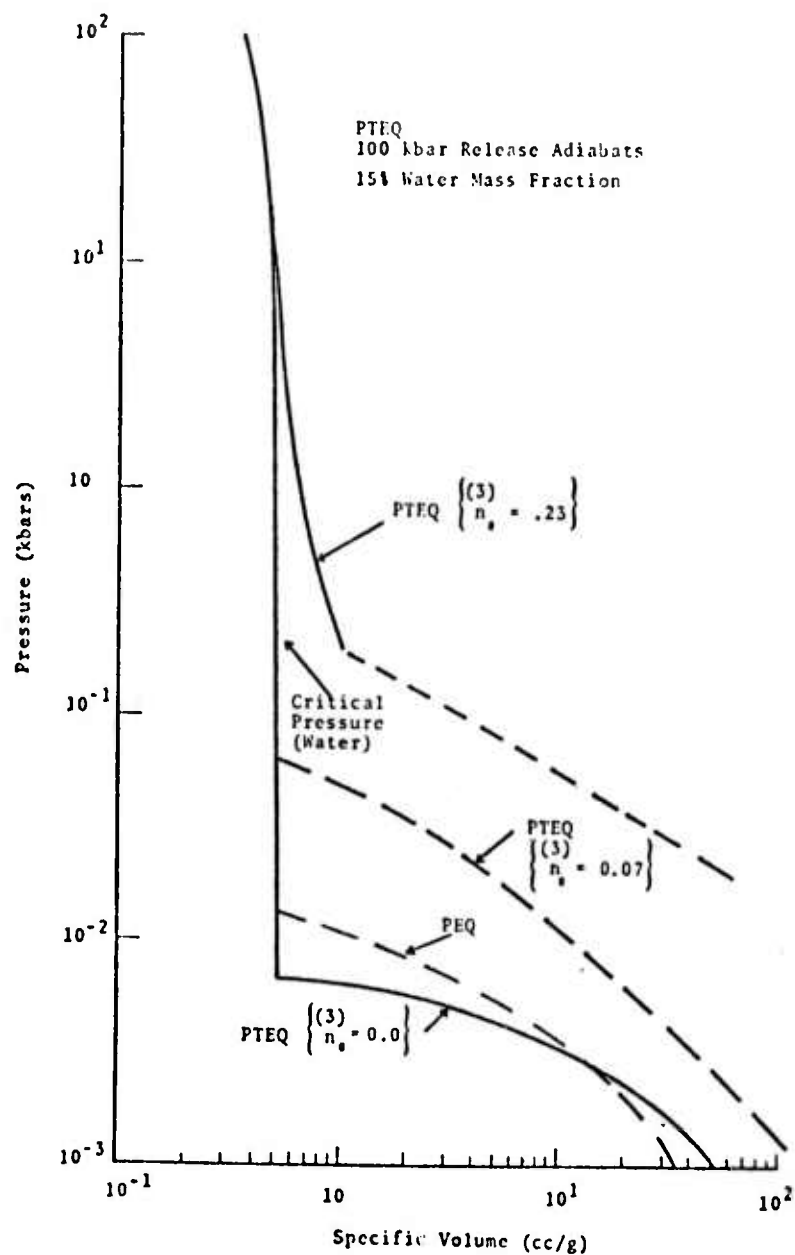


Fig. 2.2--Porosity-enhanced vaporization of water component in shock processed wet tuff.

A computer routine has been developed which calculates the isotropic thermodynamic states of rock-water-void mixtures, including a description of irreversible collapse of the air-filled pores (void volume).^[3] These states are tabulated and may be utilized in conjunction with a table look-up procedure as a subroutine in standard ground motion codes. Primary inputs to the TAMEOS subroutine (for Tabular Arrays of Mixture Equation Of State) are the homogenized model to be utilized (e.g., one of the PTEQ, PEQ or P*EQ models), equations of state of the isolated rock and water components, and initial volume fractions of rock, water and air-filled pores. For cases in which experimental data are unavailable, a simple crushup model is employed requiring the zero pressure extension (α_0), zero pressure bulk modulus (k), pressure at elastic crush limit (p_e), and crushup pressure (p_c). In cases where experimental data are available, the crushup curve can be directly incorporated into the TAMEOS subroutine.

The TAMEOS subroutine has been incorporated into the S³ single continuum code SKIPPER and a series of spherical calculations illustrating the effect on ground motion of the rock-water-void volume fractions were earlier reported^[3] for representative NTS tuff. Some additional parameter calculations to examine the effect of water vaporization at a free surface will be described here. First, however, the results of predictive ground motion calculations conducted prior to the Mine Dust HE test will be presented along with the stress-time and velocity-time histories measured at various radial distances from the working point. The good agreement between the predictions and the measurements provides us with some confidence in the TAMEOS subroutine for generating equations of state for partially saturated sedimentary materials.

2.2 MINE DUST HE PREDICTIONS

2.2.1 Background

The Mine Dust HE experiment working point (WP) was located 15 ft below the floor of a tunnel at a distance of 45 ft from the U16 a.05 drift at Construction Site (C5) 1+25.66. The layout of the test is presented in the drawing in Fig. 2.3. The section shown in Fig. 2.4 depicts the approximate location of the gate emplacement holes relative to the WP. The WP and all gages were located in Bed 3 (as was the earlier Diamond Mine HE shot) tuff. Bed 3 is more homogeneous than Beds 2 and 4 which lie below and above it, respectively. The primary reason for choosing Bed 3, however, is its higher volume of air-filled porosity as illustrated in Fig. 2.5. The representative load-unload hydrostats shown there were constructed by Terra Tek^[8] from laboratory data from nine core samples drawn from sites of previous tests in Area 16. An earlier test, also employing a 1000-lb nitromethane high explosive source, was conducted for a WP in nearly saturated tuff in the Hudson Moon reentry drift in NTS Area 4.^[9] The two shots are part of a combined theoretical and experimental investigation of the relevance of material properties to the ground motion and stress pulse attenuation characteristics in the amplitude range of interest to the stemming and containment problem (approximate range of 20 to 1 kbar). The program was directed by the DNA Materials Properties Subcommittee, chaired by C. B. McFarland of Headquarters, DNA.

The Mine Dust HE test provided an excellent opportunity to test the ground motion predictive techniques developed under this contract. Radial stress and velocity gages were fielded at radii selected to provide a description of the stress pulse propagated from the explosive source out to a distance where its amplitude attenuates to the order of

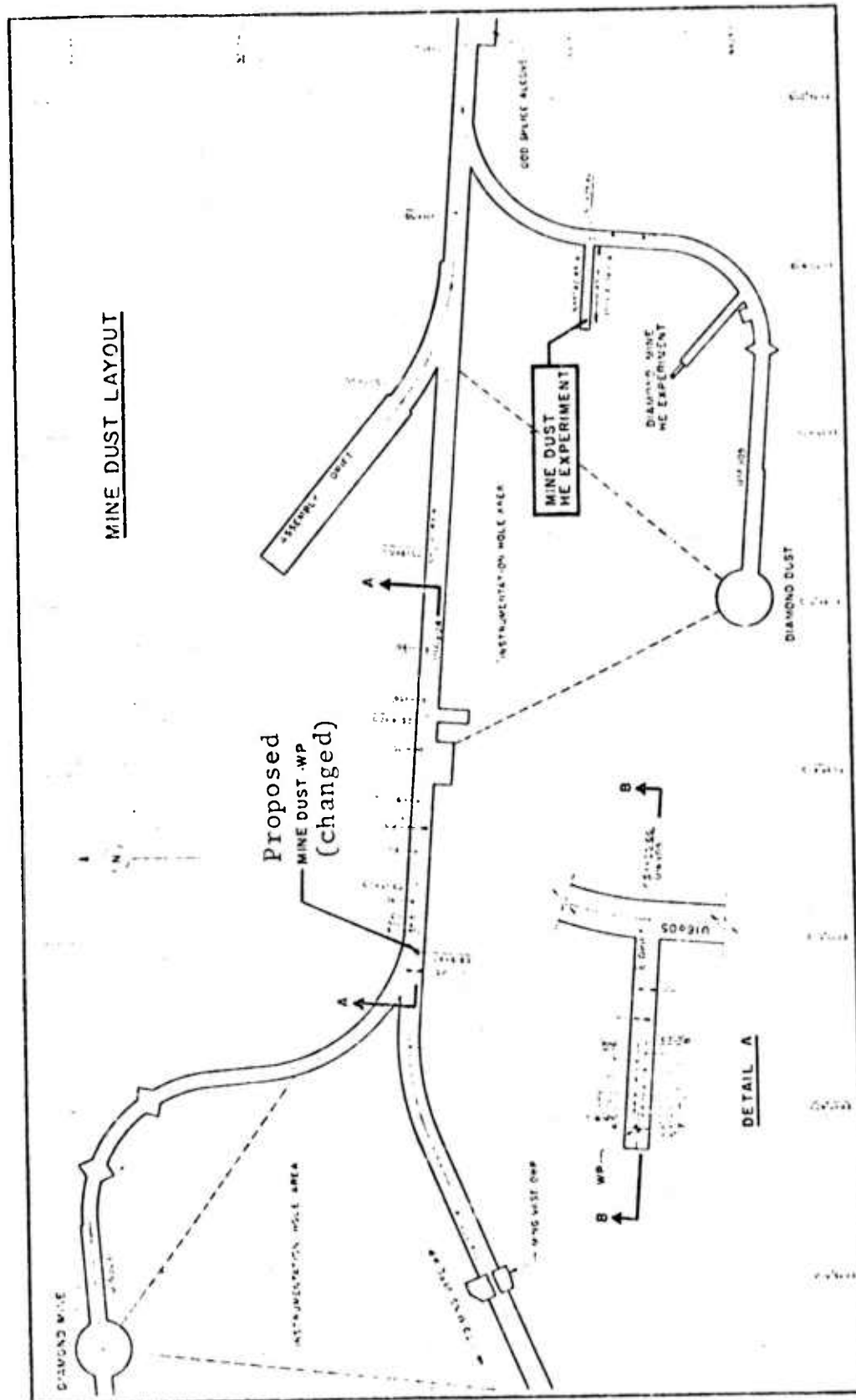


Fig. 2.5--Layout of Mine Dust HE experiment.

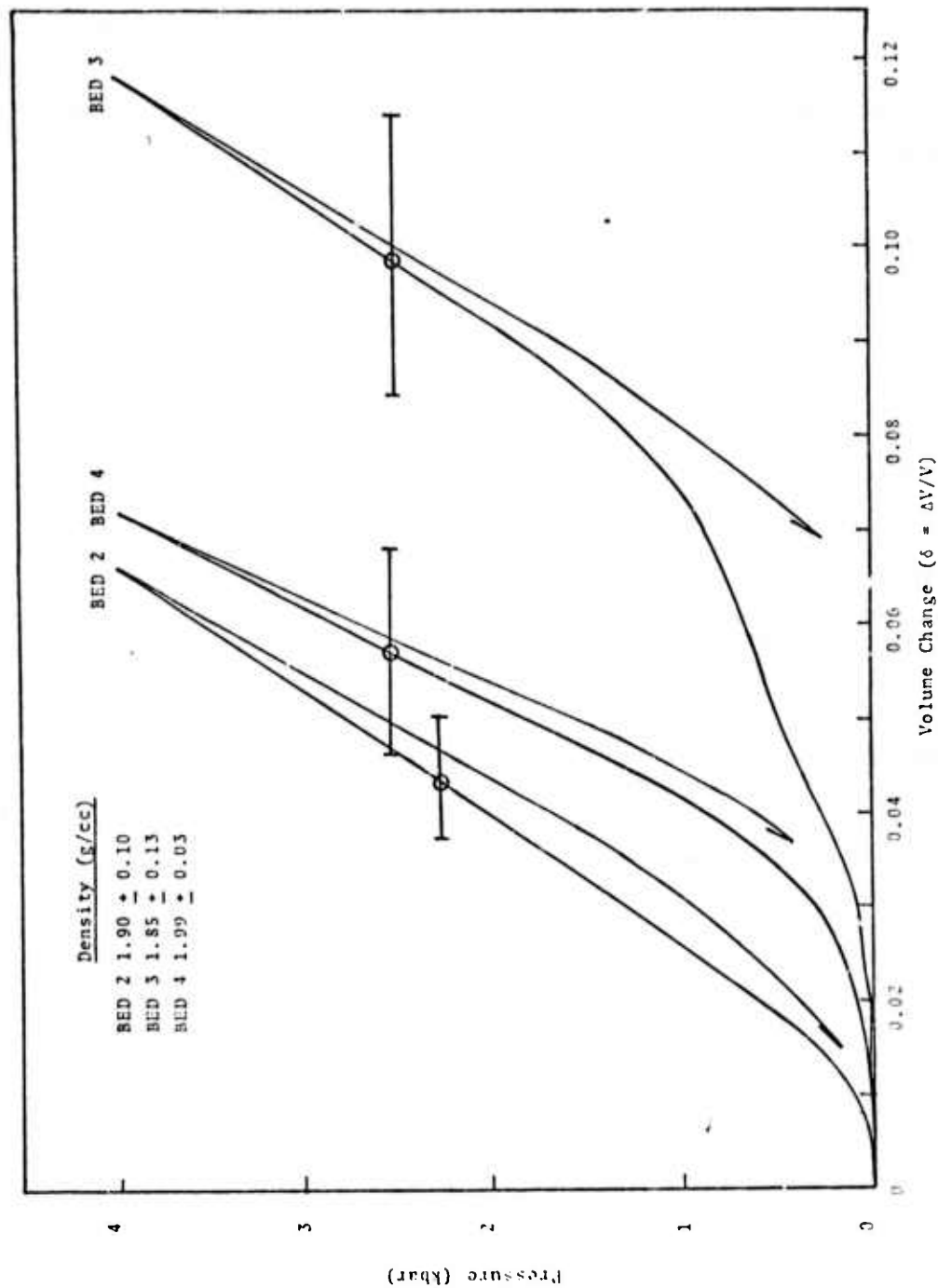


Fig. 2.5--Representative hydrostatic data for three beds in NTS Area 16.
Data generated by Terra Tek. [Ref. 8]

0.1 kbar. The test was conducted on May 10, 1972. Two pre-test calculations were made using the 1D SKIPPER computer code--one on May 7 and one on May 8. The high explosive burn portion of the calculations utilized an available equation of state for nitromethane. The isotropic response of the site medium was described using the S^3 general computer routine (TAMEOS) to generate the thermodynamic equation of state of partially saturated wet tuff. The pore crushup input parameter used in TAMEOS and the description of the deviatoric response of the tuff were based on limited static data for specimens taken at Mine Dust HE site.

The attenuation of the peak radial stress with distance predicted in the two calculations were sent to DNA Headquarters prior to the test.^[10] It became clear, even before gage recordings had been completely reduced, that the predictions were in close agreement with the peak stresses recorded by the in situ gages. On June 28, the DNA Materials Properties Subcommittee met at S^3 to review in detail the Mine Dust HE test results and the pre-test predictions. It was concluded from this comparison that the agreement was perhaps as good as any yet obtained in a field test.

In the following a brief description of the model used in the SKIPPER calculations is given. The predicted time resolved histories at the various gage locations are then presented on the same plot as the corresponding measured time history. Static material properties data were generated by Terra Tek (S. J. Green); radial stress histories were measured by SRI (C. Smith) and GRT (H. Kratz); velocity histories were measured by ATI (B. Hartenbaum).

2.2.2 Test Site Medium

Prior to digging the 45 ft tunnel to reach the WP (see Fig. 2.4), an exploratory core sample was drawn and hydrostatic load and unload tests were made by Terra Tek for

specimens at several locations along the borehole. Representative data from these tests are described by the "first exploratory hole" curve shown in Fig. 2.5. From the unloading path after compression above the pore crushup pressure ($p_{cr} \pm 2.0$ kbar), the volume function of the air-filled pores was estimated to be $n_0^{(3)} = 7.2\%$. After the tunnel was dug, samples were taken from these tests are described by the "instrument holes" curve shown in Fig. 2.6. From the unloading path for these data it would appear that the pore crushup pressure is $p_{cr} \pm 1.0$ kbar and the air-filled porosity is $n_0^{(3)} = 3.4\%$.

A core sample was drawn from a second exploratory hole in an attempt to better determine $n_0^{(3)}$. The value of $n_0^{(3)}$ for the second exploratory hole was determined by Terra Tek to be close to that of the instrument holes. Nevertheless, the uncertainty remained since the less compressible specimens appeared to be damaged during the coring process and more reliance was placed in the earlier data from the first exploratory hole.

The members of the DNA Materials Properties Subcommittee concluded from examination of the materials and the available hydrostatic test data that the air-filled porosity was probably bounded by

$$3.4\% < n_0^{(3)} < 7.2\% \quad (2.1)$$

and R. L. Bjork of S³ was asked to make predictive calculations for these limited cases using the same procedure that he used earlier in his successful Hudson Moon HE predictions for stresses above 1 kbar.^[9] A closer approximation for the air-filled porosity, however, was

$$n_0^{(3)} \pm 5\% \text{ to } 6.5\% \quad (2.2)$$

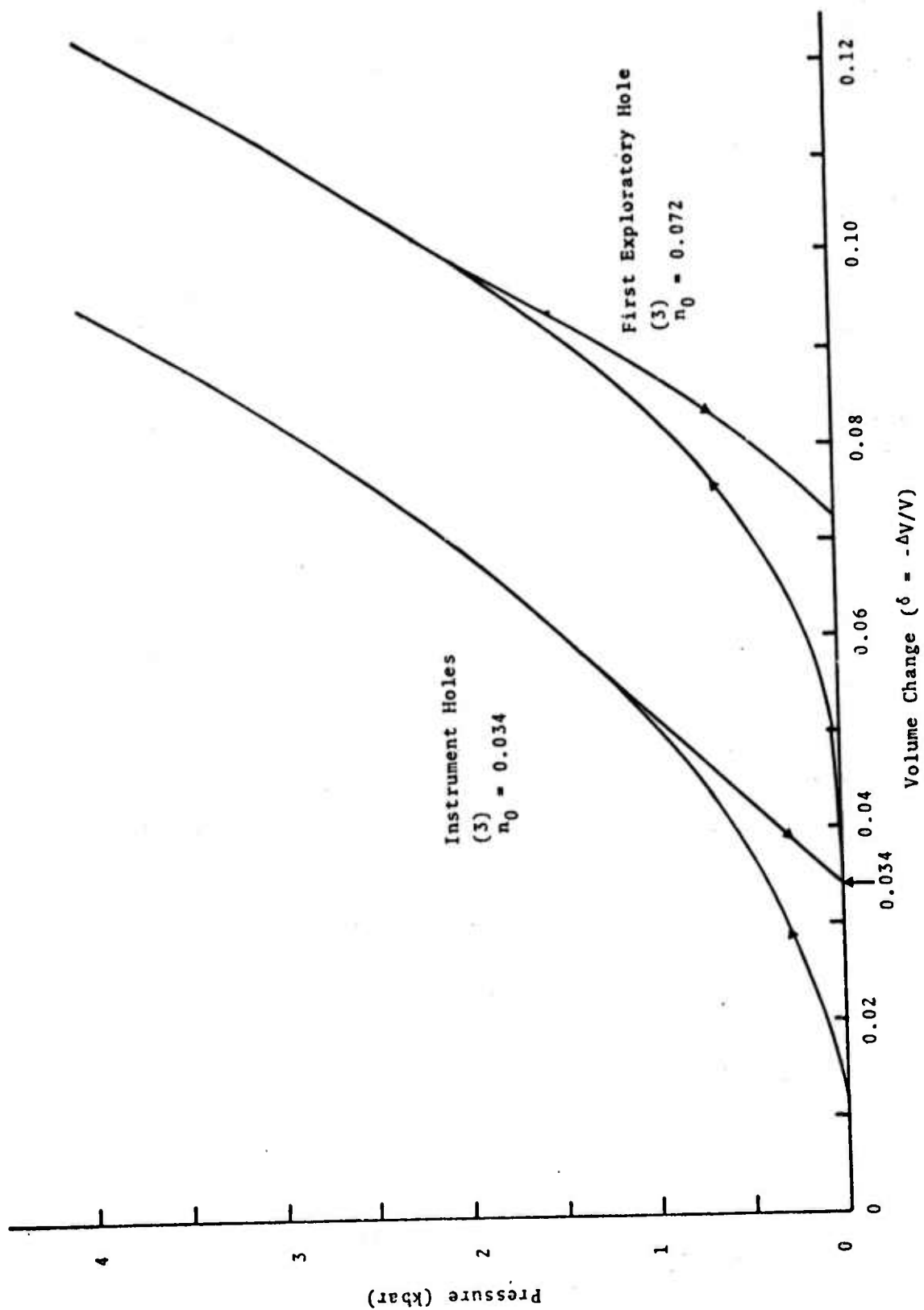


Fig. 2.6--Representative hydrostatic data for two sets of specimens taken at Mine Dust HE site. Data generated by Terra Tek.

with 5% considered is the best estimate. Consequently, S³ was also asked to make predictive calculations for these cases using a more complete material model developed under this contract in order to permit calculations down to 0.1 kbar. These latter two calculations will be described in the sequel.

The SKIPPER calculation for $n_0^{(1)} = 6.5\%$ was run on May 7 and the calculation for $n_0^{(1)} = 5\%$ was made on May 8. For both representations of the Mine Dust HE medium the water mass fraction was taken to be $M_w = 0.17$ and the tuff grain density was set equal to 2.4 g/cc. These values are representative of those measured by Terra Tek. The corresponding values of the bulk density and volume fractions of the rock-water-gas mixtures are listed in Table 2.1 for the two pre-test calculations. The corresponding percent of the pore space that is air-filled in each representation is also listed, 17.4% for the May 7 run and 13.7% for the May 8 run.

2.2.3 Isotropic Response Model for Medium

The isotropic response of the tuff was developed using the TAMEOS routine which calculates homogenized rock and water mixture states and stores them in a tabular array for use with standard ground motion codes. During a calculation, individual states are retrieved by a rapid table look-up routine. In the present calculations, the PEQ model was assumed, i.e., the two materials are assumed to shock to the same states as the pure materials and isentropically release without any heat transfer between the constituents. The equation of state utilized for the dry, compacted tuff component is a minor modification of that described in 3SR-1071 [3, p. 31]. It uses the Hugoniot shock-particle velocity fit

$$U = a + bu + du^2$$

TABLE 2.1
REPRESENTATION OF MINE DUST HE MEDIUM

	May 7 Run	May 8 Run
Water Mass Fraction, M_w	0.17	0.17
In-Situ Density (g/cc)	1.81	1.84
Tuff Grain Density (g/cc)	2.4	2.4
Grain Volume Fraction, $n_0^{(1)}$	0.62645	0.6365
Water Volume Fraction, $n_0^{(2)}$	0.30855	0.3135
Air Volume Fraction, $n_0^{(3)}$	0.065	0.05
$n_0^{(3)} / (n_0^{(2)} + n_0^{(3)})$	17.4%	13.7%

with $a = 3.5025 \text{ mm}/\mu\text{sec}$, $b = 0.70477$, and $d = 0.10055 \text{ (mm}/\mu\text{sec})^{-1}$. The solid grain density is taken to be 2.4 gm/cm^3 , and the initial density of the saturated mix (33 percent volume fraction water) is 1.9374. The Mie-Grüneisen equation of state is used for the tuff component, where the Grüneisen ratio G is determined from

$$G\rho = \text{const} = G_0 \rho_0 = 0.792.$$

The water equation of state is that of Bjork. [11]

TAMEOS also provides for several alternate treatments of air-filled porosity and the irreversible collapse of the air-filled pores, i.e., the pores may be considered as completely in the rock component or partitioned between the rock and water components. Since the Terra Tek data was available on the actual rock-water-air composite, it was convenient to select the model which treats the crushup process in a manner analogous to the p - α model of Herrmann. [12] In this version of TAMEOS [4] the porosity is defined relative to the rock-water composite,

$$\alpha = \frac{\frac{(1)}{n} + \frac{(2)}{n} + \frac{(3)}{n}}{\frac{(1)}{n} + \frac{(2)}{n}} = \frac{1}{\frac{(1)}{n} + \frac{(2)}{n}} \quad (2.3)$$

$$p = \frac{1}{\alpha} P(V/\alpha, E) \quad (2.4)$$

where P is evaluated from the PEQ table using the values of V , $\alpha(V)$ and E from the SKIPPER code for that particular time step and finite difference zone.

A form of $\alpha(V)$ in TAMEOS was selected which incorporates the key aspects of the physics of the irreversible crushup process, and requires a minimum of material para-

meter specifications. The function representing the loading curve consists of a plastic crush regime and an elastic regime. The plastic regime is modeled by the expression

$$\alpha = 1 \quad \text{for } p > p_c$$

$$\alpha = 1 + (\alpha_e - 1) \left(1 - \frac{p - p_e}{p_c - p_e} \right)^2 \quad \text{for } p_e \leq p \leq p_c \quad (2.5)$$

where

α_e = distension ratio at limit of elastic region,

p_e = pressure at upper limit of elastic region,

p_c = pressure at which air-filled pores are completely crushed.

Upon unloading the pores are assumed to completely recover for $p \leq p_e$, to remain completely closed for $p \geq p_c$, and α is allowed to vary smoothly between these end points of the plastic pore collapse regime. In the elastic regime the distension ratio is computed from

$$\alpha = \alpha_0 + \beta \left(1 - e^{-np/p_e} \right) \quad \text{for } 0 \leq p \leq p_e \quad (2.6)$$

where

α_0 = distension ratio at zero pressure.

Imposition of continuity of $d\alpha/dp$ at $\alpha = \alpha_e$ provides one equation for evaluation of the parameters β and n . The other condition is provided by evaluating the zero pressure bulk modulus (k) of the porous mixture.

In summary, the only input quantities required for the complete TAMEOS equation of state used in the present

calculations are the representative component specifications (given in Table 2.1) and values for α_0 , k , p_e (or, alternatively, α_e) and p_c . Values used for the May 7 and May 8 SKIPPER calculations are presented in Table 2.2. The values for p_c were approximated from the Terra Tek data presented in Fig. 2.6, and the value used for p_e was estimated from earlier LLL data reported by Stephens et al^[13] for the Diamond Dust Site in Area 16 at NTS. The value for k was estimated from the acoustic velocity measurements in this earlier report. In Table 2.2 the corresponding values of α_e are also listed.

In Fig. 2.7 the low pressure isotropic response model generated by TAMEOS using the input data in Tables 2.1 and 2.2 is depicted for the May 8 Run. The unloading curve after loading above the crushup pressure is seen to fall close to the data reported by Stephens et al^[13]. At high pressures the shock processing of the homogenized rock/water mix can vaporize the water. This effect is included in the TAMEOS treatment as is illustrated by the sudden volume increases in the release isentrope curves shown in Fig. 2.8. The curves are for a saturated mix ($M_w = 0.17$) whereas the actual SKIPPER calculations account for the presence of air-filled porosity; the extra pV energy in the calculations produces vaporization at pressures somewhat lower than depicted in Fig. 2.8.

2.2.4 Deviatoric Response Model for Medium

The curve marked "measured" in Fig. 2.9 summarizes the data taken by Terra Tek on deviatoric stress as a function of deviatoric strain that was available prior to the test. In the absence of more complete information, the deviatoric stress in the pre-test calculations was treated by an elastic-plastic model with a Mohr-Coulomb yield condition,

$$S_1^2 + S_2^2 + S_3^2 \leq \frac{2}{3} [Y(p)]^2 \quad (2.7)$$

TABLE 2.2
CRUSHUP PARAMETERS FOR PRE-TEST MINE DUST HE CALCULATIONS

	May 7 Run	May 8 Run
Crushup Pressure, p_c (kbar)	1.5	1.25
Elastic Pressure, p_e (kbar)	0.15	0.15
Bulk Modulus at Zero Pressure, k (kbar)	27.5	27.5
Initial Distension Ratio, α_0	1.0695	1.0526
Distension Ratio at Elastic Limit, α_e	1.0623	1.0459

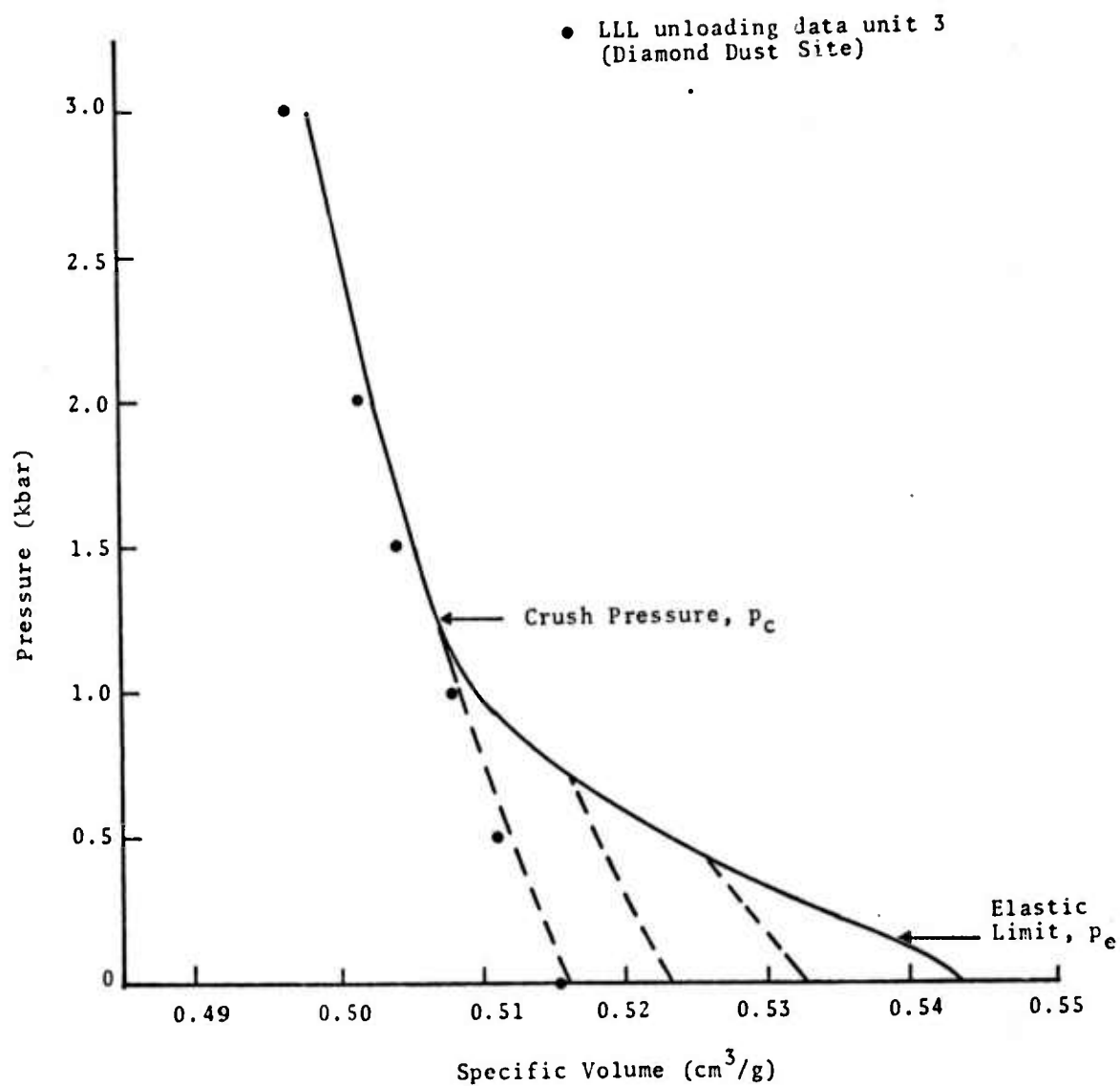


Fig. 2.7--Irreversible crushup model generated by TAMEOS for May 8 Run (5% air-filled porosity). The model closely reproduces unloading data reported by LLL for samples selected in the vicinity of the earlier Diamond Dust shot.
[Ref. 13]

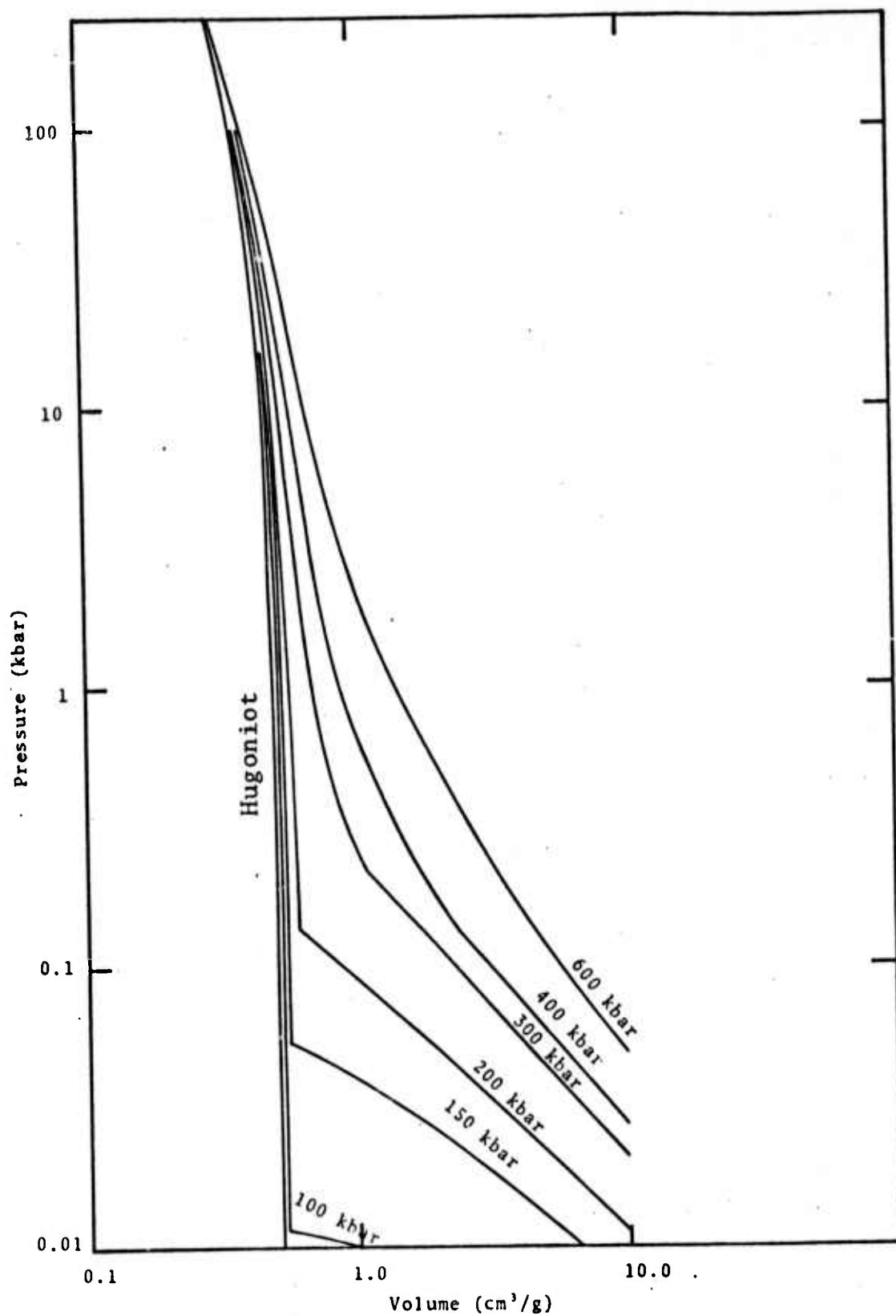


Fig. 2.8--Hugoniot and release isentrope for saturated tuff ($M_w = 0.17$).

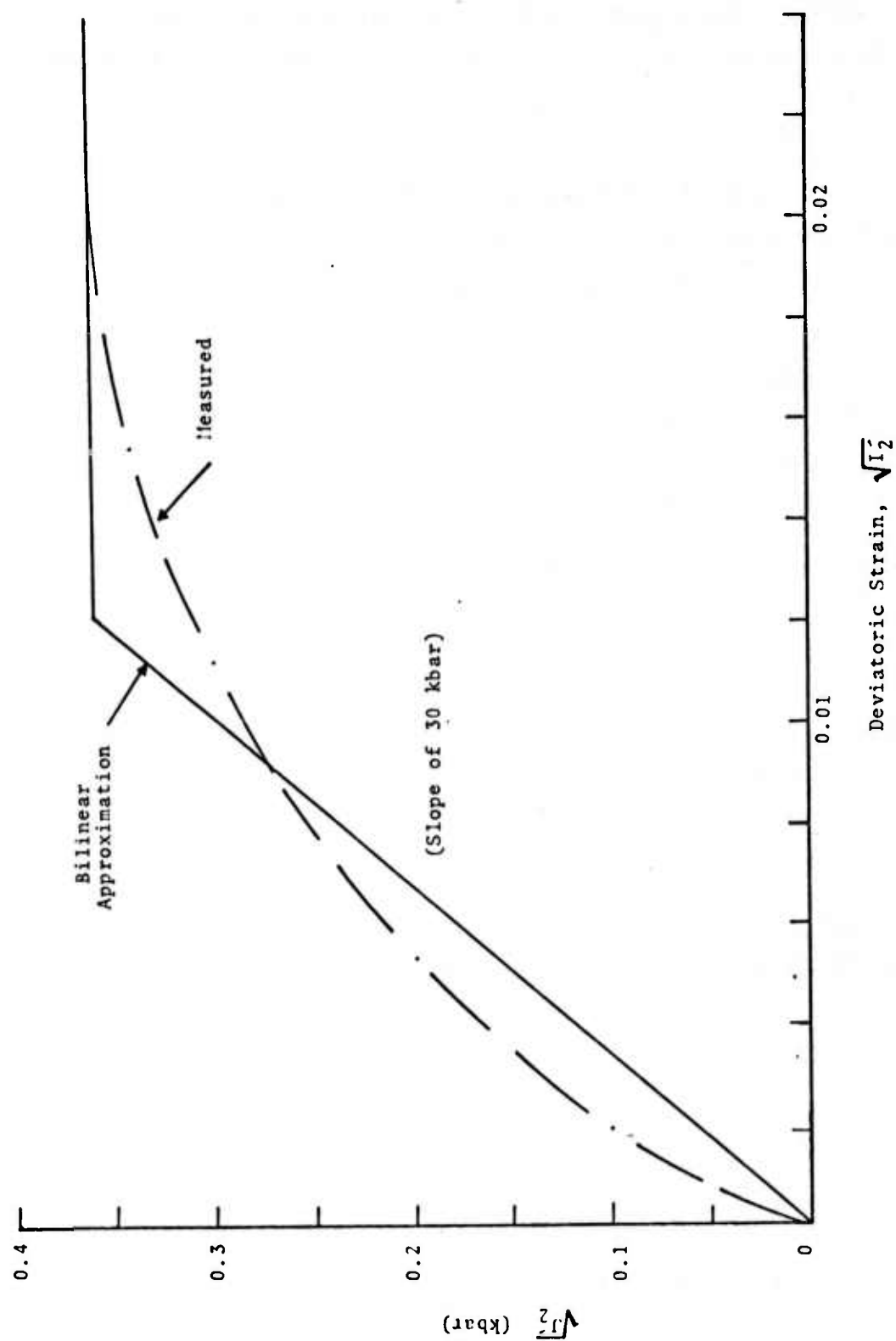


Fig. 2.9--Representative triaxial test data for specimens taken from instrument holes at Mine Dust HE site. Data generated by Terra Tek for a confining pressure of 4.0 kbar.

where the S_i are the components of the principal deviatoric stress and $Y = Y(p)$ is the yield stress in shear.

Within the elastic region the stress and strain deviators are related by Hooke's law for shear deformation,

$$s_{ij} = 2\mu e_{ij} \quad (2.8)$$

where μ is the shear modulus of the material. Multiplying both sides by itself yields

$$\sqrt{J_2} = 2\mu\sqrt{I_2} \quad (2.9)$$

where J_2 and I_2 are the second invariants of the stress and strain deviator tensors,

$$J_2 = \frac{1}{2} s_{ij} s_{ij} \quad I_2 = \frac{1}{2} e_{ij} e_{ij} \quad (2.10)$$

When the shear stress reaches a critical value,

$$J_2 = \frac{1}{3} Y(p)^2 \quad (2.11)$$

the material is restricted from going outside the yield surface, i.e.,

$$\sqrt{J_2} \leq Y(p)/\sqrt{3} \quad (2.12)$$

Since J_2 and I_2 are invariants they may be evaluated along principal axes where the expressions reduce to

$$J_2' = \frac{1}{2} (S_1^2 + S_2^2 + S_3^2) \quad (2.13)$$

$$= \frac{1}{6} [(\sigma_1 - \sigma_2)^2 + (\sigma_2 - \sigma_3)^2 + (\sigma_3 - \sigma_1)^2]$$

$$I_2' = \frac{1}{2} (e_1^2 + e_2^2 + e_3^2) \quad (2.14)$$

$$= \frac{1}{6} [(\epsilon_1 - \epsilon_2)^2 + (\epsilon_2 - \epsilon_3)^2 + (\epsilon_3 - \epsilon_1)^2]$$

In the triaxial tests the radial and hoop components of total stress (σ) and total strain (ϵ) are equal so that one has simply

$$\sqrt{J_2'} = \frac{1}{\sqrt{3}} |\sigma_1 - \sigma_2| \quad \sqrt{I_2'} = \frac{1}{\sqrt{3}} |\epsilon_1 - \epsilon_2|$$

Consequently, the slope on the "measured" curve in Fig. 2.9 can be replaced by the simple bilinear approximation shown there, i.e., a constant shear modulus of $\mu = 15$ kbar. The corresponding yield stress at the confining pressure of 4 kbar is

$$Y_0 = \sqrt{3J_2'} = 0.632 \text{ kbar}$$

At lower confining pressures the yield strength is smaller and to reflect this effect the yield surface is represented by

$$\begin{aligned} Y(p) &= Y_0 \frac{p}{p_0} (2 - p/p_0) \quad \text{for } p \leq p_0 \\ &= Y_0 \quad \text{for } p \geq p_0 \end{aligned} \tag{2.16}$$

The value of $p_0 = 0.6$ kbar listed in Table 2.3 was estimated from the earlier LLL data reported by Stephens et al^[13] for the Diamond Dust site in Area 16 at NTS.

TABLE 2.3
DEVIATORIC STRENGTH PARAMETERS FOR PRE-TEST MINE DUST HE
CALCULATIONS

	May 7 Run	May 8 Run
Shear Modulus, μ (kbar)	15	15
Maximum Shear Strength, Y_0 (kbar)	0.623	0.623
Pressure for Maximum Strength, p_0 (kbar)	0.6	0.6

2.2.5 H.E. Source Equation of State

The burning process in the HE source was treated using the empirical Jones-Wilkins-Lee equation of state^[14] to describe the nitromethane detonation products. This equation is prescribed by the pVE relation

$$p = A \left(1 - \frac{\omega}{C_1 V} \right) e^{-C_1 V} + B \left(1 - \frac{\omega}{C_2 V} \right) e^{-C_2 V} + \frac{\omega E}{V} \quad (2.17)$$

where p is the pressure in dynes/cm²; V is the specific volume in cc/g; and E is the specific internal energy in ergs/g. The constants for nitromethane are

$$A = 2.093 \times 10^{12} \text{ dynes/cm}^2$$

$$B = 5.69 \times 10^{10} \text{ dynes/cm}^2$$

$$C_1 = 4.9632 \text{ g/cc}$$

$$C_2 = 1.3536 \text{ g/cc}$$

$$\omega = 0.3$$

In the SKIPPER calculations the density of nitromethane was taken as 1.128 g/cc, the detonation front propagated from the center of the sphere at wave speed of 6.287×10^5 cm/sec, and the chemical energy released on detonation was 4.53×10^{10} ergs/g. The corresponding Chapman-Jouguet pressure and density are 1.4×10^{11} dynes/cm² and 1.644 g/cc.

According to Fig. 2.8, the C.J. pressure of 140 kbars will cause the water to be vaporized in only a very small region near the high explosive source. The vaporization plays a negligible role, at most, in the two pre-test predictive calculations since they were run at an overburden pressure of 0.04 kbar.

2.2.6 Comparison of Predictions with Measurement

The peak radial stress as a function of distance is shown in Fig. 2.10 for each of the two pre-test SKIPPER calculations. The attenuation rate change apparent from the log-log plot in Fig. 2.10 reflects the transition from hydrodynamic behavior to a low stress regime where the strength of the medium predominates. The two SKIPPER runs give very nearly the same peak stresses for the full range of the calculations. For completeness, the three measurements of peak radial stress reported by Kratz in the earlier Diamond Mine HE test are shown for comparison. The radial stress time histories for the two prediction calculations are compared at $R = 3.27$ ft and 7.67 ft in Fig. 2.11, and at $R = 8.82$ ft and 16.83 ft in Fig. 2.12. It is apparent that the general shape of the stress histories as well as the amplitudes, are quite similar. Differences in the time of arrival of the peak values, however, are indicated.

In the semi-log plot of Fig. 2.13 the peak stress measurements by SRI (Smith) and GRT (Kratz) for the present Mine Dust HE shot are compared with the predictions. The agreement between the stress amplitude predictions and the present Mine Dust HE measurements is seen to be quite good. We note, however, that the gage at $R = 16.94$ ft recorded a value about double that which would be consistent with the other data. The gage at $R = 21.5$ ft recorded a value that exceeds the prediction by about the same amount that the value measured on the earlier Diamond Mine HE shot lies below the present predictions (see Fig. 2.10).

In Fig. 2.14 the time-of-arrival of the peak radial stress for the two prediction calculations are presented. The agreement with the SRI and GRT measurements is better

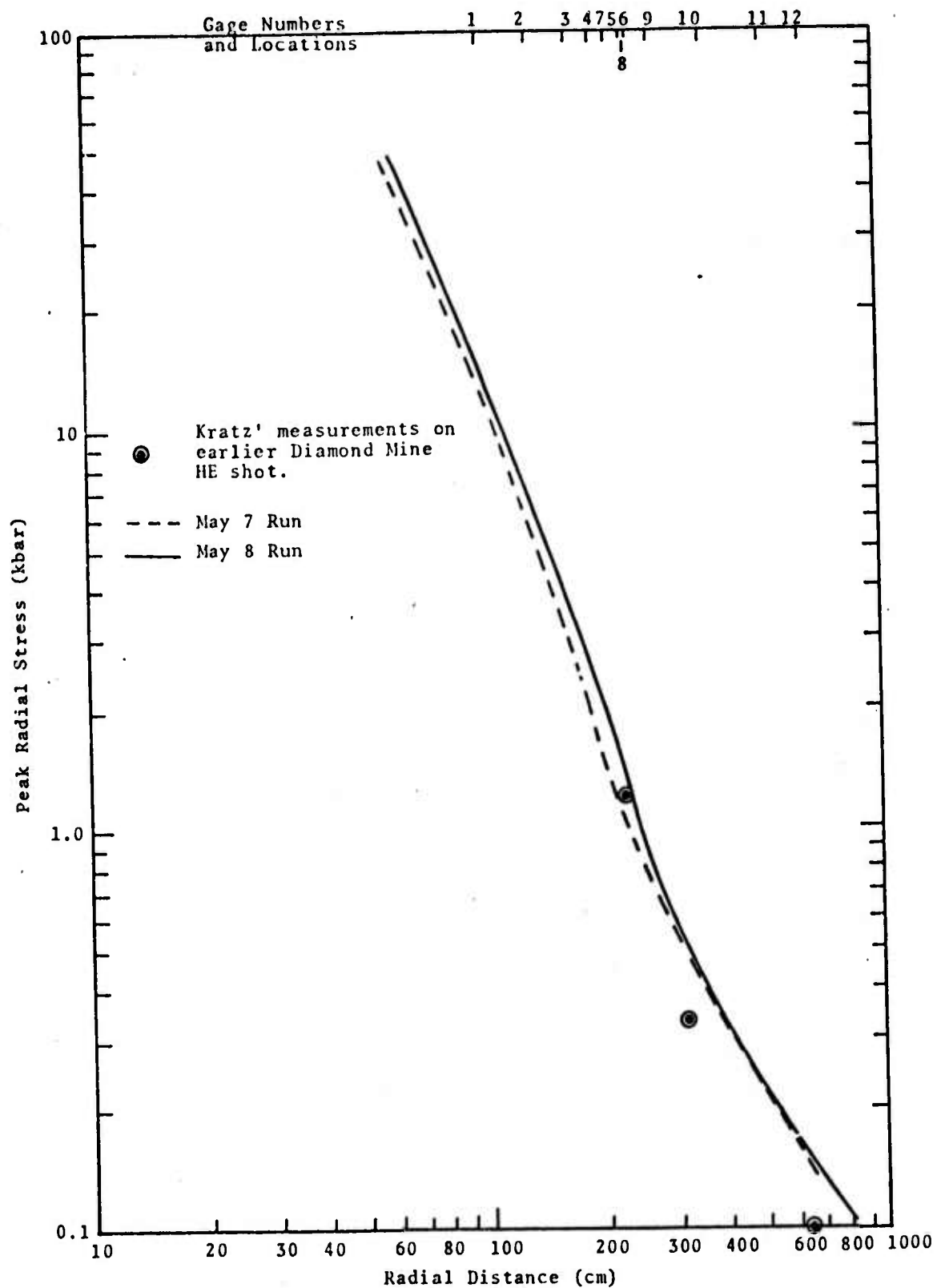


Fig. 2.10--Predicted attenuation of peak radial stress with distance from the source for the Mine Dust HE test: May 7 Run $\left(\begin{smallmatrix} (3) \\ n_0 = 6.5\% \end{smallmatrix} \right)$, May 8 Run $\left(\begin{smallmatrix} (3) \\ n_0 = 5\% \end{smallmatrix} \right)$.

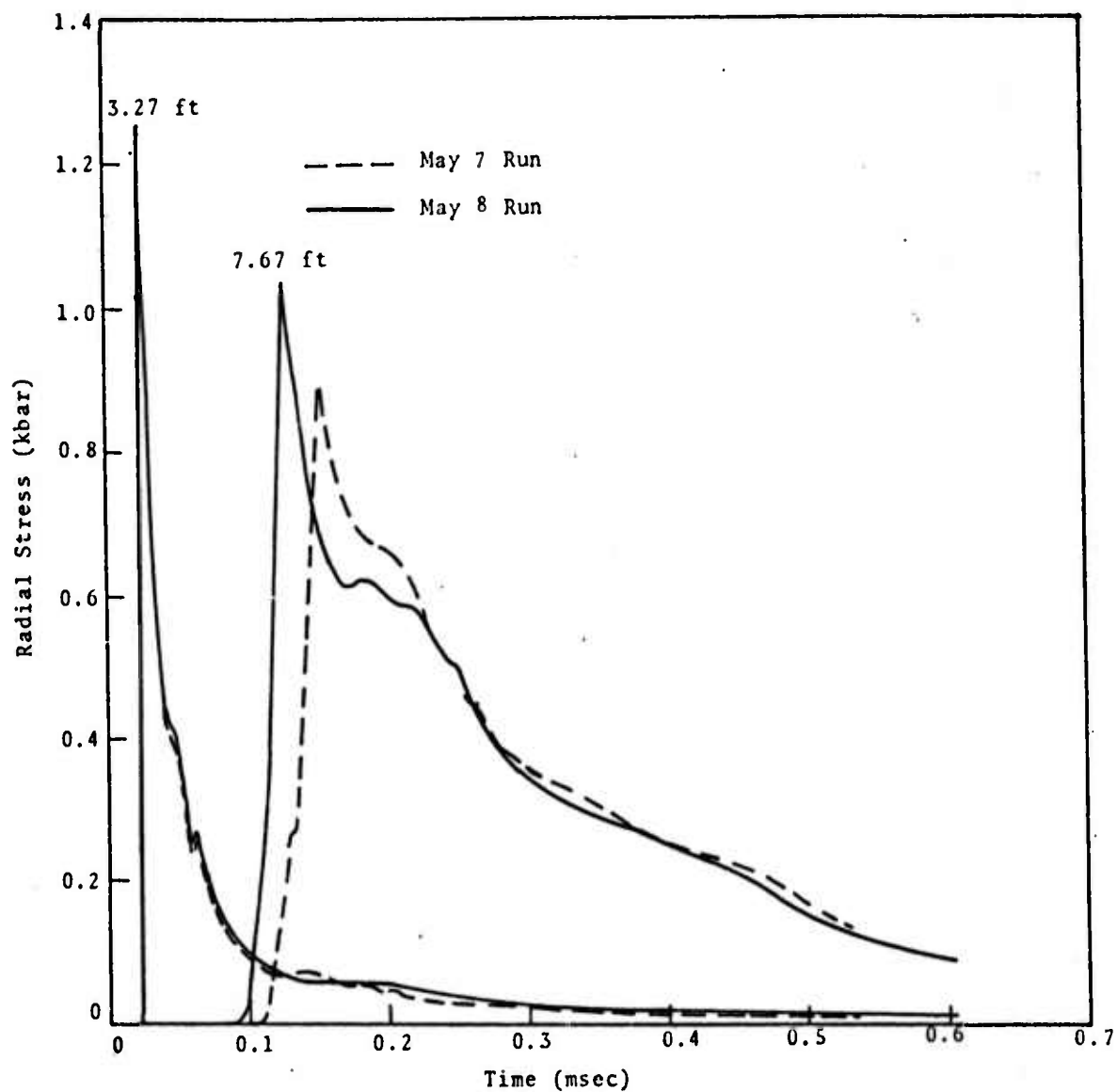


Fig. 2.11--Comparison of radial stress histories at $R = 3.27$ ft and 7.67 ft for the two Mine Dust HE prediction calculations: May 7 Run $\left(\begin{smallmatrix} (3) \\ n_0 = 6.5\% \end{smallmatrix} \right)$, May 8 Run $\left(\begin{smallmatrix} (3) \\ n_0 = 5\% \end{smallmatrix} \right)$.

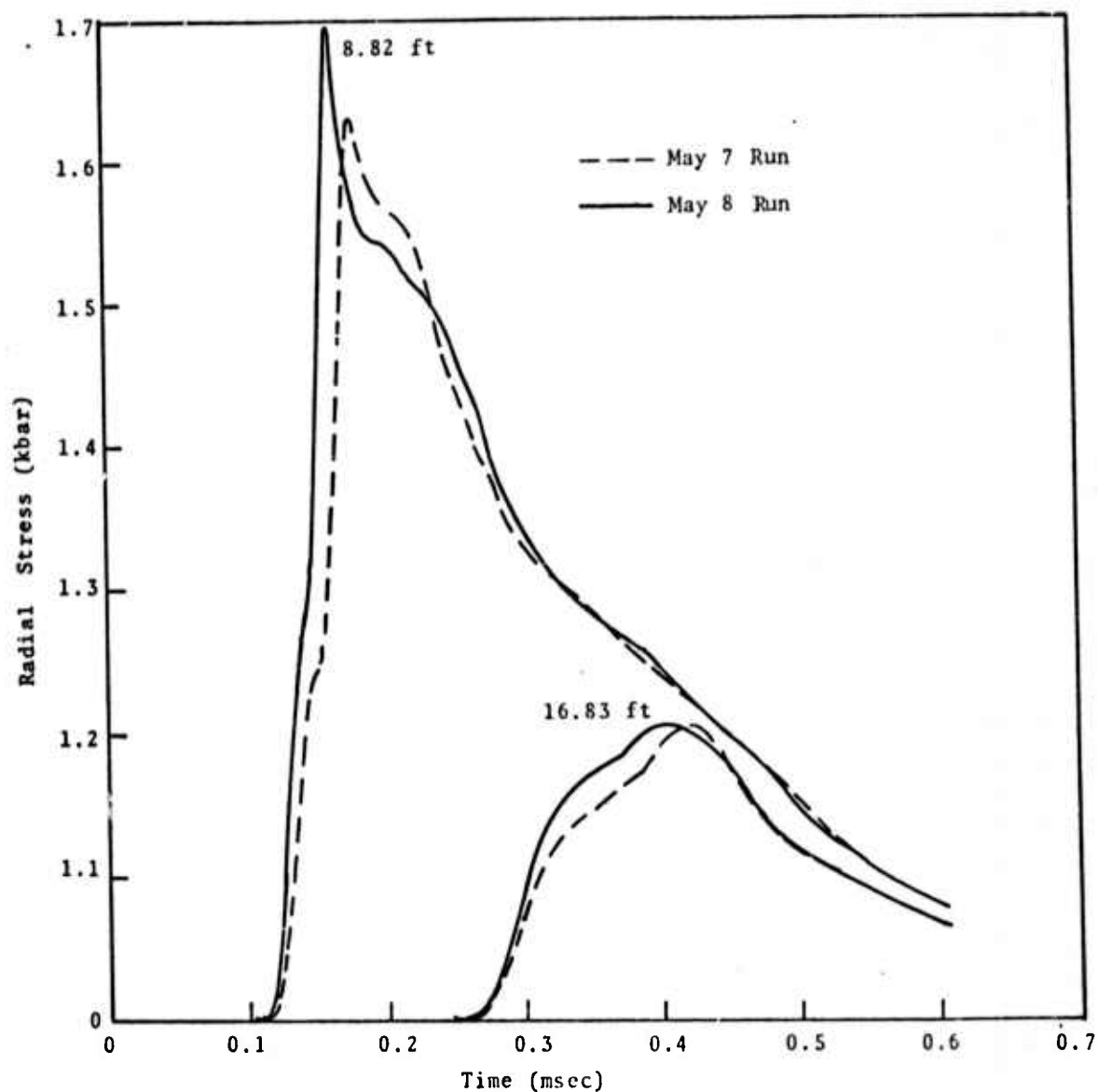


Fig. 2.12--Comparison of radial stress histories at $R = 8.82$ ft and 16.8 ft for the two Mine Dust HE prediction calculations: May 7 Run $\left(\begin{smallmatrix} (3) \\ n_0 = 6.5\% \end{smallmatrix} \right)$, May 8 Run $\left(\begin{smallmatrix} (3) \\ n_0 = 5\% \end{smallmatrix} \right)$.

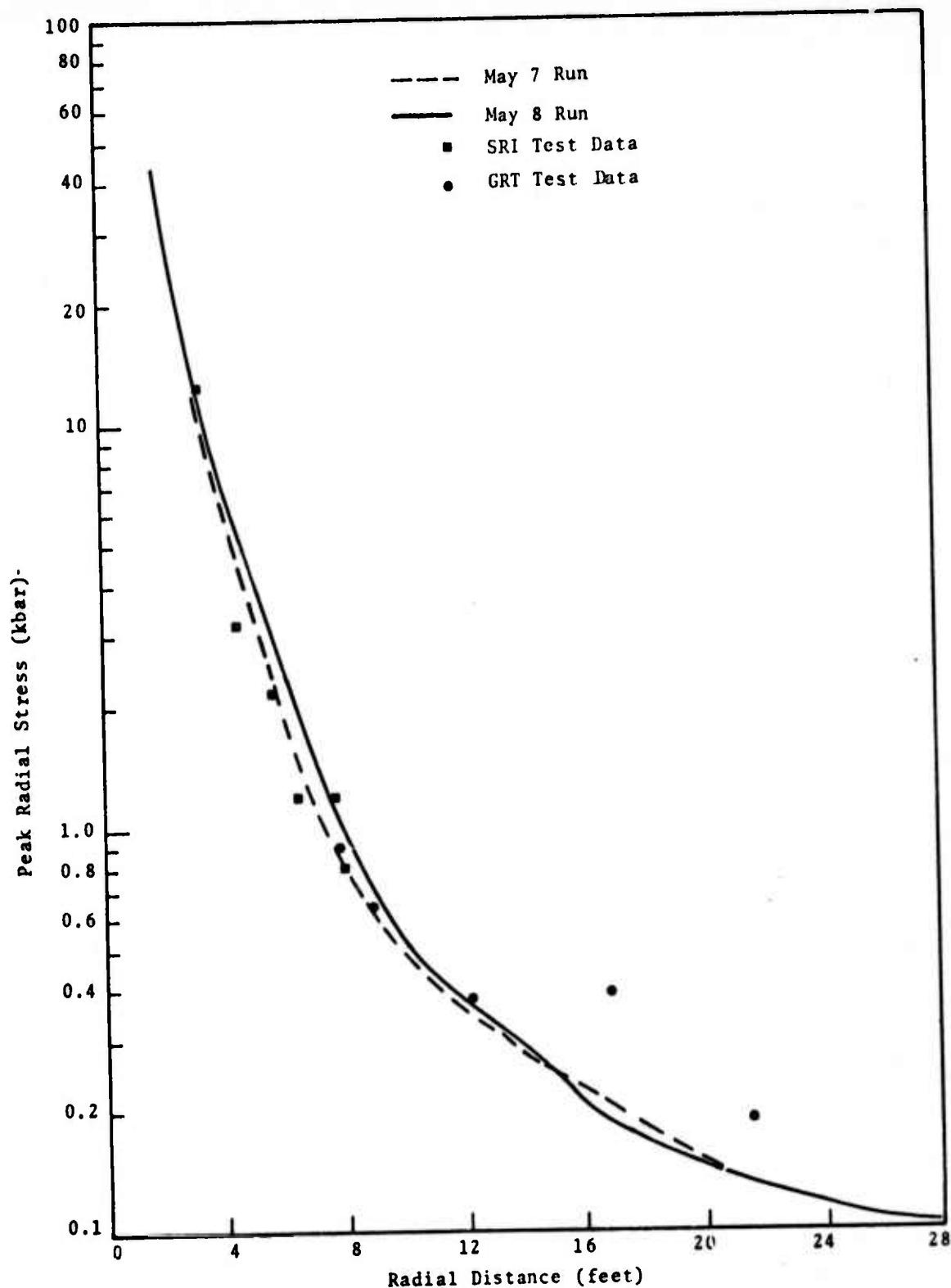


Fig. 2.13--Comparison of predicted stress attenuation curves with measured values of peak radial stress for the Mine Dust HE test: May 7 Run $\left(\begin{smallmatrix} (3) \\ n_0 = 6.5\% \end{smallmatrix} \right)$, May 8 Run $\left(\begin{smallmatrix} (3) \\ n_0 = 5\% \end{smallmatrix} \right)$.

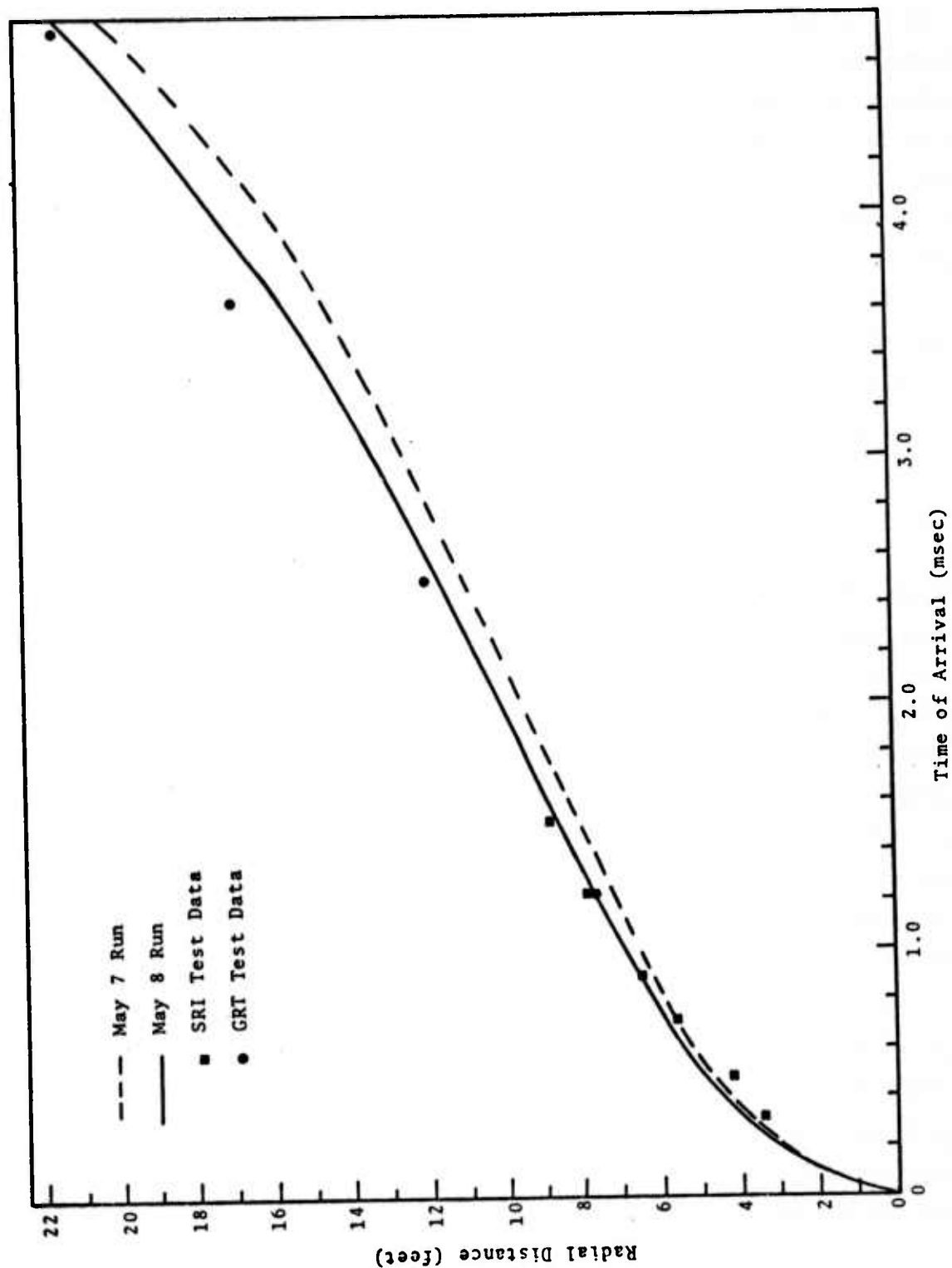


Fig. 2.14--Comparison of time-of-arrival measurements for peak stresses and predicted curves: May 7 Run $\left(n_0 = 6.5\% \right)$, May 8 Run $\left(n_0 = 5\% \right)$.

for the May 8 Run than the May 9 run; this supports the pre-test consensus that 5% air-filled porosity is the best estimate for the Mine Dust HE medium. Except for the anomalous recording on the gage at $R = 16.94$ ft, the agreement is very good. The predictions for the time-of-arrival of the foot of the pulse are not in such good agreement with the measurements as is illustrated in Fig. 2.15. These results imply that our model for the irreversible crushup behavior closely simulates the actual medium behavior, but the estimated value of the bulk modulus at zero pressure (k) was smaller than that of the medium.

Predicted radial stress profiles, for 5% air-filled porosity, are presented in Figs. 2.16 through 2.20. Once the peak pressure falls below $p_c = 1.25$ kbar, which occurs at about $R = 7$ ft according to Fig. 2.13, the model for the irreversible crushup and subsequent unloading of the medium becomes operative (see Fig. 2.7). The unloading wave travels at a velocity greater than the stress wave front. As it overtakes the front the stress profile shape changes rapidly, acquiring a two-hump character at about $t = 3.0$ msec, which persists thereafter. During this transition period the location of the peak stress, relative to the front, and its amplitude are very sensitive to the details of the irreversible crush behavior of the medium. This effect may have contributed to the anomalous GRT measurement at $R = 16.94$ ft.

Once the peak pressure falls below $p_e = 0.15$ kbar, which occurs at about $R = 20$ ft according to Fig. 2.13, the air-filled pores are no longer collapsed in the crushup model (see Fig. 2.7). The transition of the medium to an elastic regime is the basis for the increase in slope which occurs at about this value in Figs. 2.10 and 2.14.

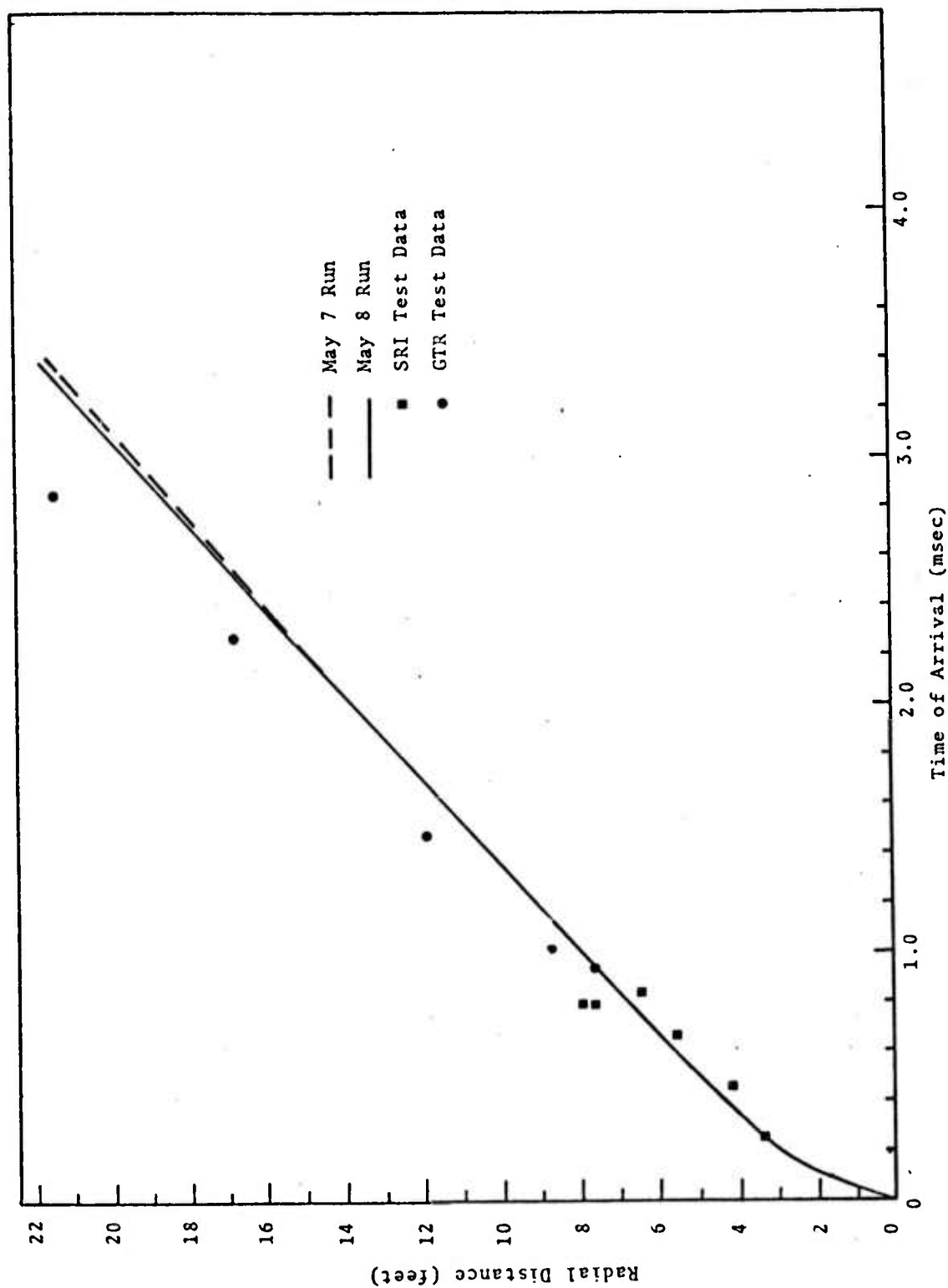


Fig. 2.15--Comparison of wave front arrival times observed with those calculated: May 7 Run $\left(n_0 = 6.5\% \right)$, May 8 Run $\left(n_0 = 5\% \right)$.

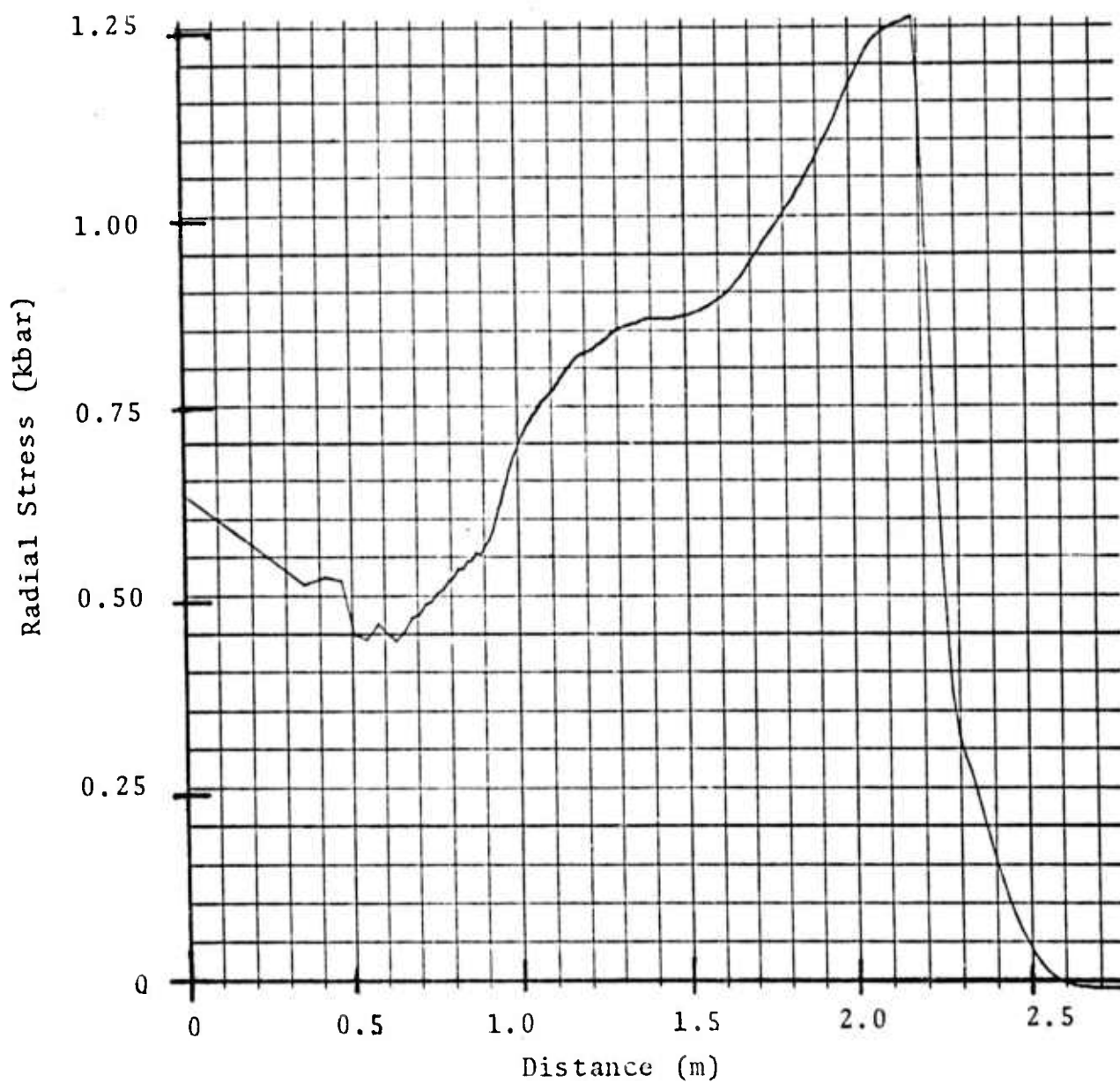


Fig. 2.16--Predicted radial stress profile at
 $t = 1.1 \text{ msec}$, May 8 Run $\left(\begin{smallmatrix} (3) \\ n_0 = 5\% \end{smallmatrix} \right)$.

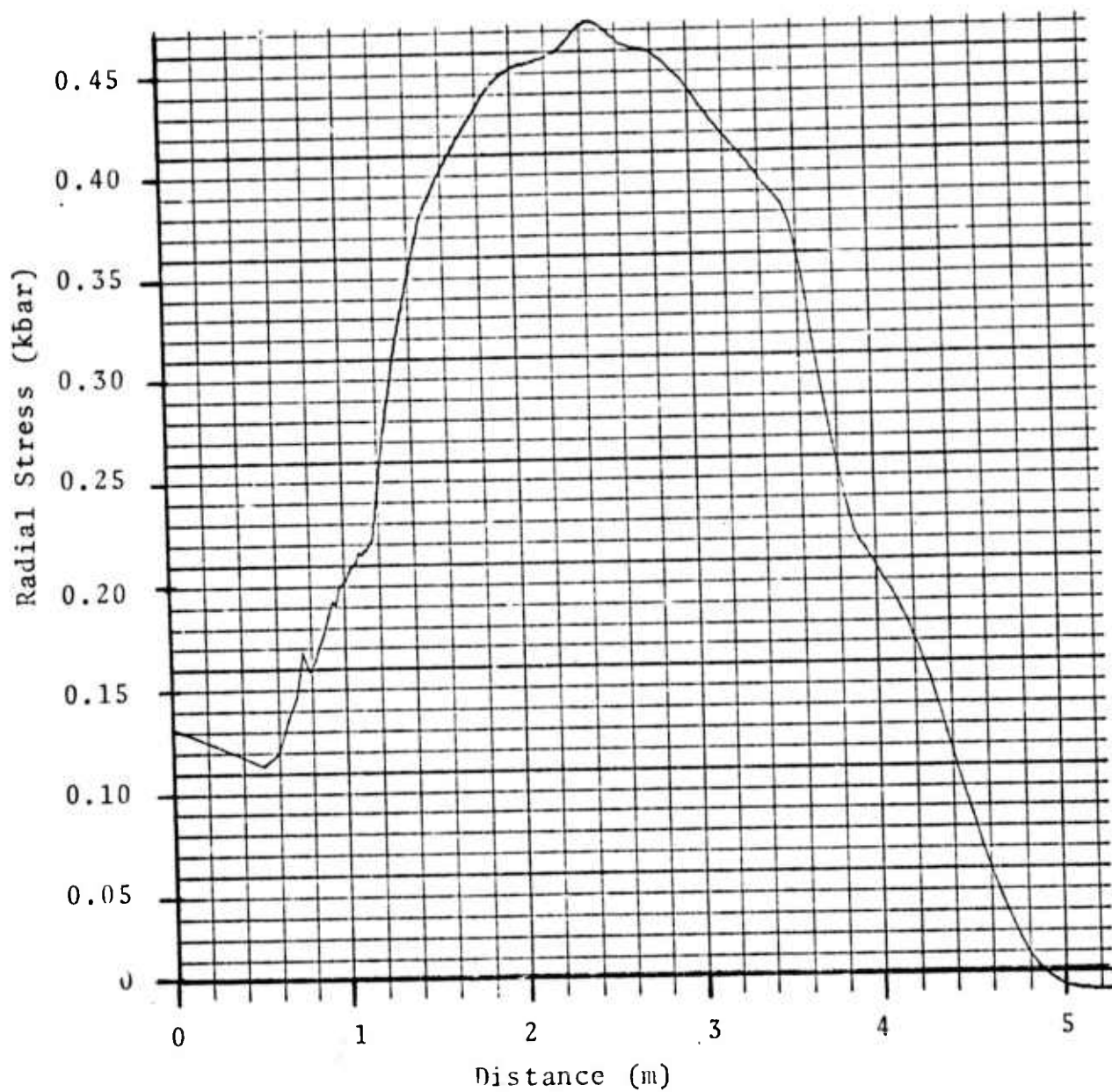


Fig. 2.17--Predicted radial stress profile at
 $t = 2.5 \text{ msec}$, May 8 Run $\left(\begin{smallmatrix} (3) \\ n_0 = 5\% \end{smallmatrix} \right)$.

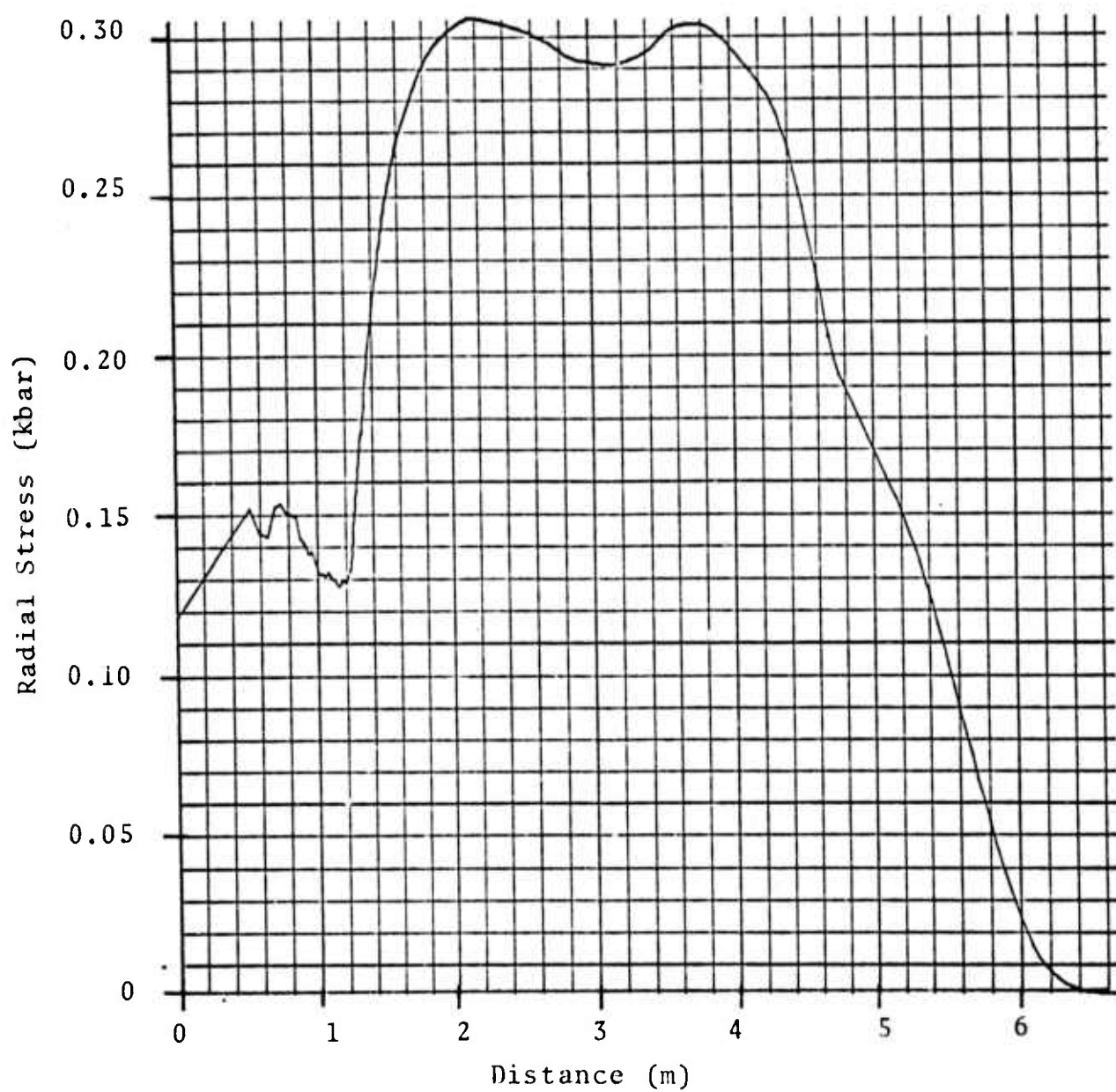


Fig. 2.18--Predicted radial stress profile at
 $t = 3.3 \text{ msec}$, May 8 Run $\left(\begin{smallmatrix} 3 \\ n_0 = 5\% \end{smallmatrix} \right)$.

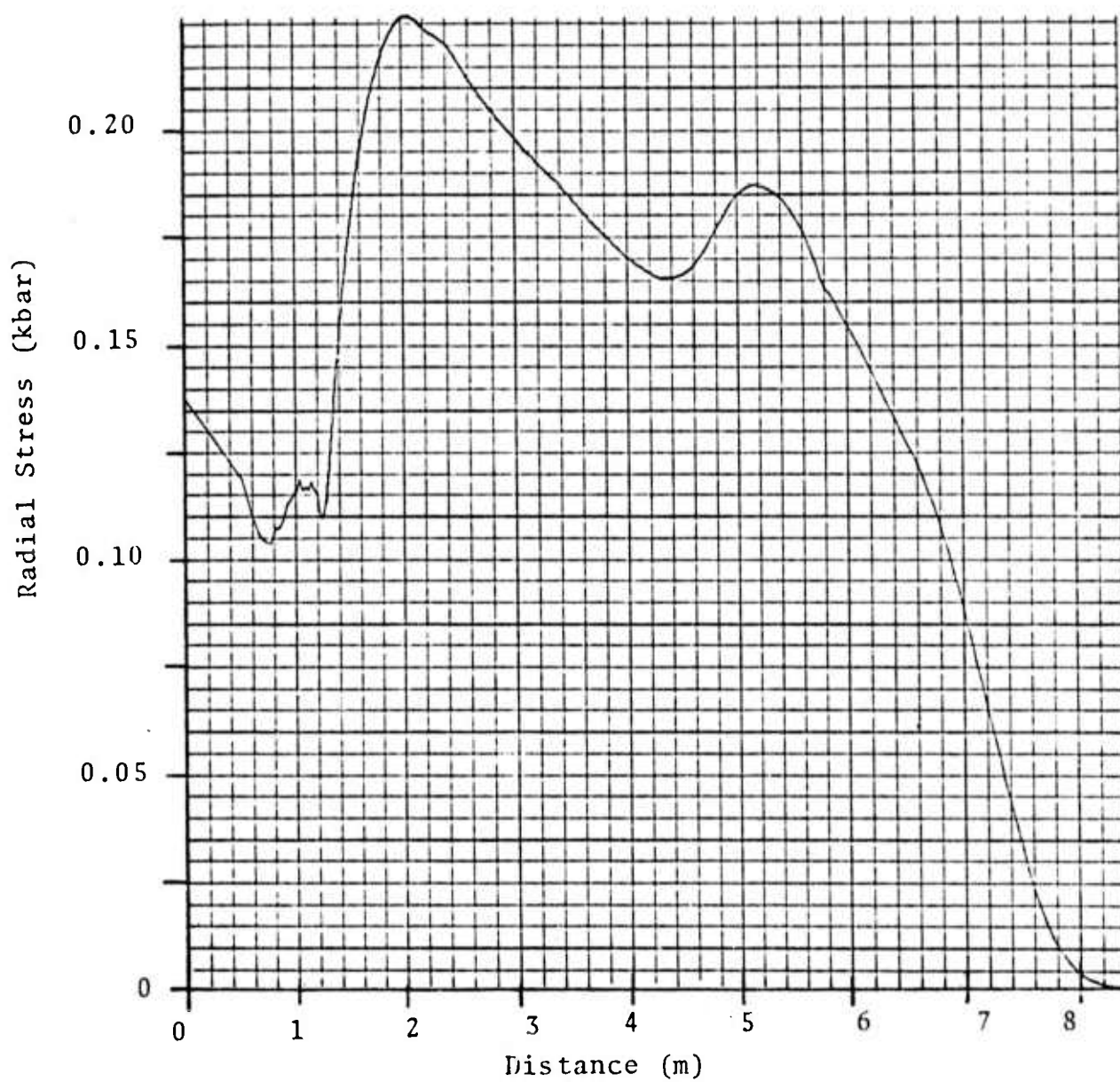


Fig. 2.19--Predicted radial stress profile at
 $t = 4.4 \text{ msec}$, May 8 Run $\left(\begin{smallmatrix} (3) \\ n_0 = 5\% \end{smallmatrix} \right)$.

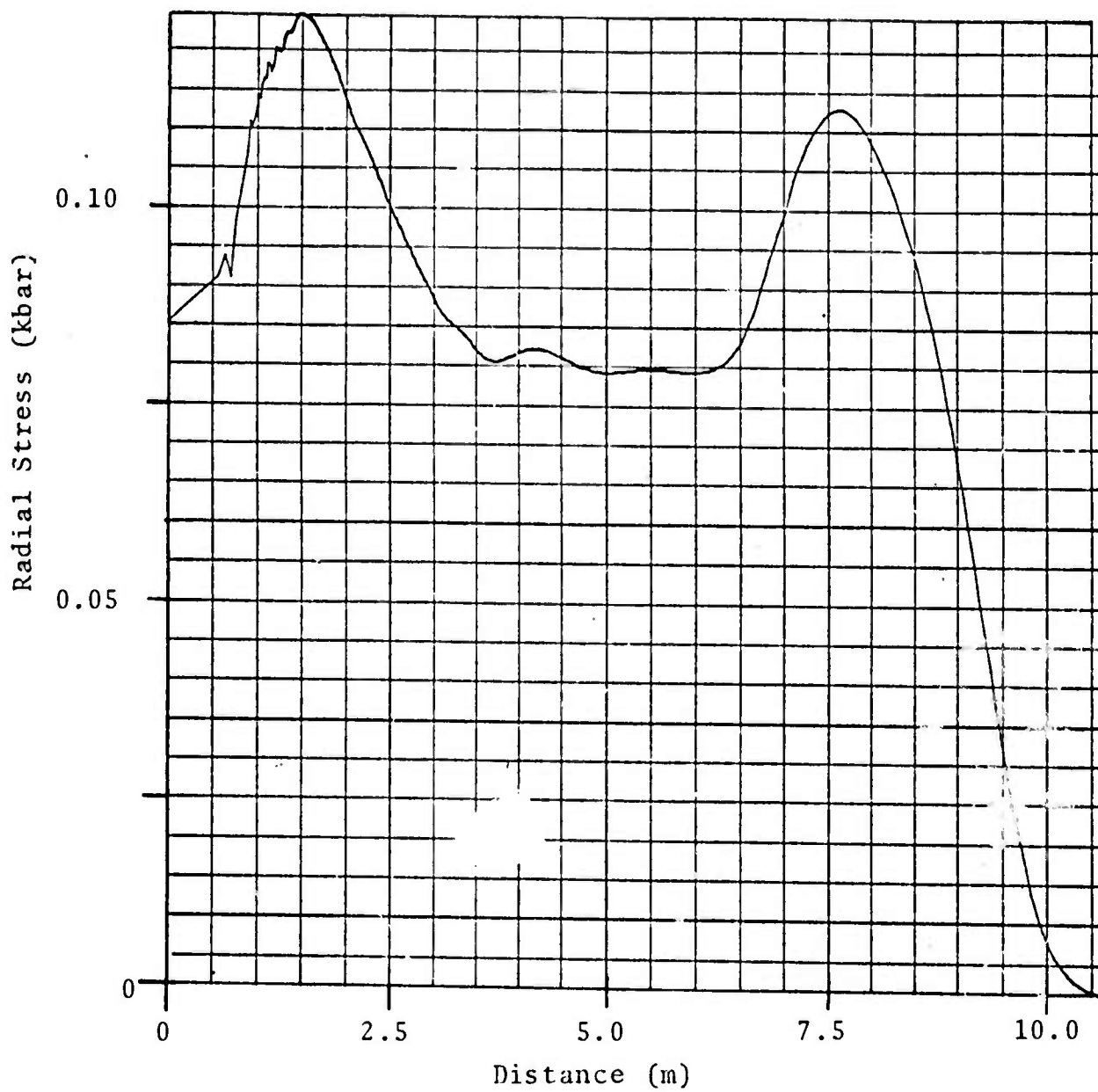


Fig. 2.20--Predicted radial stress profile at
 $t = 5.7 \text{ msec}$, May 8 Run $\left(\begin{smallmatrix} (3) \\ n_0 = 5\% \end{smallmatrix} \right)$.

In Figs. 2.21 through 2.26 the SRI measurements of radial stress history are compared with the corresponding prediction of the May 8 Run ⁽³⁾ $n_0 = 5\%$. Radial stress histories measured with the GRT gages are compared with the calculations in Figs. 2.27 through 2.31. Finally, the radial velocity histories measured with the ATI gages are compared with the predictions in Figs. 2.32 through 2.35.

The plots of the calculated stress histories clearly display an elastic precursor for radial distances between 6.34 ft and 16.83 ft. The wave front traverses this distance during the time interval of approximately 0.75 to 4.0 msec. It is difficult to detect such detail in the SRI recordings and the precursor appears to be absent from the recordings of the closer GRT gages. One explanation for this is a strong noise signal present in all the measurements. The signal was caused by the electronic circuitry and persisted from 0.4 to 1.7 msec (see Fig. 2.27). In subtracting out this signal it is possible that the detail required to resolve the precursor was lost when the front was located in the time interval affected.

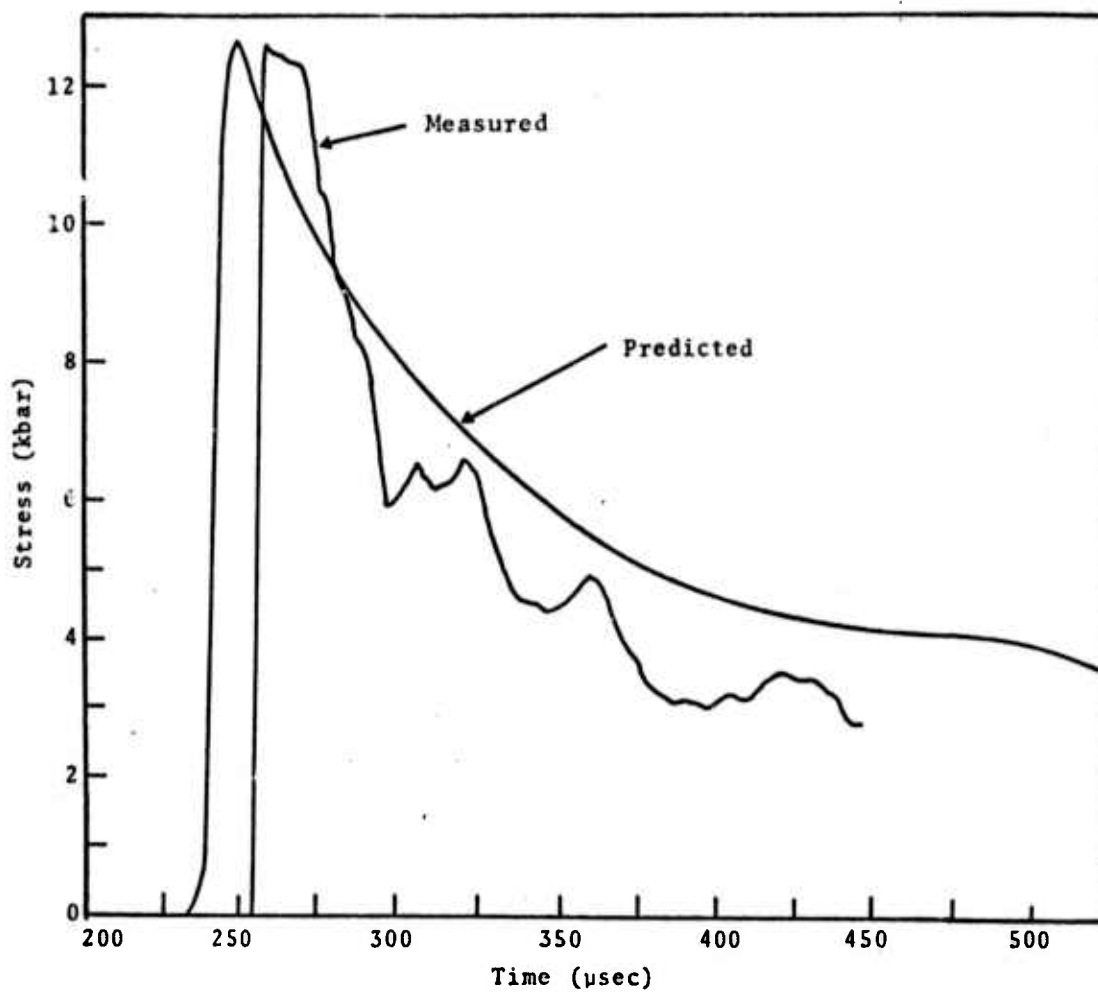


Fig. 2.21--Predicted (May 8 Run) and measured (SRI) stress histories at $R = 3.27$ ft and 3.35 ft respectively.

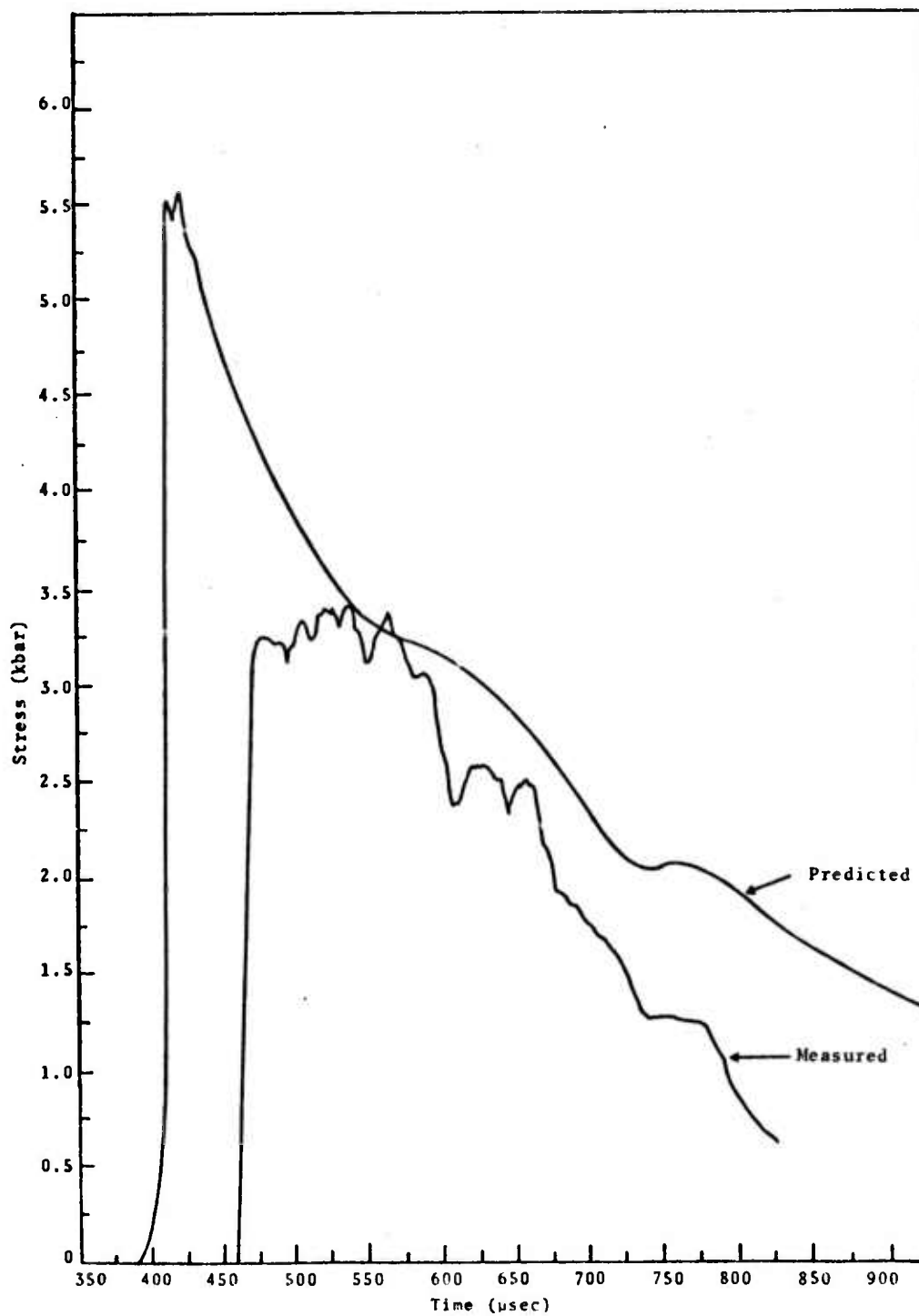


Fig. 2.22--Predicted (May 8 Run) and measured (SRI) stress histories at $R = 4.37$ ft and 4.46 ft respectively.

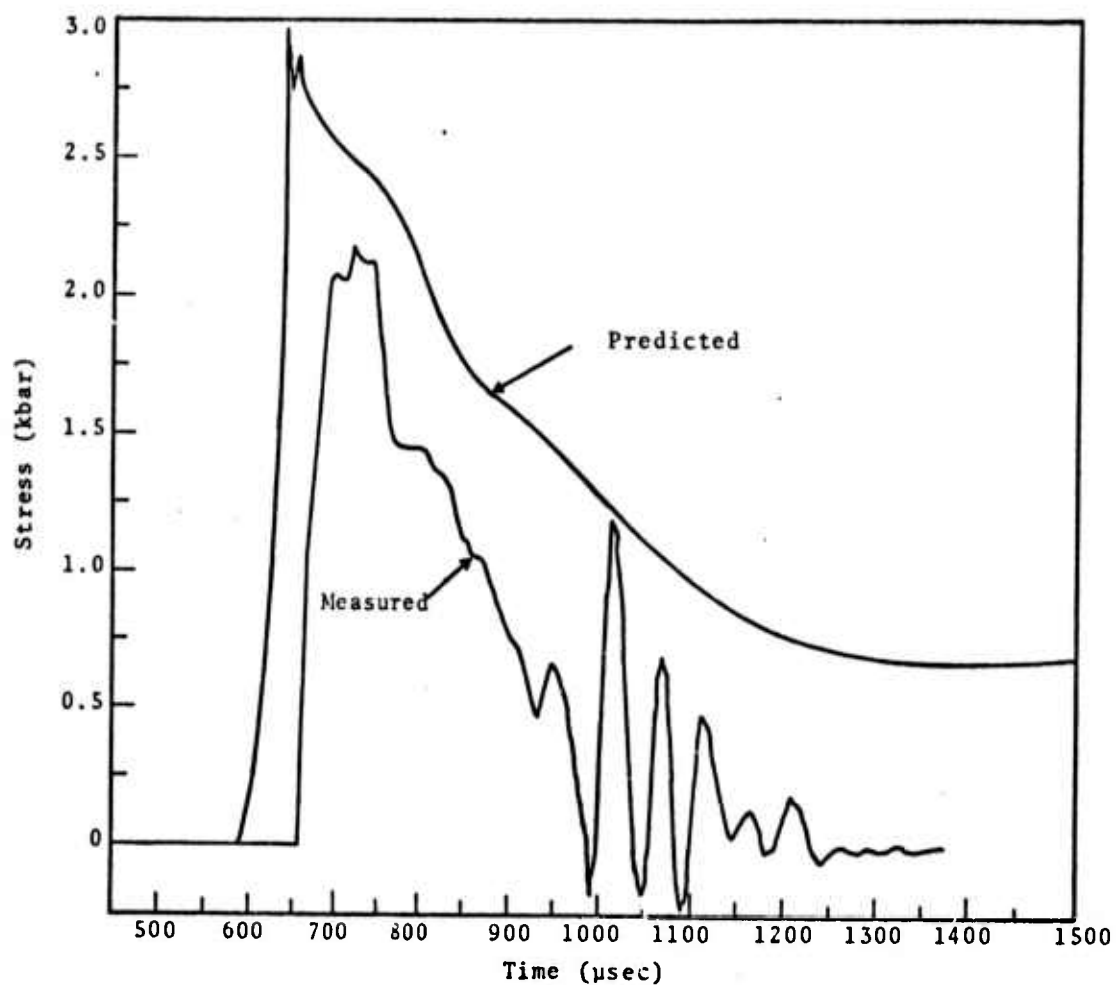


Fig. 2.23--Predicted (May 8 Run) and measured (SRI) stress histories at $R = 5.51$ ft and 5.63 ft respectively.

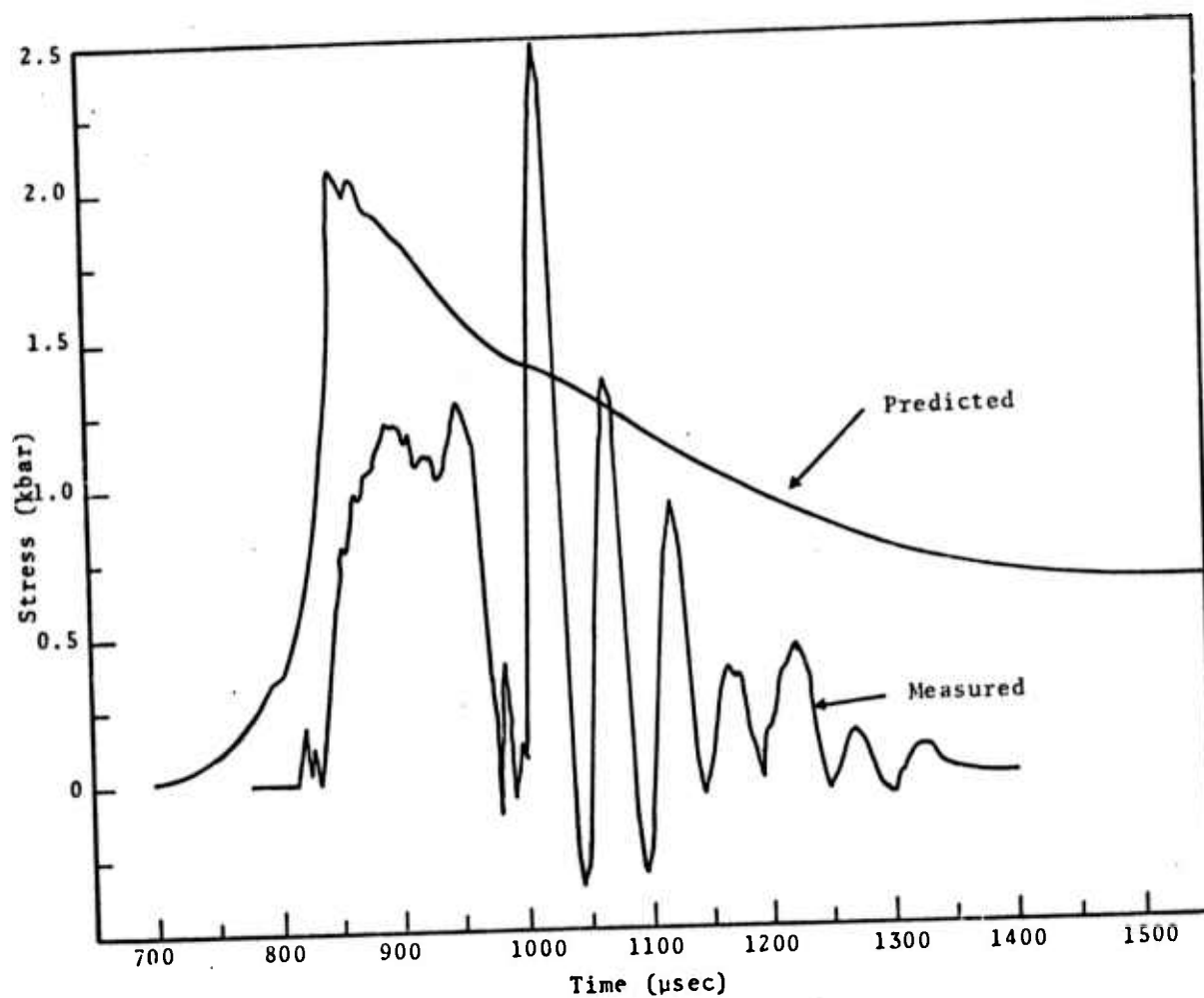


Fig. 2.24--Predicted (May 8 Run) and measured (SRI) stress histories at $R = 6.34$ ft and 6.45 ft respectively.

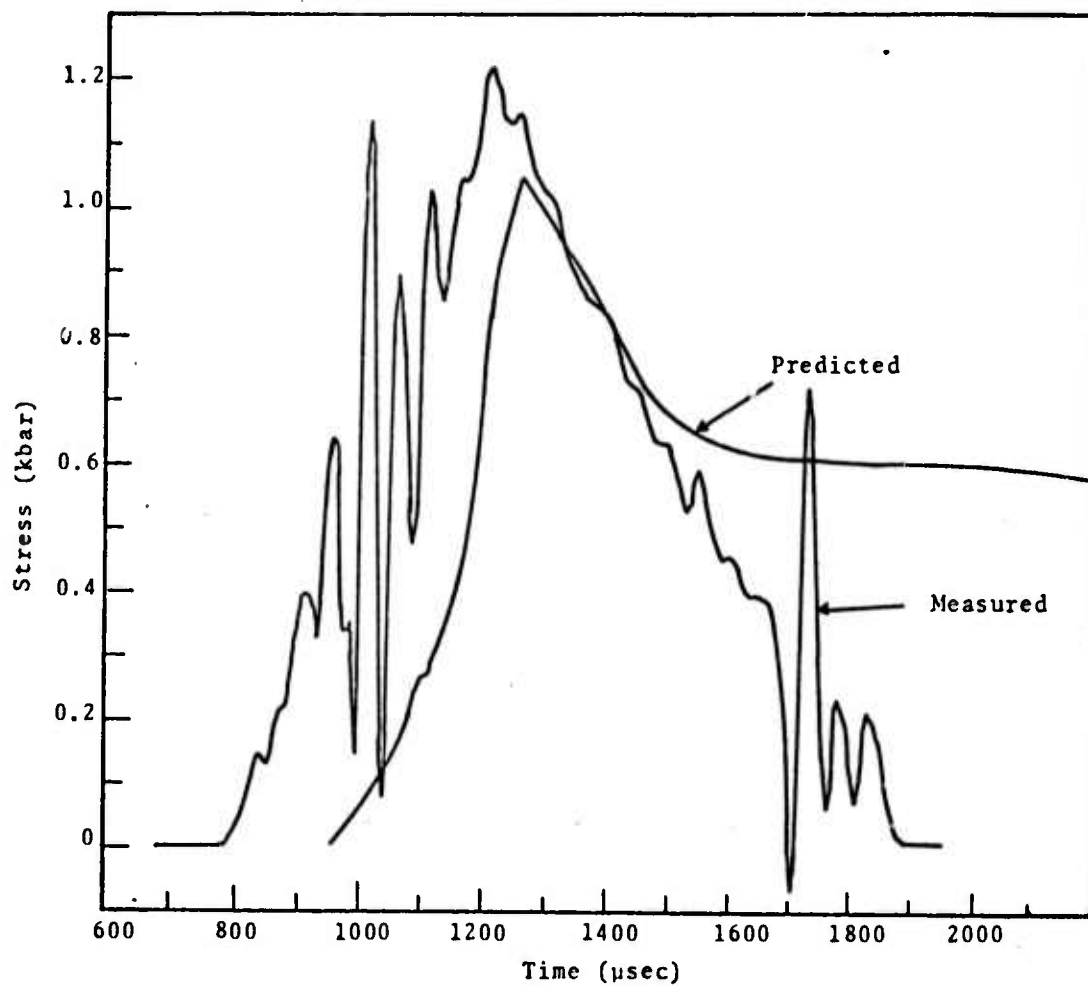


Fig. 2.25--Predicted (May 8 Run) and measured (SRI) stress histories at R = 7.67 ft and 7.70 ft respectively.

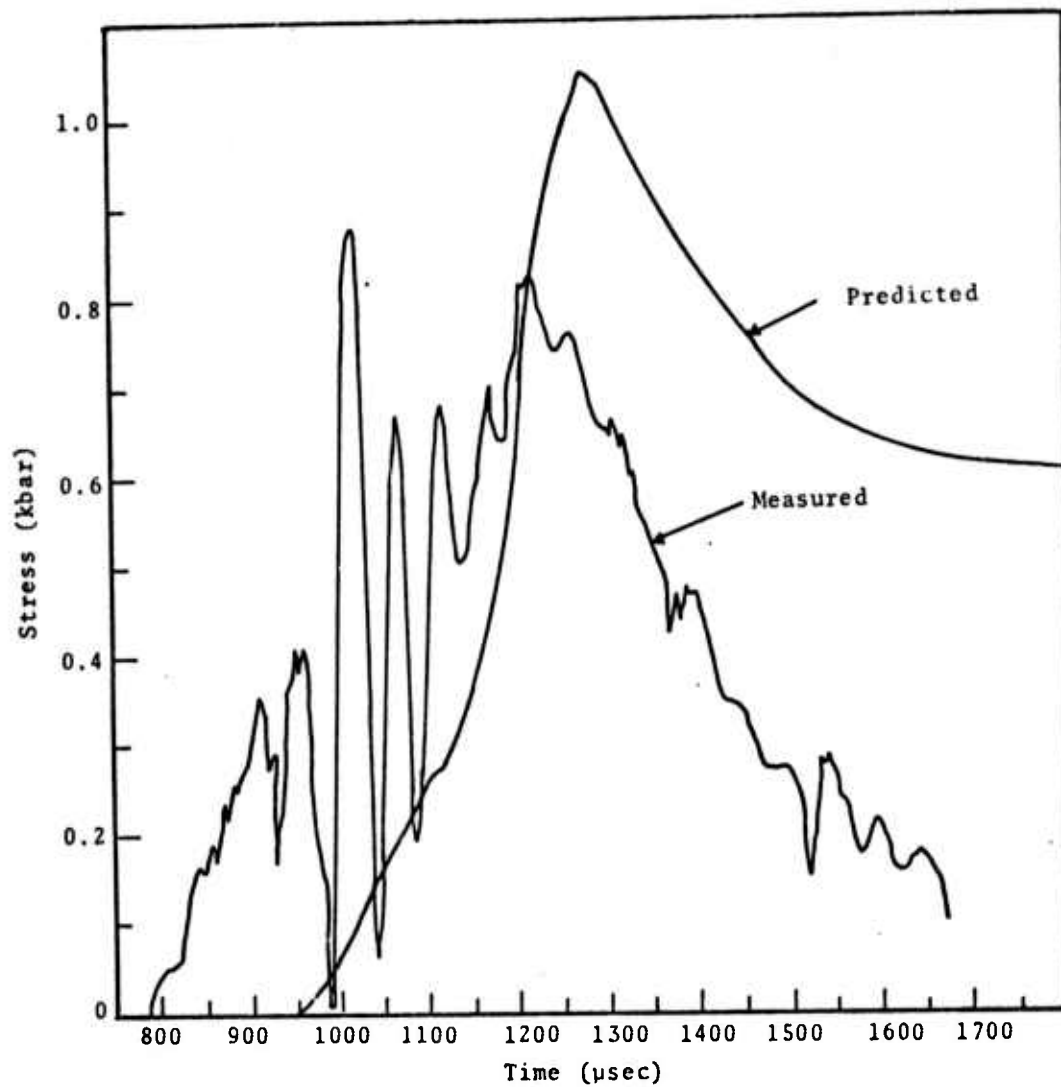


Fig. 2.26--Predicted (May 8 Run) and measured (SRI) stress histories at $R = 7.67$ ft and 7.88 ft respectively.

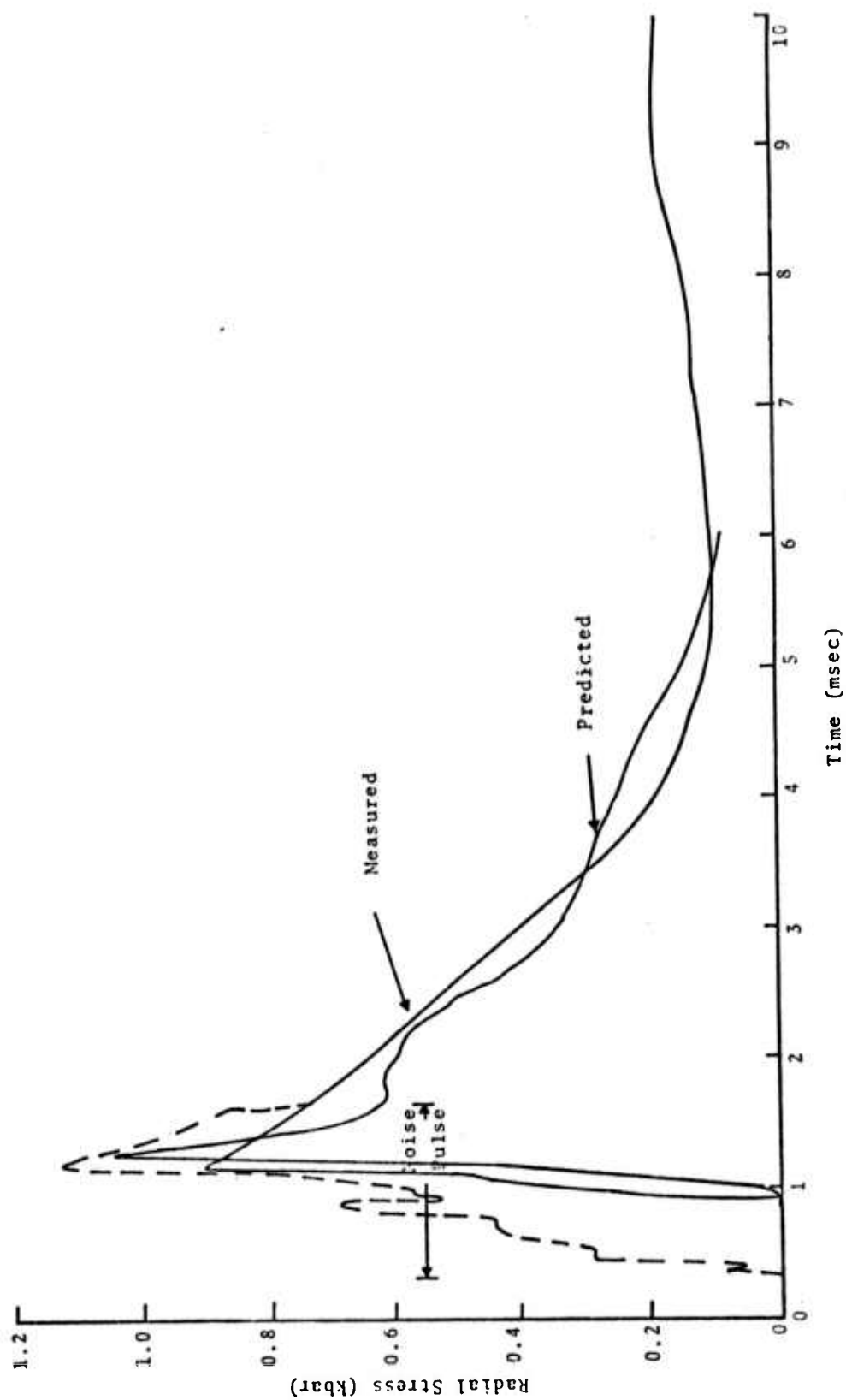


Fig. 2.27--Predicted (May 8 Run) and measured (GRT) stress histories at $R = 7.67$ ft and 7.8 ft respectively.

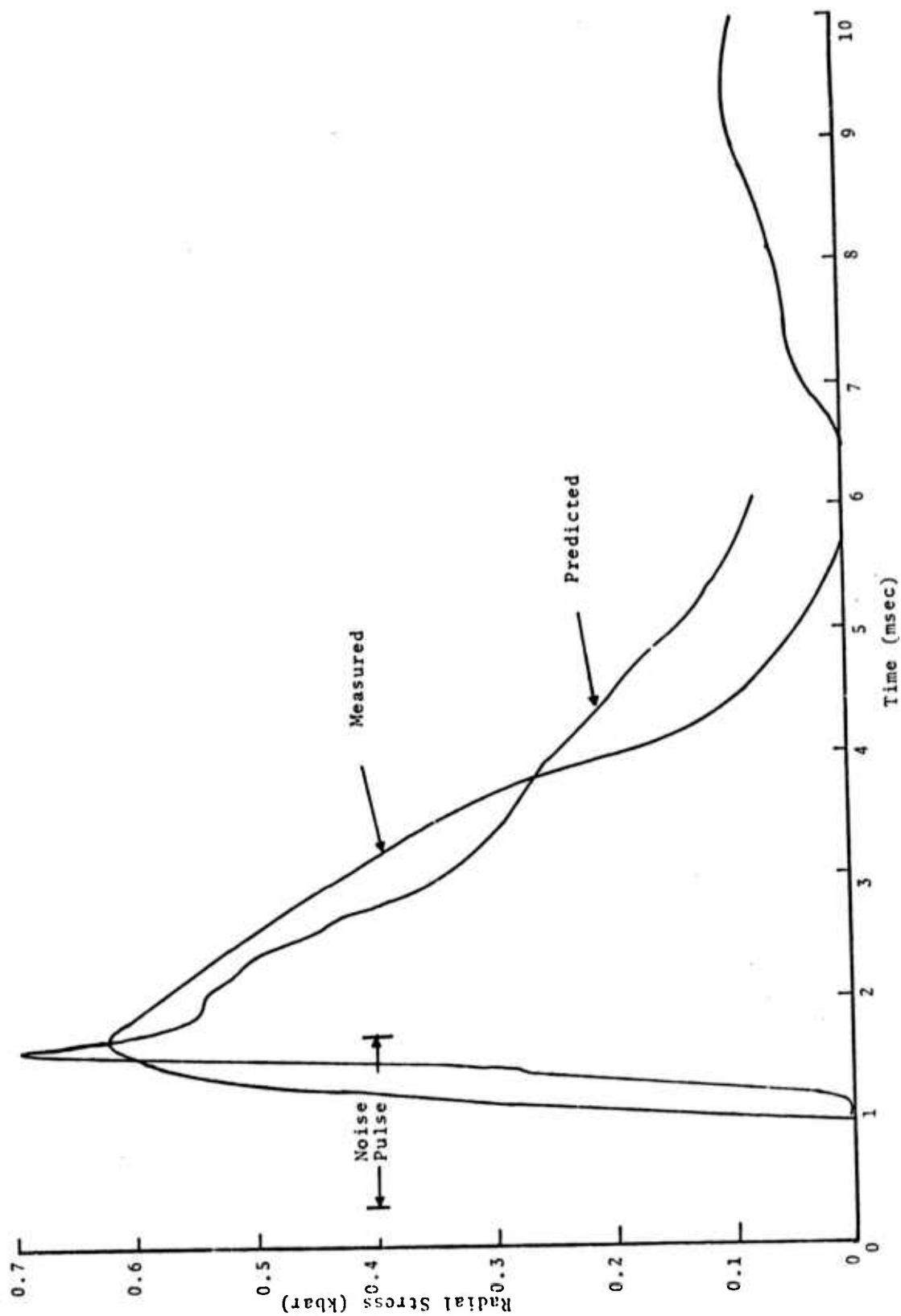


Fig. 2.28--Predicted (May 8 Run) and measured (GRT) stress histories at $R = 8.82$ ft and 8.9 ft respectively.

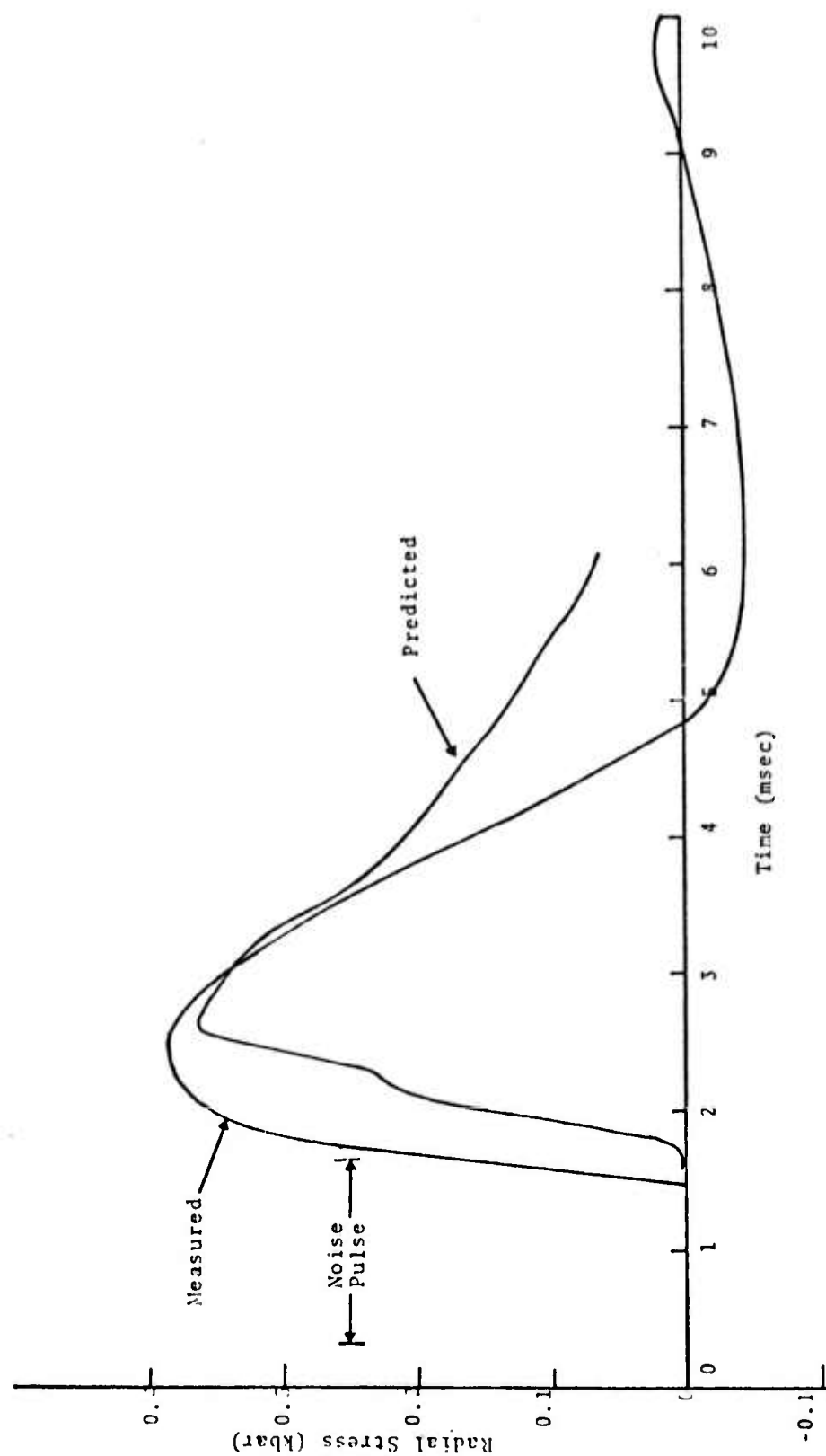


Fig. 2.29--Predicted (May 8 Run) and measured (GRT) stress histories at $R = 11.95$ ft and 12.1 ft respectively.

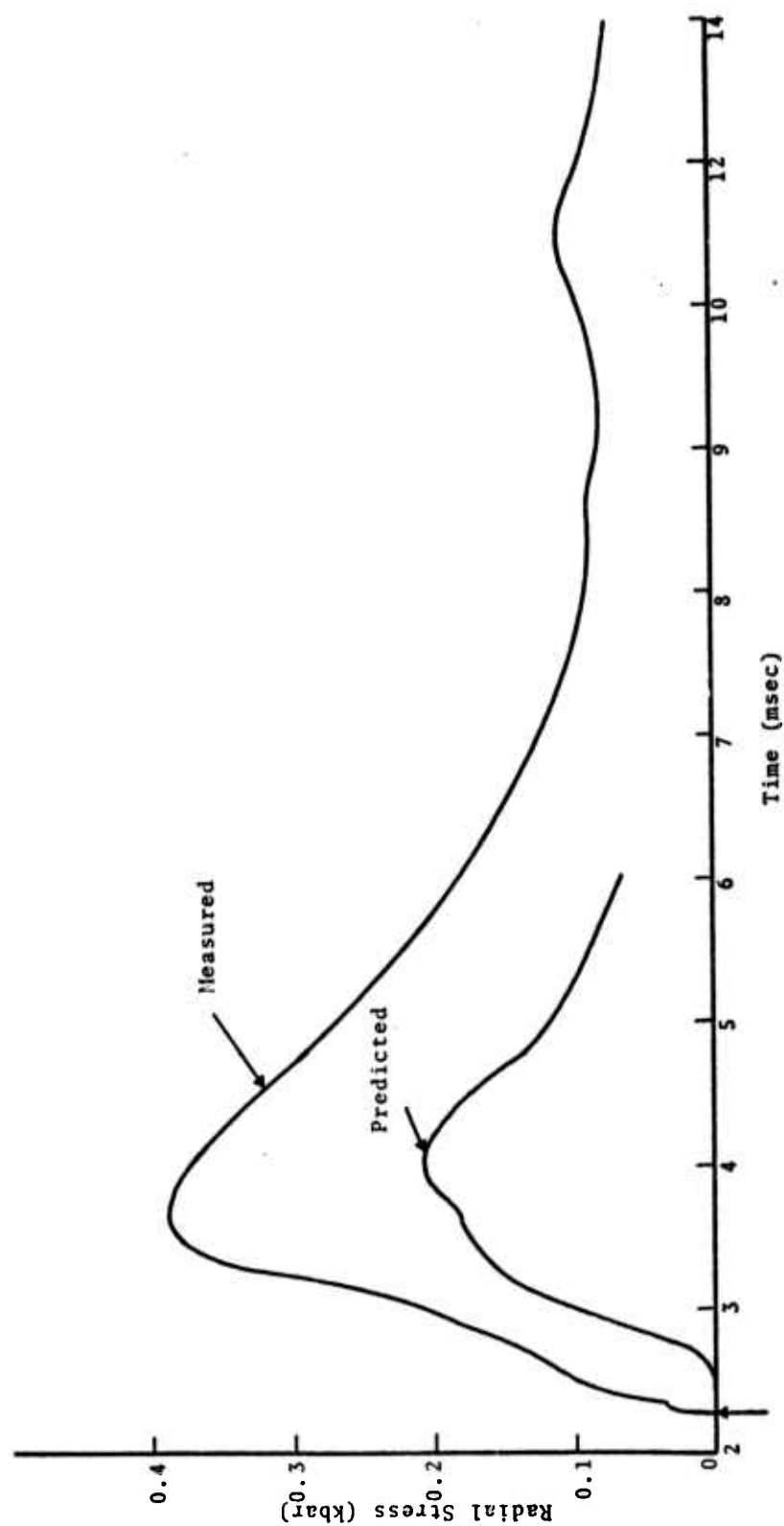


Fig. 2.30--Predicted (May 8 Run) and measured (GRT) stress histories at $R = 16.83$ ft and 16.9 ft respectively.

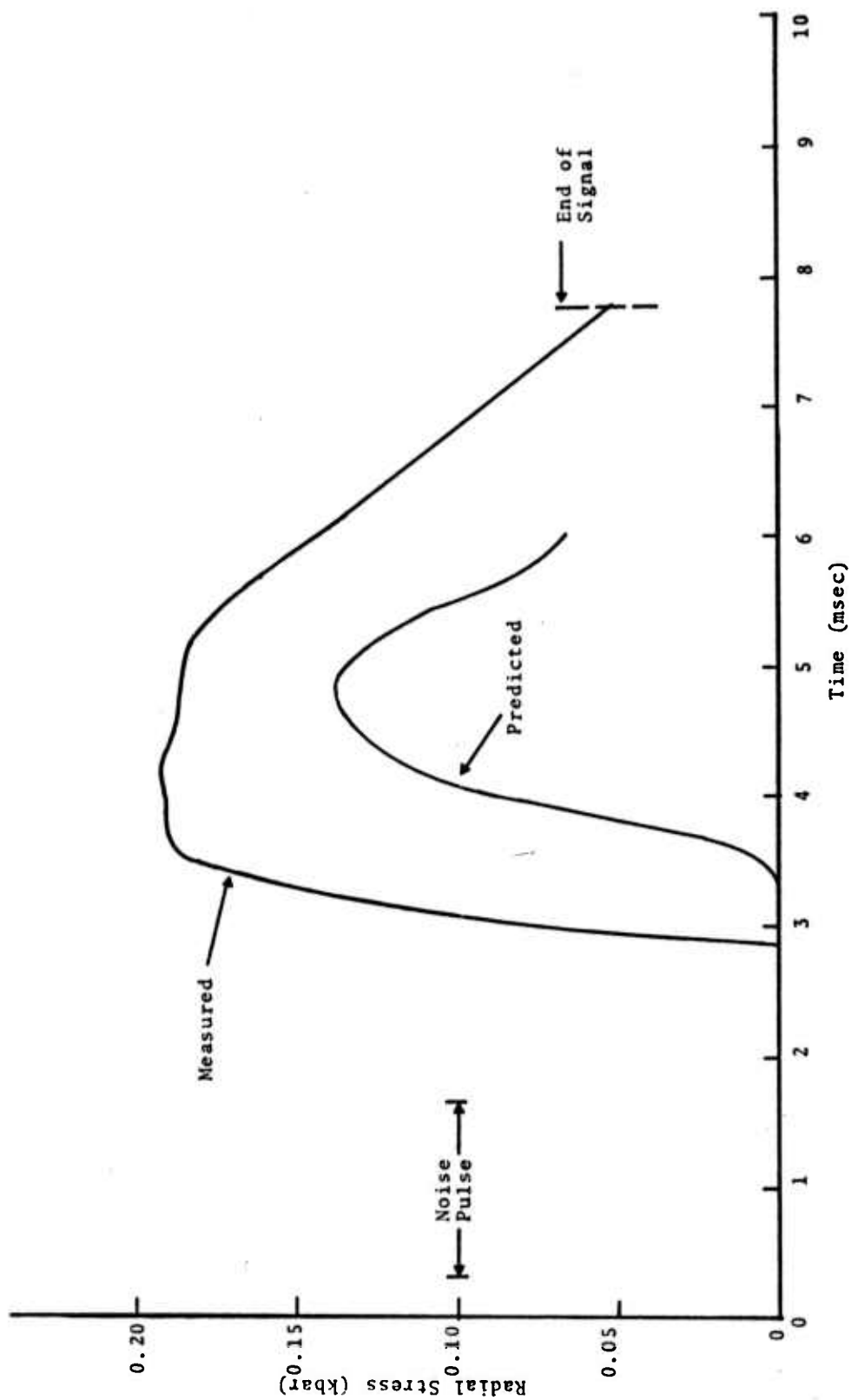


Fig. 2.31--Predicted (May 8 Run) and measured (GRT) stress histories at $R = 21.49$ ft and 21.6 ft respectively.

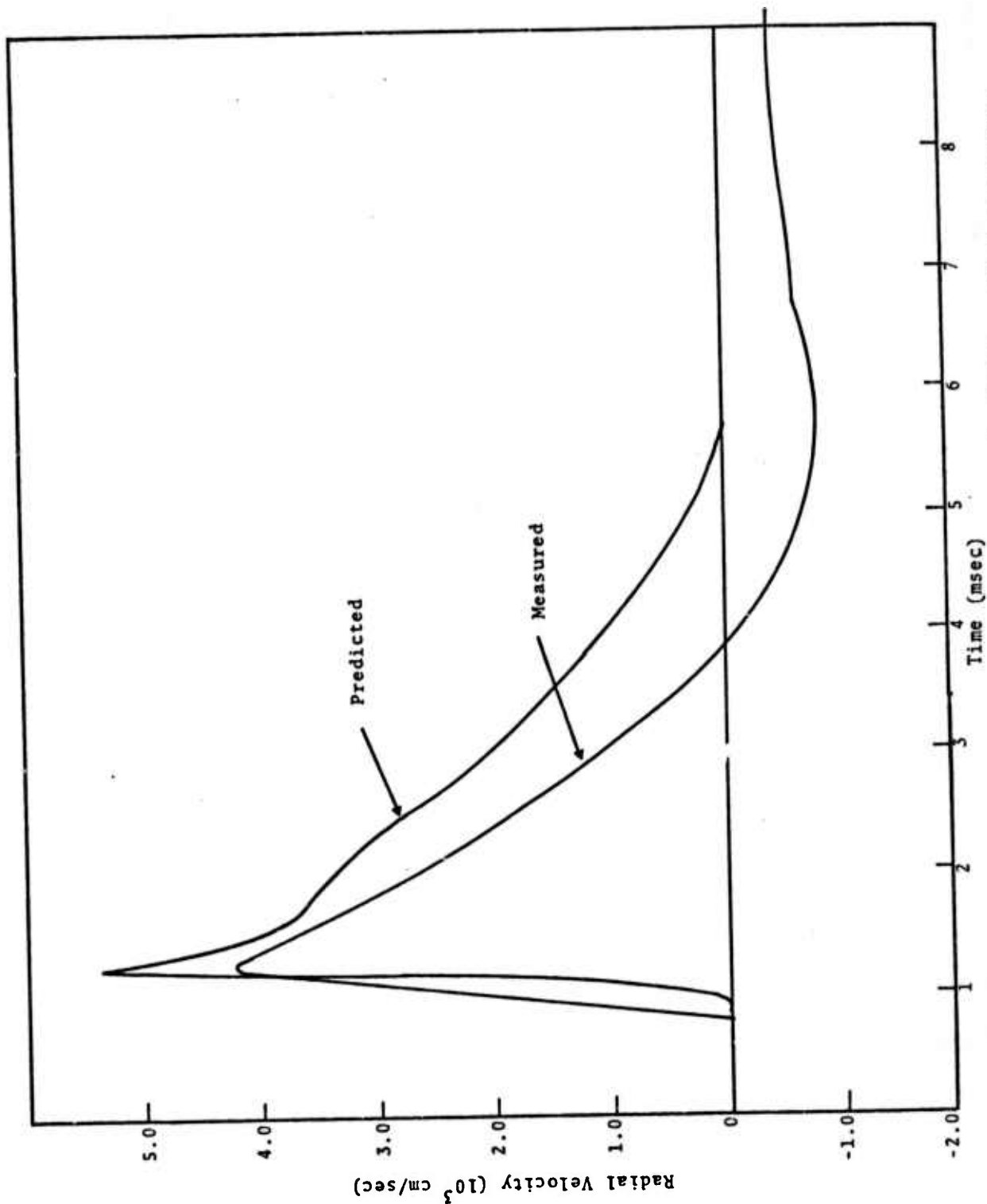


Fig. 2.32--Predicted (May 8 Run) and measured (ATI) radial velocity histories at $R = 7.67$ ft and 7.78 ft respectively.

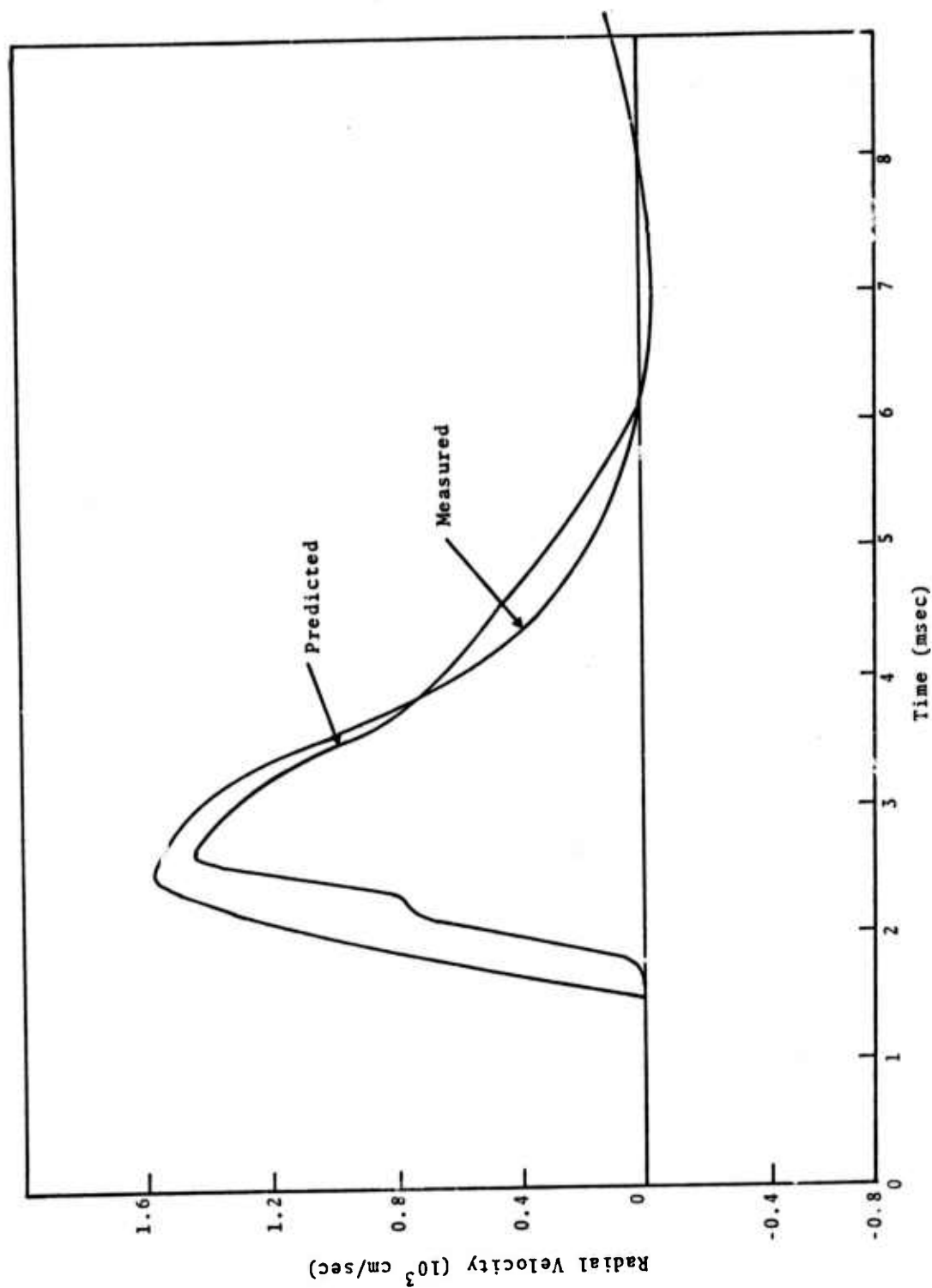


Fig. 2.33--Predicted (May 8 Run) and measured (ATI) radial velocity histories at $R = 11.95$ ft and 12.09 ft respectively.

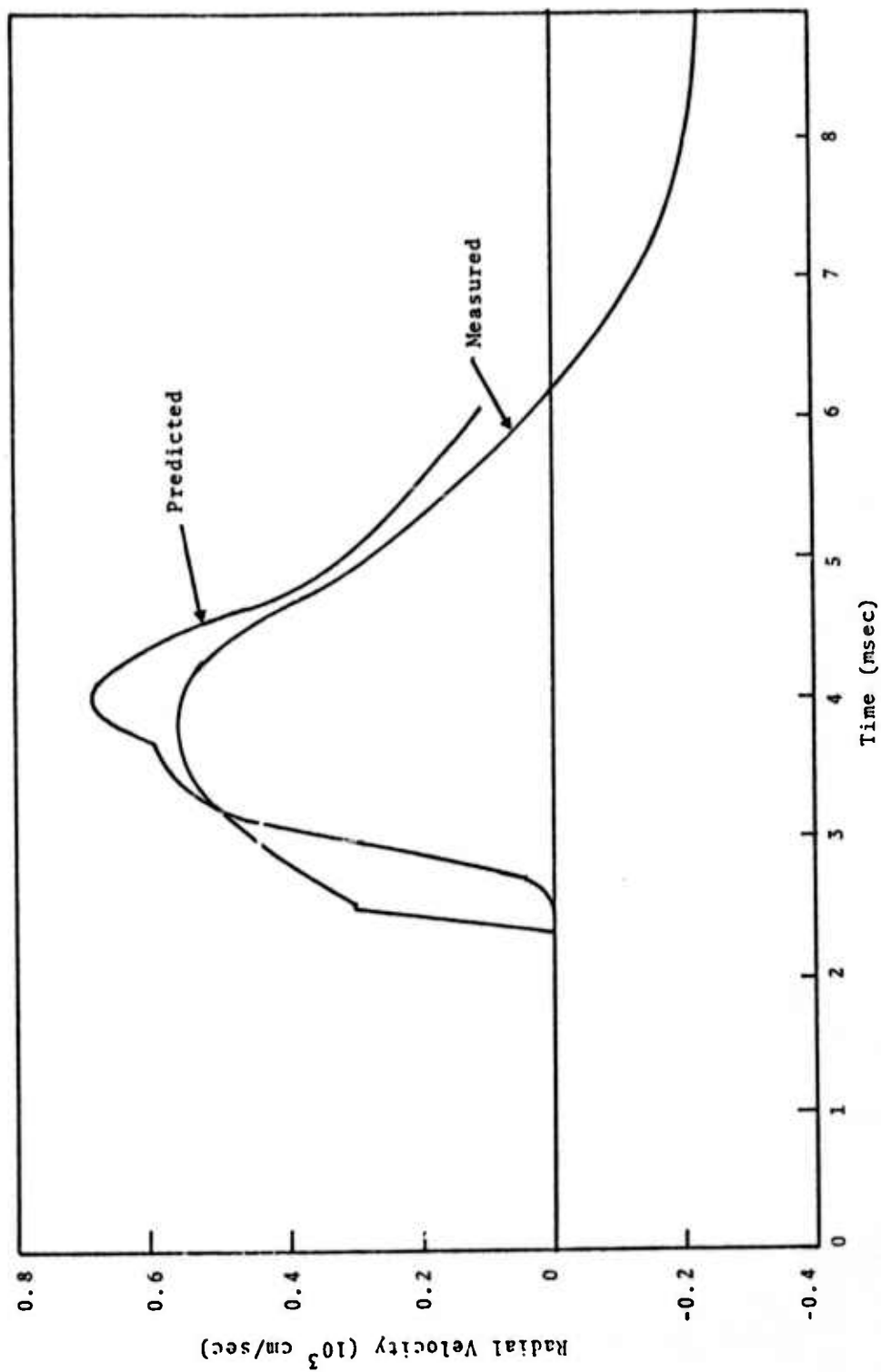


Fig. 2.34--Predicted (May 8 Run) and measured (ATI) radial velocity histories at 16.83 ft and 16.94 ft respectively.

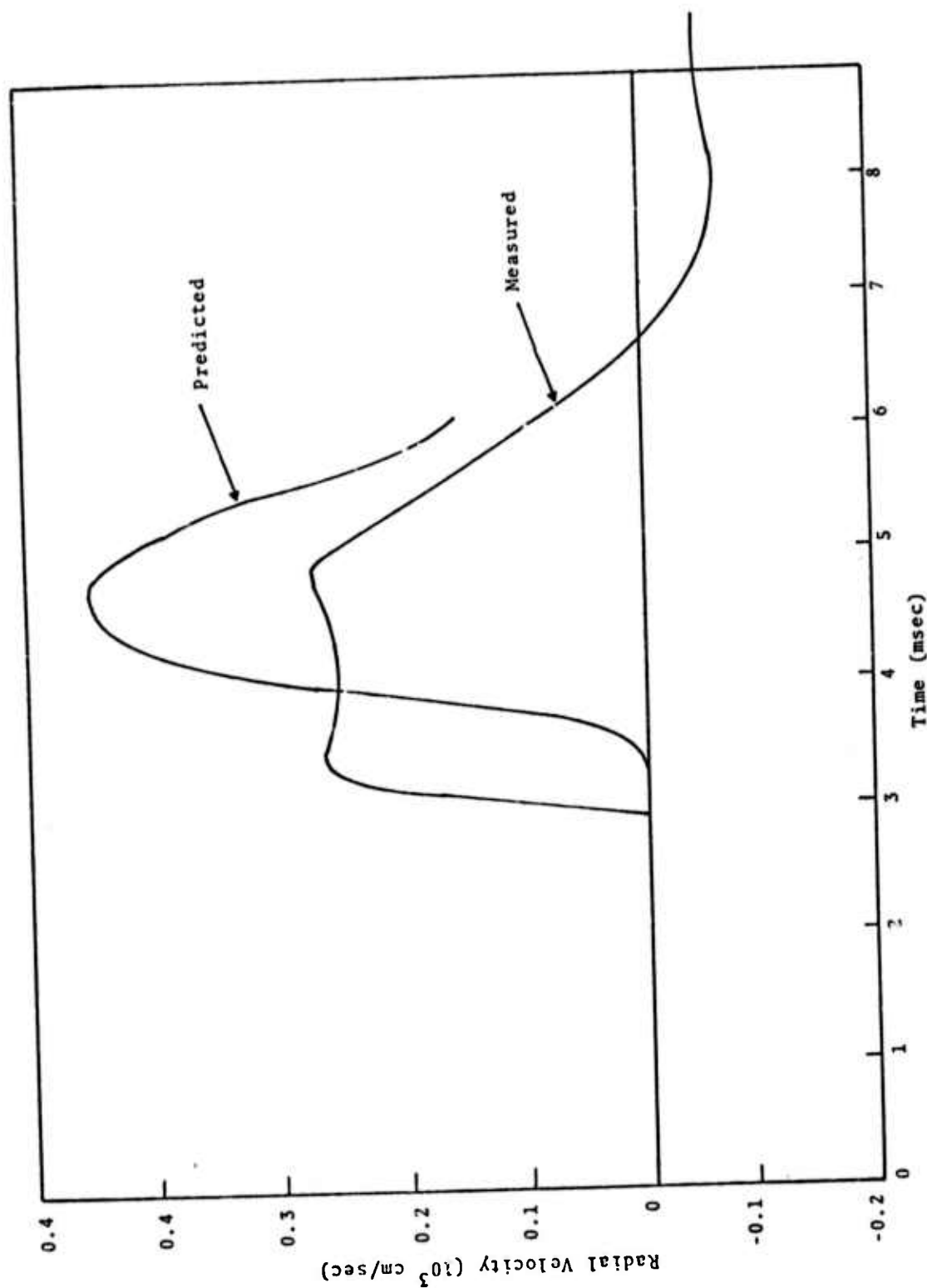


Fig. 2.35--Predicted (May 8 Run) and measured (ATI) radial velocity histories at $R = 21.49$ ft and 21.6 ft respectively.

The agreement between the predictions and the measurements is quite good. The results significantly reinforce our confidence in ground motion prediction calculations for energy sources in NTS tuff. The success of the test, like the earlier Hudson Moon HE tests,^[9] required a careful integration of the theoretical and experimental parts of the program with the actual field measurements. There was even less laboratory test data available from the Mine Dust HE site and yet the calculations were successfully carried out to predict stress attenuation to lower amplitudes. This was accomplished by relying heavily upon the TAMEOS equation of state routine which included a treatment of irreversible void collapse.

Subsequent to the Mine Dust HE test, Terra Tek has generated much more complete test data on the core samples drawn from near the WP. This includes uniaxial strain data and triaxial tests in which proportional loading was imposed.^[15] It would be of interest to use this new information to construct a more complete model of the deviatoric behavior of the medium and to repeat the calculation. In a related current study at S³, Cherry, et al.^[16] are conducting a series of spherical SKIPPER calculations in which the crushup parameters used in TAMEOS are varied. These calculations, for a buried nuclear source, are designed to determine the sensitivity of the ground motion at remote distances to the overburden pressure at the energy source and the details of the crushup model.

2.3 SURFACE LOADING PARAMETER STUDY

The Mine Dust HE results give us some confidence that in soft rock media an integrated theoretical-experimental-field test program can lead to successful predictions of ground motions for buried spherically symmetric sources. It is apparent, however, that the problem is more difficult in the case of near surface energy sources since both energy coupling and cratering processes are multi-dimensional, and they require a wider range for the material response models. For some applications, such as assessing the vulnerability of deep underground structures, the problem is alleviated since interest is focused on material within a cone centered below the burst point. In this case the details of the cratering process should have a second order effect on the stress pulse propagated to the structure, but the impulse carried downward with the pulse must offset the total backward momentum carried by the debris thrown out of the crater.

To assess the effect of water vaporization the PEQ version of TAMEOS was used in the planar SKIPPER code to calculate the time history of 400 kbar and 550 kbar pressure pulses in a 17 percent water-mass-fraction tuff. In order to see the effect of water vaporization, explicitly treated in TAMEOS, comparison is made with calculations using a Mie-Gruneisen analytic equation of state which approximates TAMEOS at high pressures but does not allow for the large expansions of the water on release. Comparison of Hugoniot points in the shock-particle velocity plane is shown in Fig. 2.36.

For the analytic approximation the thermodynamic derivative

$$\left(\frac{\partial P}{\partial E}\right)_V \equiv G\rho \quad (2.18)$$

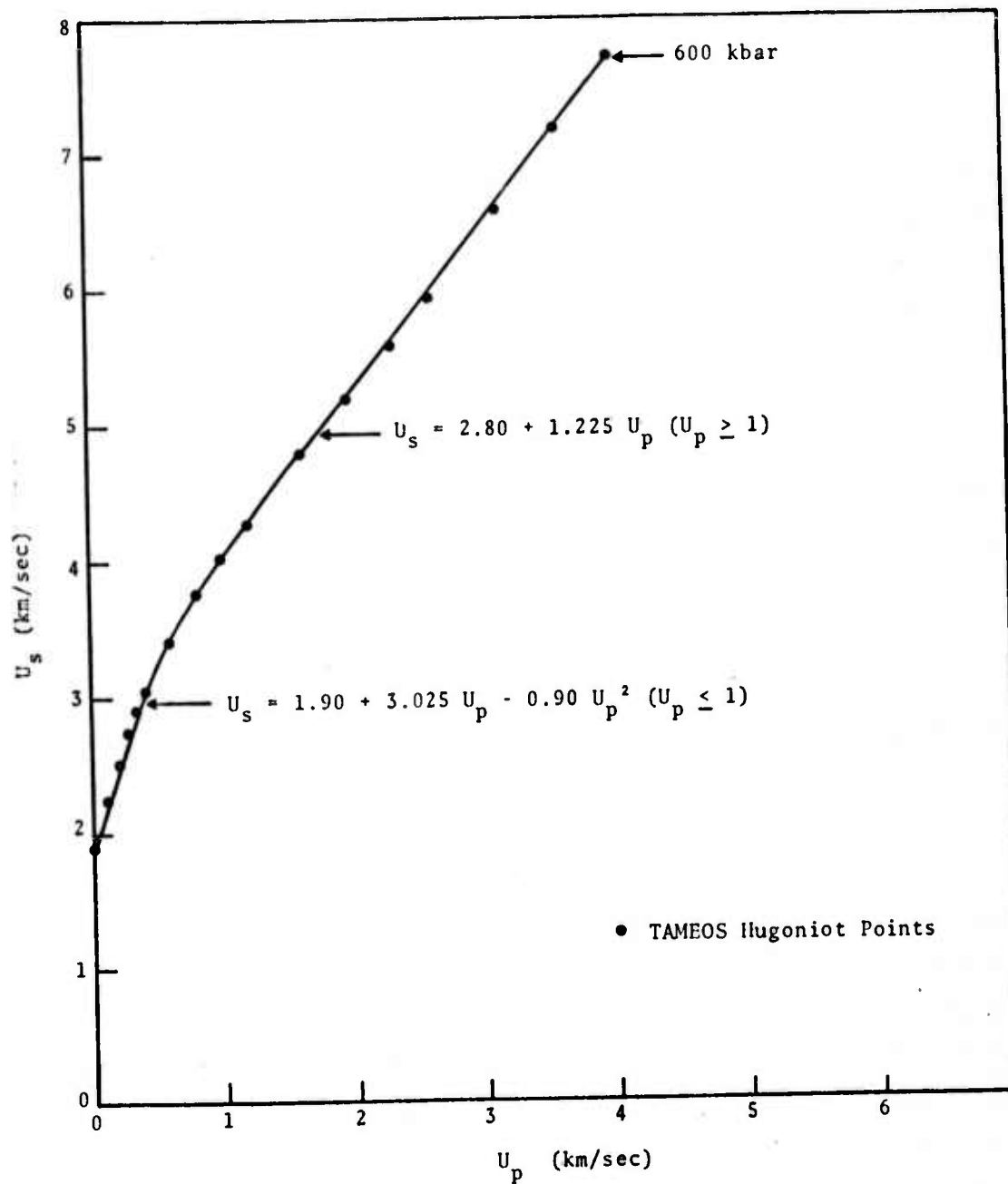


Fig. 2.36--Hugoniot for saturated wet tuff with water mass fraction of $M_w = 17\%$.

is taken to be constant (it isn't, of course, for the tabulated PEQ states) so that the equation of state is

$$P = G_0 \rho_0 E + P_H(V) \left[1 - \frac{G_0 \rho_0}{2} (V_0 - V) \right] . \quad (2.19)$$

The value $G_0 \rho_0 = 1.0$ is representative of values calculated from high-pressure points in the table. For release states with $V > V_0$, the Hugoniot was extended to negative pressures with the rather arbitrary straight-line fit

$$U = 1.90 + 0.717u, \quad u < 0. \quad (2.20)$$

In the runs the left boundary was loaded with a 20 μ sec flat-topped pulse. The loading was ramped up with a cosine function

$$P(t) = \frac{1}{2} P_0 \left[1 - \cos\left(\frac{\pi t}{t_0}\right) \right] \quad t < 6 \mu\text{sec} \quad (2.21)$$

The load pressure was maintained at the maximum value P_0 (= 400 and 550 kbar) until $t = 20 \mu$ sec and then released to 0.1 kbar in 6 μ sec with another cosine function.

Figure 2.37 is a plot of the PEQ Hugoniot for the saturated mixture and a comparison of the release adiabats from 550 kbar as obtained from TAMEOS and the analytic equation of state. The analytic adiabat agrees with that from the table (more or less) for pressures above 2 kbar but does not reproduce the large expansion due to water vaporization below 2 kbar.

Figure 2.38 shows several particle-velocity profiles for a 550 kbar pulse after a travel of approximately 110 cm. For the TAMEOS calculation, about 24 percent of the mass that has been shocked has "rebounded", i.e., has acquired a negative particle velocity. For the analytic equation of state,

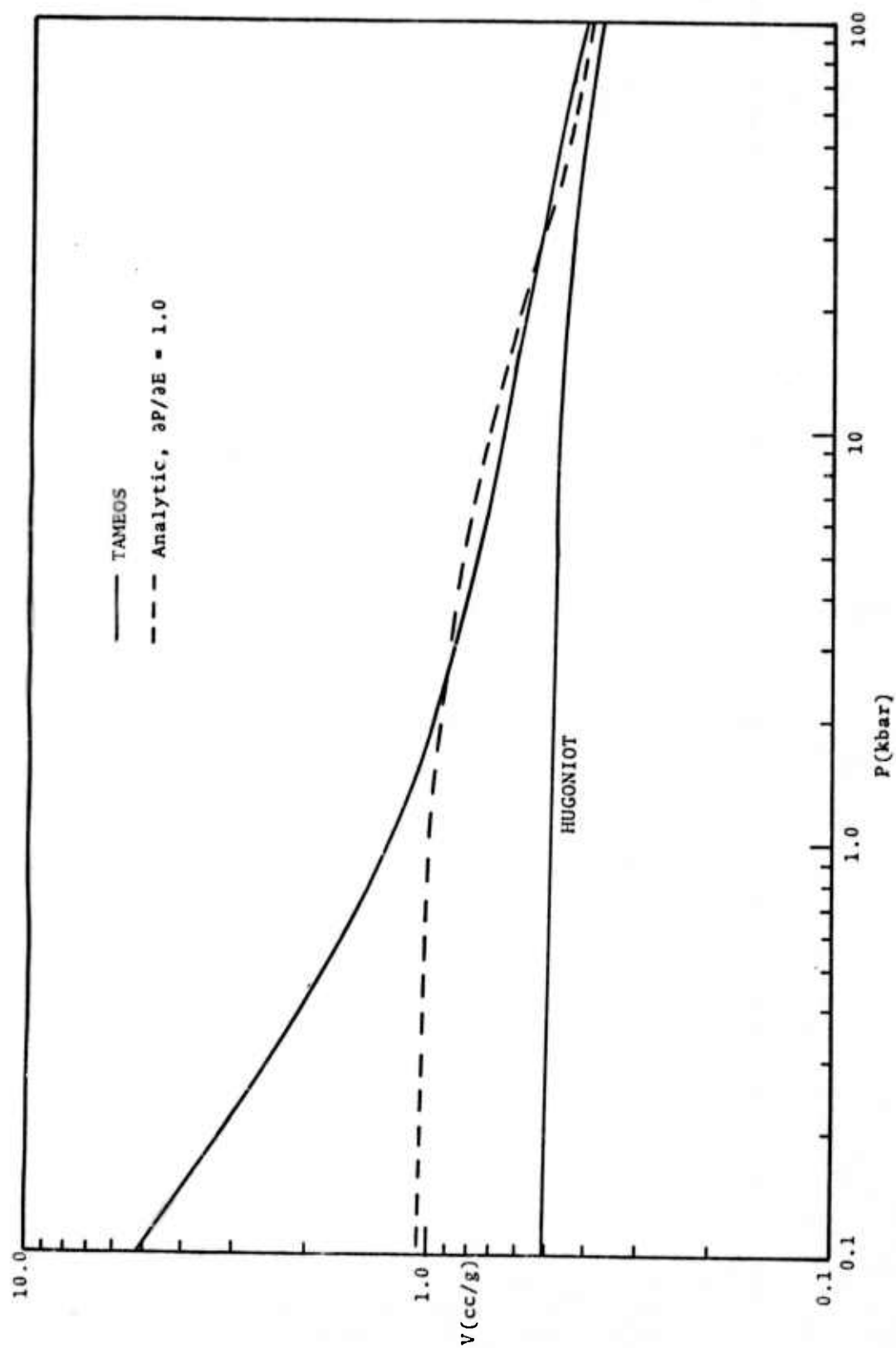


Fig. 2.37--Release adiabat from 550 kbar for saturated tuff, $M_w = 17\%$.

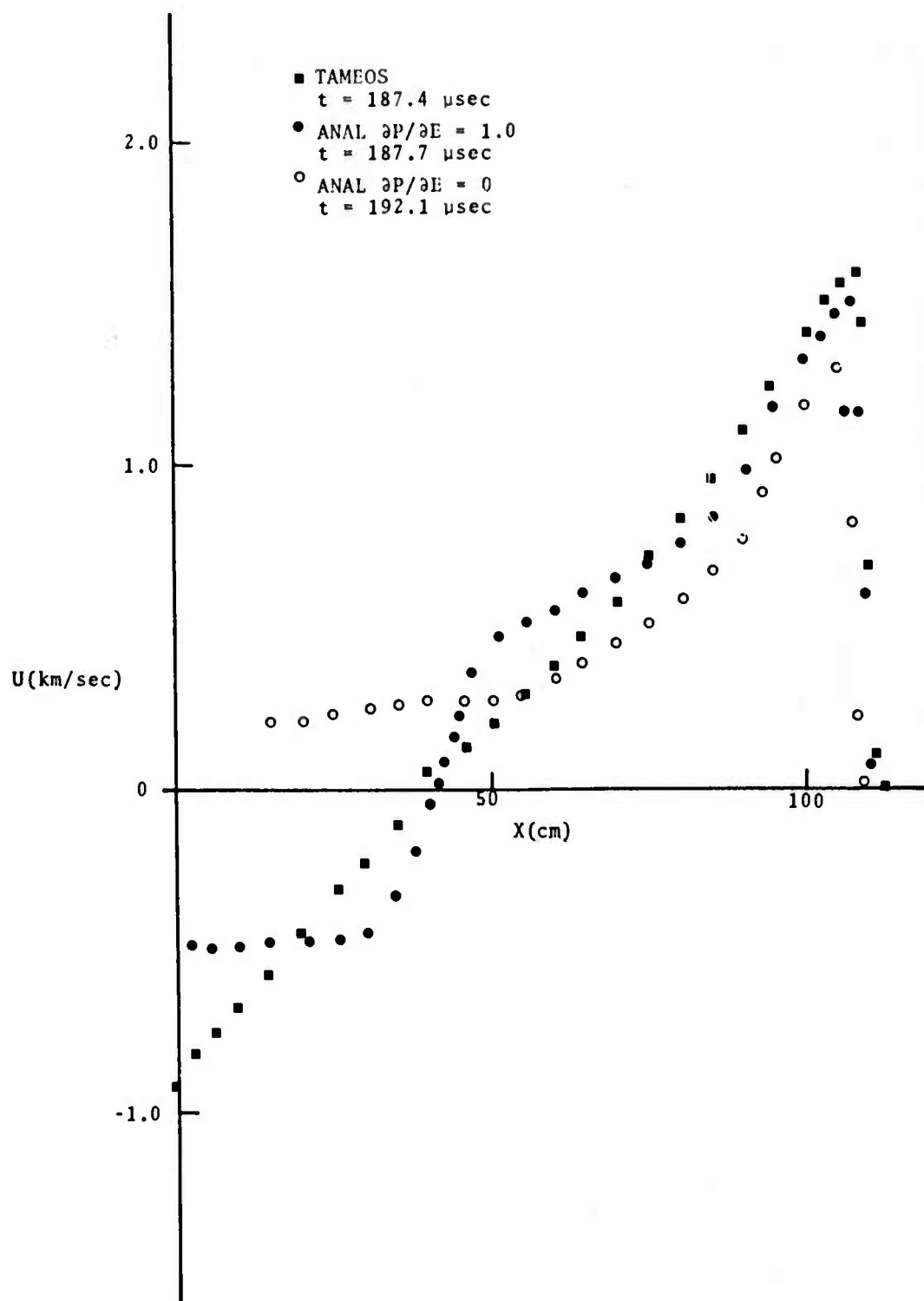


Fig. 2.38--Particle velocity profiles propagated from 550 kbar pulse in saturated tuff ($M_w = 17\%$) calculated using indicated models.

about 21 percent of the shocked mass has a negative velocity. The big difference is in the velocity acquired by the first few zones, the maximum negative velocity for the TAMEOS calculation being about twice that calculated with the analytic equation of state. Also shown in Fig. 2.38 is the extreme case of the velocity profile calculated with the analytic equation of state with $(\partial P / \partial E)_v$ set equal to zero. In this case, the release adiabat coincides with the Hugoniot, and the magnitude of the velocity acquired on release is not large enough to give a rebound. It will also be noted that the maximum particle velocity at the head of the pulse is higher for the TAMEOS calculation than for the analytic ones. This is to be expected, since the 20 μ sec pressure pulse at the left interface puts a fixed amount of positive momentum into the material. Hence the model which has acquired the largest amount of negative momentum in release must also have a larger amount of positive momentum in the lead part of the wave.

Figure 2.39 shows several pressure profiles for the 550 kbar pulse after a run of about 110 cm. The peak pressure in the TAMEOS calculation is higher than that calculated with the analytic equations of state. Figure 2.40 shows several pressure profiles for a 400 kbar pulse. Here the effect of initial porosity is more pronounced than in the velocity profiles.

Figures 2.41 and 2.42 are plots of the peak pressure in the pulse as a function of run. In all cases the rate of pressure decay as calculated with the TAMEOS scheme is significantly less than that calculated with either of the analytic models. For a nuclear surface burst the loading pressures are much greater and the enhancement of the stress pulse amplitude by the water vaporization would correspondingly be greater.

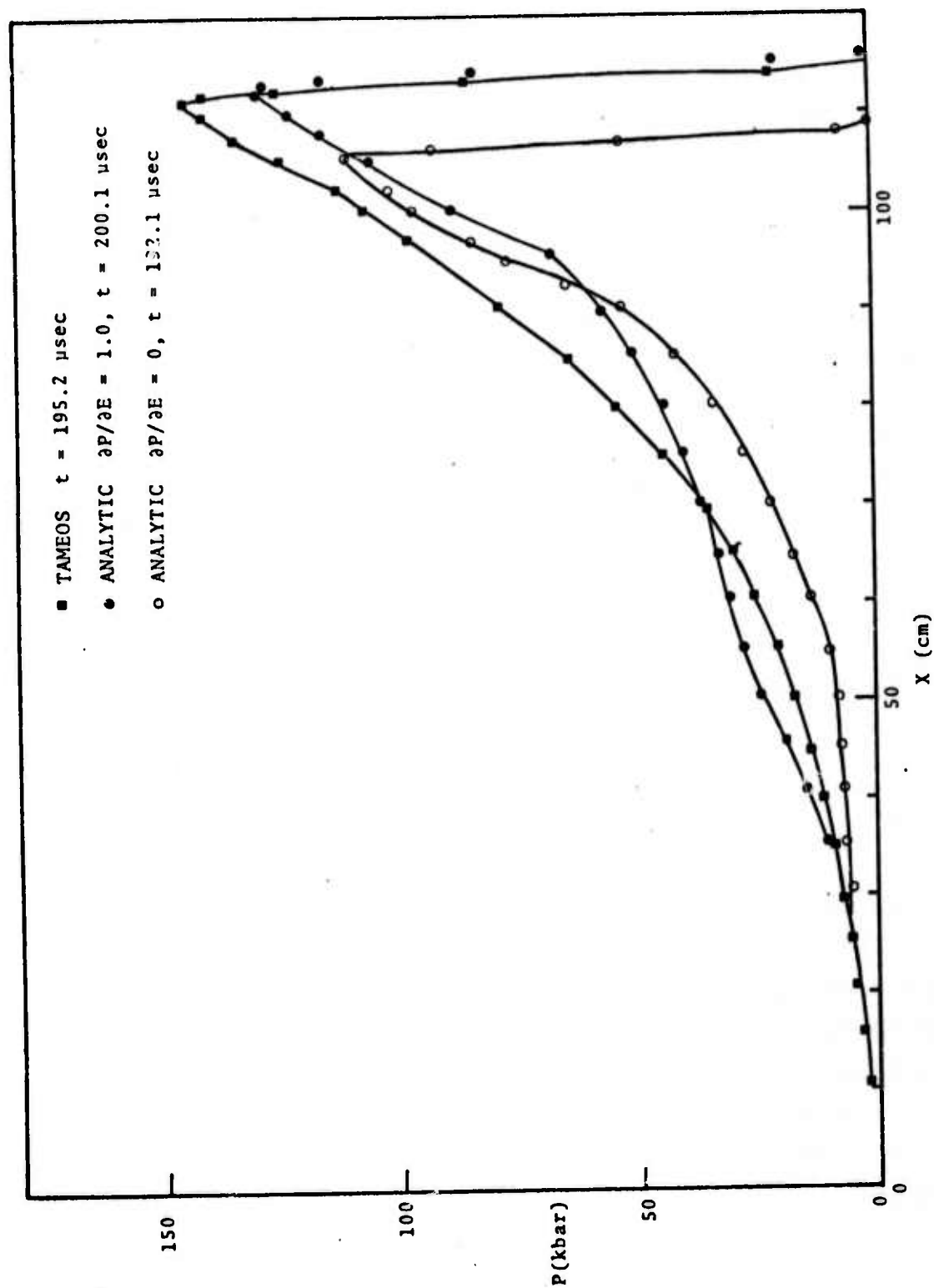


Fig. 2.39--Pressure profiles from 550 kbar pulse in saturated tuff ($M_w = 17\%$) calculated using indicated models.

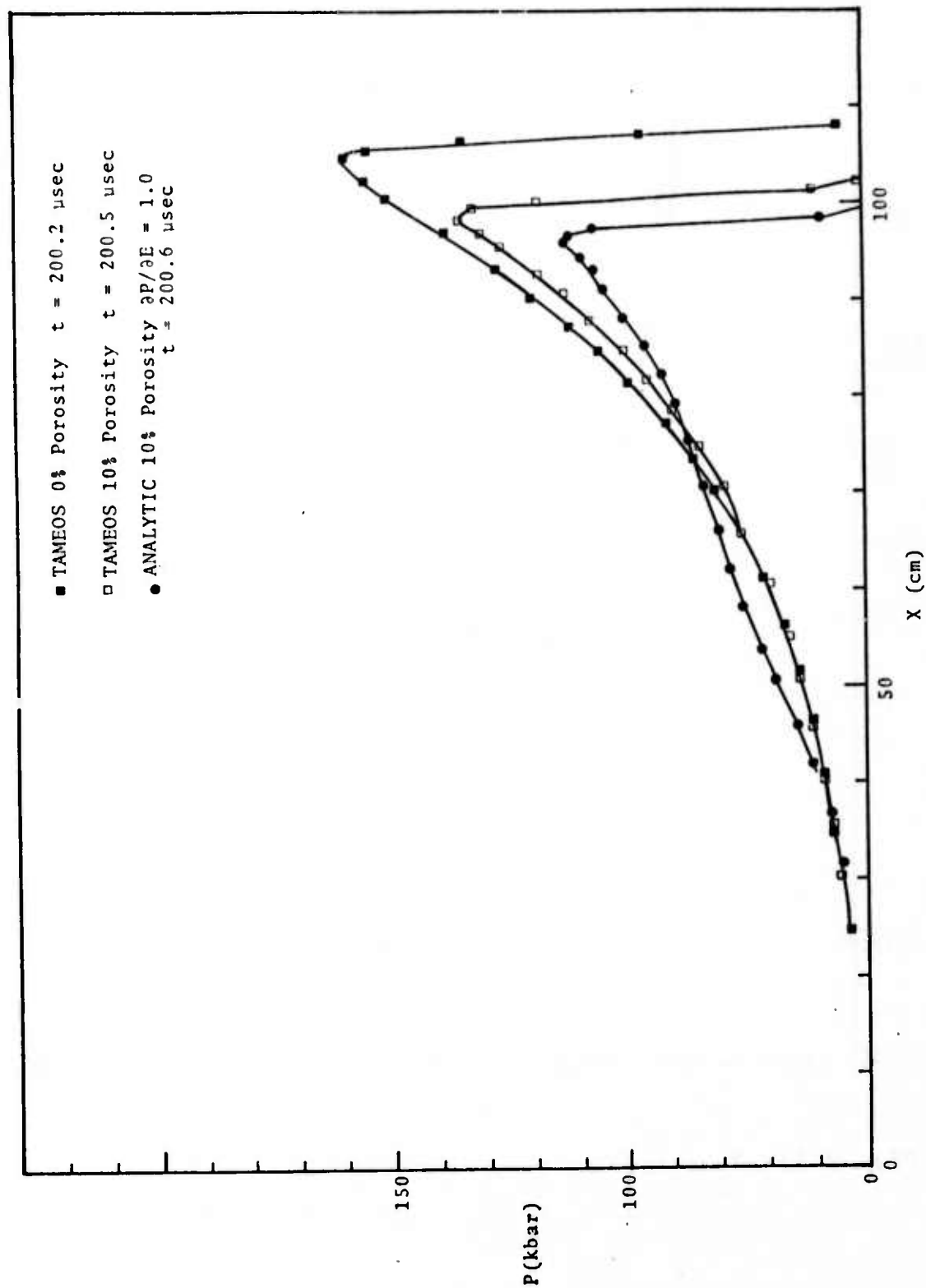


Fig. 2.40--Pressure profiles propagated from 400 kbar pulse in wet tuft
 ($M_w = 17\%$) calculated using indicated models and air-filled
 porosities.

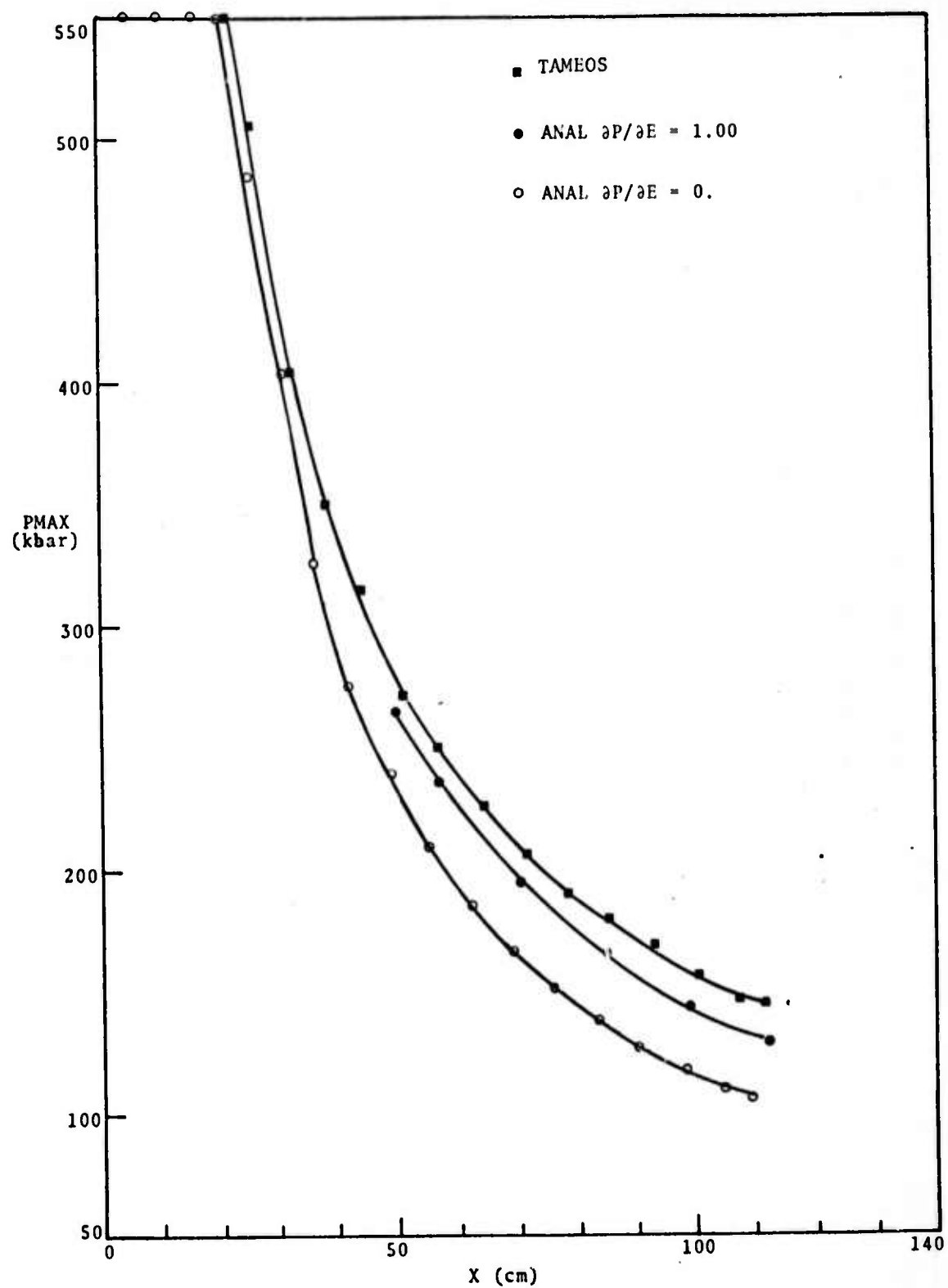


Fig. 2.41--Peak pressure attenuation curves for pressure pulse propagated from 550 kbar pulse in saturated tuff ($M_w = 17\%$) calculated using indicated models.

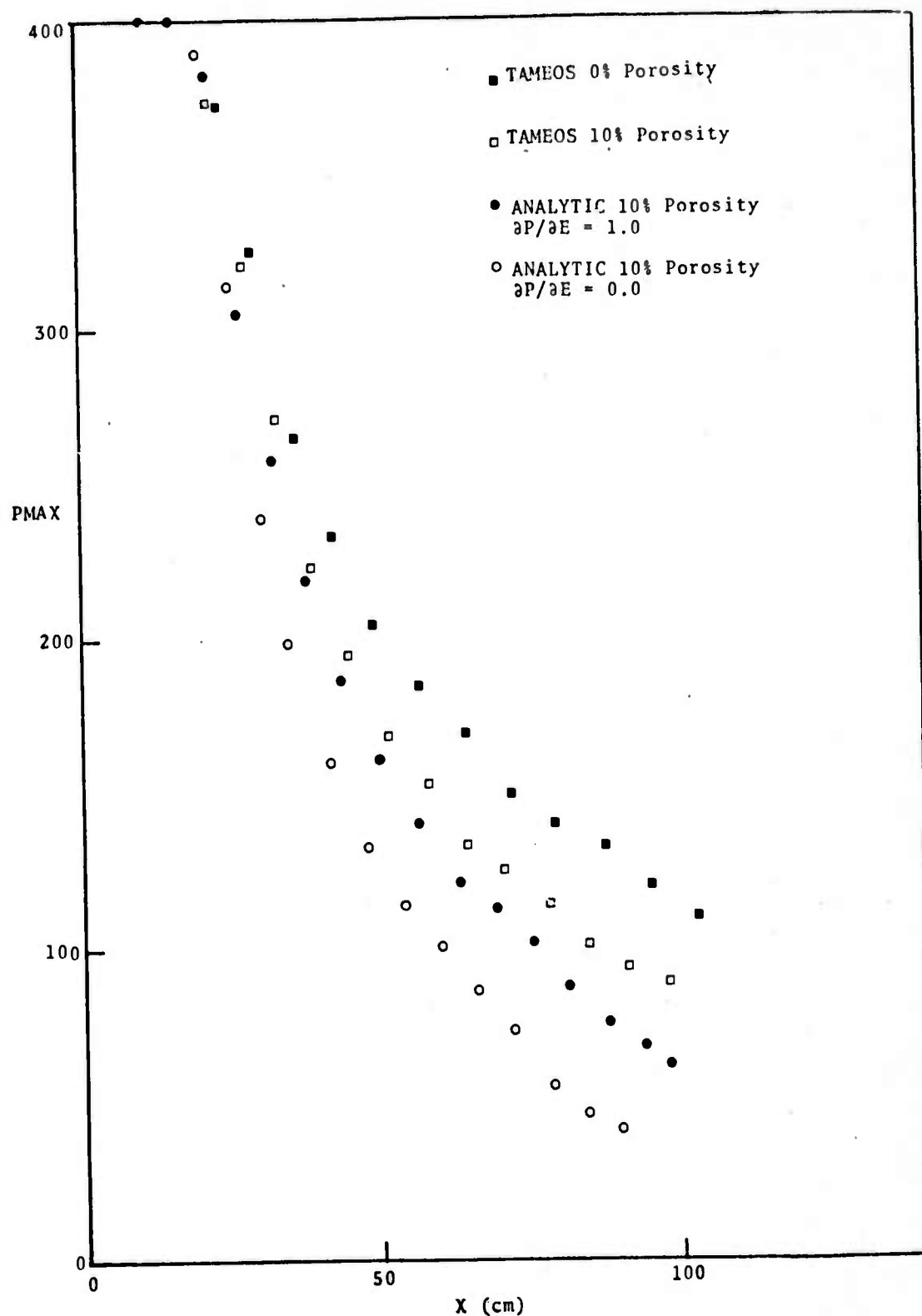


Fig. 2.42--Peak pressure attenuation curves for pressure pulse propagated from 440 kbar pulse in wet tuff ($M_w = 17\%$) calculated using indicated models^w and porosities.

III. A TWO-PHASE EQUATION OF STATE MODEL FOR GRANITE

An equation of state for granite in which the phase change at high pressures is treated explicitly was used with the one-dimensional SKIPPER code to investigate the possibility that this phase change can have important effects on the attenuation and profiles of pressure in granite.

3.1 TWO-PHASE MODEL

The experimental shock-particle velocity data of McQueen et al.^[17] for Westerly granite are shown in Fig. 3.1. The data with $U_p > 2.3$ km/sec are fitted within experimental error by the straight line

$$U_s = 2.103 + 1.629 U_p \quad (3.1)$$

and are assumed to represent equilibrium states for the high-pressure phase. The lower pressure points presumably represent mixtures of the high and low-pressure phases; and the assumptions used in developing the present two-phase model would indicate that they are not points of thermodynamic equilibrium.

The Hugoniot for the low-pressure phase is taken as the straight line

$$U_s = 4.50 + 1.25 U_p \quad (3.2)$$

(velocities in km/sec). The zero pressure "bulk" sound speed of 4.50 km/sec is for the "compacted" state and was obtained by extrapolating the longitudinal sound velocity data of Birch^[18] and the shear velocity data of Simmons^[19] to 10 kbars to zero pressure (see Ref. 20). The above value together with the slope of 1.25 give P - V points which are compatible with the hydrostatic data of Stephens^[21] for NTS granodiorite to 40 kbars.

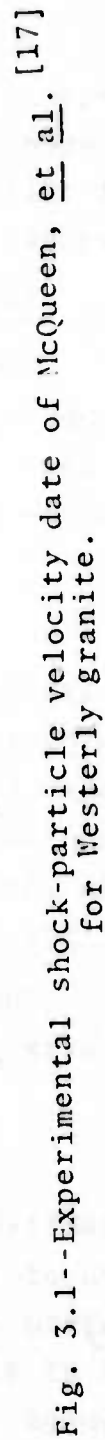


Figure 3.2 is a plot of the experimental data in the P - V plane, along with the phase lines and the low-pressure-phase Hugoniot used in the present model. Also shown in Fig. 3.2 is a "metastable" Hugoniot for the high-pressure-phase centered at zero pressure and room temperature. This metastable Hugoniot was calculated in the following manner:

The zero-pressure, room temperature density of the high-pressure phase was taken as $\rho_{00} = 3.90 \text{ gm/cm}^3$ after Davies and Anderson^[22], who obtained this value by making a fit of the experimental high-pressure-phase points to the Birch-Murnaghan equation subject to the restraint

$$\rho_{00} (\text{gm/cm}^3) = 0.049 M \phi_0^{1/3},$$

where M is the mean atomic weight and

$$\phi_0 \equiv \left(\frac{\partial P}{\partial \rho} \right)_s$$

in $(\text{km/sec})^2$ is the square of the zero-pressure bulk sound speed, the resulting value of which is

$$\phi_0 = 57 (\text{km/sec})^2. \quad (3.3)$$

Each experimental P - V point was then converted to a point appropriate to centering at $P = 0$, $\rho_{00} = 3.90$ by means of the relation

$$P'_H = \frac{P_H \left[1 - \frac{1}{2} \left(\frac{G}{V} \right) (V_0 - V) \right] + \left(\frac{G}{V} \right) (E_{00} - E_0)}{\left[1 - \frac{1}{2} \left(\frac{G}{V} \right) (V_{00} - V) \right]}. \quad (3.4)$$

where P'_H is the pressure of the metastable Hugoniot at the specific volume V and G is the Grüneisen ratio. In this calculation

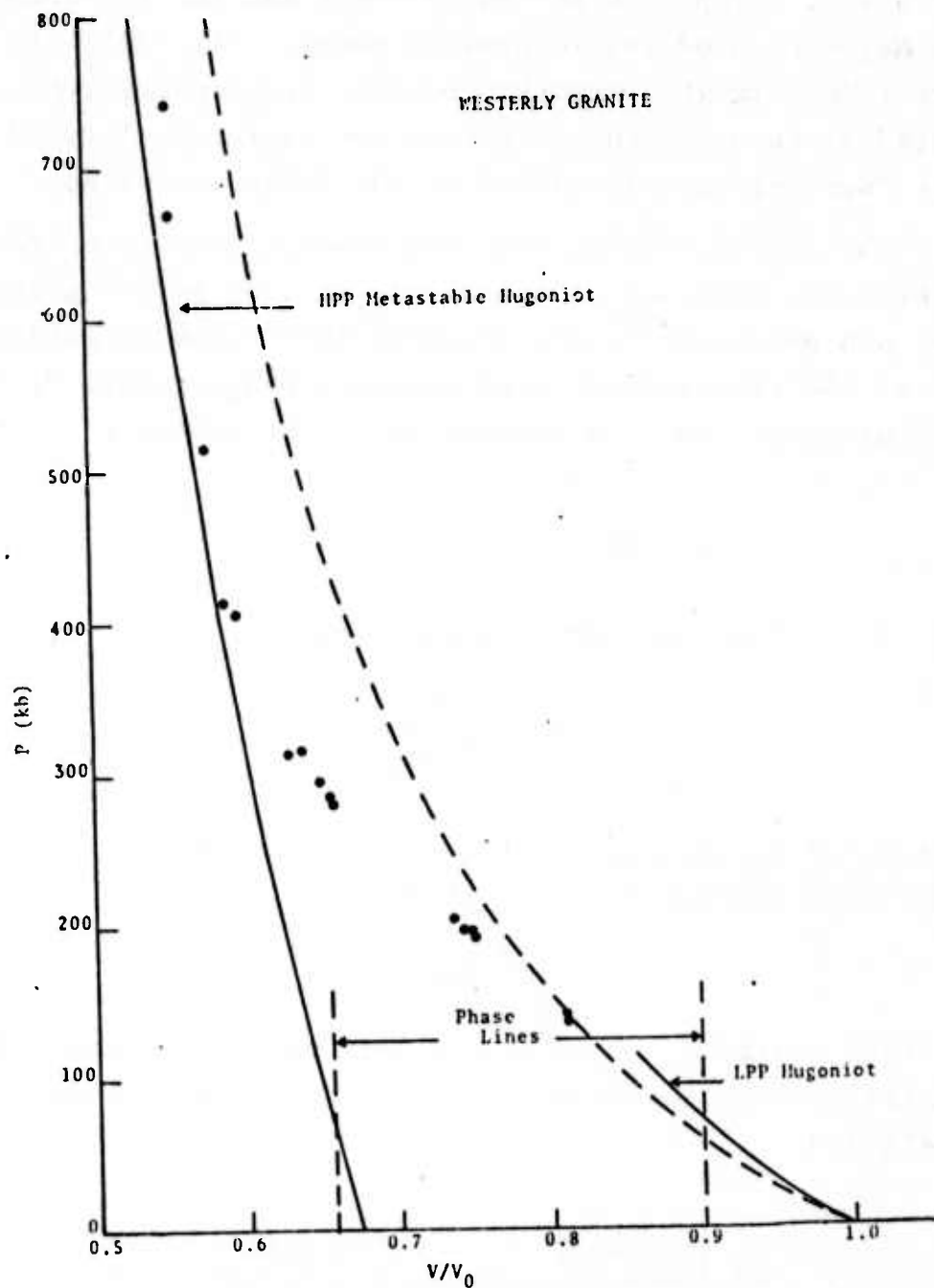


Fig. 3.2--Illustration of the two-phase model used to fit the experimental Hugoniot data.

$$\frac{G}{V} \equiv \left(\frac{\partial P}{\partial E} \right)_V$$

was assumed to have the constant value 2.63 (a zero-pressure Grüneisen ratio of 0.67 for the high-pressure phase); and the zero-pressure energy difference between the high and low-pressure phases was taken as

$$E_{00} - E_0 = 0.8 \times 10^{10} \text{ erg/gm.}$$

(after Ahrens [23]). The calculated values of P_H are not particularly sensitive to the exact value of this energy difference. The resulting $P_H - V$ points were then converted to $U_s - U_p$ points and the resulting least-squares straight-line fit is

$$U_s = 7.55 + 1.134 U_p, \quad (3.5)$$

where the intercept was constrained to have the value

$$U_s (U_p = 0) = \sqrt{\phi_0} = 7.55.$$

To summarize, then, the Hugoniot for the low-pressure phase is taken as

$$U_s = 4.50 + 1.25 U_p \quad (\text{LPP})$$

with $\rho_0 = 2.63 \text{ gm/cm}^3$, and the Hugoniot for the high-pressure phase is taken as

$$U_s = 7.55 + 1.134 U_p \quad (\text{HPP})$$

with $\rho_{00} = 3.90 \text{ gm/cm}^3$.

There appears to be no direct experimental work on the pressure-temperature phase line for the granite transition. However, granite is about one-third quartz, and the experimental work of Akimoto and Syono^[24] on the quartz \rightarrow coesite \rightarrow stishovite transformation gives the result

$$P(\text{kb}) = 69 + 0.024T(^{\circ}\text{C})$$

for the coesite-stishovite transformation, or

$$\frac{dP}{dT} = 24 \text{ bar/deg.}$$

Now, if one assumes a Grüneisen ratio of 1.0 for granite, then

$$\left(\frac{\partial P}{\partial T}\right)_V = \rho C_V G \approx (2.6)(0.8 \times 10^7)(1.0) \\ \approx 20 \text{ bar/deg.}$$

which is close enough to the slope of the coesite-stishovite phase line that a vertical phase line in the $P - V$ plane for granite was considered to be a reasonable approximation for the present purpose (see Fig. 3.2). The right phase line is located at $V = 0.9 V_0$ and intersects the LPP Hugoniot at a pressure of 69.6 kbars. The left phase line, for simplicity and for lack of other information, is assumed to be vertical also. It is located at a volume $V = 0.249 \text{ cm}^3/\text{gm}$, so that the volume change for the transition is

$$\Delta V = - 0.093 \text{ cm}^3/\text{gm}.$$

The use of the Clausius-Clapeyron equation

$$\frac{dP}{dT} = \frac{\Delta S}{\Delta V}$$

gives the value

$$\Delta S = - 0.233 \times 10^7 \text{ erg/gm/deg}$$

for the entropy change of the transition. Equating the change in the Gibbs free energy to zero,

$$\Delta G = \Delta H - T\Delta S = 0$$

gives

$$\Delta E = 5.74 \times 10^9 \text{ erg/gm}$$

for the difference in the internal energy of the two phases at the phase line. If the value for the internal energy of the low-pressure phase is taken to be zero at $P = 0$, $\rho_0 = 2.63$, then the value of the internal energy of the high-pressure phase at $P = 0$, $\rho_{00} = 3.90$ is

$$E_{00} = 0.68 \times 10^{10} \text{ erg/gm.}$$

It will be noted that this value differs from the value 0.8×10^{10} used in computing the metastable Hugoniot, but not by so much that it was considered necessary to recompute it.

The Mie-Grüneisen equation of state is used to complete the thermodynamic description of the two phases,

$$P = P_H(V) + \left(\frac{G}{V}\right) (E - E_H(V)), \quad (3.6)$$

and the present model uses the following assumptions:

- a) The thermodynamic derivative

$$\left(\frac{G}{V}\right) \equiv \left(\frac{\partial P}{\partial E}\right)_V$$

is independent of temperature and volume and has the same numerical value for both the LPP and the HPP.

- b) The specific heat at constant volume, C_V , is also independent of temperature and volume and has the same value for each phase.

These assumptions are compatible with the requirement that the Gibbs free energies of the two phases be equal at all points on the phase lines, which in this model are vertical in the P-V plane. The numerical values used are

$$C_V = 0.795 \times 10^7 \text{ erg/g/deg}$$

and

$$\left(\frac{\partial P}{\partial E}\right)_V = 2.63 \text{ g/cm}^3$$

which corresponds to a Gruneisen ratio of 1.0 at the foot of the LPP Hugoniot and a value of 0.67 at the foot of the HPP Hugoniot.

3.2 INCORPORATION OF THE MODEL INTO THE SKIPPER CODE

In the SKIPPER code the task of the equation-of-state subroutine is to compute a hydrostatic pressure from given values for the specific volume V and the specific internal energy E . If only a single phase is present, this is easily accomplished with an analytic equation of state,

$$P = f(E, V) .$$

However, when two phases are present, each phase will have its own equation of state,

$$P_1 = f_1(E_1, V_1)$$

$$P_2 = f_2(E_2, V_2)$$

and the task is to calculate the pressure given the specific volume V and the specific internal energy E of the mixture. In the following discussion the subscript 1 will denote the phase which is stable at low pressures and room temperature (LPP), and the subscript 2 will denote the phase which is stable at high pressures (HPP).

3.2.1 Interpolated-Pressure Method

A first series of exploratory calculations was done with a subroutine which calculated an approximate pressure, the only requirement being pressure equilibrium between the two phases in the mixed-phase regime. (A method which insures temperature equilibrium as well is described in the next section). The first step in this method is to compute an equilibrium pressure from the given values of V and E , i.e., the pressure which would exist if the mass fraction f in the HPP were the equilibrium value. In this equilibrium calculation, if the volume V is larger than V_{1ph} (the specific volume of the low-pressure phase at the right phase

line) the Hugoniot for the LPP is used together with the equation of state, Eq. (3.6), to compute the equilibrium pressure. If the volume V is less than V_{2ph} , the Hugoniot for the high-pressure phase is used to compute the equilibrium pressure. If the volume V is such that $V_{2ph} < V < V_{1ph}$, then for equilibrium,

$$V = (1 - f_{eq}) V_{1ph} + f_{eq} V_{2ph} \quad (3.7)$$

$$E = (1 - f_{eq}) E_{1ph} + f_{eq} E_{2ph}$$

where f_{eq} is the mass fraction in the high-pressure phase, and the subscript ph indicates evaluation on the appropriate phase line. Solving the first of these for f_{eq} and using the relation

$$E_{1ph} = E_{H_1} + \left(\frac{\partial E}{\partial P} \right)_V (P - P_{H_1})$$

in the second, where E_{H_1} and P_{H_1} are the LPP Hugoniot energy and pressure at the right phase line, gives for the equilibrium pressure in the mixed phase region

$$P_{eq} = P_{H_1} + \left(\frac{\partial P}{\partial E} \right)_V \left[E - E_{H_1} - \frac{V - V_{1ph}}{\Delta V} \Delta E \right] \quad (3.8)$$

where

$$\Delta V \equiv V_{2ph} - V_{1ph}$$

$$\Delta E \equiv E_{2ph} - E_{1ph}$$

If a finite amount of time is required for the transformation from one phase to the other, then the mass fraction f in the HPP will not necessarily be the equilibrium value. With this interpolated-pressure method, depending upon whether

the current value of f is larger or smaller than the equilibrium value, the pressure is weighted linearly away from the equilibrium value towards the pressure of the appropriate phase. For example, if V were such that $f_{eq} = 1/2$, and the current value of f is $1/4$, the pressure is taken as half way between the equilibrium value and the pressure of the LPP at the same volume and energy.

The calculation of the mass fraction f in the HPP will be discussed after a description of the pressure-temperature equilibrium method in the next section.

3.2.2 Pressure-Temperature Equilibrium Method

Subsequent to the first series of exploratory calculations, the interpolated-pressure method was replaced with a subroutine which, although requiring a longer execution time, satisfies the requirement that the pressures and temperatures of the two phases be the same in the mixed phase regime.

Assumption a) of Section 3.1 allows the pressure of each phase to be written in terms of its specific volume and specific internal energy as follows

$$P_1 = P_{H1}(V_1) + \left(\frac{G}{V}\right) [E_1 - E_{H1}(V_1)] \quad (3.9)$$

$$P_2 = P_{H2}(V_2) + \left(\frac{G}{V}\right) [E_2 - E_{H2}(V_2)] \quad (3.10)$$

In the above expressions, $P_{H1}(V_1)$ is the pressure on the LPP Hugoniot centered at $P_1 = 0$ and $V_1 = V_{10}$, and $E_{H1}(V_1)$ is the specific internal energy of the pure LPP for a state on its Hugoniot,

$$E_{H1}(V_1) = E_{10} + \frac{1}{2} (V_{10} - V_1) P_{H1}(V_1). \quad (3.11)$$

Similarly, $P_{H_2}(V_2)$ is the pressure on the HPP Hugoniot centered at the (metastable) state $P_2 = 0$ and $V_2 = V_{20}$, and

$$E_{H_2}(V_2) = E_{20} + \frac{1}{2} (V_{20} - V_2) P_{H_2}(V_2). \quad (3.12)$$

Assumptions a) and b) imply that

$$\left(\frac{\partial P}{\partial T}\right)_V \equiv \left(\frac{G}{V}\right) C_V$$

is also constant, so that the temperature of each phase can be written as

$$T_1 = T_{H_1}(V_1) + \left(\frac{V}{G}\right) \frac{1}{C_V} [P_1 - P_{H_1}(V_1)] \quad (3.13)$$

$$T_2 = T_{H_2}(V_2) + \left(\frac{V}{G}\right) \frac{1}{C_V} [P_2 - P_{H_2}(V_2)] \quad (3.14)$$

where $T_{H_1}(V_1)$ and $T_{H_2}(V_2)$ are the temperatures on the LPP and HPP Hugoniots respectively as a function of specific volume.

For a mixture of the two phases in pressure and temperature equilibrium, Eqs. (3.13) and (3.14) require that

$$P_{H_1}(V_1) - \left(\frac{G}{V}\right) C_V T_{H_1}(V_1) = P_{H_2}(V_2) - \left(\frac{G}{V}\right) C_V T_{H_2}(V_2) \quad (3.15)$$

as one connection between the specific volumes V_1 and V_2 . Another connection is (valid for any model)

$$(1 - f) V_1 + f V_2 = V, \quad (3.16)$$

where f is the mass fraction in the HPP, and V is the specific volume of the mixture. Thus, if V and f are

specified, Eqs. (3.15) and (3.16) determine V_1 and V_2 , the specific volumes of the LPP and the HPP. The numerical procedure used to solve for V_1 and V_2 will be described below.

The specific internal energy E of the mixture is related to the specific internal energies E_1 and E_2 of the LPP and HPP by

$$(1 - f) E_1 + f E_2 = E, \quad (3.17)$$

so that

$$E_1 = E - f(E_2 - E_1). \quad (3.18)$$

Equating the pressures of the two phases as given by Eqs. (3.9) and (3.10) gives

$$\left(\frac{G}{V}\right) (E_2 - E_1) = P_{H_1} - P_{H_2} + \left(\frac{G}{V}\right) (E_{H_2} - E_{H_1}). \quad (3.19)$$

The use of Eqs. (3.18) and (3.19) in Eq. (3.9) then gives for the pressure

$$P = (1 - f)P_{H_1}(V_1) + fP_{H_2}(V_2) + \left(\frac{G}{V}\right) \left[E - (1 - f)E_{H_1}(V_1) - fE_{H_2}(V_2) \right] \quad (3.20)$$

in terms of the specific internal energy E of the mixture and the values for V_1 and V_2 as determined from Eqs. (3.15) and (3.16). Note that Eq. (3.20) limits properly for the special cases $f = 0$ and $f = 1$.

To summarize, the specific volume V of the mixture is used in Eqs. (3.15) and (3.16) to calculate values for V_1 and V_2 . These values together with the specific internal energy E of the mixture are used in Eq. (3.20) to compute

the pressure. This procedure assures that in the mixed phase regime the pressures and temperatures of the two phases will be equal.

The determination of the mass fraction f in the high-pressure phase is a separate calculation. All the calculations carried out so far have used the (overly simplified) rate law originally proposed by Horie.^[25]

$$\frac{df}{dt} = (f_{eq} - f)/\tau, \quad (3.21)$$

where f_{eq} is the equilibrium value corresponding to the specific volume V and specific internal energy E , and τ is an adjustable relaxation time which governs the rate of the transformation. More nearly realistic (and complicated) models for the transformation rate are discussed by Johnson.^[26]

3.2.3. Numerical Solution for V_1 and V_2

The following method for solving Eqs. (3.15) and (3.16) for V_1 and V_2 assumes that the Hugoniot for both the HPP and the LPP are characterized by linear fits of shock velocity versus particle velocity

$$\begin{aligned} U_{s_1} &= c_1 + s_1 U_{p_1} \\ U_{s_2} &= c_2 + s_2 U_{p_2} \end{aligned} \quad (3.22)$$

The Hugoniot pressures are then given by

$$\begin{aligned} P_{H_1}(V_1) &= \rho_{10} c_1^2 \frac{\eta_1}{(1 - s_1 \eta_1)^2} \\ P_{H_2}(V_2) &= \rho_{20} c_2^2 \frac{\eta_2}{(1 - s_2 \eta_2)^2}, \end{aligned} \quad (3.23)$$

where

$$\eta_1 \equiv 1 - \frac{V}{V_{10}} \quad (3.24)$$

$$\eta_2 \equiv 1 - \frac{V}{V_{20}} .$$

The Hugoniot temperature for each phase satisfies the first-order differential equation

$$\frac{dT_H}{d\eta} - G_0 T_H = \frac{sc^2}{C_V} \frac{\eta^2}{(1 - s\eta)^3} , \quad (3.25)$$

the solution of which is

$$T_H = T_{H_0} e^{G_0 \eta} + \frac{sc^2}{C_V} e^{G_0 \eta} \int_0^\eta e^{-G_0 \xi} \frac{\xi^2}{(1 - s\xi)^3} d\xi \quad (3.26)$$

where

$$G_0 \equiv V_0 \left(\frac{\partial P}{\partial E} \right)_V$$

is the Gruneisen ratio at the foot of the Hugoniot, and T_{H_0} is the absolute temperature at the foot of the Hugoniot. The temperature as given by Eq. (3.26) is not a convenient form for numerical evaluation. A form which is convenient is

$$T_H = T_{H_0} e^{G_0 \eta} + \frac{sc^2}{3C_V} \frac{\eta^3}{(1 - s\eta)^2} \left[1 + A_1 \eta + A_2 \eta^2 + A_3 \eta^3 + \dots \right] \quad (3.27)$$

The coefficients A_1 , A_2 and A_3 are determined by substituting Eq. (3.27) directly into the differential equation, Eq. (3.25). The result is

$$A_1 = \frac{1}{4} (s + G_0)$$

$$A_2 = \frac{1}{5} \left[\frac{1}{4} (2s + G_0)(s + G_0) - G_0 s \right] \quad (3.28)$$

$$A_3 = \frac{(3s + G_0)}{30} \left[\frac{1}{4} (2s + G_0)(s + G_0) - G_0 s \right] - \frac{G_0 s}{24} (s + G_0)$$

The series converges rapidly for the range of compressions of interest. For example, for the LPP granite with

$$U_{s_1} = 4.50 \times 10^5 + 1.25U_{p_1}$$

and $G_0 = 1.00$, the values of the coefficients are

$$A_1 = 0.5625$$

$$A_2 = 0.14375$$

$$A_3 = -0.003385...$$

and the error in the computed Hugoniot temperature as computed from Eq. (3.27) is less than 0.02 percent at $\eta_1 = 0.4$ ($P_{H_1} \approx 850$ kbar). If the value of T_H as computed from Eq. (3.27) is less than T_{H_0} , it is arbitrarily set equal to T_{H_0} .

The first task here, for given values of f and V is to find the roots of the expression

$$F(V_1, V_2) \equiv (1 - f)V_1 + fV_2 - V = 0 \quad (3.29)$$

subject to the constraint

$$P_{H_2}(V_2) = P_{H_1}(V_1) - \frac{G}{V} C_V T_{H_1}(V_1) + \frac{G}{V} C_V T_{H_2}(V_2). \quad (3.30)$$

The procedure adopted is an iterative one. The zeroth-order approximation to V_1 is taken as

$$V_1^{(0)} = V.$$

This value for V_1 is substituted in (3.30) which is then solved for V_2 (see below), which will be the zeroth-order approximation $V_2^{(0)}$. These values are substituted in (3.29) to obtain

$$F^{(0)} \equiv F(V_1^{(0)}, V_2^{(0)}).$$

Next, the first-order approximation to V_1 is taken as

$$V_1^{(1)} = V_1^{(0)} + 0.05$$

Again, this value is used in Eq. (3.30) to solve for $V_2^{(1)}$, and Eq. (3.29) is used to compute

$$F^{(1)} \equiv F(V_1^{(1)}, V_2^{(1)}).$$

A linear interpolation (extrapolation) is made using the two values $F^{(0)}$ and $F^{(1)}$ to find the value $V_1^{(2)}$ which makes the interpolated (extrapolated) value of F equal to zero,

$$V_1^{(2)} = V_1^{(0)} - F^{(0)} \left[\frac{V_1^{(1)} - V_1^{(0)}}{F^{(1)} - F^{(0)}} \right].$$

Equation (3.30) is used again to compute $V_2^{(2)}$, and the new value $F^{(2)}$ is used in the above relation to obtain $V_1^{(3)}$. The general form is

$$V_1^{(k)} = V_1^{(0)} - F^{(0)} \left[\frac{V_1^{(k-1)} - V_1^{(0)}}{F^{(k-1)} - F^{(0)}} \right]$$

The process is continued until $V_1^{(k)}$ differs from $V_1^{(k-1)}$ by as small an amount as desired.

For a given value of V_1 , Eq. (3.30) is solved by a separate iteration. The second of Eqs. (3.23) is used for the left side of Eq. (3.30). The solution of the resulting quadratic equation in η_2 is

$$\eta_2 = \frac{2g}{(2gs_2 + 1) + \sqrt{4gs_2 + 1}}, \quad (3.31)$$

where

$$g \equiv \frac{1}{\rho_{20} c_{20}^2} \left[p_{H_1}(V_1) - \left(\frac{G}{V}\right) C_V T_{H_1}(V_1) + \left(\frac{G}{V}\right) C_V T_{H_2}(V_2) \right]. \quad (3.32)$$

The first time around, g is computed with $T_{H_2}(V_2)$ set equal to zero. The resulting value of η_2 from Eq. (3.31) is used to recompute g , which in turn is used in Eq. (3.31) to recompute η_2 , etc.

The above described method of calculating the pressure utilizes simplifications which result from the fact that the phase lines are taken to be vertical in the P-V plane and that the specific heat C_V and thermodynamic derivative $(\partial P / \partial E)_V$ are assumed to be the same for each phase. The use of the vertical phase lines allows an immediate calculation of f_{eq} from only the volume of the mix for use in Eq. (3.21) in updating f (mass fraction in the HPP). The calculation of f_{eq} for phase lines of arbitrary slope would also involve the pressure, through the dependence $V_{1ph}(P)$ and $V_{2ph}(P)$. This can be handled but at the expense of introducing another iteration procedure and a longer execution time. The equality of the specific heats and the derivatives (G/V) decouples the equations involving the specific internal energies E_1 and E_2 of the two

phases from those involving the specific volumes V_1 and V_2 . The result is the two simultaneous equations (3.15) and (3.16) for the specific volumes; the internal energies E_1 and E_2 are not calculated explicitly. The general case of unequal specific heats and (G/V) ratios leads to four coupled equations in V_1, V_2, E_1 and E_2 . A general iterative procedure for handling this general case is described in Ref. [1], and could be incorporated in the future if sufficient experimental data were available to warrant it.

3.3 EXPLORATORY CALCULATIONS WITH PLANAR SKIPPER

For driving pressures in the range from about 70 kbars to 280 kbars, the present two-phase model will lead to a two-wave structure. A series of planar calculations using the interpolated-pressure method (zero shear strength) were made to test the code's ability to handle this phenomenon. Figure 3.3 shows the pressure profiles obtained for constant driving pressures of 150 and 300 kbars at the left interface. For these runs the quadratic and linear viscosity coefficients were set at 1.6 and 0.4 respectively. Aside from the spurious "ringing" the results are satisfactory. The 150 kbar driving pressure produces the required two-wave structure, while the 300 kbar driving pressure does not, also as required. So far, for the equilibrium calculations ($\tau = 0$) it has not been possible to adjust the viscosity coefficients to eliminate the ringing completely. Also, in order to reduce the ringing to the level shown in Fig. 3.3 it was found necessary to introduce a fictitious sound speed in the mixed-phase region. The reason is that the thermodynamic pressure increases very slowly with decreasing volume in the mixed phase region, according to this model. Consequently, the calculated sound speeds are small. The sound speed is used in the calculation of the linear viscosity term, and the sudden jump in sound speed as a zone passed from the mixed phase region into the high-pressure phase region produced an intolerably rapid change in the viscous pressure term. This undesirable effect was eliminated by using, in the mixed phase region, a sound speed which is a linear interpolation between a value characteristic of the low-pressure phase and a value characteristic of the high-pressure phase. The remaining overshoot is presumably related to the fact that the rate of change of thermodynamic pressure undergoes a sudden increase as a zone passes from the mixed phase to the high-pressure phase. The P-T

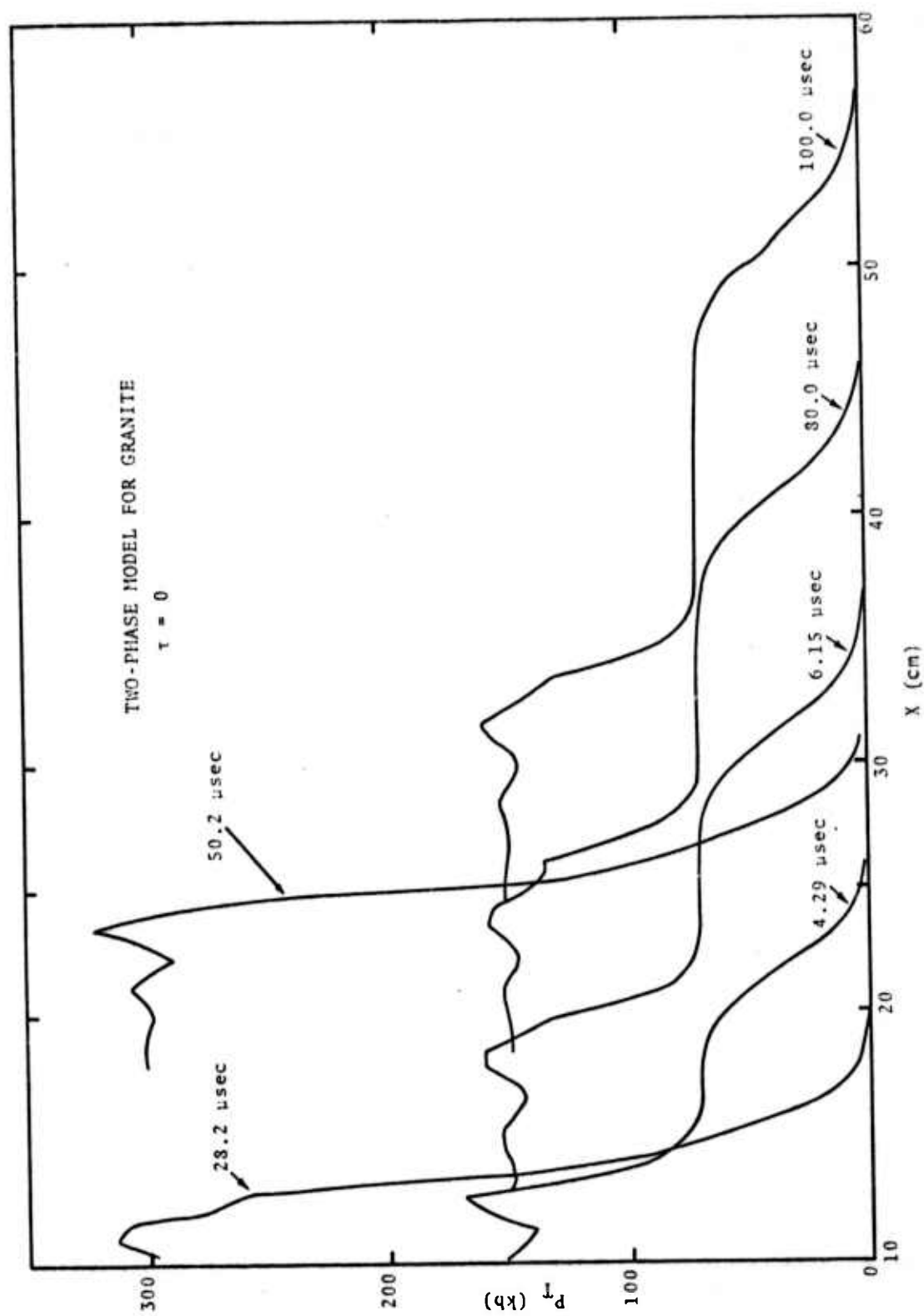


Fig. 3.3--Pressure profiles for constant driving pressure at 150 and 300 kbar at the left interface. Illustration of two-wave structure for pressures between 70 and 200 kbar. Here $\tau = 0$.

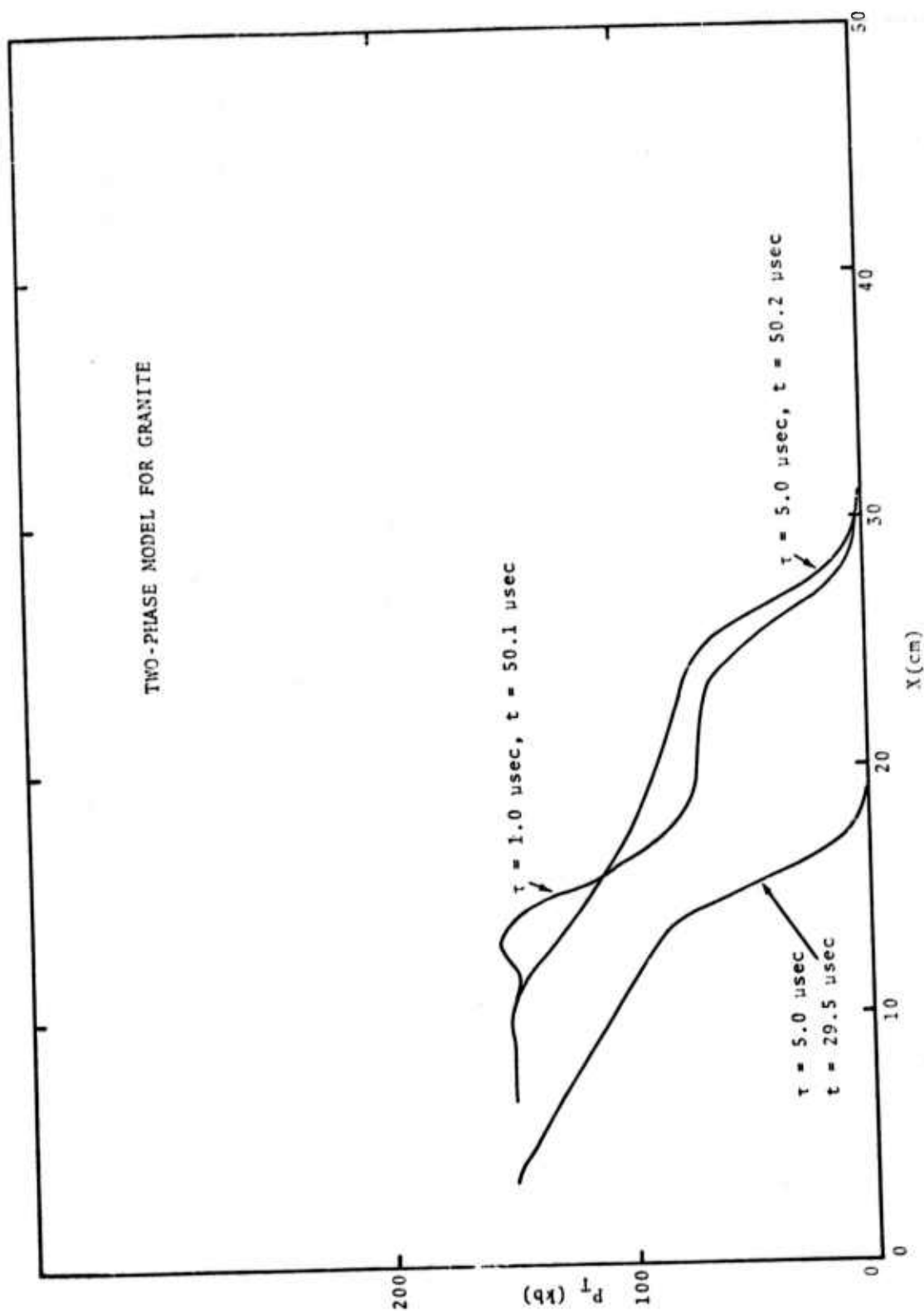


Fig. 3.4--Effect of varying relaxation time τ for a 150 kbar driving pressure. Note characteristic decay of "precursor" caused by $\tau > 0$.

equilibrium method uses a sound speed c for the mix calculated from

$$\frac{1}{\rho^2 c^2} = \frac{(1 - f)}{\rho_1^2 c_1^2} + \frac{f}{\rho_2^2 c_2^2}$$

where ρ is the density and c_1 and c_2 are the appropriate sound speeds in the LPP and HPP respectively. This value for c is the "frozen" sound speed (constant f) and gives a smooth interpolation between the sound speeds of the LPP and HPP.

The effect of varying and relaxation time τ for a 150 kbar driving pressure is shown in Fig. 3.4. The primary effect of the 1.0 μ sec relaxation time (about three time cycles) is to reduce the spurious overshoot in the second wave. The 5.0 μ sec relaxation time produces a pronounced smearing of the transition from the low-pressure phase to the high-pressure phase. Also evident in Fig. 3.4 is the characteristic decay of the "precursor" caused by the finite relaxation time.

Figure 3.5 is a plot of several pressure profiles which are the result of loading the left interface to 300 kbars for 40 μ sec and then releasing the pressure to zero. Comparison calculations with the same loading are shown for a single-phase equation of state (fit by Allen^[27]), the Hugoniot for which is shown as the dashed line in Fig. 3.2. The difference between the results with the two-phase model and the single-phase model is quite pronounced. The initial decay of peak pressure for the two-phase model is extremely rapid because of the large sound speeds characteristic of the high-pressure phase. Also, as the pressure in the lead part of the wave drops below 280 kbars, the two phase model develops the characteristic two-wave structure. The "detail" in the lead part of the second wave is not real,

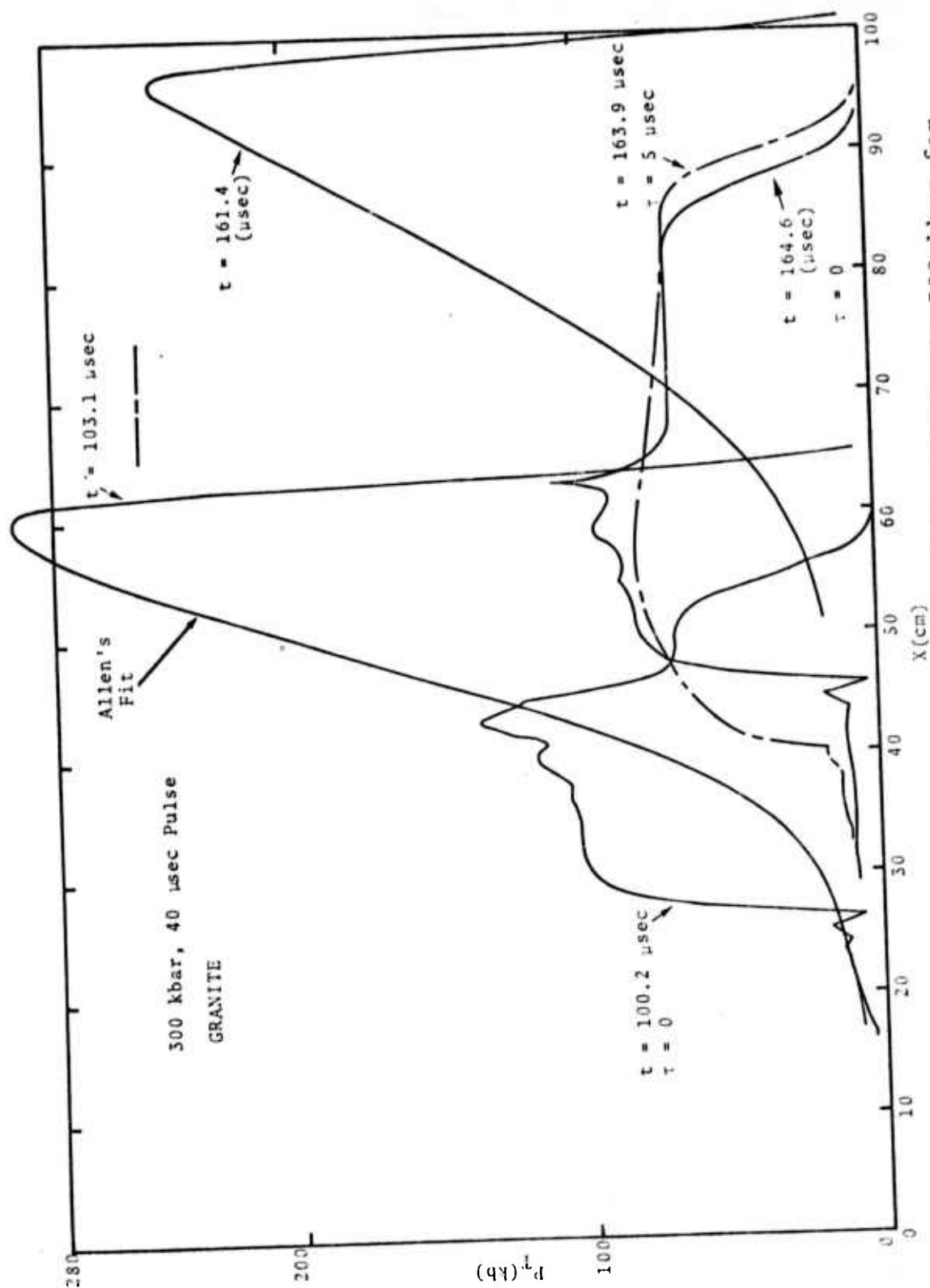


Fig. 3.5--Pressure profiles from loading left surface to 300 kbar for 40 μ sec and then releasing to zero. Comparison calculation was made using Allen's single phase fit to Tillotson's form.

but is a result of the numerical difficulties already mentioned. An additional feature of the two-phase model which is not present in the single-phase one is the occurrence of the rarefaction shock, which is clearly evident in the profiles shown in Fig. 3.5.

Figure 3.6 is a plot of the particle velocity profiles which correspond to the pressure profiles shown in Fig. 3.5. The profiles are qualitatively similar. It will be noted that the particle velocity after release for the two-phase model with 300 kbar loading does not go negative, as it does for the single-phase model. This is because the P-V release curve for the two-phase model lies so far below the Rayleigh loading line (see Fig. 3.7).

Figure 3.8 shows the effect of a 20 μ sec relaxation time on the 300 kbar, 40 μ sec pulse. The long relaxation time wipes out the two wave structure on the lead part of the pulse.

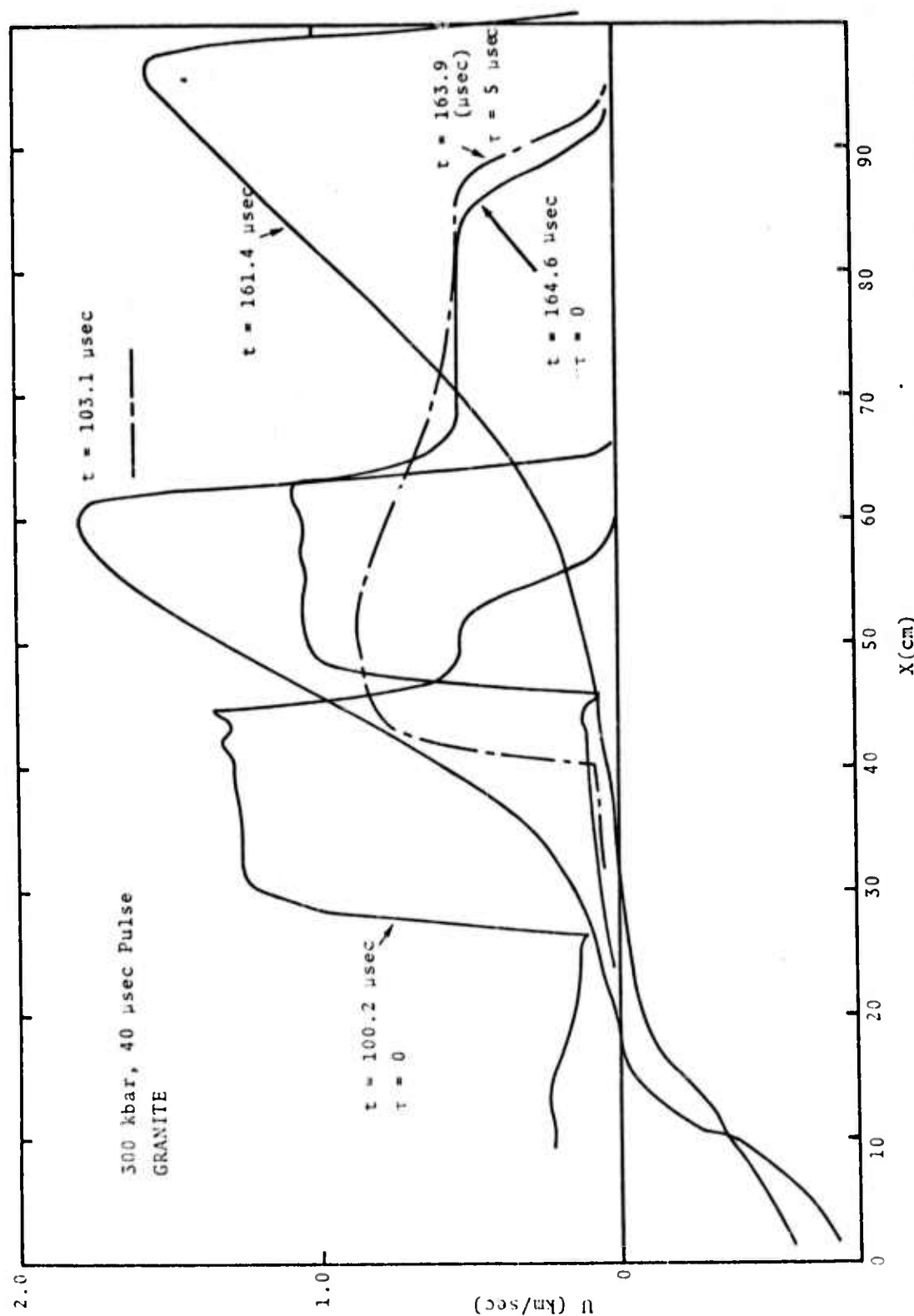


Fig. 3.6--Particle velocity profiles from loading left surface to 300 kbar for 40 μ sec and then releasing to zero. Comparison calculation was made using Allen's single-phase fit to Tillotson's form.

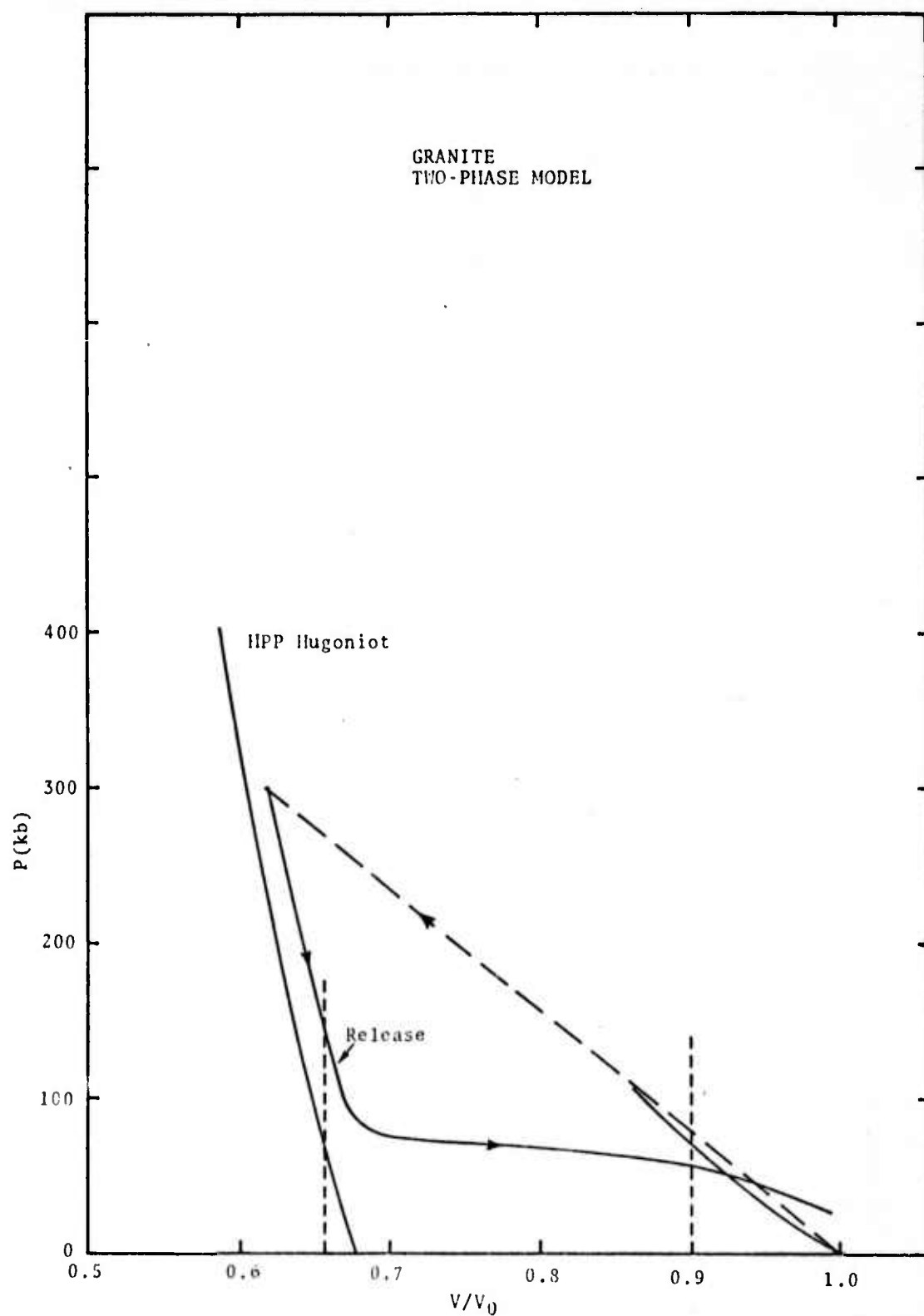


Fig. 3.7--Illustration of Hugoniot and release curves for two-phase model.

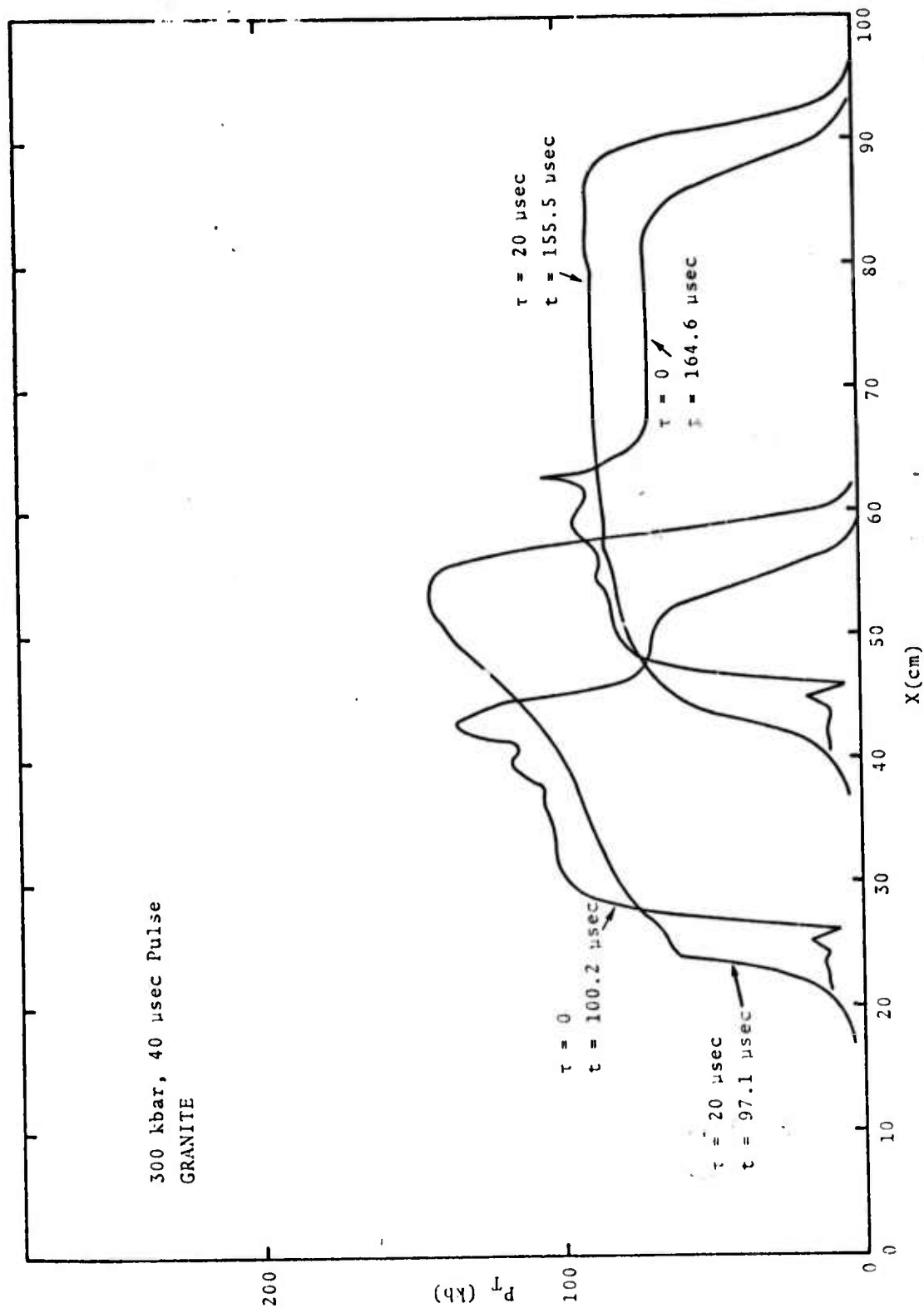


Fig. 3.8--Illustration of effect of $\tau = 20 \mu\text{sec}$ relaxation time. The long relaxation time wipes out the two-wave structure.

3.4 THE TRANSITION RATE

All the calculations carried out so far have used the rate law

$$\frac{df}{dt} = (f_{eq} - f)/\tau \quad (3.21)$$

for the rate of transformation of one phase to the other. An estimate of the relaxation time τ was obtained by trying to find a value such that the calculated transit time of a plane shock through a 1/4 inch thick sample of granite would be in agreement with the reported shock velocities of McQueen et al.^[17] Two sets of experimental data points in the mixed phase region (see Fig. 3.1) were examined. One set of four points corresponds to a shock velocity of about 7.0 mm/ μ sec in the aluminum driver, and the other set of five points corresponds to a shock velocity of 7.7 mm/ μ sec in the driver. From an impedance-match solution in the P-U_p plane, one finds that the first state in the aluminum driver would induce a shock pressure of about 215 kbar in the granite if it remained in the LPP and that the second state would produce a shock pressure of about 330 kbar in the LPP granite. The corresponding shock velocities in the pure LPP would be 6.2 and 6.8 mm/ μ sec respectively; while the actual measured shock velocities for a 1/4 inch thick sample are 5.5 and 5.7 mm/ μ sec.

Figures 3.9 and 3.10 show calculated pressure profiles at a sequence of times for constant driving pressures of 215 kbar and 330 kbar. A relaxation time of $\tau = 0.1 \mu$ sec gives a transit time for the 215 kbar wave through 1/4 inch of 1.15 μ sec, which corresponds to an average shock velocity of 5.52 mm/ μ sec for the lead part of the wave, a good agreement with the experimental value of 5.5 mm/ μ sec. The same value of $\tau = 0.1 \mu$ sec for the 330 kbar driving pressure gives

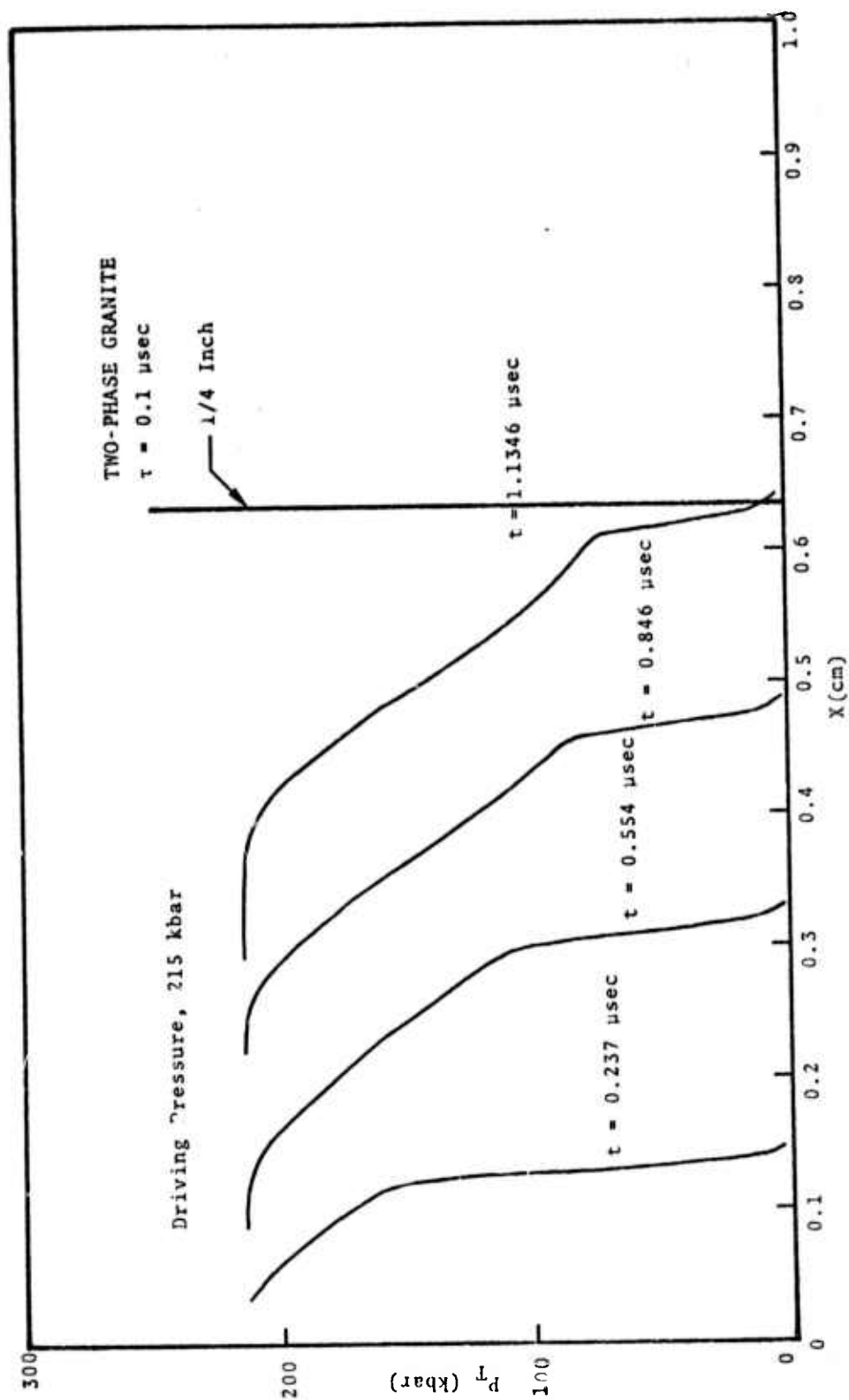


Fig. 3.9--Pressure profiles for a plane shock in granite, 215 kbar driving pressure, $\tau = 0.1 \mu\text{sec}$.

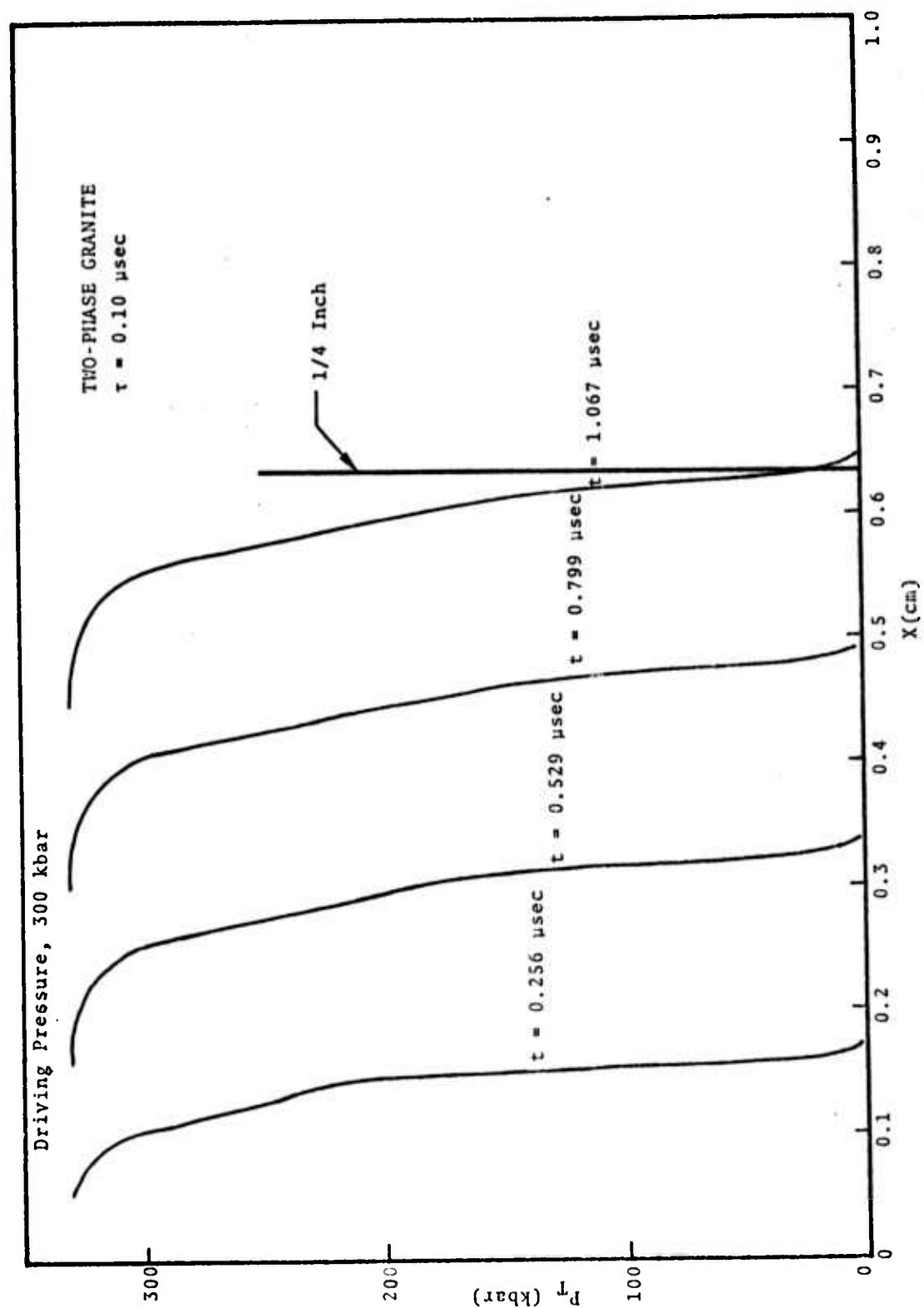


Fig. 3.10--Pressure profiles for a plane shock in granite, 330 kbar driving pressure, $\tau = 0.1 \mu\text{sec}$.

a transit time of 1.07 μsec , which corresponds to an average shock velocity for the lead part of the wave of 5.93 mm/ μsec , which is reasonably close to the measured 5.7 mm/ μsec . An increase of τ to 0.25 μsec gives an average shock velocity of 6.27 mm/ μsec for the 330 kbar wave through 1/4 inch, a value which is considerably higher than the experimental 5.7 mm/ μsec .

These considerations, although rough, indicate that a value of about 0.1 μsec for τ is appropriate for use in the rate law Eq. (3.21).

3.5 CALCULATIONS WITH SPHERICAL SKIPPER

Finally, a calculation in spherical geometry which had been done previously with a single-phase equation of state was repeated with the present two-phase model. The single-phase calculation used a Mie-Gruneisen equation of state (constant $G/V = 2.14 \text{ gm/cm}^3$) and a single fit to the experimental Hugoniot data. Figure 3.11 shows a comparison of the Hugoniot for the single-phase model with the HPP and LPP Hugoniots used in the two-phase model. The calculations are for a 20-ton source in a cavity with an initial radius of 40 cm; and both calculations used the same pressure-energy dependent yield strength model, the maximum radial stress deviator at high pressures and low energies being

$$|S_1 - \bar{S}|_{\max} = \frac{2}{3}Y = 2 \text{ kbar.}$$

The two-phase calculation was done using both the interpolated-pressure method and the more elaborate P-T equilibrium method. Both methods give essentially the same results for the calculated radial-stress profiles, as is indicated in Fig. 3.12.

However, the calculated radial-stress profiles resulting from the single-phase model and the two-phase model are significantly different. A comparison is given in Fig. 3.13. At a given radius, the peak stress as calculated with the two-phase model is about 30 percent less than that resulting from the single-phase model. Also, the stress profiles resulting from the two-phase model are broader than those of the single-phase model, although the maxima coincide. A comparison of peak radial stress as a function of distance for the two models is shown in Fig. 3.14. The cavity radius, on the other hand, is the same for the two models (at least for the first two milliseconds). Figure

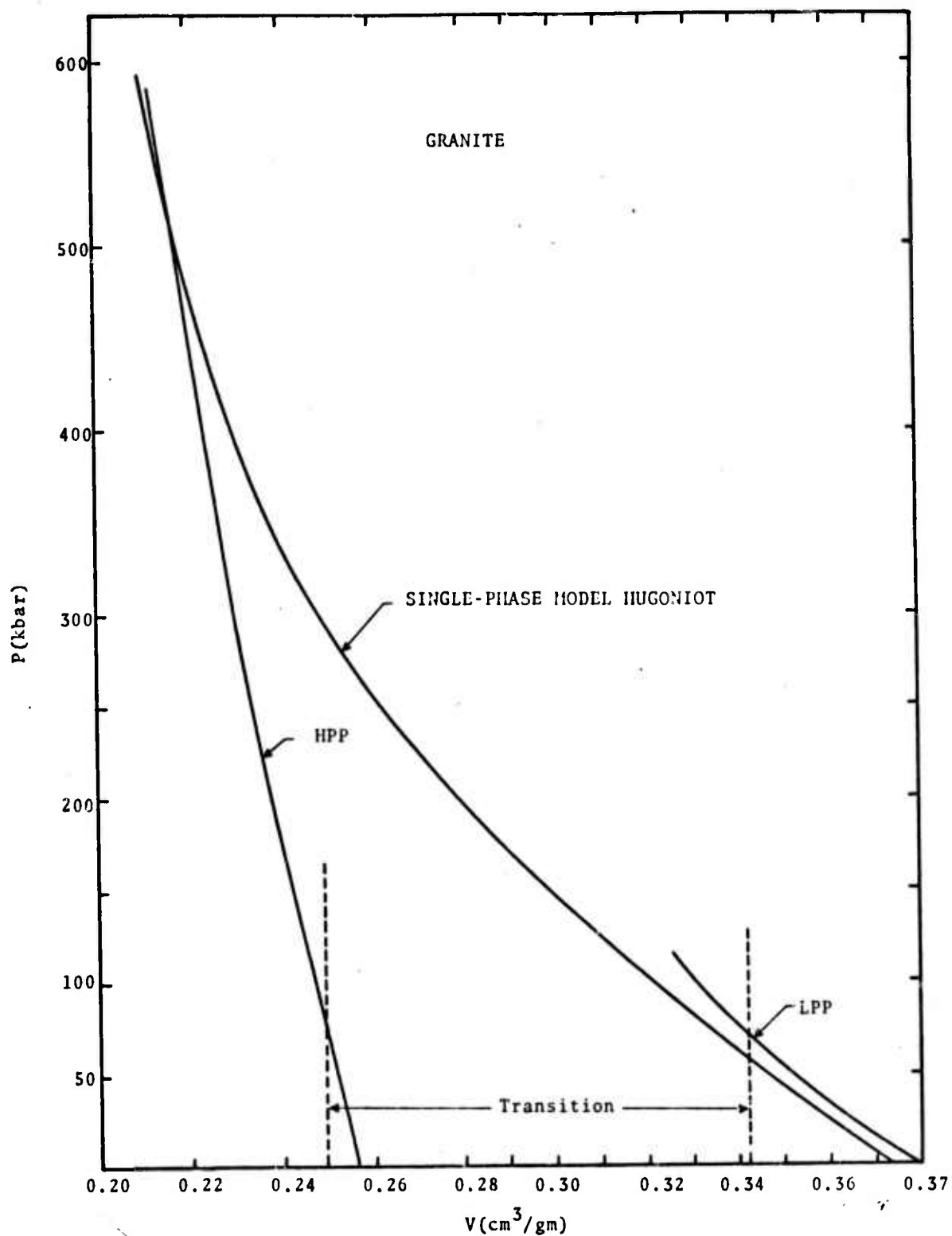


Fig. 3.11--Comparison of the Hugoniot for a single-phase model and the two-phase model used in the spherical calculation.

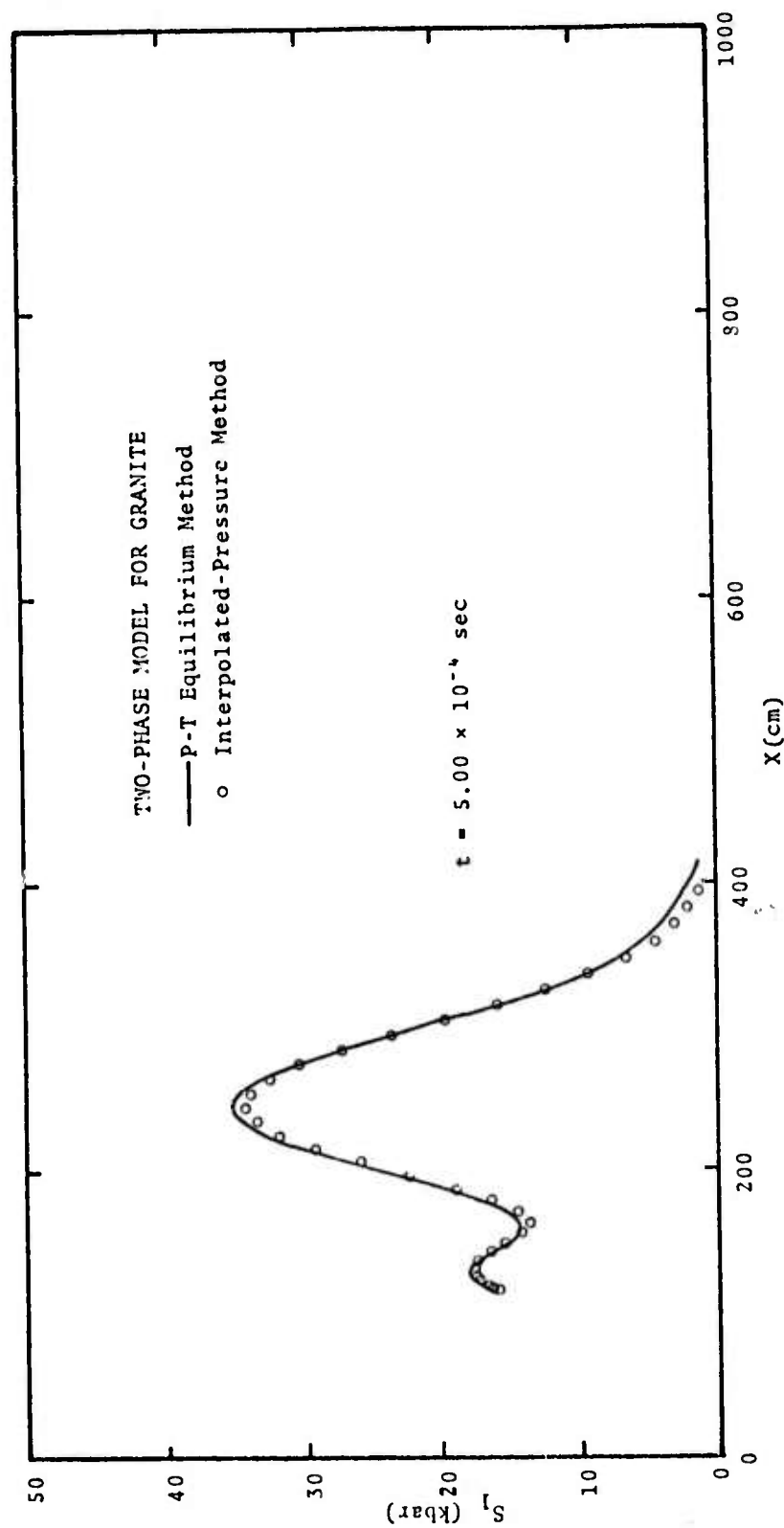


Fig. 3.12--A comparison of calculated radial-stress profiles for the two-phase model using the interpolated-pressure method and the P-T equilibrium method for a 20-ton source in a cavity with initial radius 40 cm.

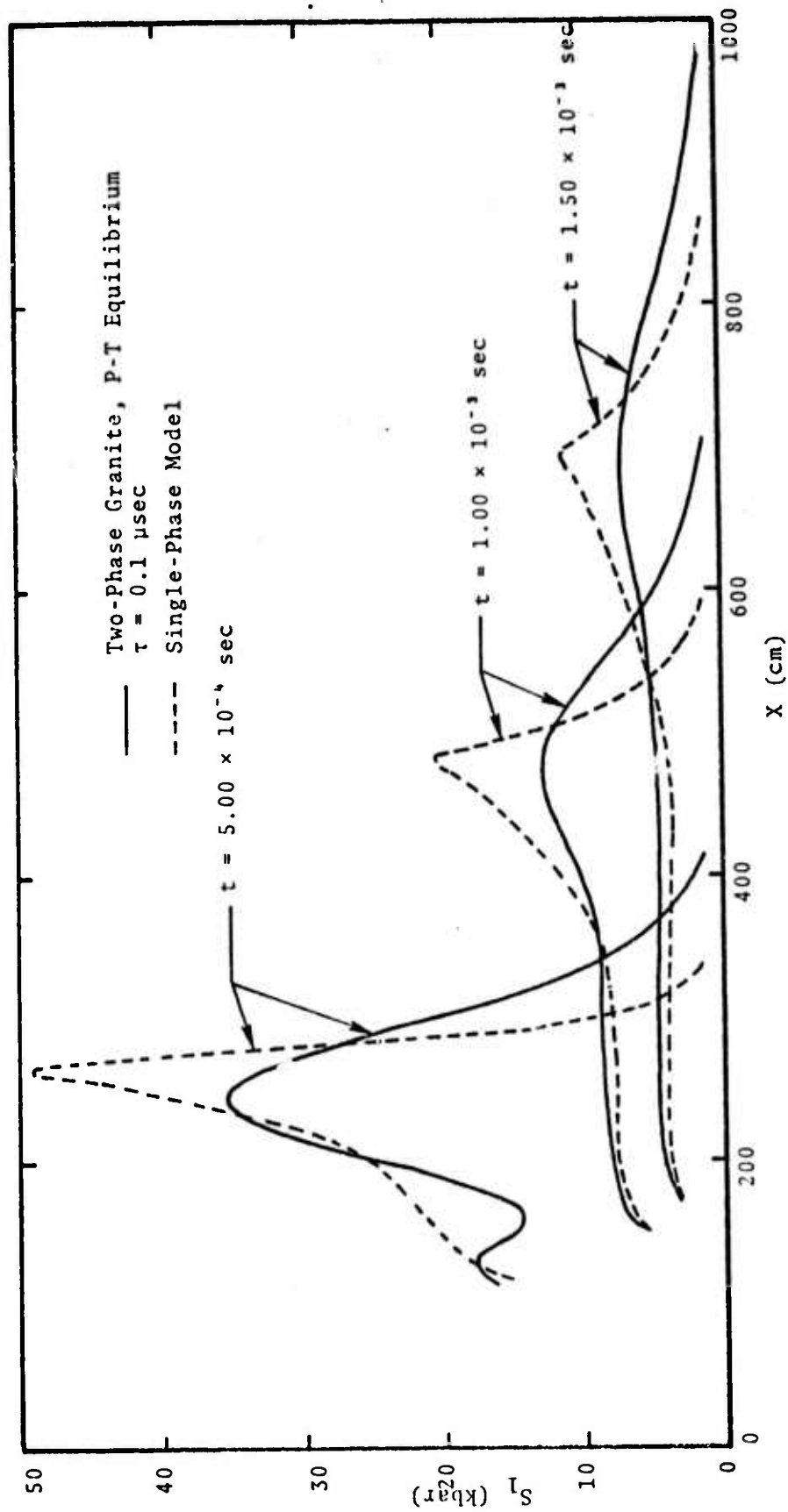


Fig. 3.13--Comparison calculations of radial stress for the single-phase model and the two-phase model for a 20-ton source in a cavity with initial radius 40 cm.

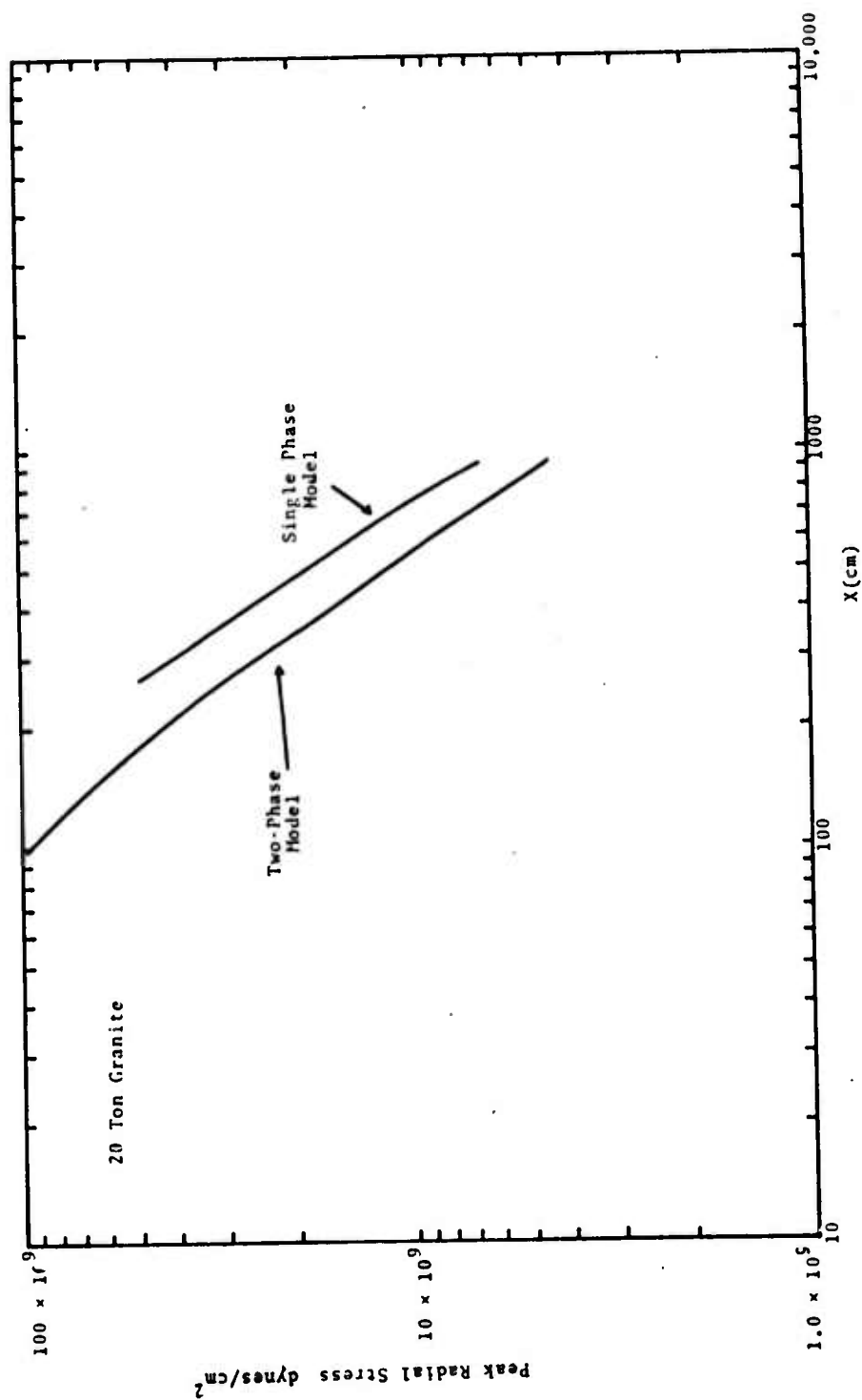


Fig. 3.14--Comparison of the peak radial stress as a function of distance for the two models used in the 20-ton source calculation.

3.15 is a comparison of the cavity radius versus time for the two-phase and single-phase calculations.

These comparisons indicate that a realistic treatment of ground motion should include explicitly any possible phase changes. Even though the maximum stress in the far field may not be large enough to cause the transformation, a phase change in the near field can have a large indirect effect in the far field because of the change in the effective source function.

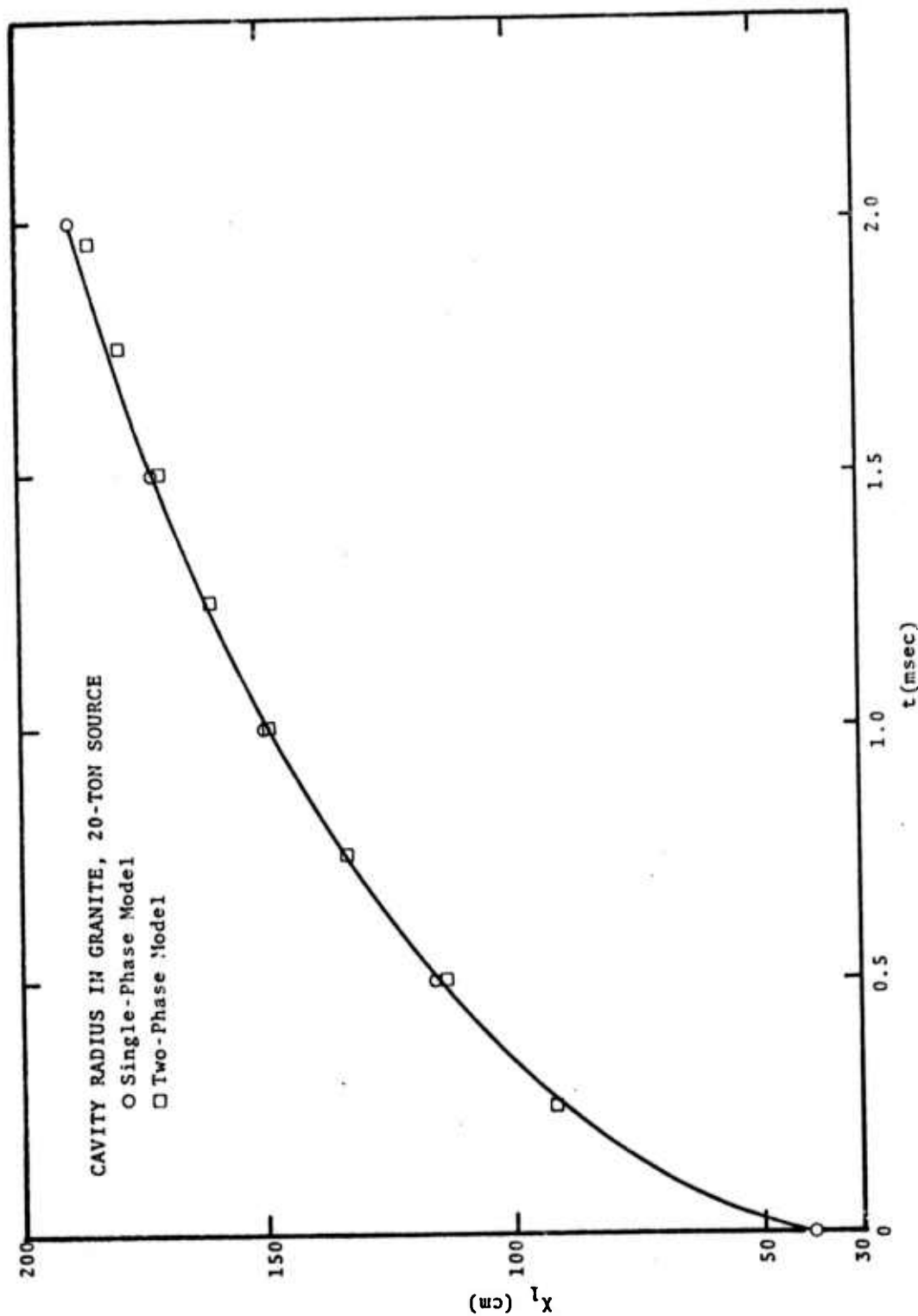


Fig. 3.15--Comparison of cavity radius as a function of time for the two models used in the 20-ton source calculations.

IV. GENERALIZED PLASTICITY MODELS IN 2D CRAM

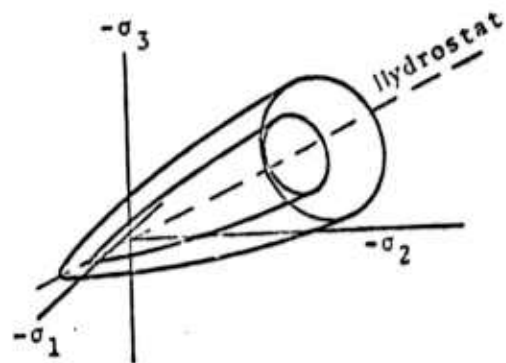
4.1 BACKGROUND AND INTRODUCTION

Successful calculations of ground motion for hard rock (e.g., granite) have proven to be much more elusive than for weaker rocks. Inaccuracies in the predictions are primarily a consequence of using inadequate material models in the calculations, especially the practice of extrapolating intact laboratory specimen strength behavior to rock masses which contain planes of weakness in the form of joints, faults and weathered regions. In Section VI preliminary results are presented from a study which has the objective of deriving a rational basis for the scaling relations between laboratory to field data by considering the medium to contain regularly spaced joints or faults. At the present time, however, the generally accepted approach is to derive constitutive models to describe the complex deviatoric stress-strain behavior measured directly on laboratory specimens. The laboratory parameters can then be adjusted in some consistent manner, hopefully, when the model is used in computer codes to calculate field test phenomena. Early attempts to match the velocity-time and displacement-time wave forms measured in granite were notably unsuccessful. The constitutive models employed neglected important physical effects and were based on incomplete material properties data. Many of the hydrodynamic elastic-plastic computer codes used in these attempts employed the von Mises yield criterion to calculate the plastic deviatoric stresses.^[28 - 30] Their technique was to multiply the deviatoric stresses that are calculated assuming elastic behavior by a common factor which insures that the newly calculated stress state lies on the von Mises yield surface. Cherry^[31] has shown that this technique is equivalent to the associated flow rule as long as the von Mises criterion

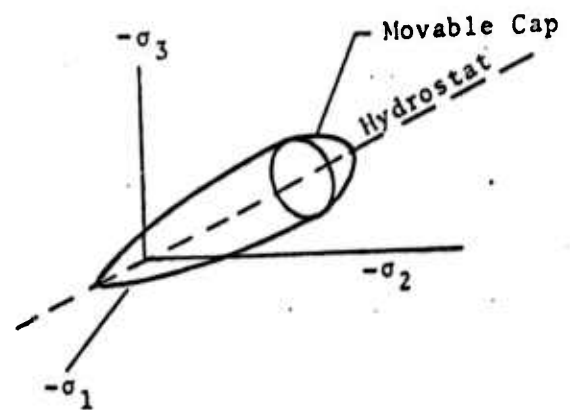
is being imposed. However, for more sophisticated yield criteria this method is not equivalent to the associated flow rule. In 3SR-1071^[3] generalized plasticity models were developed that reproduce the complex deviatoric strength properties observed in laboratory tests and faired the model into a high pressure equation of state. In each case, an associated flow rule for the deviatoric stress response was assumed in developing the flow law. Generalized Mohr-Coulomb constitutive equations developed include one without work hardening, one with isotropic work hardening, and one with kinematic work hardening. The Weidlinger cap model^[32] was also generalized to treat the required range of pressure and strain. The yield surfaces associated with these models are illustrated in Fig. 4.1.

All four plasticity models were incorporated into the 1D SKIPPER Lagrangian computer code as options. The code was applied to compare the Hard Hat and Pile Driver ground motion measurements with the calculations obtained using the generalized cap model and the kinematic work hardening model.^[33] It was found that the latter model yields ground motion calculations in much better agreement with field measurements than is possible with the cap model. In fact, inclusion of the Bauschinger effect (kinematic hardening) reduced the velocity of the rarefaction waves so that unloading takes place more slowly. The velocity pulse at a fixed station is also stretched out over a longer time and this effect caused the calculations to be brought into better agreement with the measurements than had ever been possible in previous calculations which considered hardening to be isotropic. The presence of the Bauschinger effect has been clearly demonstrated by triaxial tests on competent granite specimens (e.g., Swanson^[36]).

- Isotropic Strain Hardening



- Yield Surface with Movable Cap



- Kinematic Hardening

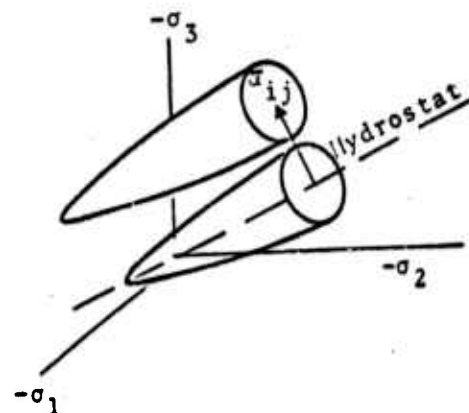


Fig. 4.1--Hardening models.

In Fig. 4.2 a sample result of the SKIPPER Piledriver calculation for the generalized cap model and the kinematic work hardening model are reproduced from 3SR-1071. The better agreement with the displacement-time measurements that is achieved with the latter model is clearly demonstrated. To match the field data it was necessary to reduce the flow stress from that measured on laboratory specimens.

Both the kinematic work hardening and the Weidlinger cap plastic yield criteria have now been generalized to two space dimensions. The mathematical descriptions of these plasticity models are formulated using the associated flow rule and, except for a few minor modifications, are consistent with the earlier work for one-dimensional continua. The effects of material porosity have been included. Both models have been incorporated into the 2D CRAM Lagrangian computer code as options. This computer code is able to treat two-dimensional continua in either plane or rotationally symmetric geometry. The influence of material rotation on the stress behavior has been accounted for in the formulation. The difference equations describing the conservation of mass, momentum, and energy have been presented many times^[28, 29, 30] and will not be repeated here.

The plasticity models are applicable for a material with a moderate amount of porosity. The procedure for incorporating porosity is to assume that the pressure is equal to the value indicated by the equation of state of the matrix material evaluated at the current matrix density and multiplied by the volume fraction of the matrix. The matrix density, in turn, is determined from the average density by assuming that all of the plastic dilatation (or compaction) is due to porosity changes. The derivation of the expression for the matrix density also includes a term which reproduces pure elastic behavior. The use of a homogeneous equation of state for a porous material ignores the material substructure which is capable of scattering and dispersing waves.

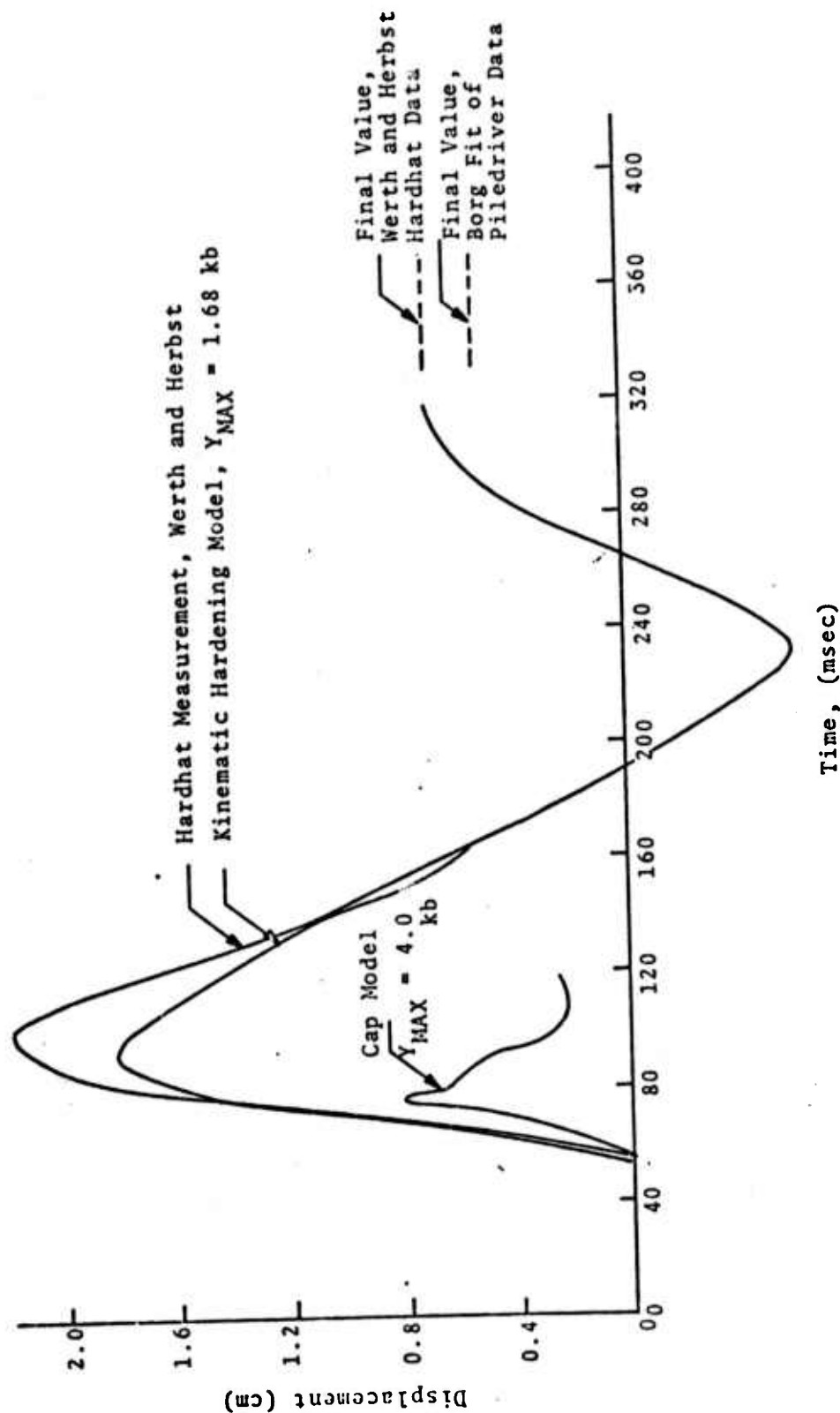


Fig. 4.2--Displacement at 267 m from a 1-kT source (scales to 457 m from Hard Hat source--location of measurement 3VR), based on data of Werth and Herbst [35]. The values of Y_{max} were chosen for the calculations to match the final cavity radius data.

In Section 4.2 the mathematical formulations for the generalized plasticity models and the isotropic equation of state incorporated into CRAM are described. A particular analytic form of the equations of state is used but the coding has been arranged so as to facilitate future changes. A different analytic form or a tabular form (e.g. TAMEOS) can be introduced without major modifications. The developments particular to the kinematic work hardening and Weidlinger cap models are described in Sections 4.3 and 4.4 respectively. Finally, in Section 4.5, results of a calculation with the latter model using the 2D CRAM code is shown to be in excellent agreement with a 1D SKIPPER calculation for the same problem.

4.2 DEVELOPMENT OF MATHEMATICAL MODEL

4.2.1 The Equation of State

The equation of state defining the total pressure P is assumed to be of the following form:*

$$P = \frac{V_m}{V} P_m(V_m, E) \quad (4.1)$$

where V_m and V are the matrix and composite specific volumes respectively, E is the internal energy per unit mass, and the function $P_m(V_m, E)$ may be thought of as the equation of state of the poreless matrix material. The matrix specific volume will be related to the state of strain in Section 4.2.3. Representations similar to Eq. (4.1) have been used previously. Analyses equating the pressure to P_m without the volumetric fraction multiplier are found in [12, 31, 33]. Whereas equations of state with a form identical to Eq. (4.1) are used in [3, 36] for crushable materials and in [3] for the Theory of Interacting Continua (TINC). The analytic form of the function P_m presently being used is that found in [5]. It is given by

$$P_m = \left[a + \frac{d}{\frac{E}{E_0} \left(\frac{V_m}{V_m^0} \right)^2 + 1} \right] \frac{E}{V_m} + B\mu^2 + \frac{1}{3\beta_0} \ln \left(a_0 + (1 - a_0) e^{3\beta_0 A_0 \mu} \right) \quad (2)$$

* In the notation of Section 2.2.3, $\alpha = V/V_m$ and $n = 0$.

where μ equals $V_{m_0}/V_m - 1$, V_{m_0} is the initial matrix specific volume, and $(a, d, E_0, B, \beta_0, a_0, A)$ are parameters defining the shape of the equation of state function. This equation of state has been incorporated into CRAM as a function sub-program and, therefore, can be easily changed. Thus it follows that either the tabular (TAMEOS) or the newly developed high pressure granite equation of state forms (see Section III) can be considered with a minimum amount of effort. The partial derivatives of P_m with respect to either V_m or E which are required in the plasticity calculations are obtained numerically in the following fashion:

$$\frac{\partial P_m}{\partial V_m} = \frac{P_m(V_m + \Delta V_m, E) - P_m(V_m, E)}{\Delta V_m}$$

4.2.2 Elastic and Plastic Strains

As is usual in plasticity theory the total strain rate tensor $\dot{\epsilon}_{ij}$ is separated into elastic and plastic components denoted as $\dot{\epsilon}_{ij}^e$ and $\dot{\epsilon}_{ij}^p$ respectively. Therefore

$$\dot{\epsilon}_{ij} = \dot{\epsilon}_{ij}^e + \dot{\epsilon}_{ij}^p \quad (4.3)$$

The elastic strain rates are assumed to satisfy Hooke's law. This relationship may be written as:

$$\dot{S}_{ij} = 2\mu\dot{e}_{ij} + \frac{\Delta_{ij}}{\Delta T} \quad (4.4)$$

where S_{ij} and e_{ij} are the deviatoric stress and strain tensors, μ is the elastic shear modulus, and $\Delta_{ij}/\Delta T$ are the corrections due to material rotation divided by the time

step used in the numerical integration. The terms S_{ij} and e_{ij} are related to the stress tensor σ_{ij} and strain tensor ϵ_{ij} by the following relationships.

$$S_{ij} = \sigma_{ij} - \frac{\sigma_{kk}}{3} \delta_{ij}$$

$$e_{ij} = \epsilon_{ij} - \frac{\epsilon_{kk}}{3} \delta_{ij}$$

where δ_{ij} is the Kroneker delta function and double subscripts denote summation. The shear modulus appearing in Eq. (4.4) is actually a composite property and thus, in general, is a function of the matrix volumetric fraction. However, in the present formulation μ is taken to be a constant. The stress correction terms are included in Eq. (4.4) in a form consistent with the values calculated in CRAM. These terms can be found in [28] and were originally given by Wilkins.^[29]

The yield function may be represented as

$$f = f(\sigma_{ij}, \gamma)$$

where γ is some hardening parameter. The material is elastic when $f < 0$ and plastic for $f = 0$. When plastic flow occurs the associated flow rule^[37] relates the plastic strain rate to the yield function. This relationship is given by

$$\dot{\epsilon}_{ij}^p = \lambda \frac{\partial f}{\partial \sigma_{ij}} \quad (4.5)$$

The multiplier λ appearing in the above equation is determined by utilizing the fact that f equals zero for plastic behavior. The derivation of expressions for λ

will be discussed in detail for the kinematic work hardening and Weidlinger cap yield functions in future sections.

4.2.3 Matrix Volume Governing Equation

A concept usually introduced in metal plasticity is that the plastic dilatation is zero (compaction may be thought of as negative dilatation). However, when dealing with porous media some plastic volume change does occur due to pore deformation. An expression relating the matrix volume to the state of strain in the continuum will be derived by assuming that all of the dilatation is due to the change in void content. This expression will be modified by a term which better correlates elastic behavior.

The continuity equation may be written in terms of specific volume and strains in the following manner

$$\frac{\dot{V}}{V} = \dot{\epsilon}_{ii} \equiv \dot{\epsilon}_{ii}^e + \dot{\epsilon}_{ii}^p. \quad (4.6)$$

One expression relating the matrix specific volume to the state of strain and analogous to the above equation is given by

$$\frac{\dot{V}_m}{V_m} = \dot{\epsilon}_{ii}^e. \quad (4.7)$$

Equation (4.7) follows from the assumption that when the change in dilatation ($\dot{\epsilon}_{ii}$) is entirely plastic, matrix specific volume does not change and the change in composite specific volume must be due to the change in porosity content. This description of purely plastic behavior will be maintained in the final expression for \dot{V}_m . An expression identical to Eq. (4.7) has been presented by Cherry^[31] and an analogous expression relating the matrix volume (not its derivative) to the elastic strains is used by Dienes.^[33] It should

also be noted that in Ref. 37 the pressure is a function of $\dot{\epsilon}_{ii}^e$ and thus is essentially following this same approach.

The purely plastic behavior of Eq. (4.7) having now been deemed satisfactory, its pure elastic behavior will be examined. If V_p is the porosity specific volume (equals $V - V_m$) and $\dot{\epsilon}_{ij}^p$ equals zero, Eqs. (4.6) and (4.7) yield

$$\frac{\dot{V}_m}{V_m} = \frac{\dot{V}_p}{V_p} \quad (4.8)$$

Thus for elastic behavior the relative changes in matrix and porosity volumes are equal. However, if one utilizes the hollow sphere as an analog for porous materials a phenomenon different from Eq. (4.8) is indicated. For a hollow sphere with the stress-free state characterized by V_{m_0} and V_{p_0} and subjected to a uniform external pressure, the porosity and matrix specific volumes satisfy

$$\frac{V_m}{V_{m_0}} - 1 = \beta \left(\frac{V_p}{V_{p_0}} - 1 \right) \quad (4.9)^*$$

where β is a function of the matrix Poisson ratio ν_m and is defined by

$$\beta = \frac{2}{3} \left(\frac{1 - 2\nu_m}{1 - \nu_m} \right)$$

Differentiating Eq. (4.9) yields

* See Illustration 4.1, Description of Eq. (4.9).

ILLUSTRATION 4.1

DESCRIPTION OF EQUATION (4.9)

Consider the hollow sphere of internal radius a and external radius b subjected to an external pressure p . In its undeformed state the total volume, matrix volume, and void volume are given by

$$V_0 = \frac{4}{3} \pi b^3 \quad V_{m_0} = \frac{4}{3} \pi (b^3 - a^3) \quad V_{p_0} = \frac{4}{3} \pi a^3$$

After applying p , the internal and external radii become $a + \Delta a$ and $b + \Delta b$, respectively. For elastic behavior $b \gg \Delta b$ and $a \gg \Delta a$, therefore the deformed volumes become

$$V = V_0 - 4\pi b^2 \Delta b \quad V_m = V_{m_0} - 4\pi (b^2 \Delta b - a^2 \Delta a)$$

$$V_p = V_{p_0} - 4\pi a^2 \Delta a$$

From Roark^[38], Δa and Δb are given by

$$\Delta a = p \frac{a}{E} \left[\frac{3b^3}{2(b^3 - a^3)} (1 - \nu) \right] \quad \Delta b = p \frac{a}{E} \left[\frac{a^3 + 2b^3 + \nu(a^3 - 4b^3)}{2(b^3 - a^3)} \right]$$

where E and ν are the matrix Young's modulus and Poisson's ratio. Substituting these expressions into V_m and V_p yields

$$\frac{V_m}{V_{m_0}} = 1 - \frac{3p}{E} \frac{V_0}{V_{m_0}} (1 - 2\nu) \quad \frac{V_p}{V_{p_0}} = 1 - \frac{3p}{E} \frac{V}{V_{m_0}} \frac{3}{2} (1 - \nu)$$

Therefore

$$\frac{V_m}{V_{m_0}} - 1 = \beta \left(\frac{V_p}{V_{p_0}} - 1 \right)$$

where

$$\beta = \frac{2}{3} \frac{1 - 2\nu}{1 - \nu}$$

$$\frac{\dot{V}_m}{V_{m_0}} = \beta \frac{\dot{V}_P}{V_{P_0}} \quad (4.10)$$

Eliminating V_{P_0} from Eqs. (4.9) and (4.1) yields

$$\frac{\dot{V}_m}{V_m} = \left[1 - (1 - \beta) \frac{V_{m_0}}{V_m} \right] \frac{\dot{V}_P}{V_P}$$

Therefore for V_m in the neighborhood of V_{m_0} the relative change in matrix specific volume equals β times the relative porosity change. For the hollow sphere analog and v_m equal to 0.25, β equals 0.44.

The following expression relating the change in matrix specific volume to the state of strain is postulated as a replacement for Eq. (4.7). It is:

$$\dot{V}_m = \frac{V \dot{\epsilon}_{ii}^e}{1 + \frac{V_0 - V_{m_0}}{\beta V_{m_0}}}$$

or, with $\frac{1}{\beta'} = 1 + \frac{V_0 - V_{m_0}}{\beta V_{m_0}}$,

$$\dot{V}_m = \beta' V \dot{\epsilon}_{ii}^e \quad (4.11)$$

where V_0 is the initial volume. As can easily be determined either Eqs. (4.7) or (4.10) are reproduced when the state of strain is purely plastic or elastic respectively.

The hollow sphere analog represents a simple minded approach to a very difficult problem. In general, the

expression for β is considerably more involved and, like μ , is a function of the matrix volume fraction. A more general approach may be found in Hashin^[39]. In the present analysis β is taken to be a constant. It should be mentioned that the value of V_{m_0} used in Eq. (4.11) equals the initial matrix specific volume only for the first loading cycle. Upon unloading and reloading this value should be interpreted as the most recent stress-free value.

An equation required for plasticity calculations will be introduced at this time. If J_1 is the first stress invariant (σ_{KK}) and equals $-3P$, then \dot{J}_1 follows from Eq. (4.1). It is

$$\dot{J}_1 = -3 \left[\left(\frac{P_m}{V} + \frac{V_m}{V} \frac{\partial P_m}{\partial V_m} \right) \dot{V}_m - \frac{V_m P_m}{V^2} \dot{V} + \frac{V_m}{V} \frac{\partial P_m}{\partial E} \dot{E} \right]$$

Replacing \dot{V}_m using Eq. (4.11) yields

$$\dot{J}_1 = -3 \left[\left(P_m + V_m \frac{\partial P_m}{\partial V_m} \right) \beta \dot{\epsilon}_{ii} - \frac{V_m P_m}{V^2} \dot{V} + \frac{V_m}{V} \frac{\partial P_m}{\partial E} \dot{E} \right] \quad (4.12)$$

4.3 KINEMATIC WORK HARDENING MODEL

The concept of kinematic work hardening was originally introduced by Prager^[40] and is consistent with Drucker's^[41] work hardening definition. The yield surface in general is some function of J_1 and translates in stress space without a change in shape according to the plastic strain history. The shape of the yield surface is defined by

$$f = \left[\frac{1}{2} \bar{S}_{ij} \bar{S}_{ij} \right]^{1/2} - g(J_1) \quad (4.13)$$

where the function g represents the shape of the yield surface and \bar{S}_{ij} are related to the deviatoric stresses by

$$\bar{S}_{ij} = S_{ij} - \alpha_{ij} \quad (4.14)$$

The tensor α_{ij} represents the translation of the yield surface and, if linear hardening is assumed, is determined from

$$\dot{\alpha}_{ij} = b \dot{\epsilon}_{ij}^P \quad (4.15)$$

where b is some constant. Therefore for kinematic work hardening, Eq. (4.5) becomes

$$\dot{\epsilon}_{ij}^P = \frac{\lambda}{2g} (\bar{S}_{ij} - 2g g' \delta_{ij}) \quad (4.16)$$

where $g' = \frac{dg}{dJ_1}$. The multiplier λ will now be determined. Differentiating Eq. (4.13) yields

$$\dot{\bar{S}}_{ij} \bar{S}_{ij} = 2g g' \dot{J}_1$$

Replacing $\dot{\epsilon}_{ij}^e$ in Eq. (4.12) using Eqs. (4.3) and (4.16) and substituting the resulting expression for \dot{J}_1 into the above equation yields

$$\begin{aligned} \bar{S}_{ii} \dot{\bar{S}}_{ij} = & -6g g' \left[\left(P_m + V_m \frac{\partial P_m}{\partial V_m} \right) \beta' (\dot{\epsilon}_{ii} + 3\lambda g') \right. \\ & \left. - \frac{V_m P_m}{V^2} \dot{V} + \frac{V_m}{V} \frac{\partial P_m}{\partial E} \dot{E} \right] \end{aligned} \quad (4.17)$$

Another expression for $\dot{\bar{S}}_{ij}$ may be obtained from Hooke's law. Using Eqs. (4.14), (4.15), and (4.16) to eliminate S_{ij} and $\dot{\epsilon}_{ij}^e$ from Eq. (4.4) yields

$$\dot{\bar{S}}_{ij} = 2\mu \dot{\epsilon}_{ij} - \left(\frac{b}{2} + \mu \right) \frac{\lambda}{g} \bar{S}_{ij} + \frac{\Delta_{ij}}{\Delta T}$$

Multiplying this expression by \bar{S}_{ij} and using $\bar{S}_{ij} \bar{S}_{ij} = 2g^2$ leads to the following expression:

$$\bar{S}_{ij} \dot{\bar{S}}_{ij} = 2\mu \dot{\epsilon}_{ij} \bar{S}_{ij} - (b + 2\mu) \lambda g + \frac{\Delta_{ij} \bar{S}_{ij}}{\Delta T} \quad (4.18)$$

Equating the expressions for $\dot{\bar{S}}_{ij}$ given in Eqs. (4.17) and (4.18) yields the following expression for λ . It is

$$\begin{aligned} \lambda = & \left\{ 2\mu \dot{\epsilon}_{ij} \bar{S}_{ij} + \frac{\Delta_{ij} \bar{S}_{ij}}{\Delta T} + 6g g' \left[\left(P_m + V_m \frac{\partial P_m}{\partial V_m} \right) \beta' \dot{\epsilon}_{ii} \right. \right. \\ & \left. \left. - \frac{V_m P_m}{V^2} \dot{V} + \frac{V_m}{V} \frac{\partial P_m}{\partial E} \dot{E} \right] \right\} \div \left[g(b+2\mu) - 18g g'^2 \left(P_m + V_m \frac{\partial P_m}{\partial V_m} \right) \beta' \right] \end{aligned} \quad (4.19)$$

The g function used in this study is described by Dienes [33] and is given by

$$g = \tau_0 + (\tau_1 - \tau_0)e^{\beta_1 J_1}$$

where τ_0 , τ_1 and β_1 are parameters defining the yield surface shape. The specific form of this function can, of course, be easily changed.

4.4 WEIDLINGER CAP MODEL

The yield surface of the Weidlinger cap model^[32] is composed of two parts. One being a surface fixed in stress space (g_p) and the other being an elliptical cap (g_c) which is tangent to g_p . The cap portion moves outward in response to plastic deformation. The main advantage of cap models is that they reproduce the dilatation seen at low pressures and the compaction observed at high pressures.^[33] The yield function is defined by*

$$f = \left[\frac{1}{2} S_{ij} S_{ij} \right]^{1/2} - g(J_1, K) \quad (4.20)$$

where

$$g = \begin{cases} g_p, & \text{for } J_1 > J_{1f} \\ g_c, & \text{for } J_1 \leq J_{1f} \end{cases}$$

The term J_{1f} is related to the plastic history by

$$J_{1f} = -wK$$

where w is a constant and the hardening parameter K is determined from

$$\dot{K} = (g_p - g_c) \sqrt{\dot{\epsilon}_{ij}^p \dot{\epsilon}_{ij}^p} \quad (4.21)$$

* The following analysis concerns a particular cap model. However, these same techniques can easily be applied to alternate versions of this yield model such as the one found in Ref. [42].

The fixed and cap portions are defined by

$$g_p(J_1) = \tau_0 + (\tau_1 - \tau_0)e^{\beta_1 J_1}$$

and

$$g_c(J_1, K) = \sqrt{Q - \left(\frac{J - J_c}{R}\right)^2}$$

where Q , J_c and R are functions of K and are given by,

$$Q = g_F^2 (1 + R^2 g_F'^2)$$

$$J_c = J_{1F} + R^2 g_F g_F'$$

$$R = \left\{ R_0 e^{\beta_2 WK}, R_0 e^{-\beta_2 WK} \right\}_{\text{minimum}}$$

$(\tau_0, \tau_1, \beta_1, R_0, \text{ and } \beta_2)$ are parameters, and g_F and g_F' are defined by

$$g_F = g_p(J_{1F})$$

$$g_F' = \left. \frac{\partial g_p}{\partial J_1} \right|_{(J_1 = J_{1F})}$$

The determination of λ for the cap model follows a similar procedure as that seen in the previous section. In fact, when the yield point is on the fixed portion the expression for λ may be obtained from Eq. (4.19). Replacing \bar{S}_{ij} by S_{ij} , setting $b = 0$, and replacing g by g_p yields the appropriate value for λ in this case.

When the yield point is on the cap portion the procedure for determining λ is only slightly different from that used in deriving Eq. (4.19). In this case, using Eqs. (4.5) and (4.20), $\dot{\epsilon}_{ij}^p$ becomes

$$\dot{\epsilon}_{ij}^P = \frac{\lambda}{2g_c} (S_{ij} - 2g_c g_c' \delta_{ij}) \quad (4.22)$$

where $g_c' = \frac{\partial g_c}{\partial J_1}$. Taking the time derivative of F yields

$$S_{ij} \dot{S}_{ij} = 2g_c \left(g_c' \dot{J}_1 + \frac{\partial g_c}{\partial K} \dot{K} \right)$$

Using Eqs. (4.12), (4.21), and (4.22), the above expression becomes

$$\begin{aligned} S_{ij} \dot{S}_{ij} = 2g_c \left\{ - 3g_c' \left[\left(P_m + V_m \frac{\partial P_m}{\partial V_m} \right) \beta' (\dot{\epsilon}_{ii} + 3\lambda g_c') \right. \right. \\ \left. \left. - \frac{V_m P_m}{V^2} \dot{V} + \frac{V_m}{V} \frac{\partial P_m}{\partial E} \dot{E} \right] \right. \\ \left. + \frac{\partial g_c}{\partial K} (g_p - g_c) \lambda \left(\frac{1}{2} + 3g_c'^2 \right)^{1/2} \right\} \quad (4.23) \end{aligned}$$

Hooke's law yields

$$S_{ij} \dot{S}_{ij} = 2\mu (\dot{\epsilon}_{ij} S_{ij} - \lambda g_c) + \frac{\Delta_{ij} S_{ij}}{\Delta T} \quad (4.24)$$

Combining Eqs. (4.23) and (4.24) yields

$$\begin{aligned} \lambda = \left\{ 2\mu \dot{\epsilon}_{ij} S_{ij} + \frac{\Delta_{ij} S_{ij}}{\Delta T} + 6 g_c g_c' \left[\left(P_m + V_m \frac{\partial P_m}{\partial V_m} \right) \beta' \dot{\epsilon}_{ii} \right. \right. \\ \left. \left. - \frac{V_m P_m}{V^2} \dot{V} + \frac{V_m}{V} \frac{\partial P_m}{\partial E} \dot{E} \right] \right\} \div \left[2\mu g_c - 18g_c g_c'^2 \left(P_m + V_m \frac{\partial P_m}{\partial V_m} \right) \beta' \right. \\ \left. + 2g_c \frac{\partial g_c}{\partial K} (g_p - g_c) \left(\frac{1}{2} + 3g_c'^2 \right)^{1/2} \right] \quad (4.25) \end{aligned}$$

4.5 SUMMARY

The equations developed in the previous sections have been incorporated in the CRAM code. The procedure has been to retain as much of the original CRAM logic as possible and thus minimize errors. The computation procedure in CRAM is to calculate the velocities, positions, and volume using the equations of motion and the continuity equation at time $t^{n+1/2}$ and then calculate the stress state at time t^{n+1} using these new values. This procedure has not been altered. Therefore the strain rates and volume terms appearing in the expressions for λ are evaluated at the time $t^{n+1/2}$.

A typical comparison of the results of CRAM and SKIPPER calculations for granite may be found in Fig. 4.3. The Weidlinger cap model with zero porosity is used with the values of the required parameters appearing in Table 4.1. The geometry is a symmetric spherical cavity of radius 100 cm and the loading is a suddenly applied internal pressure of 18 kbar. Plotted in Fig. 4.3 is the pressure at a radius of 105 cm as a function of time. Plastic flow was initiated at approximately 7 μ sec and continued throughout the run. As can be seen the correlation is excellent.

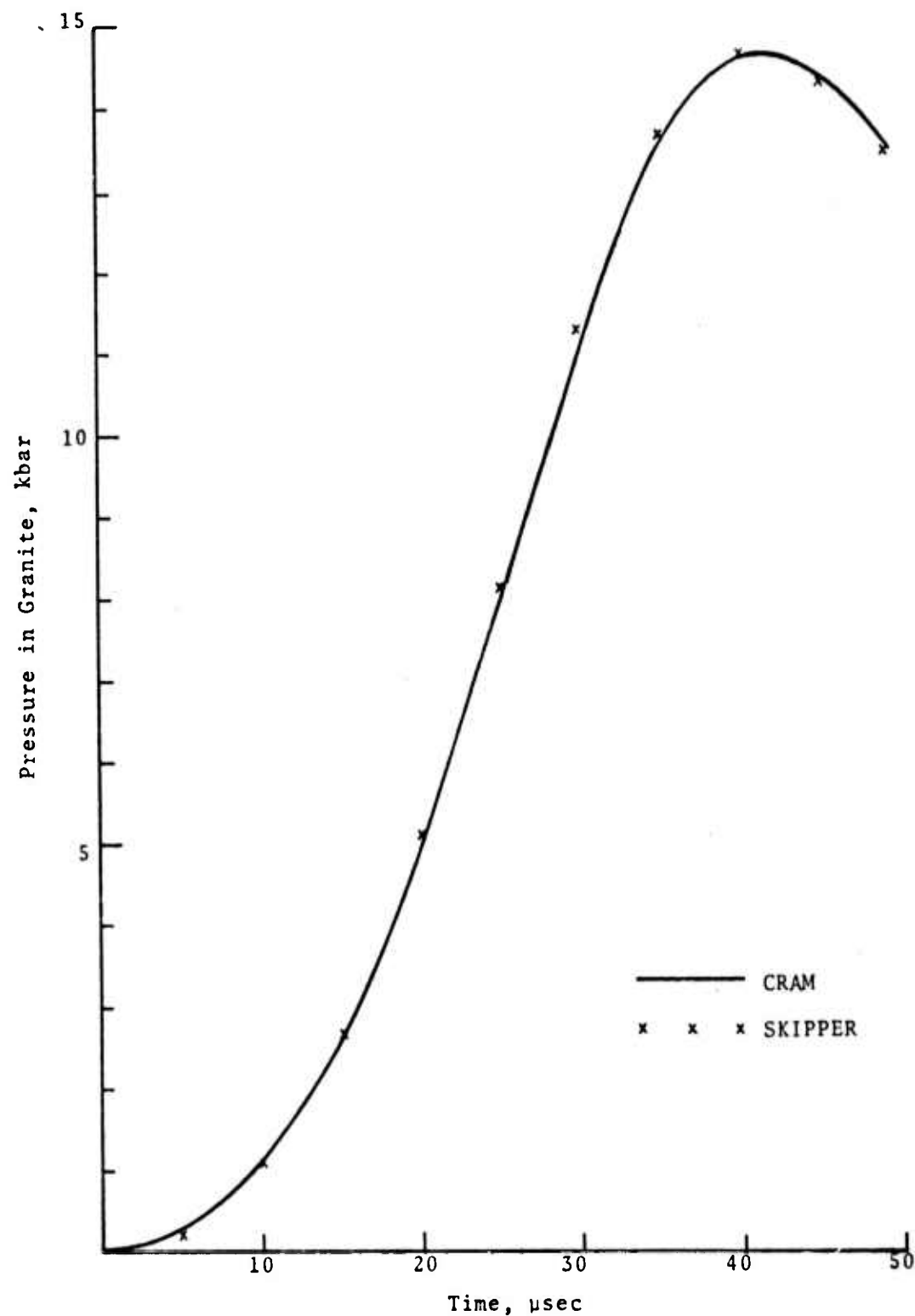


Fig. 4.3--Comparison of CRAM and SKIPPER Weidlinger cap results for a suddenly applied pressure of 18 kbar on the inside surface of a 100 -cm spherical cavity. Depicted is the pressure in granite at a radius of 105 cm versus time.

TABLE 4.1
WEIDLINGER CAP AND EQUATION OF STATE PARAMETER
VALUES (CEDAR CITY TONALITE)

τ_0	10.45 kbar
τ_1	0.49 kbar
β_1	0.042 kbar ⁻¹
R_0	4.0
β_2	0.724 kbar ⁻¹
β_0	0.029 kbar ⁻¹
μ	227.5 kbar
A_0	518.0 kbar
a_0	0.7
B	180.0 kbar
a	0.5
d	1.3
E_0	160.0 kbar cm ³ /gm

V. TINC DEVELOPMENT AND THE POROUS CODE

5.1 INTRODUCTION

A geologic medium generally consists of a rock or soil matrix containing cracks or pores that may be partially or completely saturated with water, and as such may be regarded as a geologic composite. Such materials possess certain characteristics (wave dispersion, internal dissipation) which cannot be adequately modeled within the usual restrictions of homogeneous, isotropic media. In applications where these characteristics are important, it is necessary to seek a description of the dynamic response in terms of the behavior of the isolated rock matrix and water components. Reference to the detailed microstructure of the composite, however, must be avoided since the phenomena of interest are on a much larger geometrical scale. The Theory of Interacting Continua (TINC) provides a framework general enough to allow explicit treatment of pore pressure effects and relative motion between the rock and water components. This theory does not require the explicit consideration of the detailed microstructure. The microstructure is implicitly considered in specifying the various interaction terms.

This theory was previously introduced in 3SR-267,^[1] 3SR-678,^[2] and 3SR-1071^[3] to model the behavior of geologic composites. In particular, a thermodynamic model was presented in 3SR-1071. This model was incorporated into the POROUS (1D spherical and planar) code. During the past year, the prime objectives have been to (1) refine constitutive relations and (2) further develop the POROUS code. Since the conservation relations and the interaction terms have already been presented in 3SR-1071, we will not repeat them here. The new constitutive relations (in particular the crushup model) are discussed in Section 5.2. The various modifications of the POROUS code are described

in Section 5.3. Finally, in Section 5.4 we present material parameter calculations utilizing the POROUS code. Comparison with SKIPPER results is also given.

5.2 CONSTITUTIVE LAWS

The TINC definitions and constitutive laws have been previously presented in 3SR-1071. However, for sake of completeness, we will briefly review this work here. We shall denote by $\delta^{(1)}$, $\delta^{(2)}$ and $\delta^{(3)}$ the rock grain, the pore fluid and the void space, respectively. The mass of constituent $\delta^{(\alpha)}$ per unit volume of the composite is called its partial density $\rho^{(\alpha)}$ and the total mass per unit volume of composite ρ is given by

$$\rho = \sum_{\alpha=1}^2 \rho^{(\alpha)} \quad (5.1)$$

(In the preceding equation, summation is over $\alpha=1$ and 2 only since the voids have no mass). The total stress $\underline{\sigma}$ associated with a unit area of the composite is decomposed into partial stresses $\underline{\sigma}^{(\alpha)}$ associated with each component $\delta^{(\alpha)}$

$$\underline{\sigma} = \sum_{\alpha=1}^2 \underline{\sigma}^{(\alpha)} \quad (5.2)$$

Partial stresses $\underline{\sigma}^{(\alpha)}$ and partial densities $\rho^{(\alpha)}$ are related to effective stresses $\underline{\sigma}^{(\alpha)e}$ and effective densities $\rho^{(\alpha)e}$ through the relations

$$\begin{aligned} \underline{\sigma}^{(\alpha)} &= \frac{(\alpha)}{n} \underline{\sigma}^{(\alpha)e} \\ \rho^{(\alpha)} &= \frac{(\alpha)}{n} \rho^{(\alpha)e} \end{aligned} \quad (5.3)$$

where $\left(\frac{\alpha}{n}\right)$ denotes the volume fraction of $\delta^{(\alpha)}$. In writing down the preceding relations, it is assumed that the geologic composite is isotropic (See 3SR-1071).

Partial volumetric strains are now defined as

$$\left(\frac{\alpha}{\epsilon}\right) = \left(\frac{\alpha}{J}\right) - 1 \quad (5.4)$$

where

$$\left(\frac{\alpha}{J}\right) \equiv \frac{\left(\frac{\alpha}{\rho_0}\right)\left(\frac{\alpha}{\rho}\right)}{\rho_0/\rho} \quad (5.5)$$

and the subscript $_0$ denotes the initial value of the subscripted variable. Partial volumetric strains $\left(\frac{\alpha}{\epsilon}\right)$ are related to the effective volumetric strains by the relation

$$\left(\frac{\alpha}{\epsilon}\right)_e = \left(\frac{\alpha}{J}\right)_e - 1 = \frac{\left(\frac{\alpha}{\rho_0}\right)_e}{\left(\frac{\alpha}{\rho}\right)_e} - 1 = \frac{\left(\frac{\alpha}{n}\right)}{\left(\frac{\alpha}{n_0}\right)} \left(1 + \left(\frac{\alpha}{\epsilon}\right)\right) - 1 \quad (5.5)$$

Partial volumetric strain for $\delta^{(1)}$ is often denoted in literature as the bulk volumetric strain. We note here that the partial strain tensor for $\delta^{(1)}$, $\epsilon_{ij}^{(1)}$, is identical with the bulk strain tensor measured in the laboratory tests.

With the above definitions, we are ready to introduce the TINC constitutive laws (see also 3SR-1071).

(1)
s

$$\sigma_{ij}^{(1)} = - p^{(1)} \delta_{ij} + S_{ij}^{(1)}$$

$$p^{(1)} = p_1^{(1)} \left(\epsilon^{(1)} e, \frac{(1)}{E} \right)$$

$$= p_1^{(1)} \left[\frac{\frac{(1)}{n}}{\frac{(1)}{n_0}} \lambda - 1, \frac{(1)}{E} \right]$$

$$S_{ij}^{(1)} = 2\mu_p e_{ij} \quad (\text{elastic flow})$$

$$S_{ij}^{(1)} S_{ij}^{(1)} = \frac{2}{3} Y_p^2 \quad (\text{plastic flow}) \quad (5.6)$$

where

$$\lambda = \frac{(1)}{J}$$

$$e_{ij} = \epsilon_{ij}^{(1)} - \frac{\epsilon^{(1)}}{3} S_{ij}^{(1)}$$

Here $p_1 \left(\epsilon^{(1)} e, \frac{(1)}{E} \right)$ denotes the equation of state of the isolated rock component, $\frac{(1)}{E}$ is the specific internal energy, μ_p is the shear modulus of the porous rock and Y_p is the yield stress of the porous rock in simple tension or compression.

(2)
 δ

$$\sigma_{ij}^{(2)} = - p^{(2)} \epsilon_{ij}$$

$$p^{(2)} = n^{(2)} P_2 \left(\epsilon^{(2)} e, \frac{(2)}{E} \right)$$

$$= n^{(2)} P_2 \left[\frac{\frac{(2)}{n}}{\frac{(2)}{n_0}} \gamma - 1, \frac{(2)}{E} \right] \quad (5.7)$$

where

$$\gamma = \frac{(2)}{J}$$

Here $P_2 \left(\epsilon^{(2)} e, \frac{(2)}{E} \right)$ denotes the equation of state for water and $\frac{(2)}{E}$ is the specific internal energy.

Specific form for P_1 and P_2 were given in 3SR-1071. For present purposes, it is not necessary to utilize these specialized equations of state. The constitutive relations as given above are complete only when the volume fractions $n^{(1)}$, $n^{(2)}$ and $n^{(3)}$ are specified. In the previous work on TINC, we utilized a form of pressure equilibrium to determine $n^{(1)}$ and $n^{(2)}$ (and hence $n^{(3)}$ since $n^{(1)} + n^{(2)} + n^{(3)} = 1$). During the past year, an alternate formulation has been developed. This formulation does not require pressure equilibrium and is believed to be more realistic especially at low pressures. At high stress levels, the results of the present analysis differ but little from those given by pressure equilibrium. In the following, we will outline the analysis first for a saturated material ($n^{(3)} \equiv 0$) and then extend it to the unsaturated case.

5.2.1 Saturated Media

To simplify the following discussion we will consider the isotropic response ($S_{ij}^{(1)} \equiv 0$) only. A little reflection will reveal that the analysis is valid, under the stated assumptions, for non-isotropic loading as well. We will regard $n^{(1)}$ and $n^{(2)}$ ($\equiv 1 - n^{(1)}$) as functions of λ and γ only. Alternately $n^{(1)}$ and $n^{(2)}$ may be postulated to be functions of $P_c - P_p$ and P_p , where

$$P_c = n^{(1)} P_1 + n^{(2)} P_2 \quad (5.8)$$

$$P_p = P_2$$

Constitutive relations (5.6) and (5.7) may be rewritten as:

$$d p^{(1)} = \frac{\partial p^{(1)}}{\partial \epsilon^{(1)}} d \epsilon^{(1)} + \frac{\partial p^{(1)}}{\partial \epsilon^{(2)}} d \epsilon^{(2)} \quad (5.9)$$

$$d p^{(2)} = \frac{\partial p^{(2)}}{\partial \epsilon^{(1)}} d \epsilon^{(1)} + \frac{\partial p^{(2)}}{\partial \epsilon^{(2)}} d \epsilon^{(2)}$$

where

$$\epsilon^{(1)} = \lambda - 1$$

$$\epsilon^{(2)} = \gamma - 1$$

$$\frac{\partial}{\partial \epsilon} \frac{p}{(1)} = \frac{\partial}{\partial \epsilon} \frac{n}{(1)} P_1 + \frac{(1)}{n} P_1' \left\{ \frac{(1)}{(1)} \frac{n}{n_0} + \frac{\lambda}{(1)} \frac{\partial}{\partial \epsilon} \frac{n}{(1)} \right\}$$

$$= \frac{\partial}{\partial \epsilon} \frac{n}{(1)} \left[P_1 + \frac{(1)}{(1)} \frac{n}{n_0} \lambda P_1' \right] + \frac{\left(\frac{(1)}{n} \right)^2}{(1)} P_1'$$

$$\frac{\partial}{\partial \epsilon} \frac{p}{(2)} = \frac{\partial}{\partial \epsilon} \frac{n}{(2)} P_1 + \frac{(1)}{n} P_1' \left[\frac{\lambda}{(1)} \frac{\partial}{\partial \epsilon} \frac{n}{(2)} \right]$$

$$= \frac{\partial}{\partial \epsilon} \frac{n}{(2)} \left[P_1 + \frac{(1)}{(1)} \frac{n}{n_0} \lambda P_1' \right]$$

$$\frac{\partial}{\partial \epsilon} \frac{p}{(1)} = - \frac{\partial}{\partial \epsilon} \frac{n}{(1)} \left[P_2 + \frac{(1)}{(1)} \frac{n}{n_0} \gamma P_2' \right]$$

$$\frac{\partial}{\partial \epsilon} \frac{p}{(2)} = - \frac{\partial}{\partial \epsilon} \frac{n}{(2)} \left[P_2 + \frac{1 - \frac{n}{(1)}}{1 - \frac{n}{n_0}} \gamma P_2' \right]$$

$$+ \frac{\left(1 - \frac{(1)}{n} \right)^2}{1 - \frac{(1)}{n_0}} P_2'$$

(5.10)

$$P_1' \equiv \frac{dP_1}{d \left(\frac{\frac{(1)}{n}}{\frac{(1)}{n_0}} \lambda \right)}$$

$$P_2' \equiv \frac{dP_2}{d \left(\frac{\frac{(1)}{1 - \frac{n}{n_0}} \gamma}{1 - \frac{n}{n_0}} \right)}$$

We will now assume that the energy changes associated with dissipative forces are small as compared with those due to mechanical deformation. Thus, in a first order theory, the system may be regarded as conservative. This implies that the final state be independent of the loading path.

Let us now consider strain energy changes associated with the following loading sequence:

- (1) We increase $p^{(1)}$ by an incremental amount $d p^{(1)}$ while keeping $p^{(2)}$ constant. This results in partial strains $d \epsilon_1^{(1)}$ and $d \epsilon_1^{(2)}$ in $\delta^{(1)}$ and $\delta^{(2)}$, respectively.
- (2) Next we increase $p^{(2)}$ to $p^{(2)} + d p^{(2)}$ while keeping pressure in $\delta^{(1)}$ at $p^{(1)} + d p^{(1)}$. Strain changes associated with this load step are $d \epsilon_2^{(1)}$ and $d \epsilon_2^{(2)}$.

Therefore, the change in strain energy is:

$$\begin{aligned} dU = & \left(p^{(1)} + \frac{1}{2} d p^{(1)} \right) d \epsilon_1^{(1)} + p^{(2)} d \epsilon_1^{(2)} \\ & + \left(p^{(2)} + \frac{1}{2} d p^{(2)} \right) d \epsilon_2^{(2)} + \left(p^{(1)} + d p^{(1)} \right) d \epsilon_2^{(1)} \end{aligned} \quad (5.11)$$

If we now reverse the order of loads, we obtain

$$dU = \left(\frac{(2)}{p} + \frac{1}{2} d \frac{(2)}{p} \right) d \epsilon_2 + \frac{(1)}{p} d \epsilon_2 \quad (5.12)$$

$$+ \left(\frac{(1)}{p} + \frac{1}{2} d \frac{(1)}{p} \right) d \epsilon_1 + \left(\frac{(2)}{p} + d \frac{(2)}{p} \right) d \epsilon_1$$

Equating the two expressions for strain energy, we have:

$$d \frac{(1)}{p} d \epsilon_2 = d \frac{(2)}{p} d \epsilon_1 \quad (5.13)$$

Substituting $d \frac{(2)}{p} = 0$ in Eqs. (5.9), we obtain after some algebraic manipulation:

$$d \epsilon_1^{(2)} = \frac{\frac{\partial p}{\partial \epsilon_1} d p^{(1)}}{\frac{\partial p}{\partial \epsilon_2} \frac{\partial p}{\partial \epsilon_1} - \frac{\partial p}{\partial \epsilon_1} \frac{\partial p}{\partial \epsilon_2}} \quad (5.14)$$

Similarly, we have

$$d \epsilon_2^{(2)} = \frac{\frac{\partial p}{\partial \epsilon_2} d p^{(2)}}{\frac{\partial p}{\partial \epsilon_2} \frac{\partial p}{\partial \epsilon_1} - \frac{\partial p}{\partial \epsilon_1} \frac{\partial p}{\partial \epsilon_2}} \quad (5.15)$$

Combining Eqs. (5.13) through (5.15), there follows

$$\frac{\partial p}{\partial \epsilon_2} = \frac{\partial p}{\partial \epsilon_1} \quad (5.16)$$

An analogous relation for linear elastic materials was previously obtained by Biot^[43] on the basis of essentially similar arguments.

Next, substituting from Eqs. (5.10) into Eq. (5.16), we obtain

$$\frac{\partial n^{(1)}}{\partial \lambda} = - \frac{\partial n^{(1)}}{\partial \gamma} \frac{P_1 + \frac{n^{(1)}}{n_0} \lambda P_1'}{P_2 + \frac{1 - \frac{n^{(1)}}{n_0}}{(1)} \gamma P_2'} \quad (5.17)$$

An incremental change in $n^{(1)}$ is then given by

$$d n^{(1)} = \frac{\partial n^{(1)}}{\partial \lambda} d\lambda + \frac{\partial n^{(1)}}{\partial \gamma} d\gamma \quad (5.18a)$$

$$= \frac{\partial n^{(1)}}{\partial \lambda} \left\{ d\lambda - \frac{P_2 + \frac{1 - \frac{n^{(1)}}{n_0}}{(1)} \gamma P_2'}{P_1 + \frac{n^{(1)}}{n_0} \lambda P_1'} d\gamma \right\} \quad (5.18b)$$

Equation (5.18b) constitutes a prescription for $d n^{(1)}$ in terms of $d\lambda$, $d\gamma$ and $\partial n^{(1)}/\partial \lambda$. To prescribe a functional relationship for the unknown function $\partial n^{(1)}/\partial \lambda$, it is convenient to regard $n^{(1)}$ as a function of $P_c - P_p$ and P_p instead of λ and γ . Simple algebraic manipulations yield:

$$\frac{\partial \frac{(1)}{n}}{\partial \lambda} = \frac{\left(\frac{(1)}{n}\right)^2}{\frac{(1)}{n_0}} P_1' \frac{\partial \frac{(1)}{n}}{\partial (P_c - P_p)} / X \quad (5.19)$$

$$\frac{\partial \frac{(1)}{n}}{\partial \gamma} = \left\{ - \frac{\frac{(1)}{n} \left(1 - \frac{(1)}{n}\right)}{1 - \frac{(1)}{n_0}} \frac{\partial \frac{(1)}{n}}{\partial (P_c - P_p)} P_2' + \frac{\left(1 - \frac{(1)}{n}\right)}{1 - \frac{(1)}{n_0}} P_2' \frac{\partial \frac{(1)}{n}}{\partial P_p} \right\} / X$$

where

$$X = 1 - \frac{\partial \frac{(1)}{n}}{\partial (P_c - P_p)} \left[P_1' + \frac{\frac{(1)}{n}}{\frac{(1)}{n_0}} \lambda P_1' - P_2' + \frac{\frac{(1)}{n}}{1 - \frac{(1)}{n_0}} \gamma P_2' \right] + \frac{\gamma}{1 - \frac{(1)}{n_0}} P_2' \frac{\partial \frac{(1)}{n}}{\partial P_p} .$$

Combining Eqs. (5.17) and (5.19) there follows:

$$\frac{\partial \frac{(1)}{n}}{\partial P_p} = - \frac{\partial \frac{(1)}{n}}{\partial (P_c - P_p)} \left(\frac{(1)}{n} \left\{ \frac{\frac{(1)}{n}}{\frac{(1)}{n_0}} P_1' \left[P_2' + \frac{1 - \frac{(1)}{n}}{1 - \frac{(1)}{n_0}} \gamma P_2' \right] \right. \right. \right. \quad (5.20)$$

$$\left. - \frac{\left(1 - \frac{(1)}{n}\right)}{1 - \frac{(1)}{n_0}} P_2' \left[P_1' + \frac{\frac{(1)}{n}}{\frac{(1)}{n_0}} \lambda P_1' \right] \right\} \left/ \left\{ \frac{1 - \frac{(1)}{n}}{1 - \frac{(1)}{n_0}} P_2' \left[P_1' + \frac{\frac{(1)}{n}}{\frac{(1)}{n_0}} \lambda P_1' \right] \right\} \right.$$

Equations (5.19) and (5.20) now express $\frac{\partial n^{(1)}}{\partial \lambda}$ in terms of $\frac{\partial n^{(1)}}{\partial (P_c - P_p)}$.

At this stage, we will postulate that $\frac{\partial n^{(1)}}{\partial (P_c - P_p)}$ does not explicitly depend upon P_p , i.e.,

$$\frac{\partial n^{(1)}}{\partial (P_c - P_p)} = f(P_c - P_p) \quad (5.21)$$

Function $f(P_c - P_p)$ may be determined from hydrostatic tests with P_p kept at zero. This completes our discussion for the saturated material.

5.2.2 Unsaturated Case

In 3SR-648^[2] and 3SR-1071,^[3] two crushup hypotheses were discussed, viz:

1. Disconnected Pores
2. Connected Pores

The two hypotheses are tantamount to assuming the void space as being completely embedded in either solid (1st) or fluid (2nd). The first of these was utilized to construct various crushup schemes reported in 3SR-648 and 3SR-1071. We will now find it convenient to utilize the second of these. This allows a straightforward extension of the results of the saturated case to the present one. In other words, we consider an extended fluid (Vol. Fraction = $1 - \frac{n^{(1)}}{n} = \frac{n^{(2)}}{n} + \frac{n^{(3)}}{n}$) filling the pore space. The fluid pressure, Eq. (5.7) is now modified to read as:

$$P^{(2)} = \left(1 - \frac{n^{(1)}}{n}\right) P_2 \left(\frac{1 - \frac{n^{(1)}}{n_0}}{\frac{n^{(2)}}{n_0}} \frac{1 - \frac{n^{(1)}}{n}}{1 - \frac{n^{(1)}}{n_0}} \gamma^{-1, E} \right) \quad (5.22)$$

Note that on loading $P_2 \equiv 0$ for $\frac{1 - \frac{(1)}{n_0}}{(2)} \cdot \frac{1 - \frac{(1)}{n}}{1 - \frac{(1)}{n_0}} \gamma \geq 1$.

Upon unloading, it is possible to admit expanded states by relaxing this condition. Also,

$$P'_2 = \frac{dP_2}{d\left(\frac{1 - \frac{(1)}{n}}{1 - \frac{(1)}{n_0}} \gamma\right)}$$

Again on loading $P'_2 \equiv 0$ for $\frac{1 - \frac{(1)}{n_0}}{(2)} \cdot \frac{1 - \frac{(1)}{n}}{1 - \frac{(1)}{n_0}} \gamma > 1$.

With these new definitions for P_2 and P'_2 , the entire analysis of the preceding section applies to the present case as well.

A few remarks are here in order. On loading for

$$\frac{1 - \frac{(1)}{n_0}}{(2)} \cdot \frac{1 - \frac{(1)}{n}}{1 - \frac{(1)}{n_0}} \gamma > 1,$$

1. The fluid does not undergo any pressurization and plays no role in overall deformation. It is easy to verify that

$$\frac{\partial \frac{(1)}{n}}{\partial P_p} = \frac{\partial \frac{(1)}{n}}{\partial \gamma} \equiv 0.$$

2. The material undergoes reversible (for $p \leq p_e$) and irreversible ($p \geq p_e$) void collapse.

Upon unloading from some pressure P_1^* and subsequent re-loading, we require that for $P_1 > 0$ and $P_2 = 0$,

$$\frac{\partial^{(1)} n}{\partial (P_c - P_p)} = 0 \quad \text{for} \quad P_1^* \geq p \geq p_e$$

For $p \leq p_e$, $\frac{\partial^{(1)} n}{\partial (P_c - P_p)}$ retains its usual functional relationship.

5.2.3 Data Fit for $\frac{\partial^{(1)} n}{\partial (P_c - P_p)}$

It was remarked in Section 5.2.1 that the function $\frac{\partial^{(1)} n}{\partial (P_c - P_p)}$ may be determined from hydrostatic tests with P_p kept to zero. If the matrix material is significantly weakened by physico-chemical interaction with water (e.g., tuff), it is important to utilize the data on the wet material. In the present study, we will fit the present model to the data for NTS tuff used in constructing the homogenized model employed in the May 8 Mine Dust HE calculation (Section 2.2). The assumptions underlying the present fit, in particular no fluid pressurization as long as $n^{(3)}$ is non-zero, of course differ from those employed in Section 2.2. The equations of state for the compacted tuff and water components are the same as reported in 3SR-1071. Other parameters are listed in Tables 5.1 and 5.2.

TABLE 5.1

PARAMETERS FOR $\frac{\partial n^{(1)}}{\partial (P_c - P_p)}$ FIT

P_c (kbar)	P_p (kbar)	$n^{(1)}$	$n^{(2)}$	$n^{(3)}$
0	0	0.6365	0.3135	0.05
0.15	0	n_e (not given)		
1.25	0	0.668587959 ^(*)		0
15 ^(**)	0	1		

(*) Calculated by assuming fluid pressure P_p to be zero and taking $P_c = \frac{(1)}{n} P_1 = \frac{(1)}{n} K_s \left(1 - \lambda \frac{(1)}{n} / \frac{(1)}{n_0} \right)$.
 Here $K_s = 294$ kbar, $\lambda = \gamma = \frac{(2)}{n_0} / \left(1 - \frac{(1)}{n_2} \right) \left[P_p = P_2 = 0 \rightarrow \gamma \left[1 - \frac{(1)}{n} \right] / \frac{(2)}{n_0} = 1 \text{ etc.} \right]$. Tuff matrix is assumed to behave in a linearly elastic manner over the pressure range 0 - 1.25 kbar.

(**) Extrapolated. Dry tuff is assumed to be voidless at 15 kbars. This value is consistent with previous estimates of this parameter.

TABLE 5.2

ADDITIONAL PARAMETERS IN THE $\frac{\partial n^{(1)}}{\partial (P_c - P_p)}$ FIT

Zero pressure compacted tuff density $\left(\rho_0^{(1)}\right)_e = 2.4 \text{ g/cc}$

Zero pressure composite bulk modulus $^{(*)}(K) = 27.5 \text{ kbar}$

$p_e = 0.15 \text{ kbar}$

(*) If $P_p = 0$, then $P_c = \frac{(1)}{n} K_S \left(1 - \frac{\frac{(1)}{n}}{\frac{(1)}{n_0}} \lambda \right)$

$$K \Big|_{P_c=0} = - \frac{dP_c}{d\lambda} \Big|_{P_c=0} = \frac{(1)}{n} K_S / \left[1 + K_S \frac{\partial \frac{(1)}{n}}{\partial P_c} \Big|_{P_c=0} \right]$$

The following piecewise continuous function was fitted to the above data:

$$\begin{aligned}
 {}^{(1)}n &= {}^{(1)}n_0 + a_1 P_c + a_2 P_c^2 \quad 0 \leq P_c \leq p_e \\
 &= n_e + \bar{a}_1 (P_c - p_e) + \bar{a}_2 (P_c - p_e)^2 + \bar{a}_3 (P_c - p_e)^3 \\
 p_e &\leq P_c \leq 15 \text{ kbars}
 \end{aligned} \tag{5.23}$$

The six unknown constants are found by applying the following conditions:

(1) Matching zero pressure bulk modulus. This yields:

$$a_1 = \frac{{}^{(1)}n_0 - K/K_S}{K} = 0.019744094 \text{ kbar}^{-1}.$$

(2) Requiring continuity in ${}^{(1)}n$ and $\frac{\partial {}^{(1)}n}{\partial P_c}$ at $P_c = p_e$. This yields

$$n_e = {}^{(1)}n_0 + a_1 p_e + a_2 p_e^2 \tag{5.24}$$

and

$$a_1 + 2a_2 p_e = \bar{a}_1 \tag{5.25}$$

(3) ${}^{(1)}n = 0.668587959$ at $P_c = 1.25$ kbars. This gives:

$$\begin{aligned}
 0.668587959 &= n_e + \bar{a}_1 (1.25 - p_e) \\
 &\quad + \bar{a}_2 (1.25 - p_e)^2 + \bar{a}_3 (1.25 - p_e)^3
 \end{aligned} \tag{5.26}$$

(4) $\frac{\partial n}{\partial P_C} = 1$ and $\frac{\partial n}{\partial P_C} = 0$ at $P_C = 15$ kbars. These requirements are equivalent to

$$1 = n_e + \bar{a}_1 (15 - p_e) + \bar{a}_2 (15 - p_e)^2 + \bar{a}_3 (15 - p_e)^3 \quad (5.27)$$

$$0 = \bar{a}_1 + 2\bar{a}_2 (15 - p_e) + 3\bar{a}_3 (15 - p_e)^2 \quad (5.28)$$

Solution of the algebraic set of equations (5.24 - 5.28) finally gives the required constants.

$$a_2 = 0.015945583 \text{ [kbar]}^{-2}$$

$$n_e = 0.639820389$$

$$\bar{a}_1 = 0.024527770 \text{ [kbar]}^{-1}$$

$$\bar{a}_2 = 0.001596499 \text{ [kbar]}^{-2}$$

$$\bar{a}_3 = -0.000108747 \text{ [kbar]}^{-3}$$

Given the function $\frac{\partial n}{\partial P_C}$ (1) (and hence $\frac{\partial n}{\partial (P_C - P_p)}$ (1)) may be obtained by simply differentiating Eq. (5.23) w.r.t. P_C . Thus we have

$$\begin{aligned} \frac{\partial n}{\partial (P_C - P_p)} &= a_1 + 2a_2 (P_C - P_p) \quad 0 \leq P_C - P_p \leq p_e \\ &= \bar{a}_1 + 2\bar{a}_2 ((P_C - P_p) - p_e) + 3\bar{a}_3 ((P_C - P_p) - p_e)^2 \\ p_e \leq P_C - P_p &\leq 15 \text{ kbars} \quad (5.29) \end{aligned}$$

Since data are usually unavailable for negative $P_C - P_p$ (or negative P_C at zero pore pressure) and since such states may be attained during stress wave propagation, it is necessary to estimate $\frac{\partial n}{\partial (P_C - P_p)}$ (1) for $P_C - P_p < 0$. In the present case, we will assume that the functions given by Eq. (5.29) are symmetric functions of $P_C - P_p$, i.e.

$$\frac{\partial n}{\partial (P_c - P_p)} \stackrel{(1)}{=} a_1 + 2a_2 |P_c - P_p| \quad 0 \leq |P_c - P_p| \leq p_e$$

$$= \bar{a}_1 + 2\bar{a}_2 (|P_c - P_p| - p_e) + 3\bar{a}_3 (|P_c - P_p| - p_e)^2$$

$$p_e \leq |P_c - P_p| \leq 15 \text{ kbars.} \quad (5.30)$$

In Fig. 5.1, we show the loading-unloading response predicted by the present model for low composite pressures. A comparison with the results of the homogenized model of Section 2.2 is also shown. In general, the present model predicts stiffer material response at low pressures. This is a consequence of the assumption that water does not pressurize as long as $\stackrel{(3)}{n} \neq 0$. At higher pressures (not shown here), the response predicted by this model differs but little from the one predicted by the pressure equilibrium model.

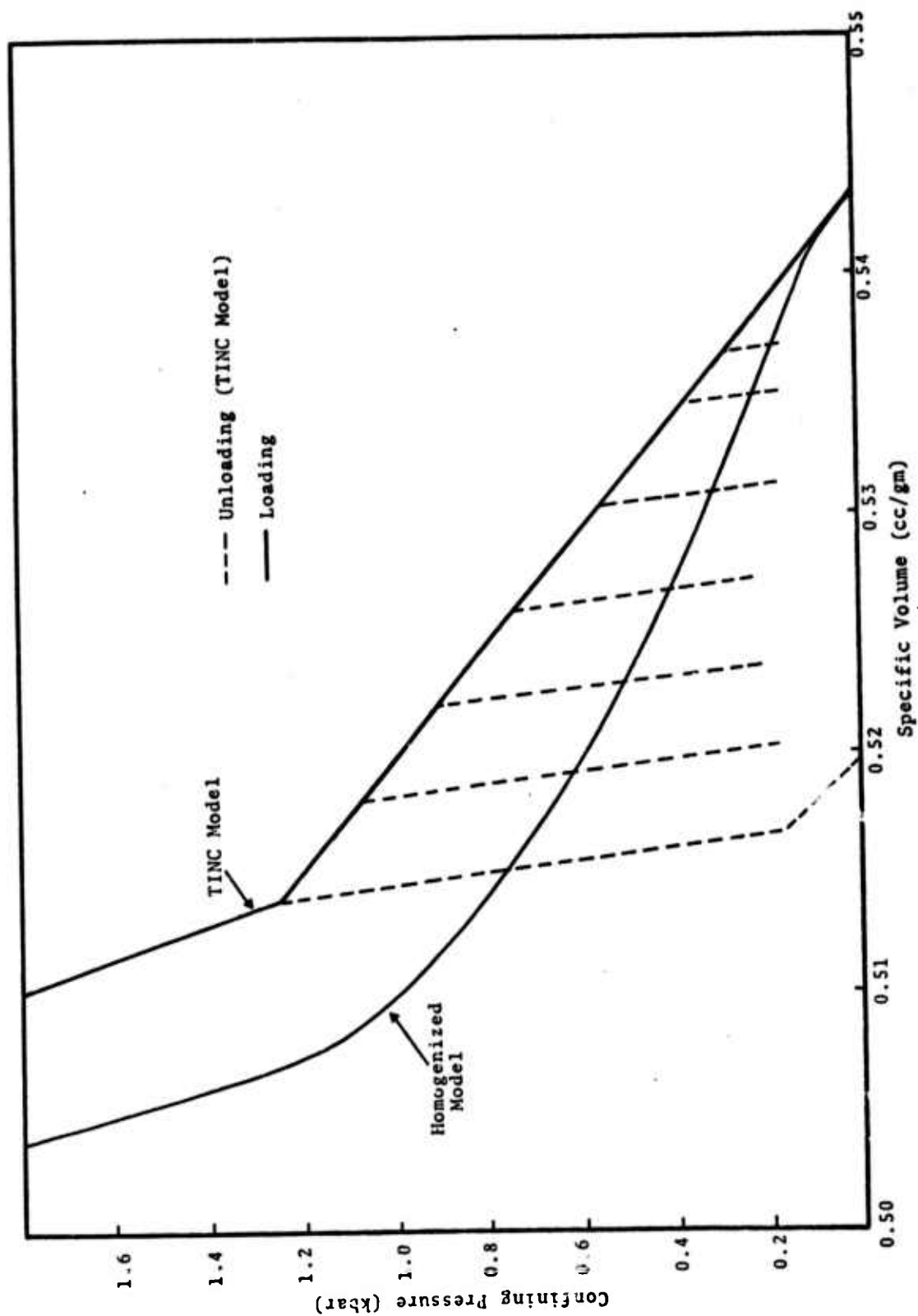


Fig. 5.1--Static loading and unloading curves.

5.3 THE POROUS CODE

The POROUS code is a one-dimensional (either planar or spherical symmetry) time-dependent numerical scheme designed to solve the TINC equations for binary composites of a solid porous matrix (such as tuff) and water. Both saturated and unsaturated cases may be treated. The basic methodology used in POROUS has been described at length in 3SR-1071; in the present report, recent improvements in the scheme will be discussed.

Numerically, POROUS employs a fundamentally Lagrangian explicit forward-time finite-difference procedure to solve the mass, momentum and energy conservation laws for the tuff — thus, the coordinate system may be visualized as anchored to individual tuff particles. On the other hand, the water is treated in a pseudo-Eulerian fashion, in that water may flow from one grid cell to the next. Therefore, the mass, momentum and energy conservation laws for the water contain advection terms, with the advective velocity at each point equal, numerically, to the difference between the local water and tuff particle velocities. In a given computational cell, the tuff mass remains constant but the water mass may vary with time.

The present POROUS code differs from the earlier version described in 3SR-1071 in four essential respects. First, the boundary conditions have been generalized. The earlier version allowed only a "prescribed velocity history" boundary condition to drive the calculation. In the present code, either the velocity history or the total stress history may be prescribed. As an additional option, in spherical geometry a "high-explosive burn" capability has been added to allow simulation of underground explosions. Second, the interaction terms in the momentum and energy equations for both media are now integrated implicitly,

which removes a constraint on the time step size. Third, the assumption of pressure equilibrium between the two media has been eliminated; instead, the formulation described in Section 5.2 is employed. Finally, the finite-difference equations have been recast in a form which allows arbitrarily weak signals to be treated without loss of accuracy due to computer round-off error.

5.3.1 Boundary Conditions

In 3SR-1071, the basic procedure for imposing a prescribed velocity history at the left edge of the grid is described. The water and tuff velocities are constrained to be the same at the boundary, and equal to the prescribed overall boundary velocity. To impose a stress boundary condition at the boundary, a similar condition is imposed: the separate stresses for each component to be used in the "fictitious" cell to the left of the grid are determined by demanding that (1) the total stress evaluated at the boundary (the average of the stresses in the fictitious cell and in the first actual cell) match the prescribed total stress, and that (2) the accelerations of the two components at the boundary be equal.

In either case, the boundary prescription requires that the velocities of the two components be equal at the boundary. In reality, of course, there is no particular reason for believing that this is always true. If, for example, a sample of wet tuff is shocked by a piston-like impact, it may readily be visualized that the water velocities will momentarily exceed the tuff velocities. Subsequently, of course, the viscous interaction terms will equilibrate the separate component velocities, but a relative displacement will have taken place. Now, the POROUS code allows this relative displacement to occur in the interior of the grid, but is in some sense inconsistent in that such

displacement is automatically precluded at the boundary. This need be of little concern for numerical calculations, however, unless the "permanent offset" is comparable to the size of a computational cell. For practical problems involving water and tuff, the offset is exceedingly small. For other binary composites which are weakly coupled, it may be necessary to reformulate the boundary conditions to allow differential motion at the grid perimeter.

As a special-purpose option, the POROUS code (in spherical geometry) can also treat the innermost zones as containing chemical explosive, using the HE burn formulation of Section 2.2.5. This option can be useful in the study of underground explosions. At the interface between the explosive and the wet tuff, all velocities (high explosive, water and tuff) are assumed to be equal.

5.3.2 Interaction Terms

The earlier version of the POROUS code described in 3SR-1071 treated time-advancement of all field variables in an exclusively explicit manner. This treatment places stability constraints of various sorts on the maximum size of the computational time step. One of them is the classical Courant condition:

$$\tau \ll \frac{\Delta x}{C} \quad (5.31)$$

where τ is the time step, Δx is the length of a zone, and C is the shock speed. Due to the viscous interaction between the two media, an additional constraint must be imposed:

$$\tau \ll k / (\mu [n^{(2)}]^2) \quad (5.32)$$

where k is the tuff permeability, μ is the kinematic viscosity of water, and $n^{(2)}$ is the water volume fraction.

The kinematic viscosity of water is about 10^{-2} cm²/sec, a "typical" (within an order of magnitude or so) permeability for tuff is 10^{-11} cm², and a "typical" water volume fraction is 0.1. In this case, the above requirement (2) is therefore:

$$\tau \ll 0.1 \text{ } \mu\text{sec}$$

Now, a typical shock speed in tuff is 0.2 cm/ μ sec. Therefore, the two constraints will be about equally restrictive if the space interval is

$$\Delta x \approx 0.02 \text{ cm} = 200 \text{ } \mu.$$

Since computer storage limitations generally restrict the grid to 500 zones or so, this means that the entire domain under consideration must be no more than about 10 cm in extent. For practical problems, ranges of interest are generally much greater than this, and hence a purely explicit treatment would require an enormous number of time steps.

To circumvent this difficulty, the interaction terms in both media in both the momentum and energy equations were treated implicitly in the latest version of POROUS. This essentially eliminates requirement (2) above. Therefore, the only constraint on time step size is the Courant condition, as in more conventional (homogeneous) procedures.

5.3.3 Constitutive Relations

The POROUS code described in 3SR-1071 employed a stress-equilibration constraint to establish the relative volume fractions of tuff and water at each point in the composite at each time step. That is, in a particular computational cell, the mass of each component was computed directly using the mass conservation principles (the tuff mass, in fact, remains constant). The volume of the zone

as a whole is computed using the momentum equations and the kinematic condition. The specific heat content of each component separated was computed using the energy conservation principle. Now, the pressure of each component is a unique function of its density (mass/volume) and its specific heat content. Consequently, the partition of the total available volume could be determined if it was assumed that the effective stress was the same for each component. In practice, this was accomplished (for each zone at each time step) by a Newton-Raphson iteration procedure involving the equations of state of the two materials.

The pressure-equilibrium assumption is appropriate for high shock strengths (50-100 kbars or more), but at lower shock overpressures pore-pressure effect becomes important. Accordingly, in order to make the POROUS code useful for weak-shock calculations, the explicit formulation for determining component volume fractions described in Section 5.2 was employed. Numerical experiments have shown that at high shock strengths the results are essentially indistinguishable from the pressure-equilibrium case, but that for weaker shocks the medium behaves in a "stiffer" manner than was predicted by the previous method.

Implementation of the non-equilibrium explicit model involves the direct integration of field equations for the volume fraction distribution. Since the empirical relations between volume fraction, pore pressure, relative compression, etc. are ill-behaved (at best piecewise continuous), a time-step appropriate for the calculation as a whole will generally be far too large to provide accurate results for strong shocks, particularly at the shock front where the relative compression increases rapidly with time. Accordingly, the model described in Section 5.2 is solved by a "subcycling"

procedure in which the independent variable is the overall volumetric strain. Empirically, it has been found that restricting the strain change to 0.02 percent per subcycle is adequate to produce accurate results.

5.3.4 Low-Amplitude Finite-Difference Equations

The final fundamental refinement to the POROUS code is strictly numerical in character. The alterations made to the finite-difference equations in no way change their content, but are designed exclusively to minimize the effects of "round-off" error; that is, the finite number of significant figures retained by the computer. For strong-shock problems, the difficulty does not arise, but for weak signals, conventional procedures often produce numerical "hash." The problem may be simply stated as follows. The caloric equation of state for a material may be expressed in the form:

$$P = f(\psi, E) \quad (5.33)$$

Where E is the heat energy per unit mass and ψ (the relative compression) is given by:

$$\psi = \frac{\rho}{\rho_0} - 1 \quad (5.34)$$

where ρ is density and ρ_0 is "ambient" density. In the present context, the pressure in cell i at time $= t^k$ may be expressed as:

$$P_i^{(\alpha)k} = f \left(\psi_i^{(\alpha)k}, E_i^{(\alpha)k} \right) \quad (5.35)$$

where $\alpha = 1$ or 2 (tuff or water), and

$$\psi_i^{(\alpha)k} = \frac{M_i^{(\alpha)k}}{M_i^{(\alpha)}} \frac{V_i^{(\alpha)}}{V_i^{(\alpha)k}} - 1 \quad (5.36)$$

For a weak shock, the equation of state for most materials may be approximated by a first-order Gruneisen equation of state:

$$P^{(\alpha)} = A^{(\alpha)} \psi + G^{(\alpha)} \rho^{(\alpha)} E^{(\alpha)} \quad (5.37)$$

where $A^{(\alpha)}$ is the bulk modulus of material α and G is its Grüneisen coefficient. Since, at low compressions, the quantity (ρ/ρ_0) is exceedingly close to unity, direct employment of Eq. (5.36) can lead to "quantization" errors in pressure. For example, consider a Cartesian sample material case with 1000 zones. Now, if the computer has essentially seven significant figures (which is common), the cell volume for cell number 1000 cannot be known to a greater precision than four significant figures. Accordingly, the smallest increment in ψ which the computer can consider is about 10^{-3} . Since the bulk modulus for tuff is about 300 kbars, this means that the smallest pressure increment available is 30 atmospheres. Clearly, for strong shock problems this is not particularly important but for weak shocks unacceptable signal to noise ratios may result and generate spurious high-frequency waves which will reduce the calculation to nonsense.

To circumvent this difficulty, the finite-difference equations may be re-cast in the following general way (for simplicity, Cartesian geometry will be assumed and a pure compacted-tuff problem will be considered): Let:

$$V_i^k = V_i^0 + \delta V_i^k$$

where V_i^0 is the initial cell volume at $t = 0$ and δV_i^k is the difference between the current volume at t^k and the initial volume. Now,

$$\begin{aligned} V_i^k &= X_{i+1/2}^k - X_{i-1/2}^k \\ &= X_{i+1/2}^0 - X_{i-1/2}^0 + \delta X_{i+1/2}^k - \delta X_{i-1/2}^k \end{aligned}$$

so that, for tuff ($M_i^k = M_i^0$),

$$\psi_i^k = \frac{\delta X_{i+1/2}^k - \delta X_{i-1/2}^k}{X_{i+1/2}^0 - X_{i-1/2}^0 + \delta X_{i+1/2}^k - \delta X_{i-1/2}^k}$$

where $X_{i+1/2}^0$ is the initial location of the right-hand edge of cell i and $\delta X_{i+1/2}^k$ is the difference between the current position and the initial position. Since $\delta X_{i+1/2}^k$ can be updated directly, i.e. by:

$$\delta X_{i+1/2}^{k+1} = \delta X_{i+1/2}^k + v_{i+1/2}^{k+1/2} \Delta t$$

the value of ψ may take on arbitrarily small values, irrespective of the number of significant digits available. This means in practice that whereas in the previous scheme only one "position" array ($X_{i+1/2}^k$) needed be stored in the computer memory, two ($X_{i+1/2}^0$; $\delta X_{i+1/2}^k$) are now required.

For multi-component systems (i.e. tuff and water) and for problems in spherical geometry the algebra is somewhat more complex, but the same general approach is used. For example, since the water mass in a cell may vary with time, four arrays are used to describe cell water content:

$${}^{(2)k}M_i = {}^{(2)}M_i^0 + \delta {}^{(2)k}M_i \quad (\text{mass})$$

$${}^{(2)k}n_i = {}^{(2)}n_i^0 + \delta {}^{(2)k}n_i \quad (\text{volume fraction})$$

so that

$${}^{(2)k}\psi_i = \frac{{}^{(2)}n_i^0 (V_i^0 \delta M_i^{(2)} - M_i^0 \delta V_i^{(2)k}) - \delta n_i {}^{(2)k}M_i^0 (V_i^0 + \delta V_i^{(2)k})}{M_i^0 ({}^{(2)}n_i^0 + \delta {}^{(2)k}n_i) (V_i^0 + \delta V_i^{(2)k})}$$

5.4 NUMERICAL CALCULATIONS

The spherical version of the POROUS code was exercised for a sphere of partially saturated tuff ($n_0^{(1)} = 0.6365$, $n_0^{(2)} = 0.3135$, $n_0^{(3)} = 0.0500$) which is initially 35 cm in radius and has a central 5 cm radius spherical cavity. The entire 35 cm radius sphere is divided into 200 computational zones. The central cavity is zone one. The remaining 199 zones are selected such that the mass of each zone increases by a factor of 1.02, i.e., $M_{k+1}/M_k = 1.02$. The material response was monitored as a function of time at stations which were initially at 7.5, 12.5, and 25 cms. The loading was by an exponentially decaying stress pulse of the form

$$\sigma_r(r_c, t) = 35e^{-t/10} \text{ kbar} \quad (t \text{ in } \mu\text{sec})$$

applied at the interior of the cavity. Other material parameters utilized in the calculation are listed below.

$$\mu/k \text{ (viscosity of water/permeability)} = 10^{10} \text{ g/cm}^3\text{-sec}$$

$$\mu_p \text{ (shear modulus)} = 15.0 \text{ kbar}$$

$$Y \text{ (yield stress)} = Y_0 \frac{P_c}{P_0} \left(2 - \frac{P_c}{P_0} \right)$$

$$\text{for } P_c \leq P_0 = 0.6 \text{ kbar}$$

$$= Y_0 \text{ for } P_c \geq P_0$$

$$Y_0 = 0.623 \text{ kbar}$$

For purposes of comparison, the calculation was repeated with the SKIPPER code which utilizes the homogenized model described in Section II. Results of these calculations are shown in Figs. 5.2 through 5.12. Composite radial stress

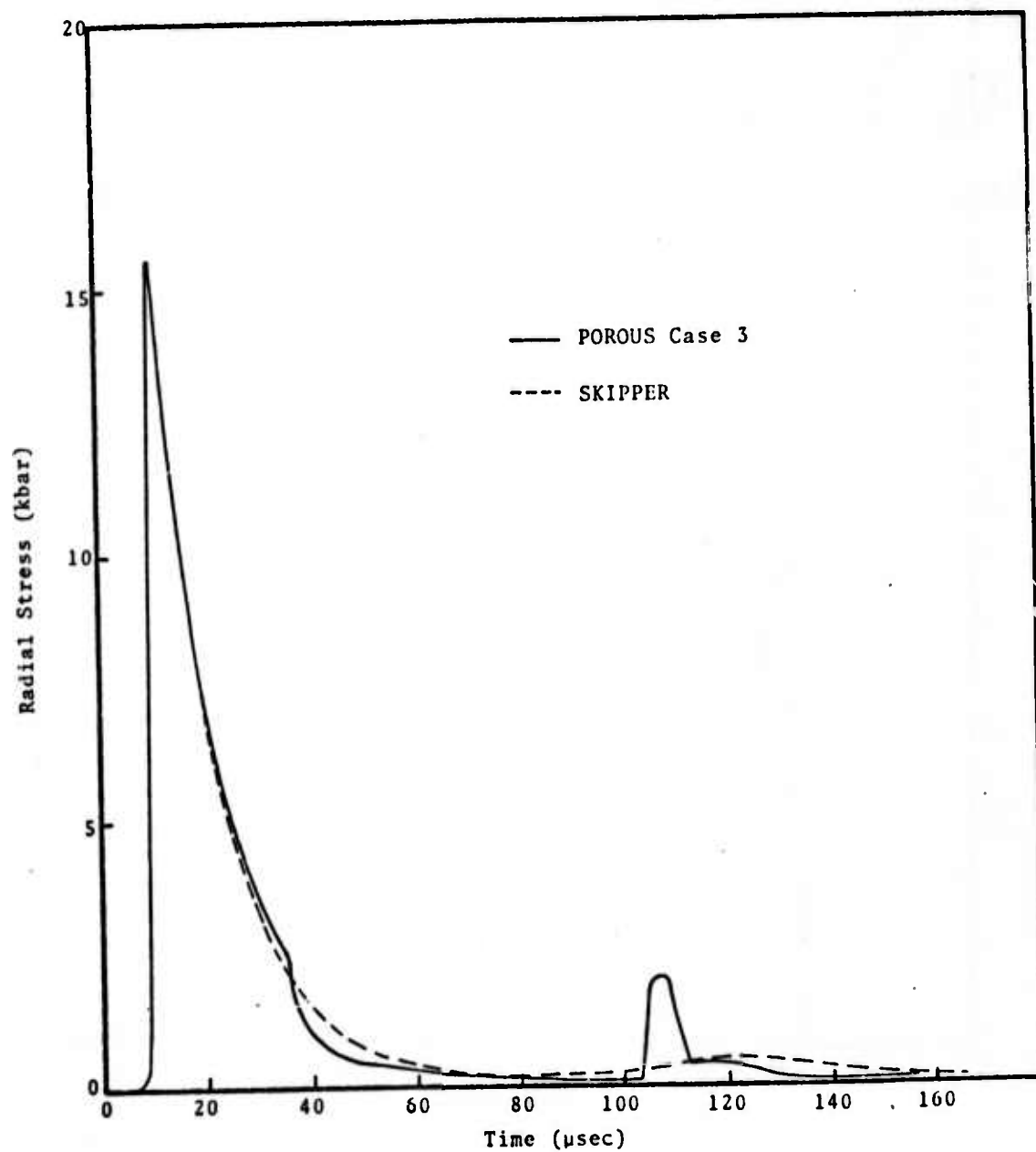


Fig. 5.2--Composite radial stress history at 7.5 cm.

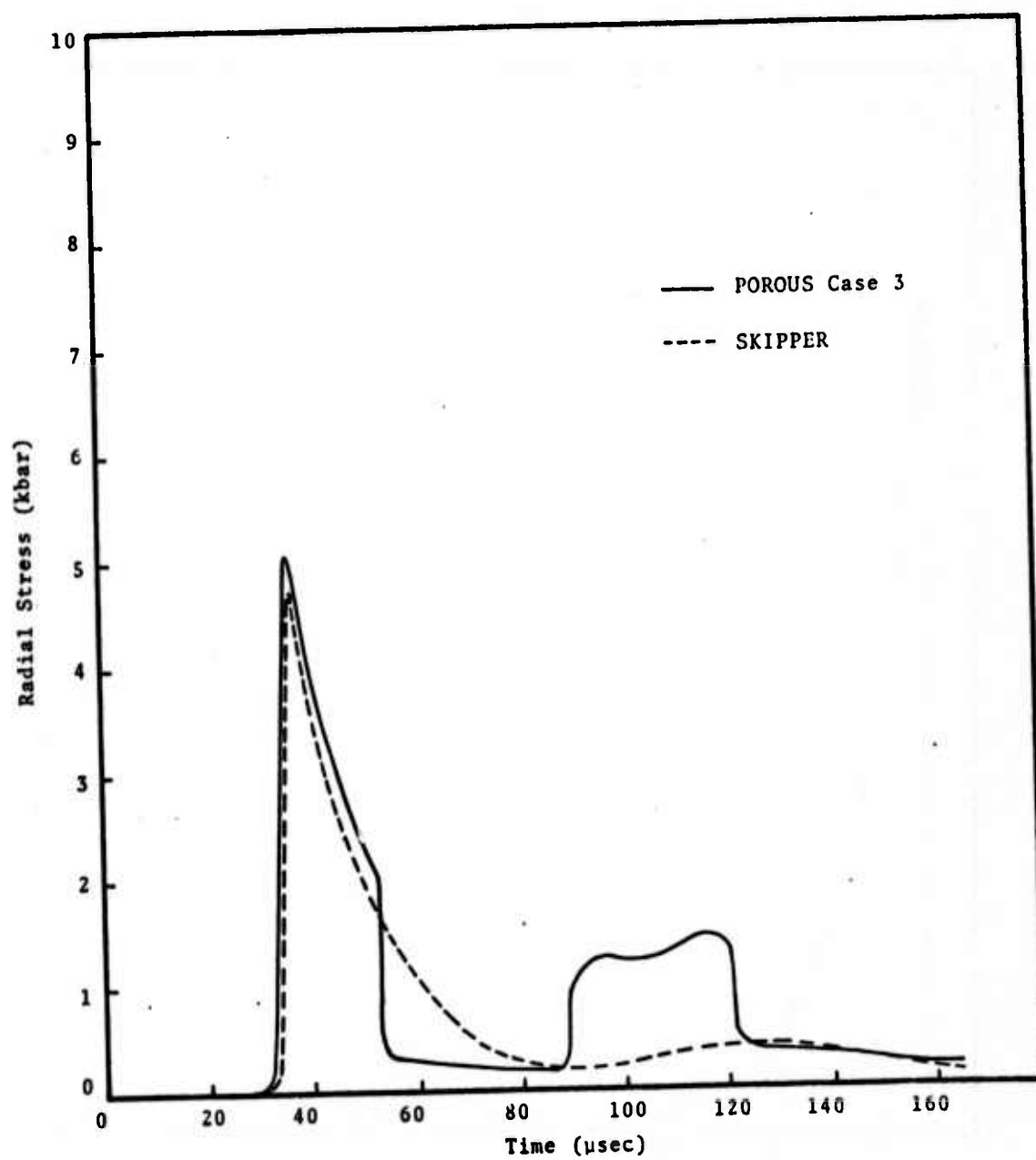


Fig. 5.3--Composite radial stress history at 12.5 cm.

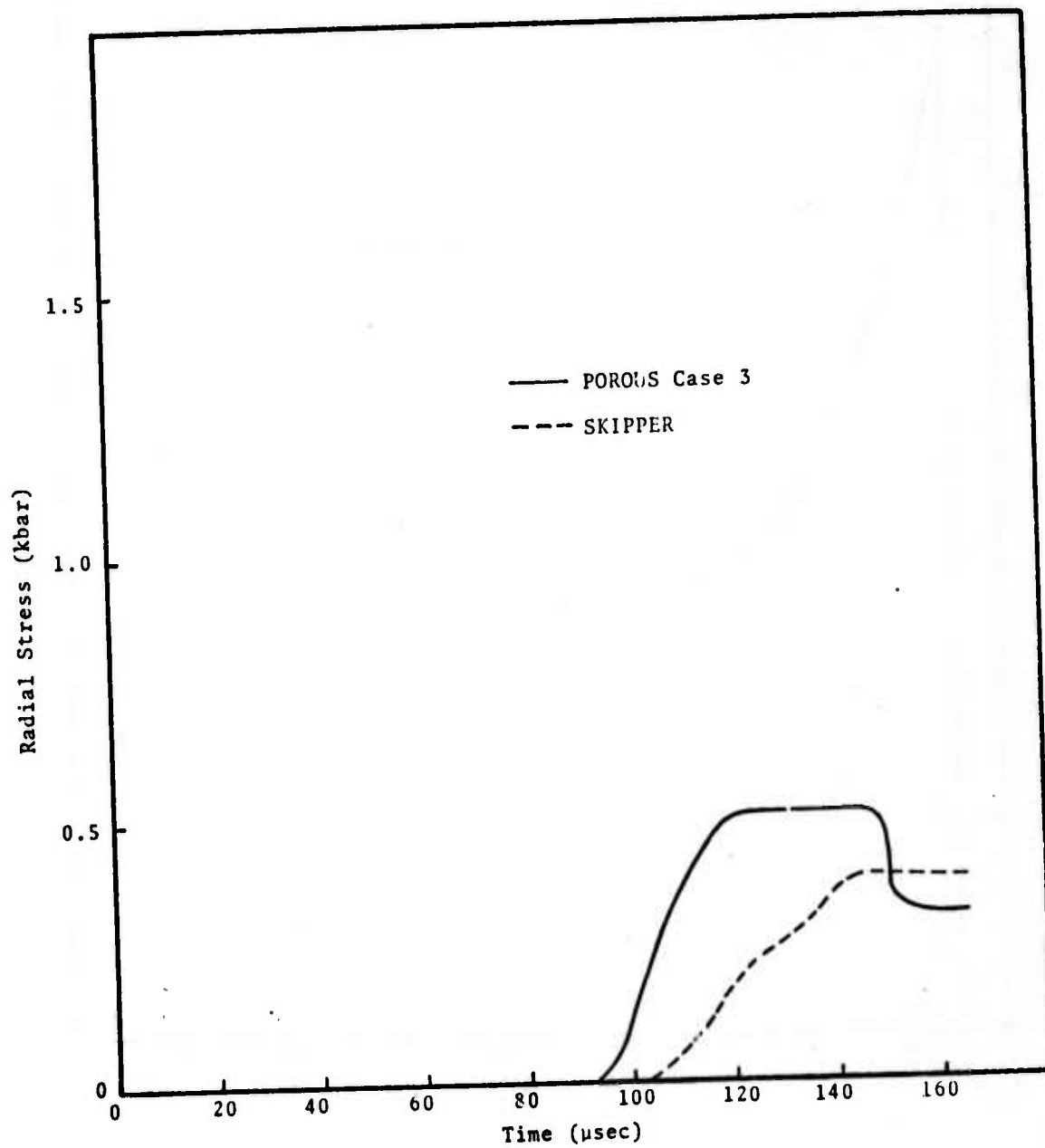


Fig. 5.4--Composite radial stress history at 25 cm.

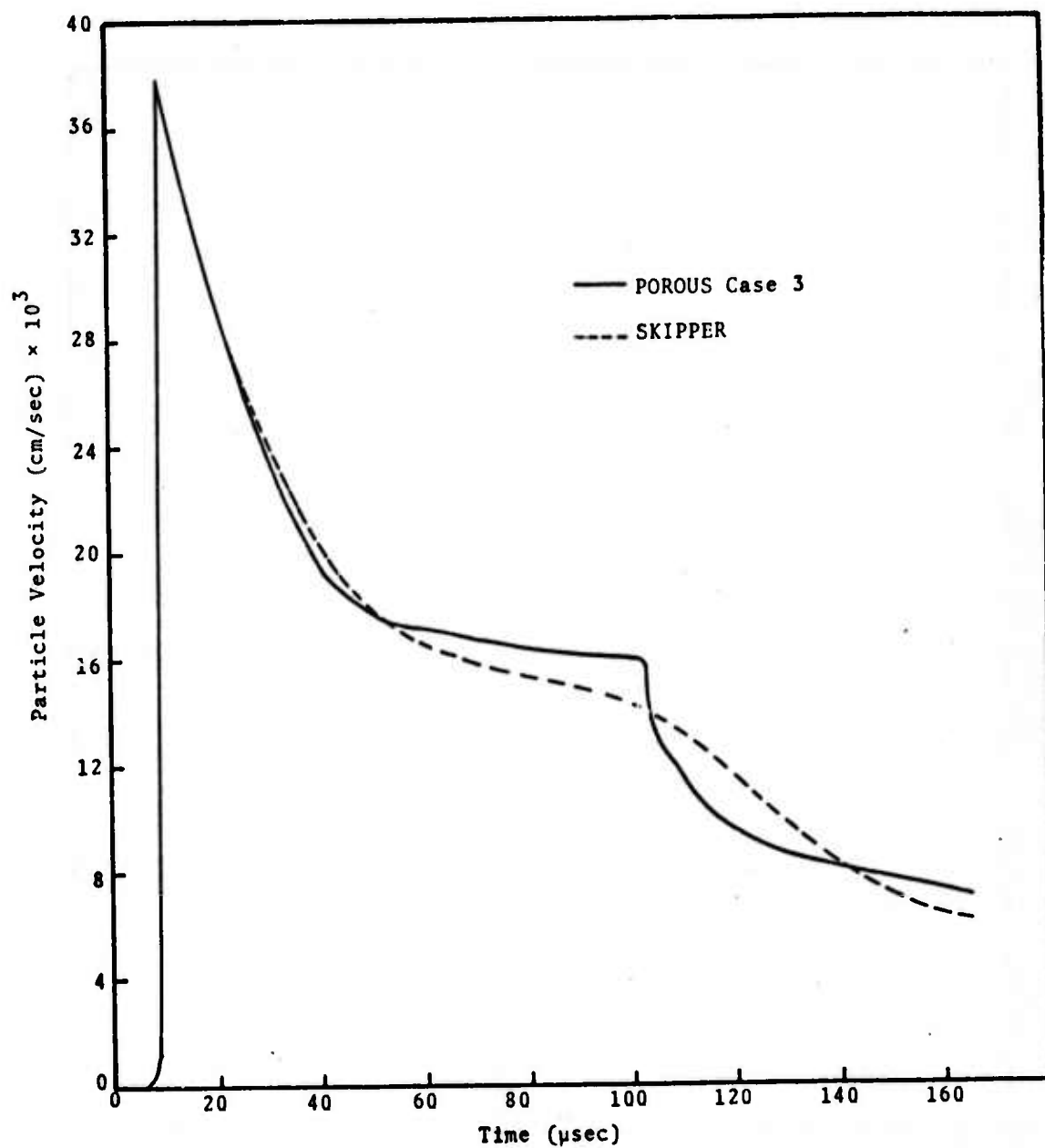


Fig. 5.5--Composite particle velocity history at 7.5 cm.

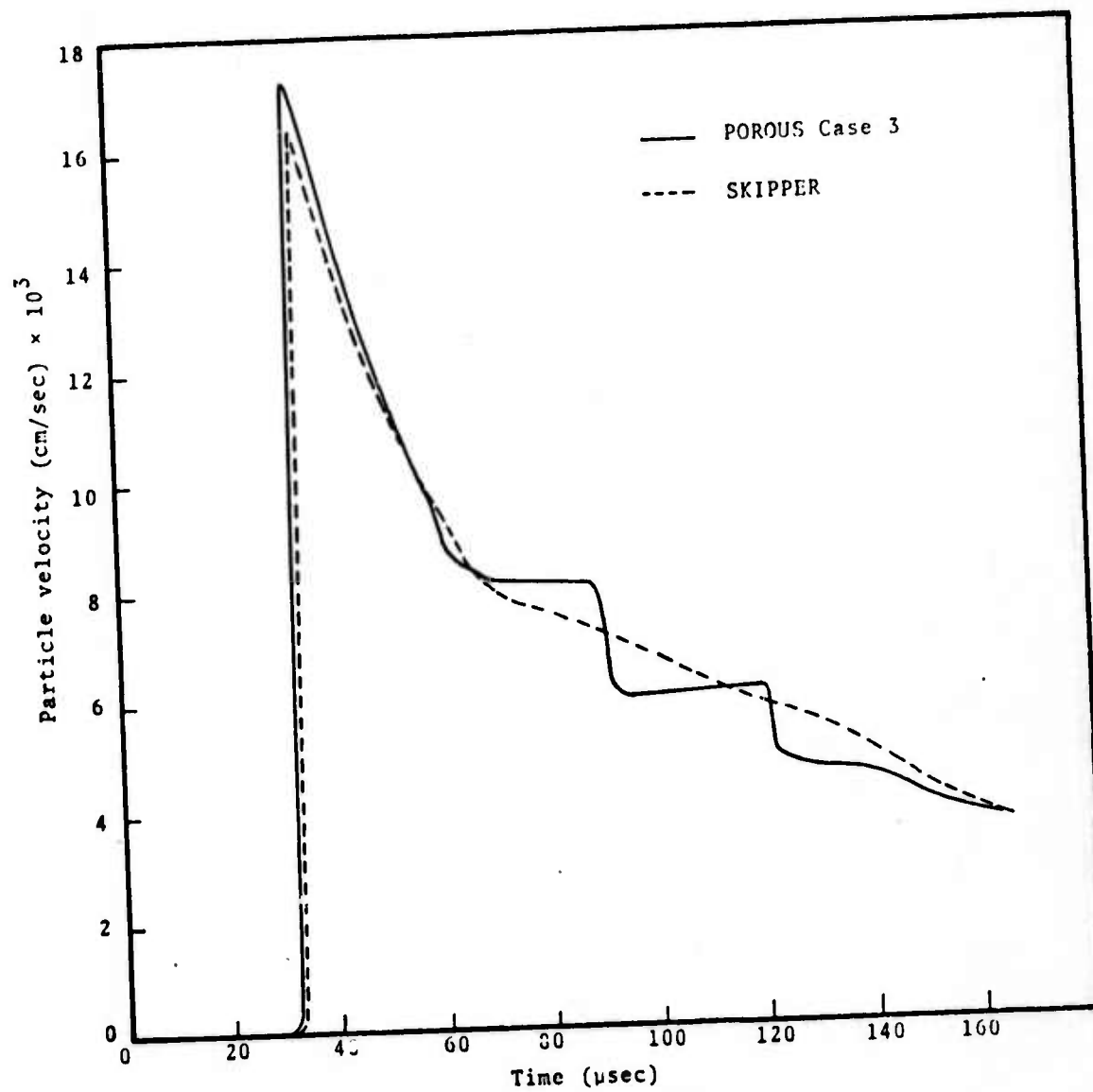


Fig. 5.6--Composite particle velocity history at 12.5 cm.

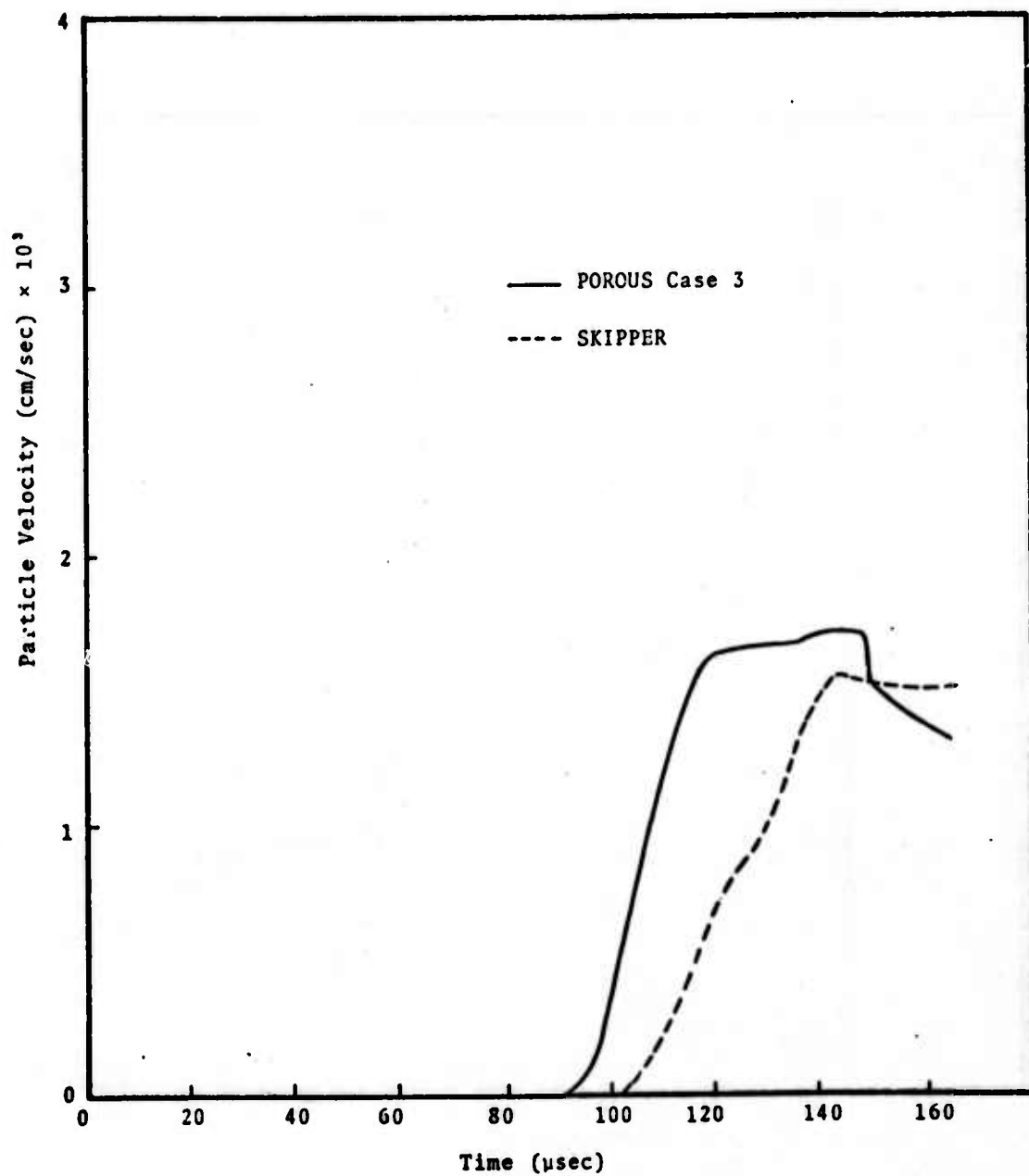


Fig. 5.7--Composite particle velocity history at 25 cm.

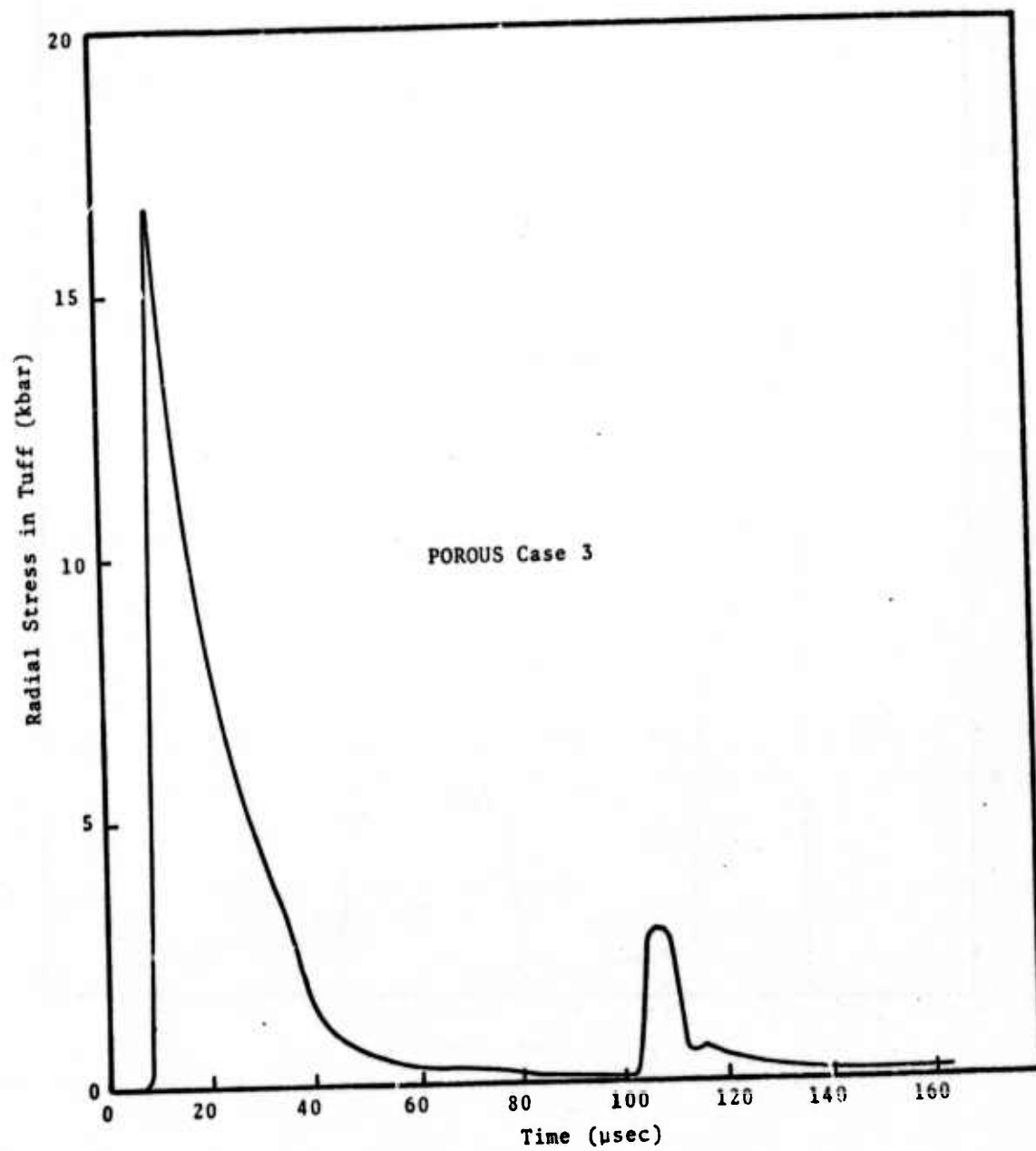


Fig. 5.8--Tuff component radial stress history at 7.5 cm.

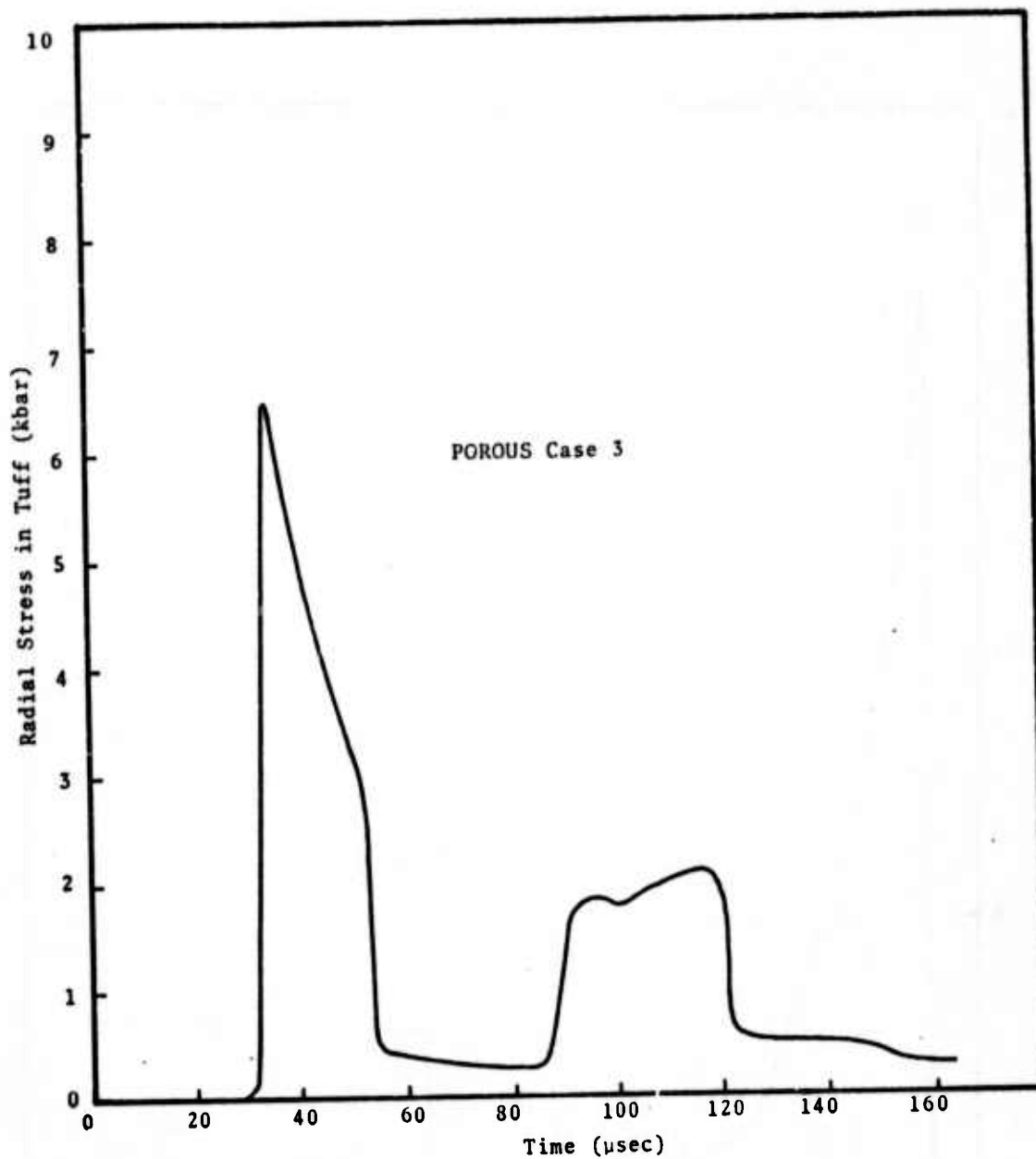


Fig. 5.9--Tuff component radial stress history at 12.5 cm.

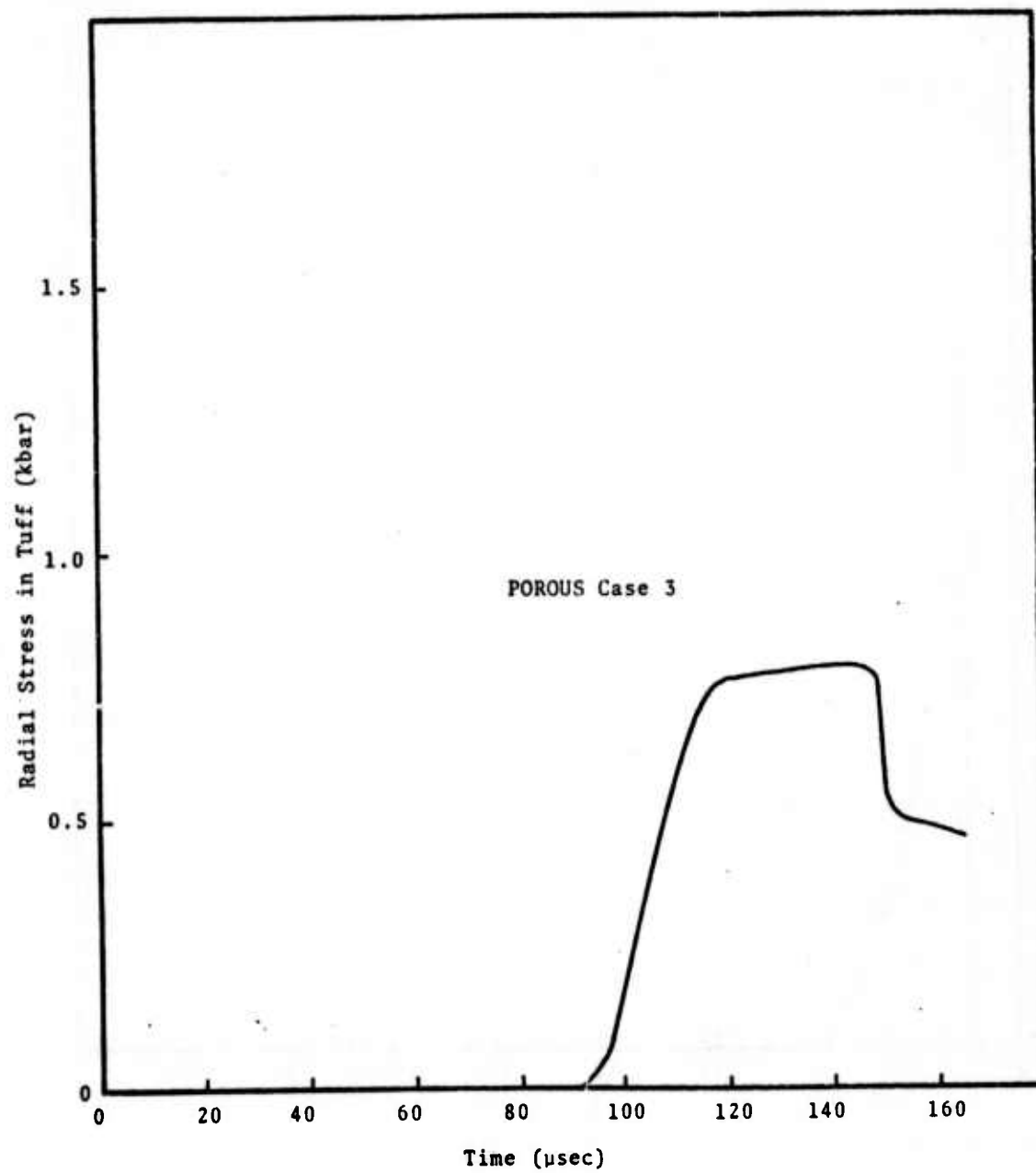


Fig. 5.10--Tuff component radial stress history at 25 cm.

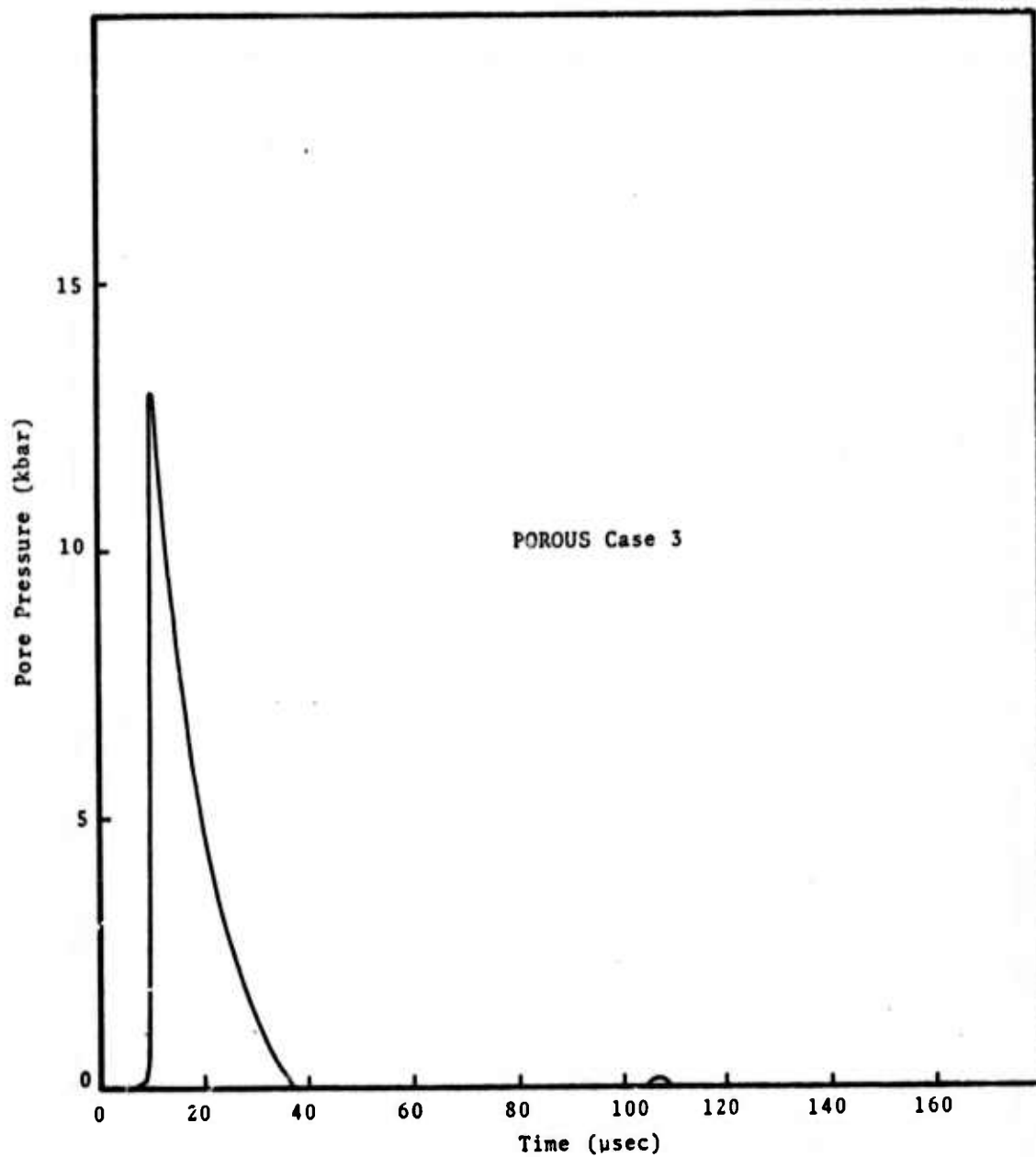


Fig. 5.11--Pore pressure history at 7.5 cm.

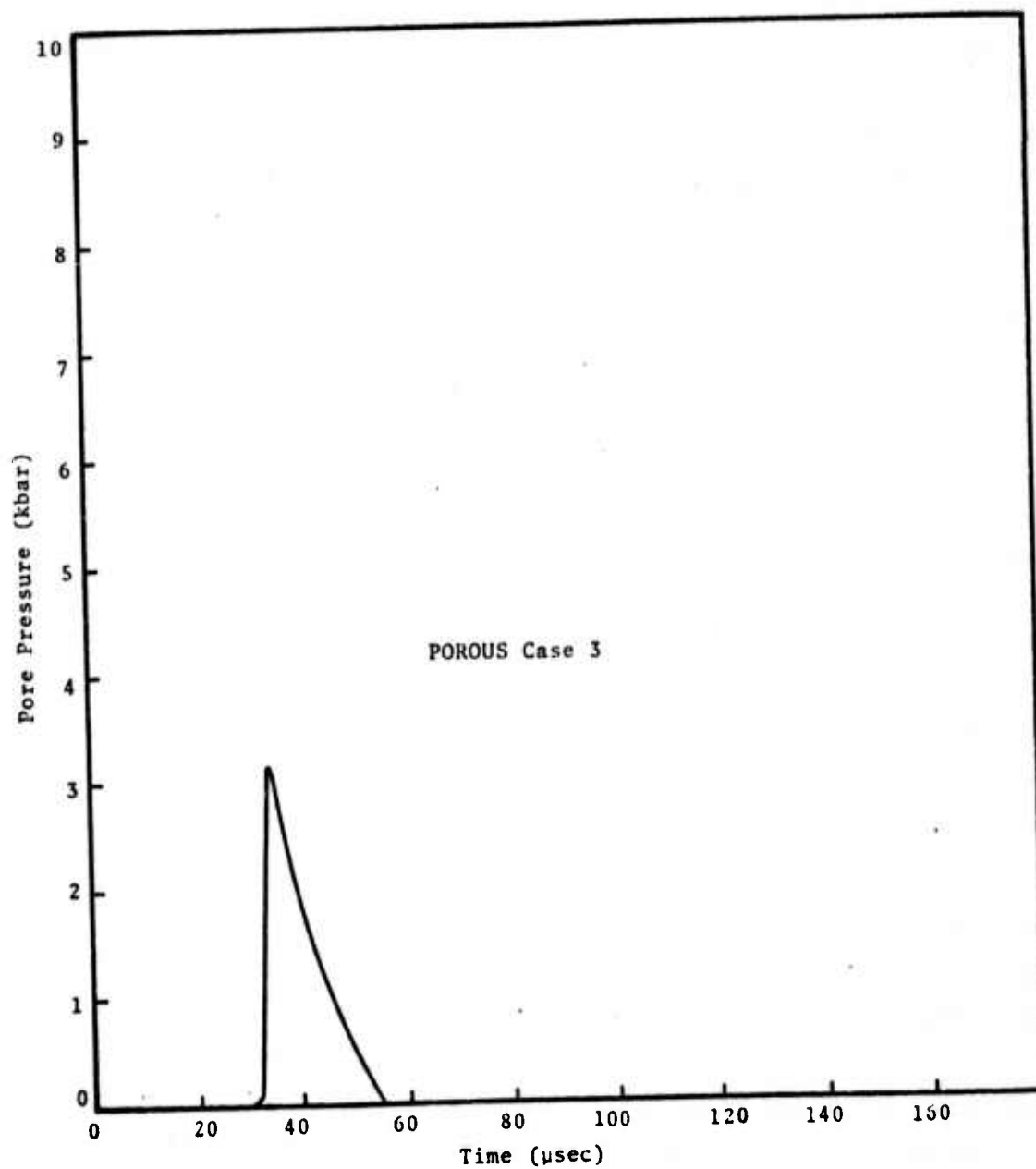


Fig. 5.12--Pore pressure history at 12.5 cm.

histories and particle velocity histories (as given by the POROUS and SKIPPER calculations) are plotted in Figs. 5.2 - 5.4 and 5.5 - 5.7 respectively. Time histories of the radial stress in the tuff component and the pressure in the pore water calculated with the POROUS code are depicted in Figs. 5.8 - 5.10 and 5.11 - 5.12 respectively. Note that no pore pressure history for the 25 cm station is shown since the pore pressure at this location remains zero throughout the calculation.

It is of interest to compare the SKIPPER and POROUS results (Figs. 5.2 - 5.7). The two calculations appear to agree well at high pressure levels (Figs. 5.2, 5.3, 5.5 and 5.6). However, the results differ significantly at low pressures. In general, the POROUS code predicts higher amplitudes and earlier times of arrival than those given by the SKIPPER calculation. These results are not really surprising since the TINC model differs but little from the pressure equilibrium model at high pressures; at lower pressures, however, the TINC model predicts considerably stiffer material response than the homogenized model.

POROUS calculations (and, to a lesser extent, SKIPPER results as well) exhibit a two-wave structure (Figs. 5.2 - 5.3, 5.5 - 5.6, 5.8 - 5.9, 5.11). To understand this phenomenon, it is useful to consider the wave diagram, Fig. 5.13. At $t = 0$, a shock wave (main shock) emanates from the boundary and propagates into the undisturbed medium ahead of it. Since the input pulse at the boundary is decaying exponentially, the main shock is immediately followed by a rarefaction wave. This rarefaction wave is coincident with the main shock. Thus, any small volume of the material is first shocked to some peak stress and then starts unloading. When the total pressure P_c decays to approximately 1.32 kbars, the pore pressure (P_2) goes to zero. Once P_2 is zero, the material is allowed to unload only along lines of

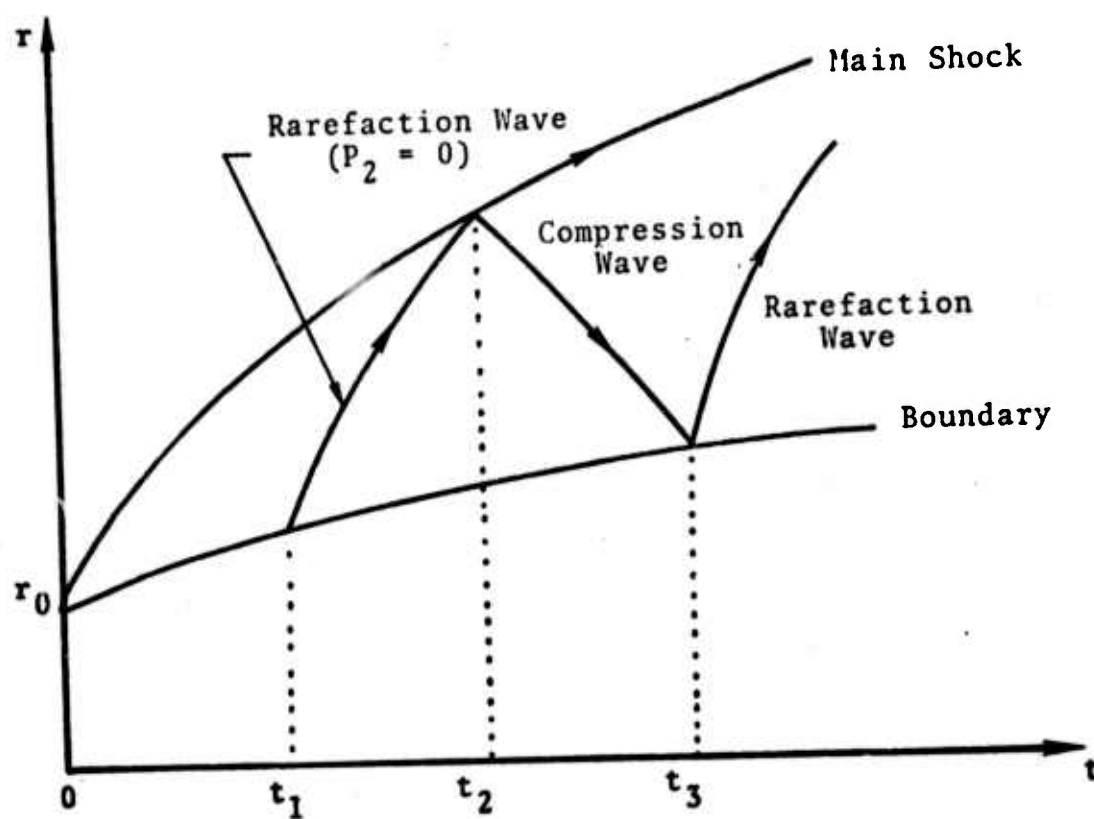


Fig. 5.13--Wave diagram corresponding to POROUS Run 3.

constant $n^{(1)}$ (dashed lines in Fig. 5.1). This results in a second rarefaction wave (indicated by $P_2 = 0$ in Fig. 5.13). It travels at a faster rate than either the main shock or the first rarefaction wave, and eventually develops into a rarefaction shock (see Figs. 5.2 - 5.3, 5.8 - 5.9). The rarefaction shock catches up with the main shock at $t = t_2$ and then reflected as a compressive wave. This compressive wave steepens as it propagates towards the boundary resulting in the two-wave structure. At a later time ($t = t_3$) the compressive wave is reflected at the boundary as a rarefaction wave.

The discussion of the preceeding paragraph attributed the two-wave structure observed in the POROUS calculation to the assumed unloading behavior ($\text{const } n^{(1)}$ for $P_2 = 0$). To further study this aspect, the calculation was repeated by permitting $n^{(1)}$ changes during unloading such that $\partial n^{(1)} / \partial P_\Delta |_{\text{load}} \equiv \partial n^{(1)} / \partial P_\Delta |_{\text{unload}}$. The results of this calculation (3A) are compared with the preceeding calculation (Case 3) are shown in Figs. 5.14 through 5.19. The two wave structure disappears in calculation 3A lending credence to the remark that such a structure is a result of discontinuous unloading. For late times (Fig. 5.16), Case 3A yields higher peak amplitudes than Case 3. This is to be expected as the unloading is much more rapid for Case 3.

There is some evidence that the yield stress of rocks is determined by the "effective stress law." This law states that the yield stress of a porous solid depends uniquely on the effective stress, which is defined as the difference between the total normal stress active on any plane and the pore pressure. In the present case, the yield stress can then be written as:

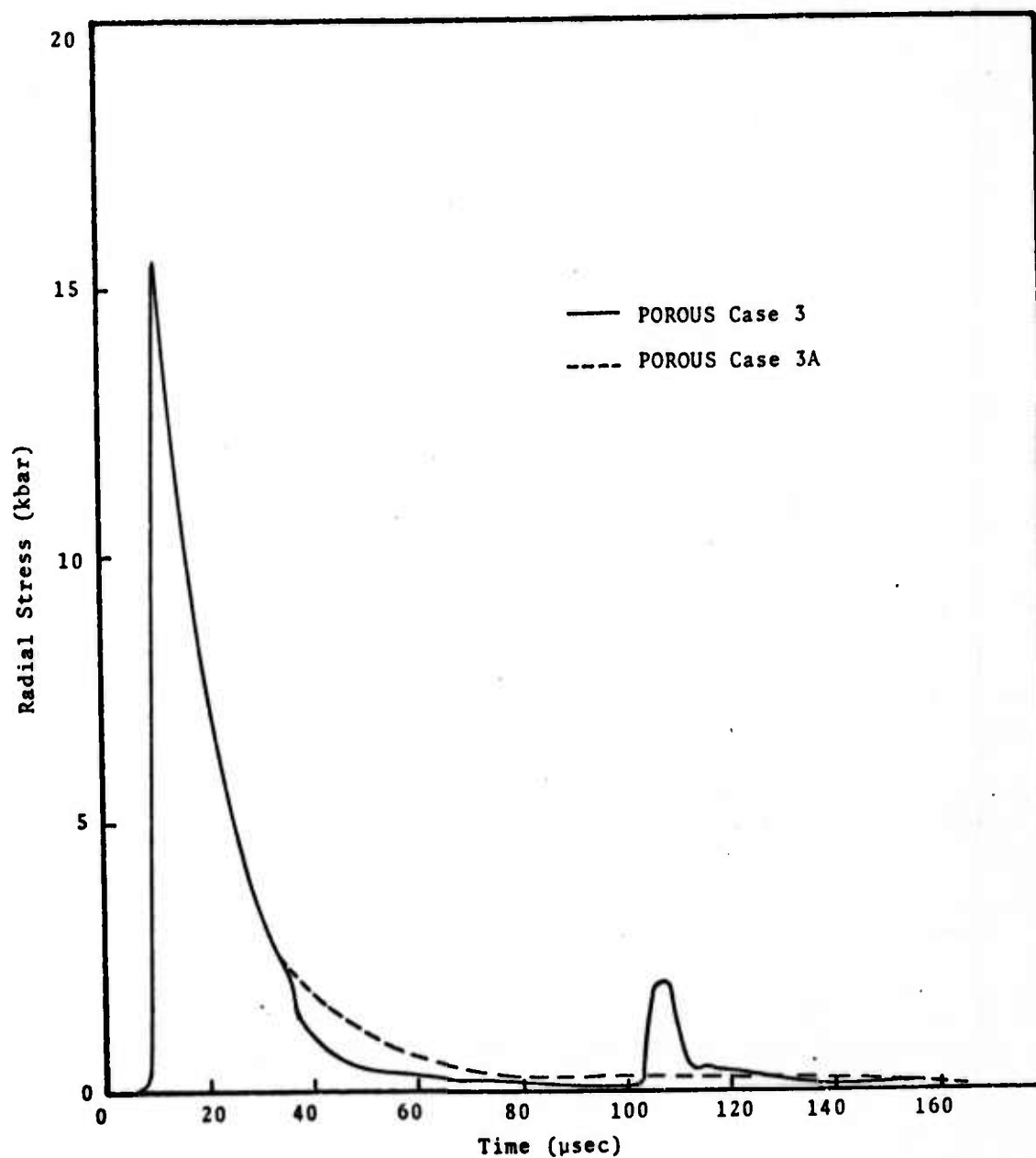


Fig. 5.14--Comparison of composite radial stress histories at 7.5 cm (POROUS Cases 3 and 3A).

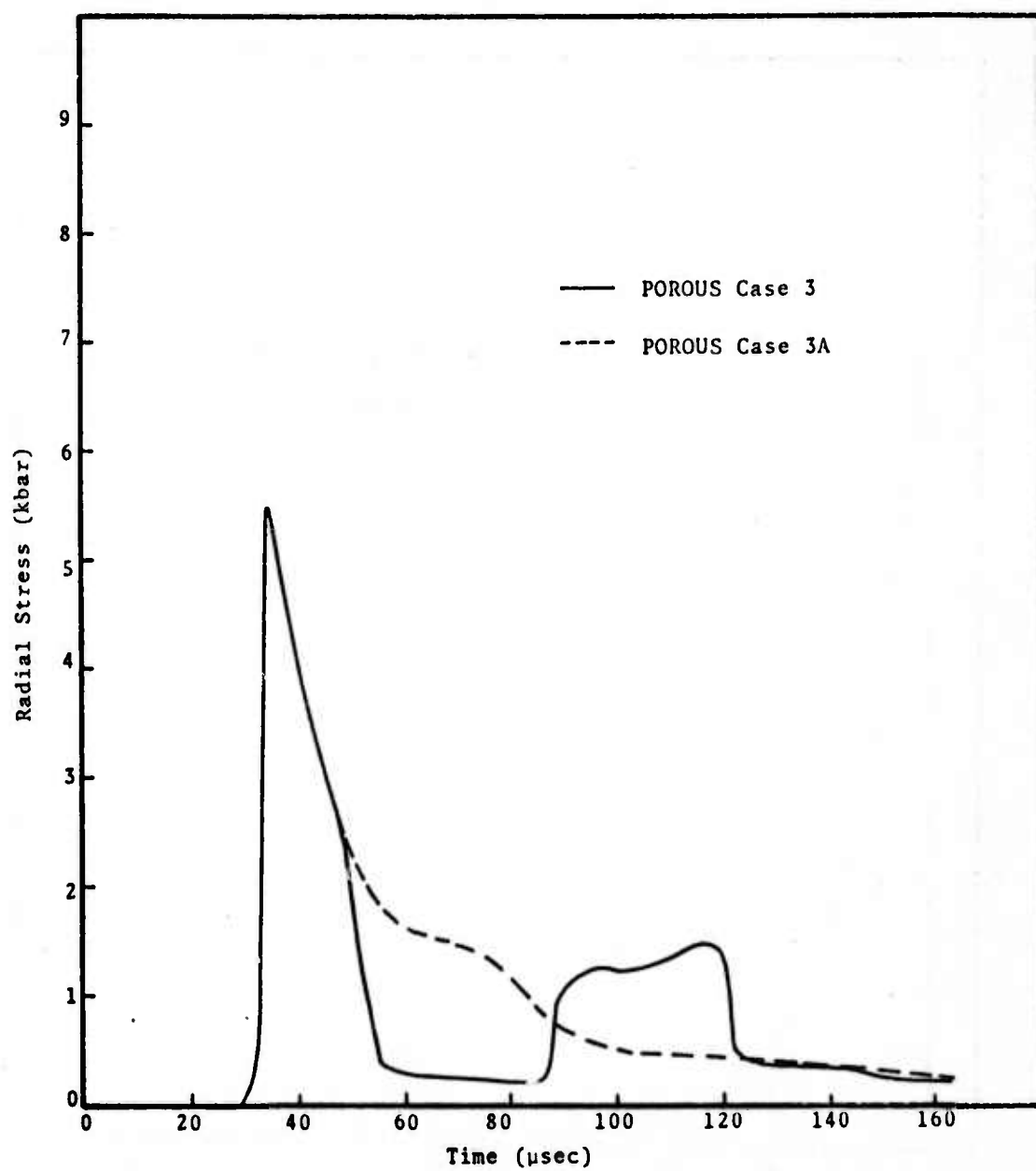


Fig. 5.15--Comparison of composite radial stress histories at 12.5 cm (POROUS Cases 3 and 3A).

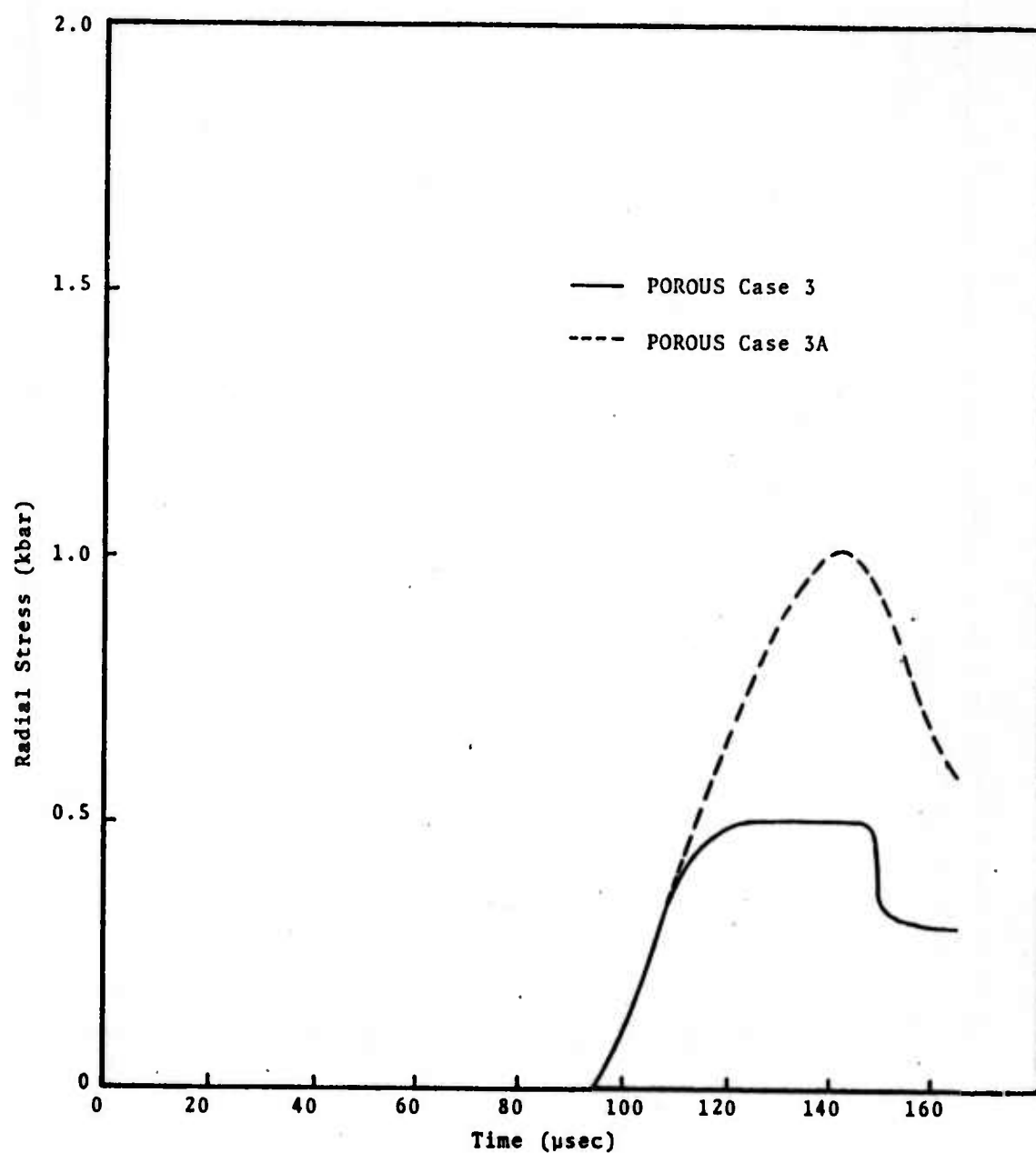


Fig. 5.16--Comparison of composite radial stress histories at 25 cm (POROUS Cases 3 and 3A).

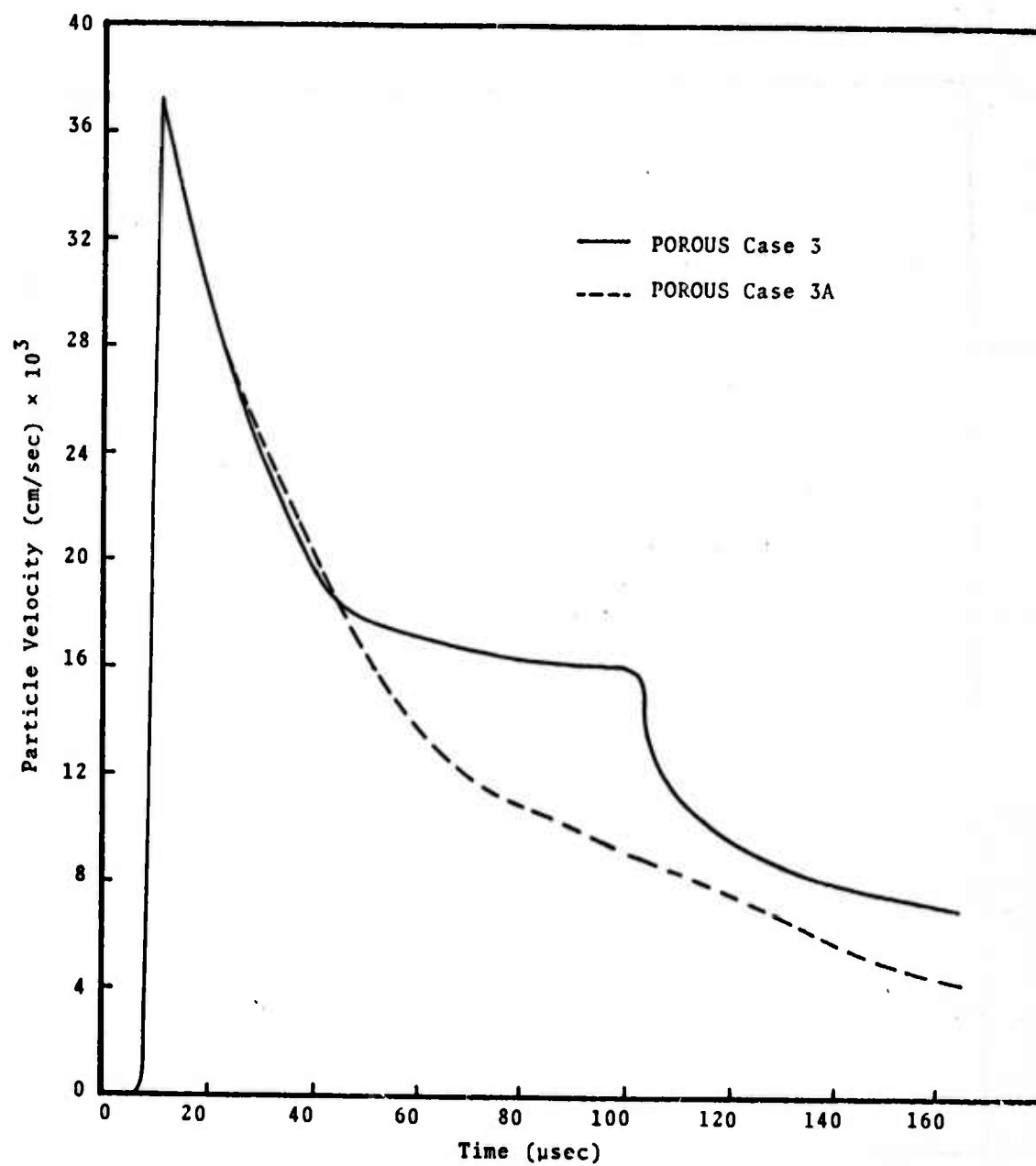


Fig. 5.17--Comparison of composite particle velocity histories at 7.5 cm (POROUS Cases 3 and 3A).

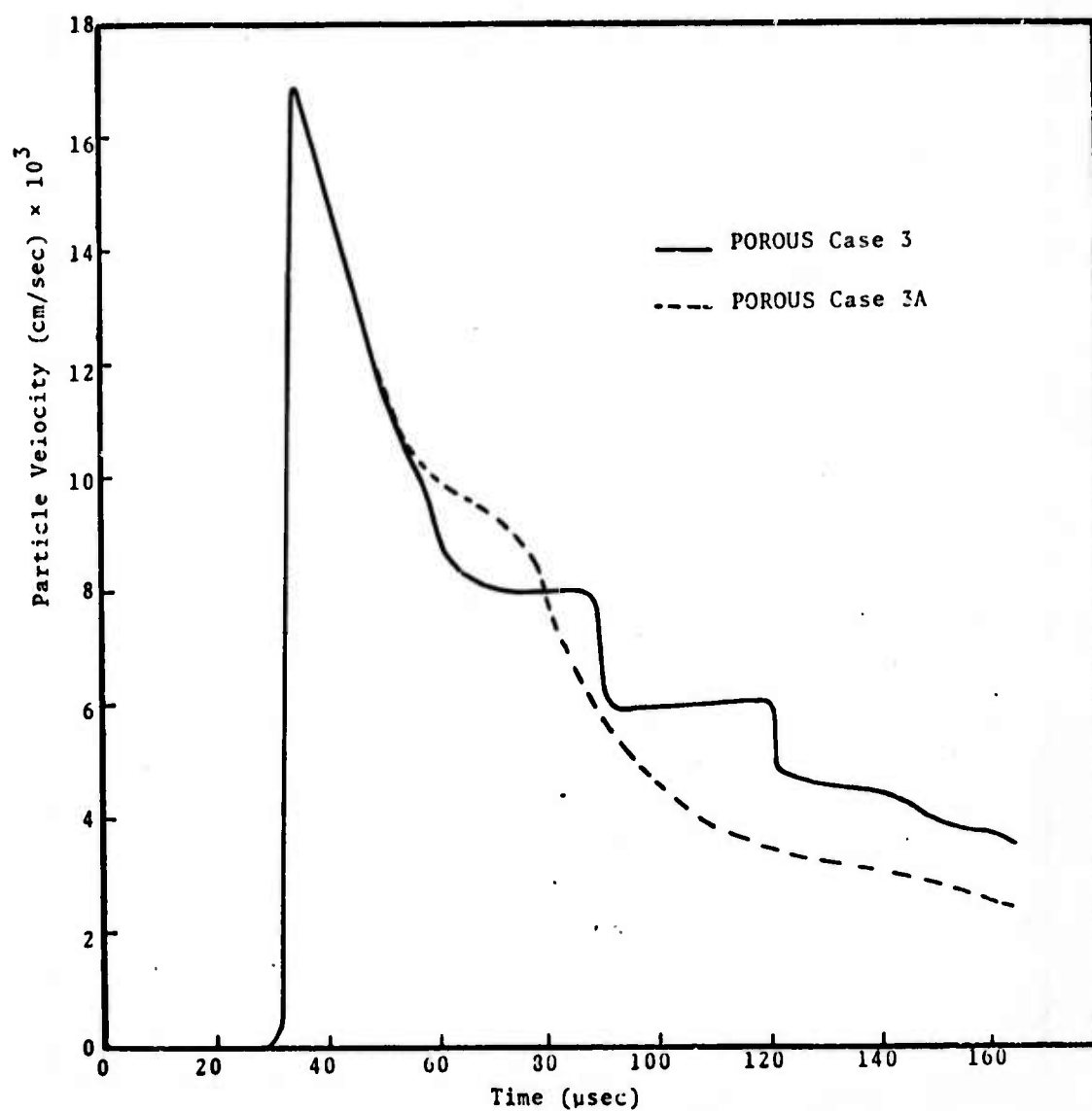


Fig. 5.18--Comparison of composite particle velocity histories at 12.5 cm (POROUS Cases 3 and 3A).

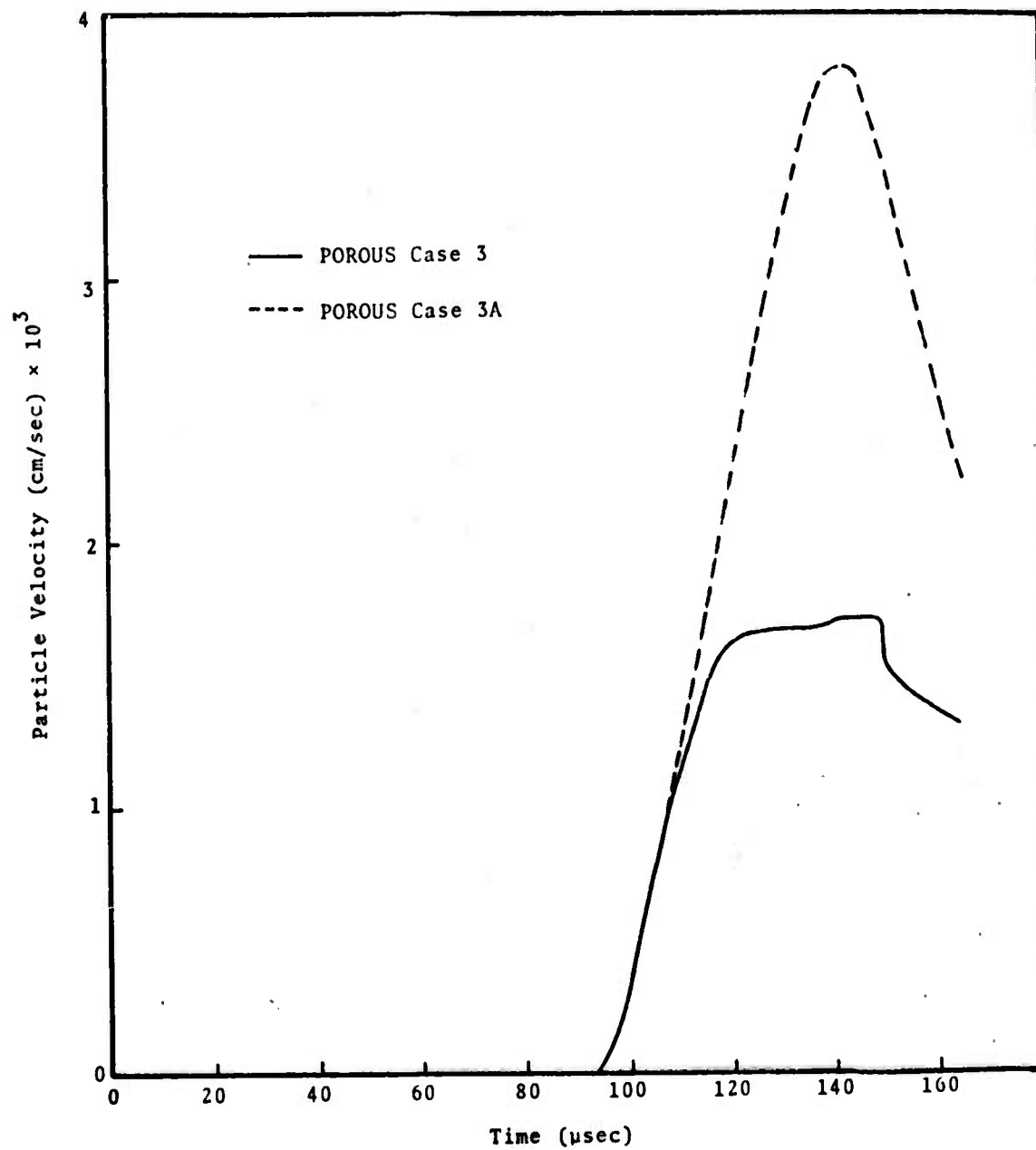


Fig. 5.19--Comparison of composite particle velocity histories at 25 cm (POROUS Cases 3 and 3A).

$$Y(\text{yield stress}) = Y_0 \frac{P_{\Delta}}{P_0} (2 - P_{\Delta}/P_0)$$

$$\text{for } P_{\Delta} = P_c - P_p \leq P_0 = 0.6 \text{ kbar}$$

$$Y_0 = 0.623 \text{ kbar.}$$

An additional calculation (Case 4) was run using this new definition of yield stress. The results of this case, however, differ but little from Case 3. This is largely due to the relatively low yield strength for the material. This effect can be expected to be more significant for stronger materials.

To further verify the TINC formulation, the SKIPPER HE calculation of May 8 (Section II) was repeated with the POROUS code. Material parameters for this calculation are listed below:

$$\mu/k \text{ (viscosity of water/permeability)} = 10^{10}/\text{sec}$$

$$\mu_p \text{ (shear modulus)} = 15.0 \text{ kbar}$$

$$Y \text{ (yield stress)} = Y_0 \frac{P_{\Delta}}{P_0} (2 - \frac{P_{\Delta}}{P_0})$$

$$\text{for } P_{\Delta} = P_c - P_p \leq P_0 = 0.6 \text{ kbar}$$

$$= Y_0 \text{ for } P_{\Delta} \geq P_0$$

$$Y_0 = 0.5 \text{ kbar}$$

Results of these calculations are shown in Figs. 5.20 through 5.28. Composite radial stress histories and particle velocity histories (as given by the POROUS and SKIPPER codes) are depicted in Figs. 5.20 through 5.25. Tuff and water radial stress histories are shown in Figs. 5.26 through 5.28.

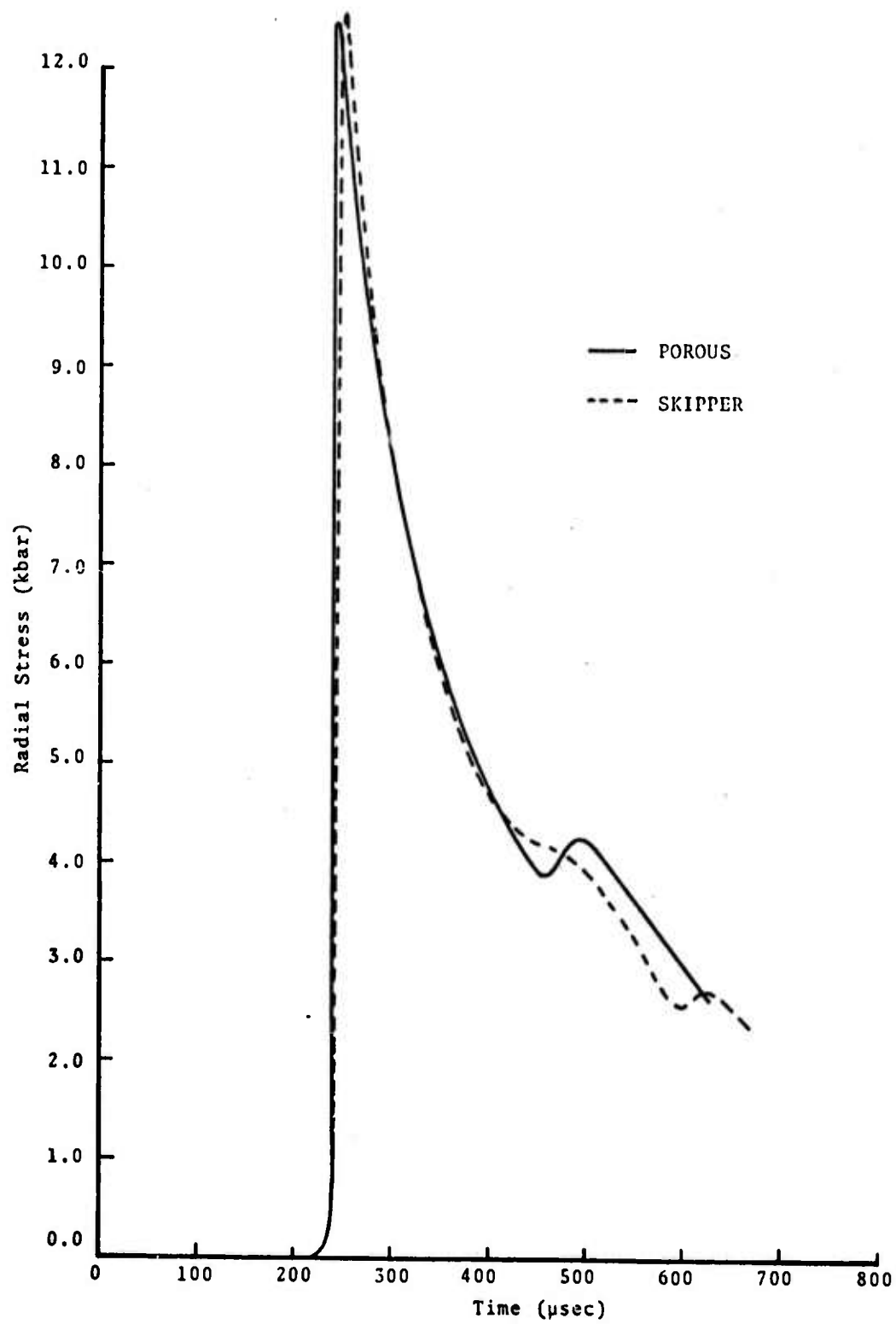


Fig. 5.20--Comparison of composite radial stress histories at 99.7 cm.

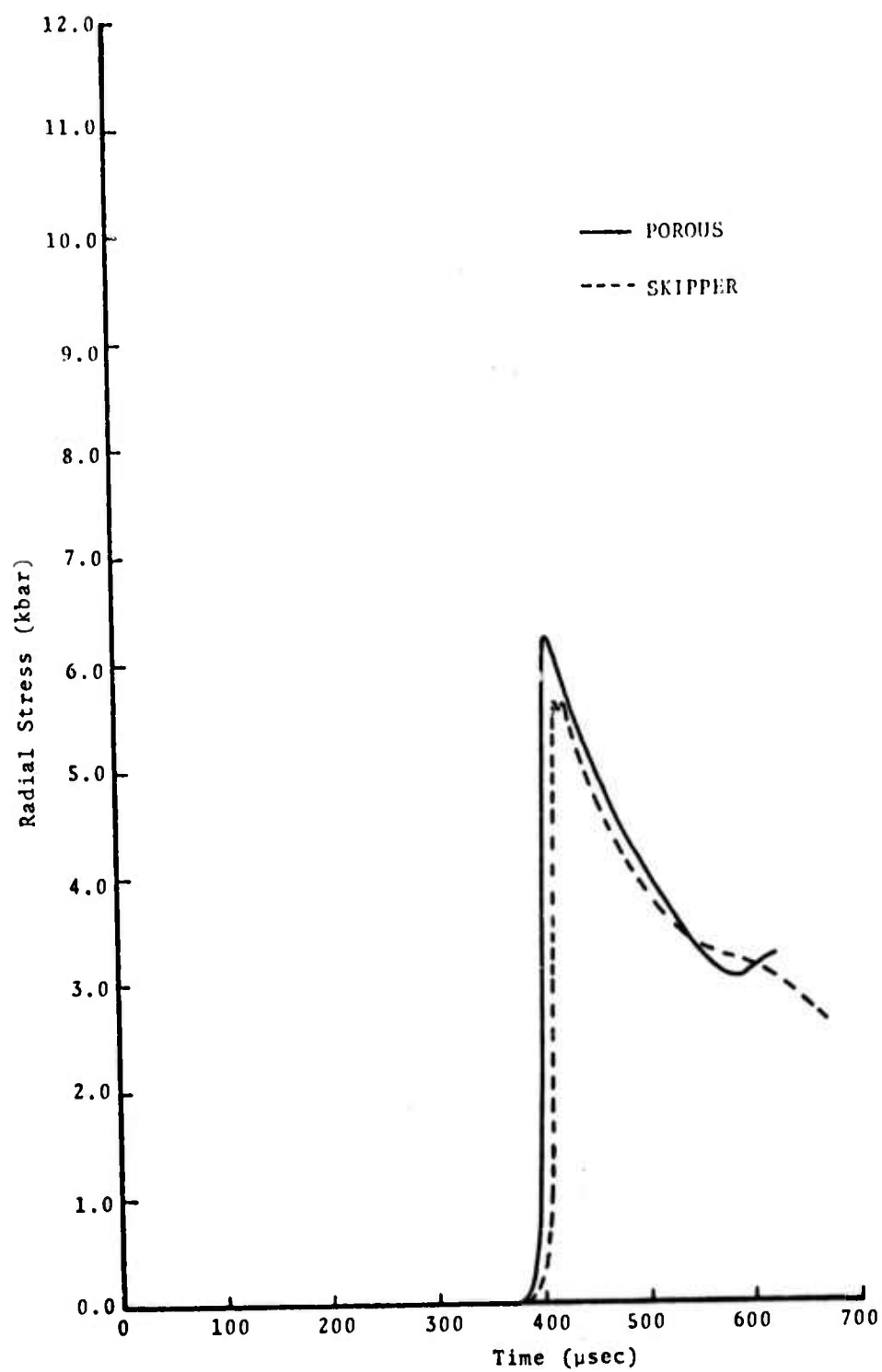


Fig. 5.21--Comparison of composite radial stress histories at 133.2 cm.

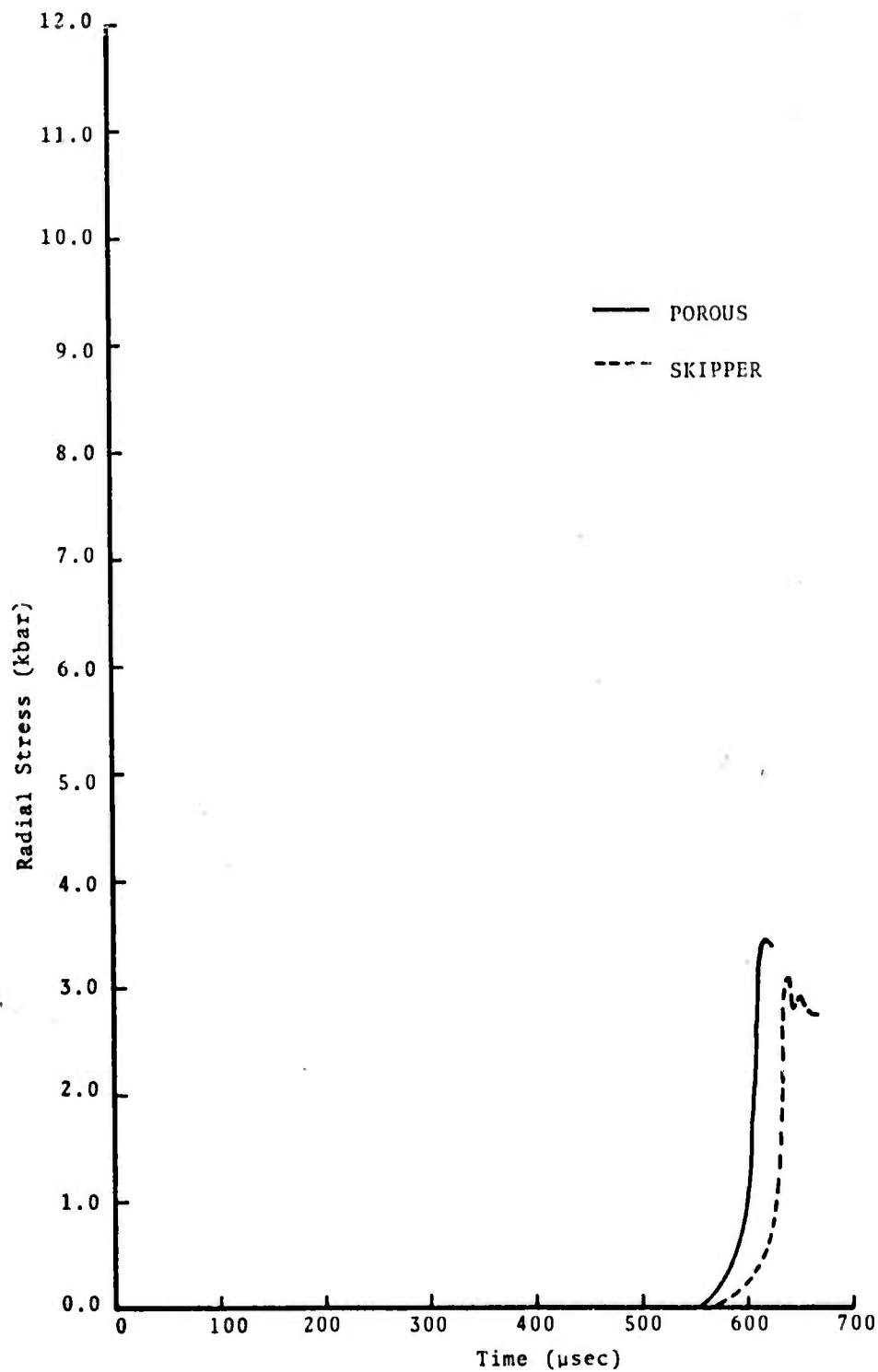


Fig. 5.22--Comparison of composite radial stress histories at 167.9 cm.

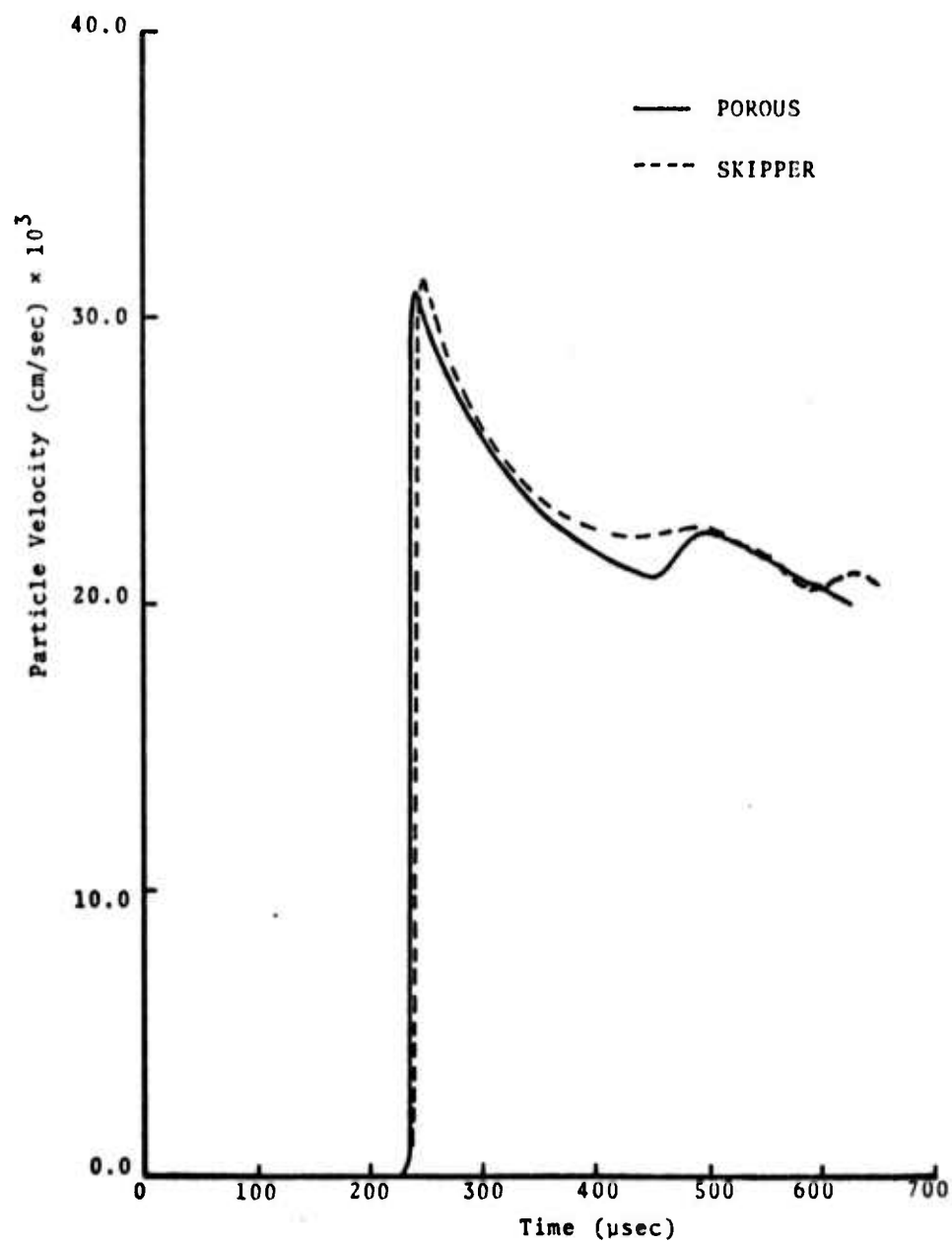


Fig. 5.23--Comparison of composite particle velocities at 99.7 cm.

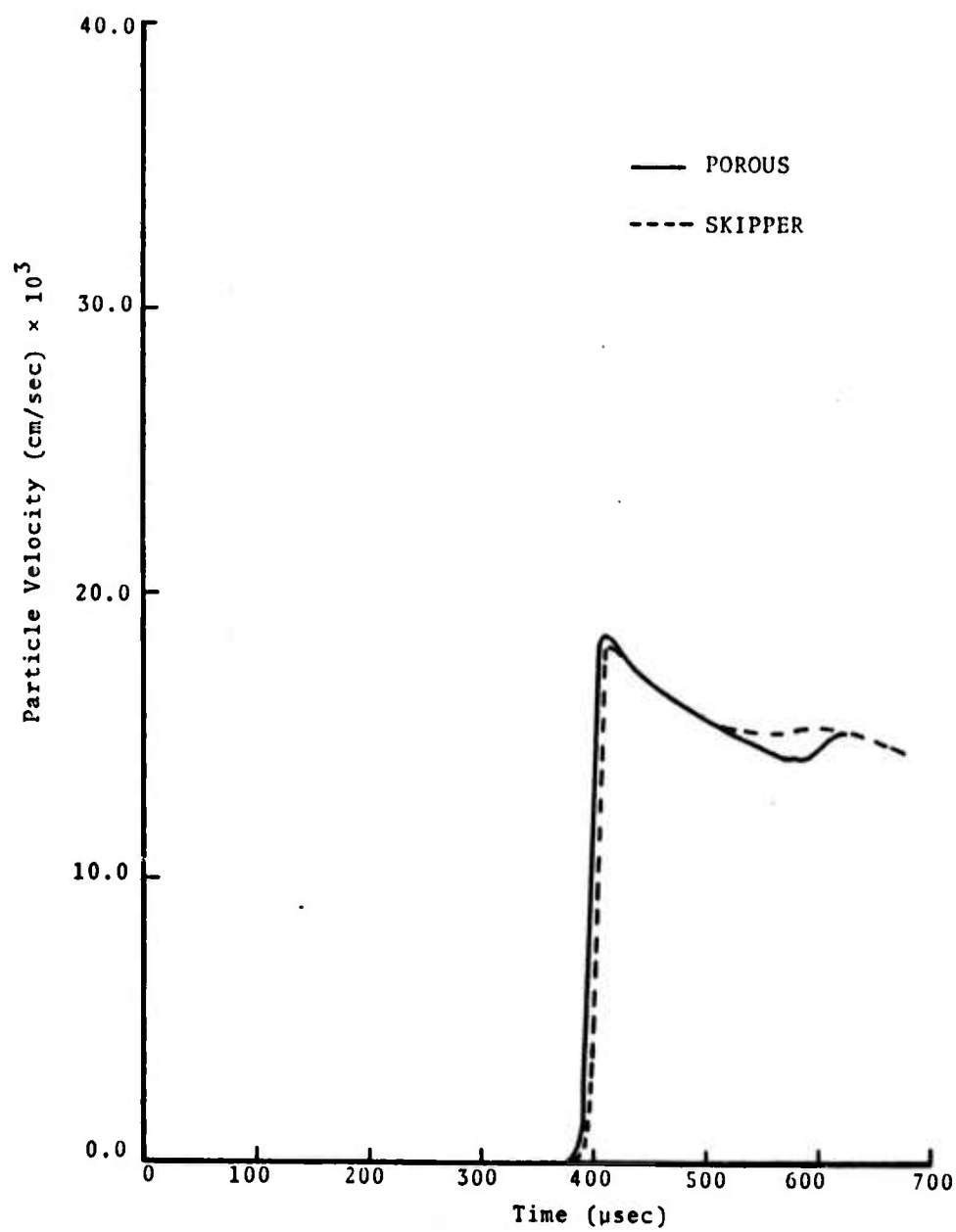


Fig. 5.24--Comparison of composite particle velocities at 133.2 cm.

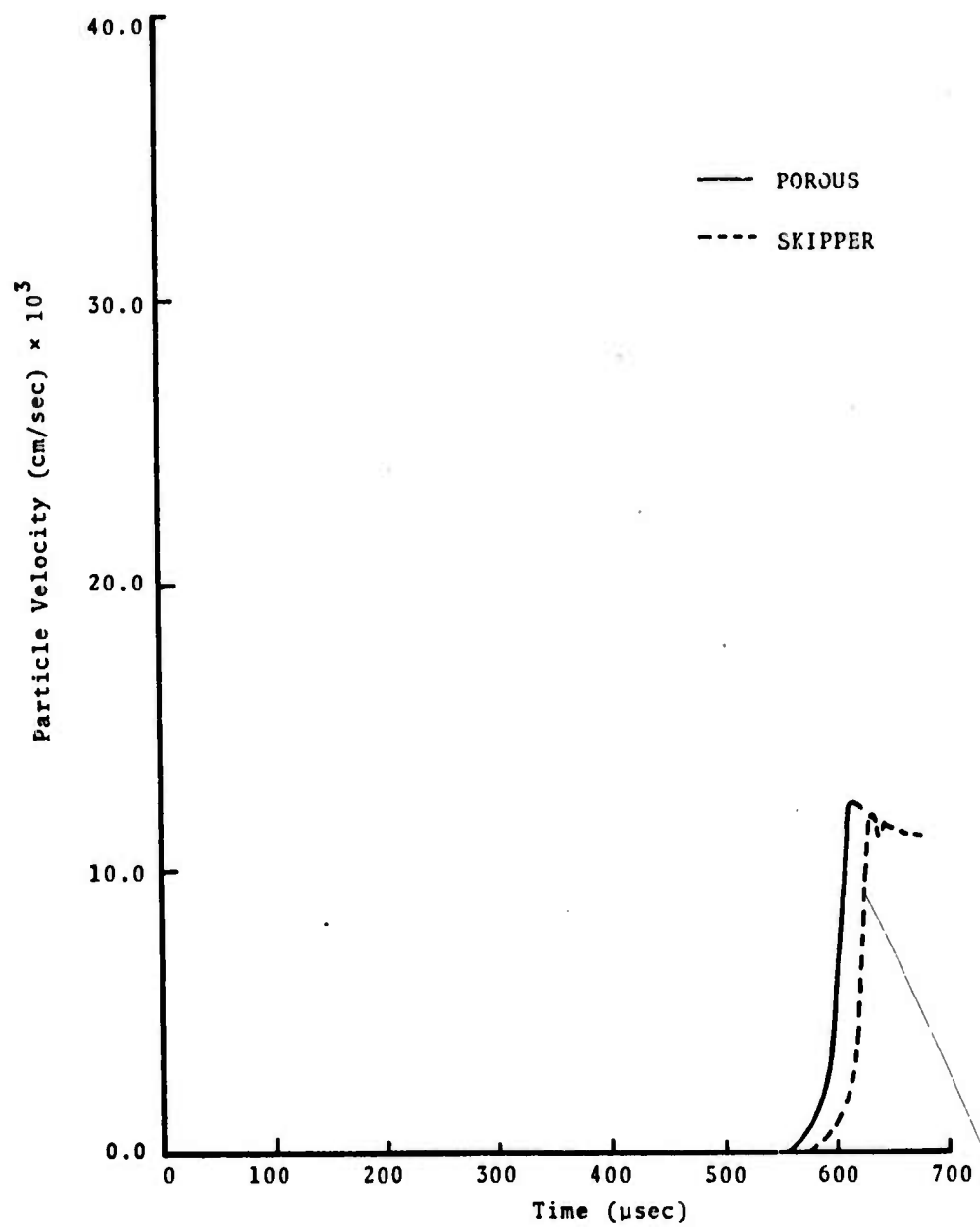


Fig. 5.25--Comparison of composite particle velocities at 167.9 cm.

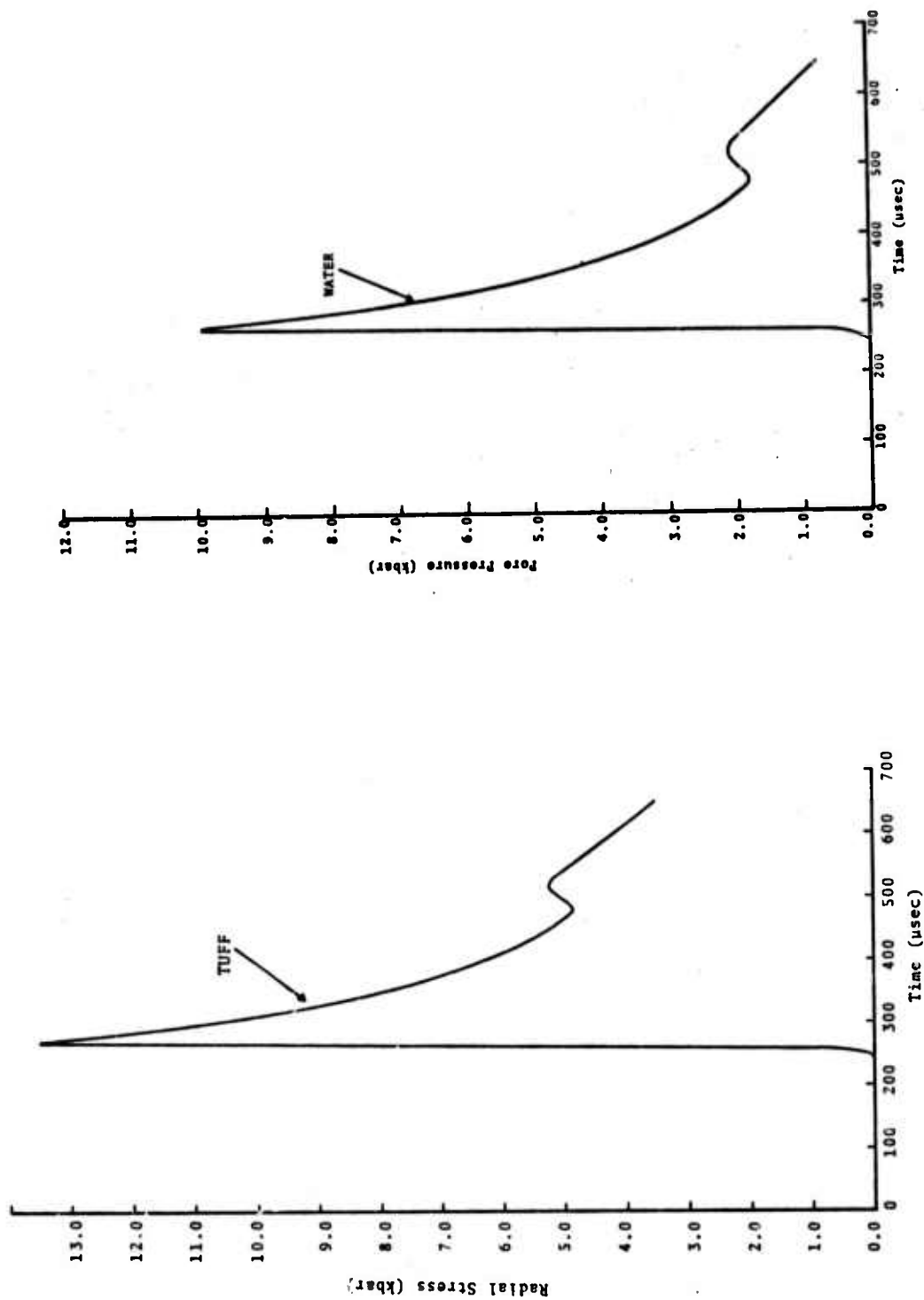


Fig. 5.26--Radial stress in tuff component and pore water pressure at 99.7 cm.

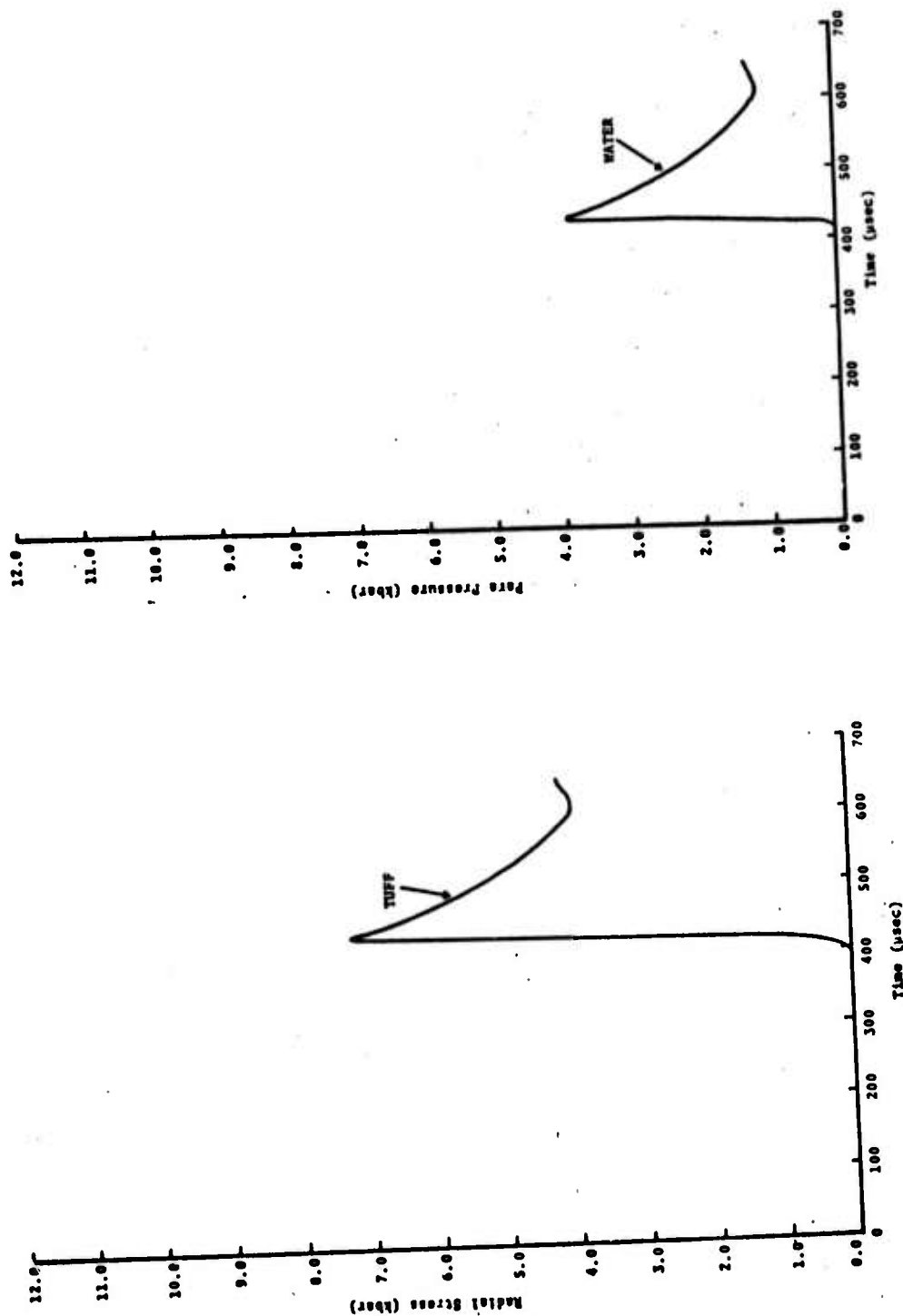


Fig. 5.27--Radial stress in tuff component and pore water pressure at 133.2 cm.

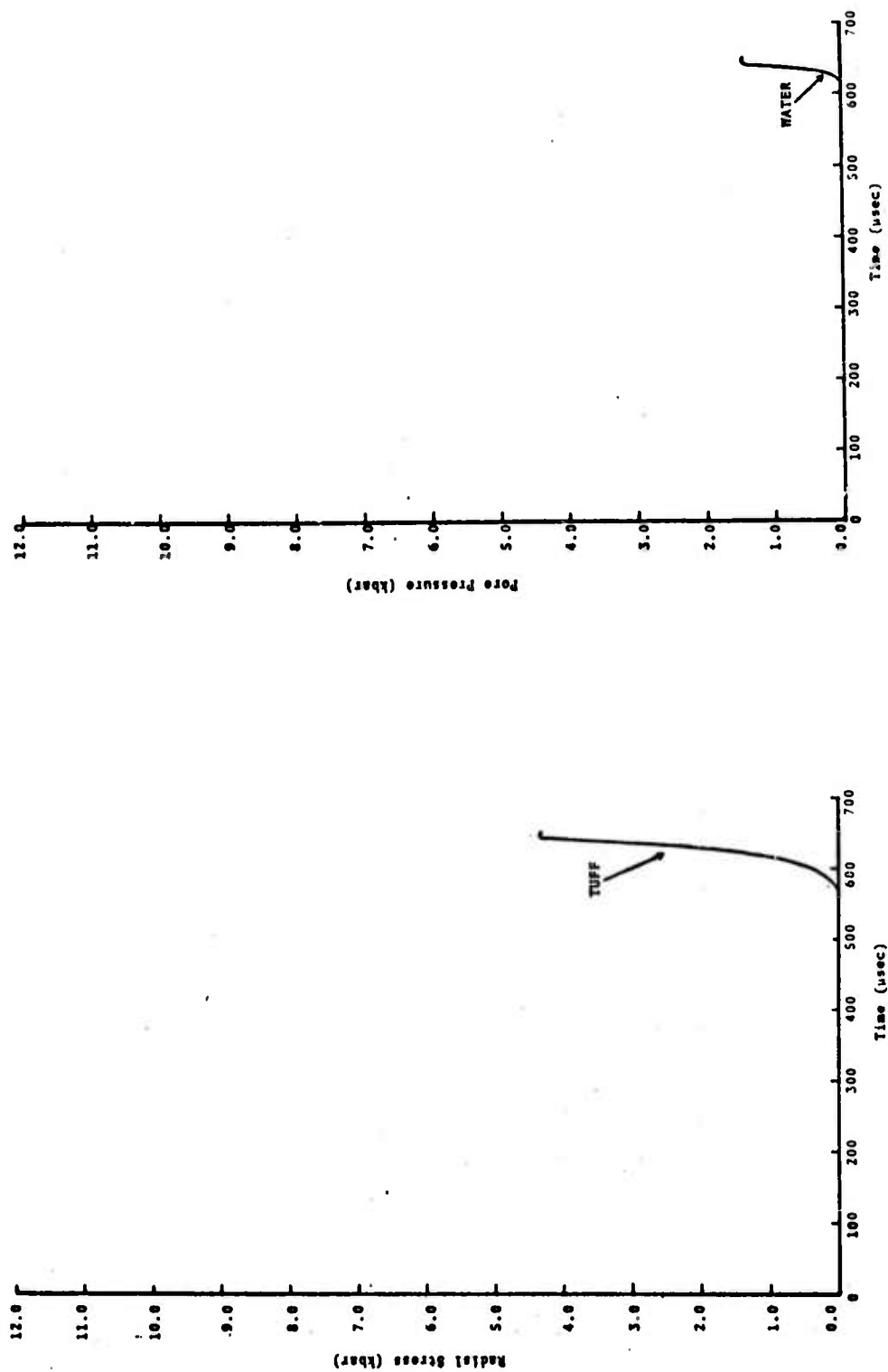


Fig. 5.28--Radial stress in tuff component and pore water pressure at 167.9 cm.

The two (POROUS and SKIPPER) calculations agree reasonably well at high pressures (Figs. 5.20, 5.23). At low pressures, however, the POROUS code predicts somewhat higher amplitudes and earlier times of arrival (Figs. 5.21, 5.22, 5.24 and 5.25) than those given by the SKIPPER calculation. It is to be noted that these conclusions for the HE case are consistent with our earlier remarks on the exponentially decaying pulse case. For the HE case, it was not possible to carry out the POROUS calculation as far as the SKIPPER calculation due to the absence of rezoning capability in the present version of the POROUS code. If detailed comparisons between the two codes are desired, it would be necessary to provide the rezone capability in POROUS.

VI. CONTINUUM MODEL OF REGULARLY JOINTED MEDIA

For theoretical calculations to match the field data it is necessary (see Section 4.1) to significantly reduce the strength from that measured on intact laboratory specimens. This size effect, due to planes of weakness in the rock mass, cannot presently be predicted without dynamic field test results. In this section, results are presented from a study which has the objective of deriving a rational basis for scaling relations between laboratory to field data by considering the medium to contain regularly spaced joints or faults. Sufficient progress was made in this preliminary study to demonstrate that a continuum model with substructure to account for planes of weakness can be developed.

Sections 6.1, 6.2 and 6.3 review what is known about planes of weakness in rock masses and in laboratory tests of rock slippage along joints. The mathematical framework for describing gross behavior of rock masses is presented in Section 6.4. Each block is considered to deform elastically but relative slippage between blocks is permitted. Incorporation of this description into a continuum model is given in Section 6.5. Finally, Section 6.6 describes the detailed formulations for the case of biaxial loading. The model is analogous to an elastic-plastic model where the shear strength is determined by the joint spacing and the frictional properties of the fault planes. Block interlock increases resistance to slippage and this effect is analogous to work hardening in plasticity theory. As a consequence of this analogy it appears that this model for regularly jointed rock media could be incorporated into a continuum mechanics code such as CRAM once sufficient data to specify the substructure are available.

6.1 ROCK MASSES IN SITU

Large rock masses in the Earth's crust are commonly broken into block structures by fracture surfaces. These are classified into two types. The most common are JOINTS which are fracture surfaces at which little or no relative displacement has taken place, and usually occur in sets of regularly spaced, more-or-less parallel planes, with a variety of orientations. Major sets can extend from feet to miles. Some cross-joints are curved and irregularly spaced. Another feature, not common in granite, is columnar jointing with a hexagonal section of side of order one foot, with the column normal to the surface, supposedly due to tensile stress set up by thermal contraction during cooling.

FAULTS are fracture surfaces at which significant relative displacement has taken place, and again are commonly planar and in parallel sets. Joints occur more frequently near faults. Together these sets of fracture planes, or planes of weakness, create a block structure in the rock masses, and the fracture planes are possible slide planes under appropriate loading. A more complete description is given by Jaeger and Cook.^[44]

Spacing between fractures ranges up to several feet with "bad rock" fractures inches apart.^[45] Fractures are loose and frequent near the surface, but with increasing depth tighten under the increasing confining pressure and become wider apart.^[46] Regular fractures occur down to thousands of feet.^[47] In a given locality the simple assumption of regular spacing between fractures of each set, perhaps differing between sets, should be an adequate first

approximation in a theory of gross response. On a large scale application, variation of spacing with change of locality may be required.

It is recognized that fractures in the rock mass have a significant effect on the gross response, see [44, 46, 48 49, 50, 51] for example, particularly at stress levels below 5 kbar. While the blocks may remain effectively elastic (with strain infinitesimal) prior to failure, either by fracture of intact material or sliding on the pre-fracture planes, the subsequent behavior at both these types of fracture plane is irreversible and greatly different in nature. One approach, necessarily using numerical techniques, is to model each elastic block together with postulated constitutive conditions at each fracture plane and determine detailed stress and displacement fields; see for example [50, 51, 52, 53]. In practice, because of the lack of detailed data, very idealized structures must be assumed. This suggests that it may be profitable to explore theories of gross response which average out individual fracture plane effects, in a sense to be determined. Such a theory would be applicable only on length scales (e.g., length of loaded regions or wavelength) much greater than the separation distance between fractures.

Fractures may be open or filled with various minerals [44, 45], such as calcite, dolomite, quartz, clay. Calcite filling, with approximately the same strength as rock, serves as a "cement" and provides a tensile resistance to opening of the fracture^[49]. Fault gouge (sliding debris) is usually rich in clay, with complex compaction properties and possibly significant time dependent response, and is observed to enhance stable sliding.^[54] Finely powdered gouge generated by sliding of various rock specimens has also been observed to cause time dependent friction which, in contrast, gives

rise to stick-slip.[55] Thus, the presence of fault gouge after initial sliding can result in complex and widely varying response.

Unfilled fractures result in weakening of adjacent rock by chemical and mechanical action[49], but more commonly, and below moderate depths, such fractures are saturated with water (and occasionally oil) under (pore) pressure [Refs. 44, 47, 54, 56, 57, 58]. Again chemical action weakens adjacent rock, but in addition there is a significant influence on the strength relations, attributed to buoyancy and commonly described by an effective stress law, see Ref. [58] for example. While this classical law has some empirical foundation, explanatory arguments and analysis [Ref. 58] are spurious, this will be discussed in more detail subsequently. The essential consequence of the pore pressure is a decrease in the effective normal stress across the solid contact surface accompanied by a decrease in the shear resistance to fracture or sliding. Above a critical rate of crack opening (dilatancy), approximately 10^{-7} /sec for igneous rocks (crystalline assemblage)[56], fluid flow is insufficient to fill new voids so that the pore pressure drops and effective stress, and hence strength, in the rock increases, described as dilatancy hardening. Increase of void space even with saturation decreases the pore pressure and exhibits the same effect.[59]

Initial stress in virgin rock mass is commonly assumed to be lithostatic, that is, an isotropic ("hydrostatic") pressure equal to the overburden stress due to the weight of overlying rock--Hein's Rule [44, Chapter 14]. However, while horizontal stresses are frequently of the same magnitude as the vertical stress, in many situations they are observed to be significantly higher. One explanation[56] is that specimens tested were originally buried considerably deeper, and the higher

horizontal stress is a locked-in residual stress. Since the time scale of the erosion and rock rise in the case described is 10^8 years, and residual stress has been retained, it also follows that the rock has a solid behavior over these time periods and does not exhibit appreciable atomic diffusion and liquid behavior. Vertical stress higher than the overburden stress is also found. A lithostatic stress in rock of density 156 lbs/cu ft increases at a rate of 220 bars (3200 psi)/1000 yds. There will also be initial shear stress much more difficult to estimate.

Pore pressure in water saturated porous rock normally ranged from $(0.4 \rightarrow 0.8) \times$ vertical stress^[56] in the undisturbed rock mass, and will be further changed by subsequent loading.* Temperature gradients with depth range from 10 - 90° C/1000 yards^[56] with a more usual range 40 - 70° C/1000 yards, the higher values representing active volcanic regions. Thus over the temperature range down to 1 mile, the variation of rock properties with temperature will not be significant, excluding of course the effects of further appreciable thermal loading.

If the individual anisotropic crystals within a rock block are randomly oriented then the block will be grossly isotropic, but when there is a preferred crystal direction, as in Yule marble for example,^[44] then the block is anisotropic. A simplifying isotropy assumption for individual intact blocks is unlikely to produce greater errors than other approximations and neglect of effects in the very complex description of rock behavior. Composition is relatively homogeneous in some limestones, but very heterogeneous in granite.^[44] However, on length scales greater than a foot, and so large compared with crystal size of order an inch and less, average

*Abnormally high fluid pressures sometimes occur in high porosity sedimentary deposits in which the confined water has been trapped for millions of years.

properties are reasonably homogeneous and continuous apart from the fracture planes.

It is recognized that overall strength decreases with size of specimen tested, usually attributed to the increasing number of flaws, but also related to a possibility that fracture will be governed by a critical stress being reached over a given volume of material which in turn can involve stress gradients [44, Chapter 7]. A simple statistical theory due to Weibull which replaces critical fracture stress by a probability distribution is also described, [44, Chapter 7], and illustrated, but without confirmed conclusions.

6.2 FRACTURE AND FAILURE CRITERIA

The minimal ingredients of a constitutive description of rock masses are the properties of the intact material, elastic or inelastic, a criterion for initiation of fracture in intact material, and conditions for sliding along newly formed and pre-existing fractures. In addition, the presence of fluid within pores or fracture zones has significant effects which cannot be neglected.

Tri-axial compression of a cylindrical rock specimen with dimensions of the order of an inch is the common laboratory test for mechanical properties and fracture criterion of intact material and of specimens with single preexisting fracture planes. Apparatus constraints limit the sliding displacement that can take place, and for larger displacements relative sliding between rectangular and triangular blocks is used. Effects of multi (parallel) fracture planes, at different orientation, are studied by "block models" formed from materials with properties qualitatively similar to rock but of lower strength for practical purposes. Fracture and failure (sliding) criteria are commonly deduced as (idealized) relations between the shear and normal stresses across the fracture plane, and presented in terms of a Mohr stress representation, see for example [44, Chapter 2] and [60, Chapter 1].

Following customary practice in soil/rock mechanics where mean stress is typically compressive, let the stress tensor $\underline{\sigma}$ be related to the traction \underline{t} on a surface with outward normal \underline{n} by

$$\underline{t} = - \underline{\sigma} \underline{n} . \quad (6.1)$$

Then for rocks at depth the principal stresses $\sigma_1, \sigma_2, \sigma_3$ are typically positive (compressive).^{*} For simplicity choose

^{*} Only here in Section VI is compression considered positive.

cartesian axes $Ox_1 x_2 x_3$ along the principal stress axes such that

$$\sigma_1 \geq \sigma_2 \geq \sigma_3. \quad (6.2)$$

Let σ_n, τ_n be the normal compressive and tangential stress acting on a plane with unit normal

$$\underline{n} = (n_1, n_2, n_3). \quad (6.3)$$

It can be shown^[60] that the stress state (σ_n, τ_n) for any \underline{n} lies in one of the two curvilinear triangles bounded by the three circles in the Mohr diagram, Fig. 6.1. The circles have centers S_1, S_2, S_3 on the σ_n axis with abscissae

$$s_1 = \frac{1}{2}(\sigma_2 + \sigma_3), s_2 = \frac{1}{2}(\sigma_3 + \sigma_1), s_3 = \frac{1}{2}(\sigma_1 + \sigma_2), \quad (6.4)$$

and, respectively, radii

$$t_1 = \frac{1}{2}(\sigma_2 - \sigma_3), t_2 = \frac{1}{2}(\sigma_1 - \sigma_3), t_3 = \frac{1}{2}(\sigma_1 - \sigma_2). \quad (6.5)$$

On the outer circle, for example, provided that there are strict inequalities in Eq. (6.2), $n_2 = 0$ and so

$$n_1 = \cos \lambda, n_3 = \sin \lambda, \quad (6.6)$$

$$\sigma_n = s_2 + t_2 \cos 2\lambda, \tau_n = \pm t_2 \sin 2\lambda, \quad (6.7)$$

defining the stress points Q, Q' in Fig. 6.1. Similarly, $n_1 = 0$ on the circle with center S_1 and $n_3 = 0$ on the circle with center S_3 , and analogous relations to Eqs. (6.6) and (6.7) hold.

In the usual triaxial test $\sigma_2 = \sigma_3$ (confining pressure same in all lateral directions) and sometimes $\sigma_1 = \sigma_2$ when the axial stress is less than the confining pressure. For the former case $t_1 = 0, t_2 = t_3$ and P_2

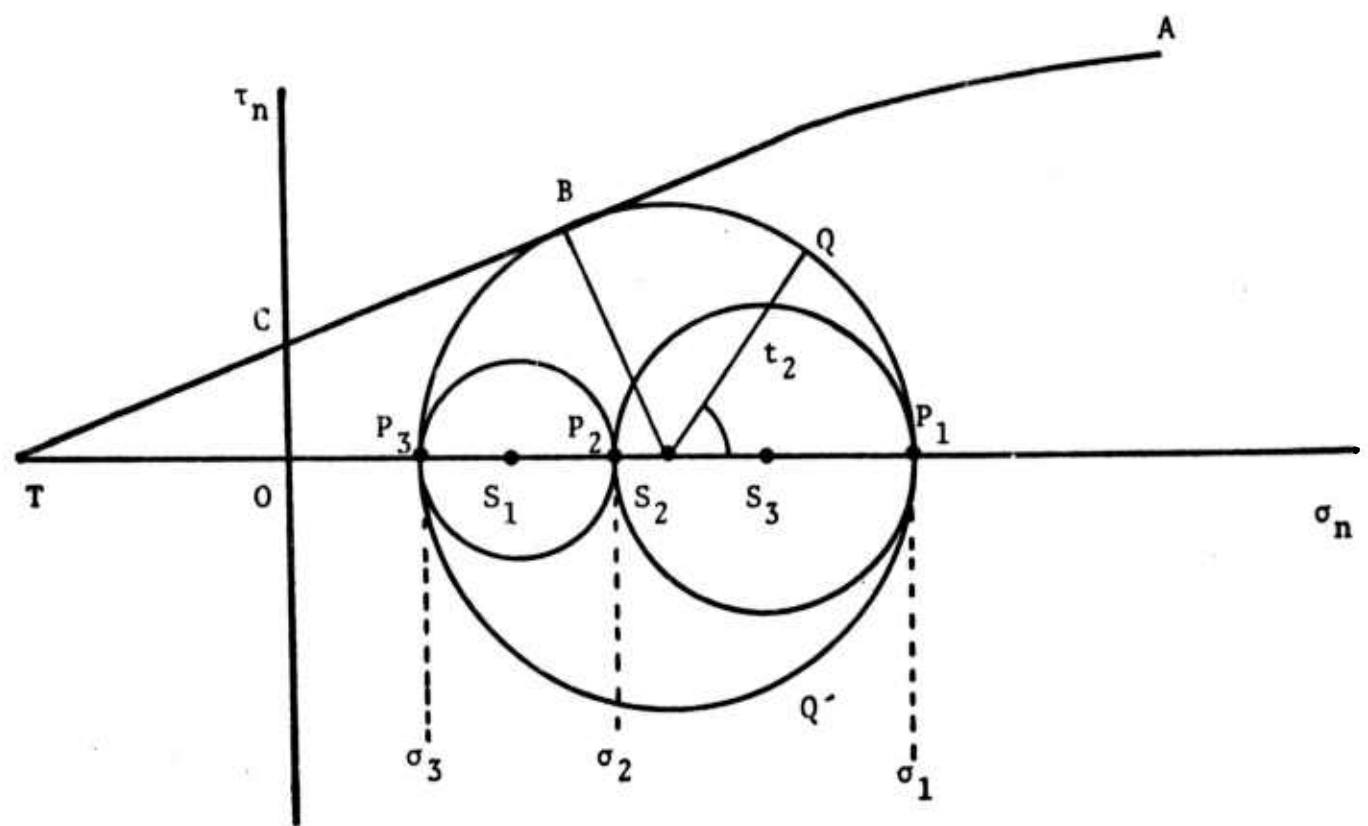


Fig. 6.1--Mohr stress representation and fracture criterion.

lies on P_1 , so that all stress states lie on the outer circle. Again Eqs. (6.6), (6.7) hold for \underline{n} lying in a plane Ox_1x_3' with Ox_3' any axis in the Ox_2x_3 plane and $n_3' = \sin \lambda$.

Adding an isotropic pressure p to the stress state adds p to s_1, s_2, s_3 and leaves t_1, t_2, t_3 unaltered, so that the circles are simply translated a distance p along the $O\sigma_n$ axis, Fig. 6.1.

Empirical data from fracture tests is commonly used to determine a relation between the values of τ_n and σ_n when fracture is initiated, that is, to determine a Mohr criterion, [44, Chapter 4],

$$|\tau_n| = f(\sigma_n). \quad (6.8)$$

For smaller values of $|\tau_n|$ at the given value of σ_n fracture does not occur. Sets of values $(\sigma_1, \sigma_2, \sigma_3)$ at which fracture is initiated determine a sequence of (outer) Mohr circles tangent to the symmetric curves represented by Eq. (6.8), which are therefore Mohr envelopes to the circles. The curves cannot intersect the circles, otherwise there are stress states (σ_n, τ_n) for which $|\tau_n|$ exceeds the critical value given by Eq. (6.8). The curve TCBA in Fig. 6.1 typifies a Mohr envelope tangent to the Mohr circle shown at B. It is clear that this criterion is independent of the intermediate principal stress σ_2 which does not influence the outer circle. The orientation of the fracture plane is given by the angle β where $\underline{n} = (\cos\beta, 0, \sin\beta)$ and 2β is the angle P_1S_2B determined by the value of σ_1, σ_2 and Eq. (6.8). A conjugate fracture plane is given by the corresponding negative values for β . For $\sigma_2 = \sigma_3$ the interpretation $n_3' = \sin\beta$ applies. The sign of τ_n determines the direction of subsequent relative sliding across the fracture plane.

The intercept OT represents the fracture strength in isotropic tension and OC represents the strength in pure shear. The strength in uniaxial compression and uniaxial tension are given by the diameters of the circles tangent to the envelope and tangent to the $O\tau_n$ axis on the positive and negative σ_n sides respectively.

A special case of the Mohr criterion is the linear Coulomb-Navier law

$$|\tau_n| = \tau_0 + \mu\sigma_n . \quad (6.9)$$

The strength at zero normal stress is $|\tau| = \tau_0$, called the cohesion, represented by the intercept OC in Fig. 6.1. The proportionality constant μ , represented by the slope of the envelope, is called the friction coefficient--a misnomer since it is a property of intact material. An approximate linear fit to data is often deduced for moderate values of σ_n , with the envelope TCBA becoming concave to the σ_n axis for increasing σ_n , as illustrated in Fig. 6.1.

A simpler form of Eq. (6.9) is the Tresca condition associated with plastic yield in metals, namely

$$\tau_n = \tau_0 \quad (6.10)$$

but this neglects the significant dependence on σ_n in practice. An alternative simple law is the requirement that the minimum principle stress is negative and equal in magnitude to the tensile strength, again not in general agreement with the data. A mathematically smooth law can be obtained by postulating an analytic condition on the stress invariants, which involves all principal stresses, but the Mohr and Coulomb-Navier criteria exhibit most over-all agreement with data.

When there is an existing fracture plane (plane of weakness) then failure (used here to denote sliding along this plane) may or may not occur before fracture along intact planes, depending on the orientation of the existing fracture plane with respect to the principal stress axes. It is commonly deduced from empirical data that the criterion for initiation of sliding has the linear Coulomb-Navier form of Eq. (6.9) with different (lower) values of cohesion and friction than the fracture law for low σ_n :

$$|\tau_n| = \tau_s + \mu_s \sigma_n. \quad (6.11)$$

A typical law is represented by the line GFE in Fig. 6.2, and stress states for the case $\sigma_2 = \sigma_3$ lie on the Mohr circle representation as shown. F and E are the points of intersection of Eq. (6.11), positive τ_n , with the circle. If the normal to this fracture plane makes an angle α with Ox_1 , then if $\alpha_E < \alpha < \alpha_F$ sliding occurs, but otherwise sliding does not occur. In the latter case, if the circle touches the Mohr envelope for fracture (between E and F), then fracture on the appropriate intact plane occurs, while in the former case intact fracture does not arise if the circle lies inside the Mohr envelope. Thus, failure by sliding on the existing plane of weakness or fracture of intact material are both possible first events as the loads are increased, the choice depending on the two laws, Eq. (6.9) or (6.8) and Eq. (6.11), and the orientation α . The situation for $\sigma_1 > \sigma_2 > \sigma_3$ is described in [44, Chapter 3].

Once fracture of intact material has taken place then the condition for subsequent sliding is Eq. (6.11) — or other appropriate law. Thus for $\tau_s < \tau_0$, $\mu_s < \mu$, the stress reached at fracture cannot be maintained for moderate σ_n and is reduced locally to satisfy Eq. (6.11) with a non-homogeneous redistribution of stress through the material.

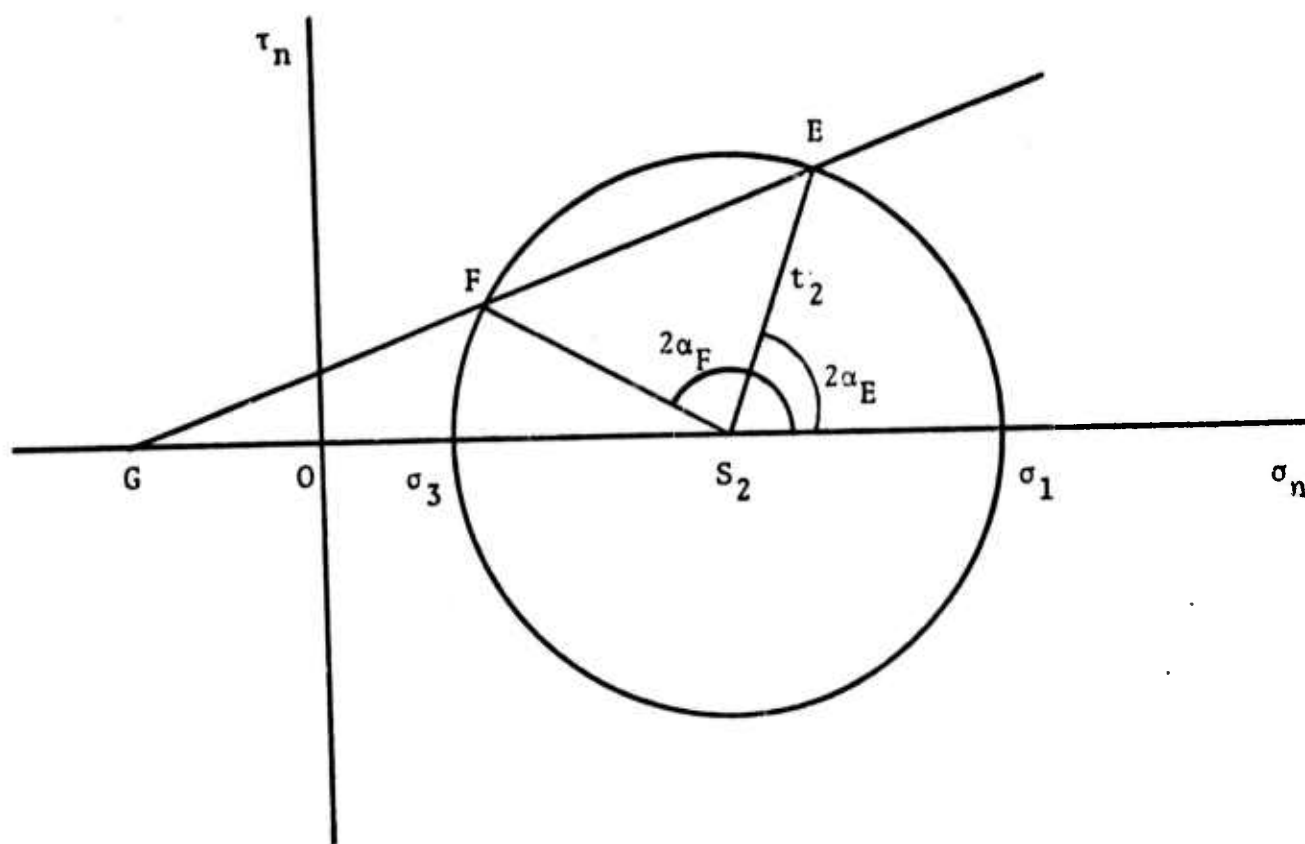


Fig. 6.2--Mohr circle and sliding criterion.

This is termed brittle fracture, [44 , Chapter 6] and is illustrated by the lower axial stress-strain curve shown in Fig. 6.3. As confining pressure, and hence σ_n , increases, the sliding law line GFE, Fig. 6.2, will approach and intersect a concave Mohr envelope and a continuous sliding response occurs, referred to as "ductile" by analogy with metal plastic flow, depicted by the middle curve of Fig. 6.3. With further increase of σ_n the upper curve (analogous to work-hardening) is typical, mainly the result of sliding across multiple intersecting fracture planes. The brittle-ductile transition point, measured by the confining pressure (or normal stress) at which the stress drop ceases is found to decrease with increase of temperature.

An alternative response under moderate and higher confining pressure is "stick slip"[61] when the relative motion on new and existing fractures is accompanied by stress drop, then ceases until the stress is again raised to initiate sliding with stress drop, and so in sequence.

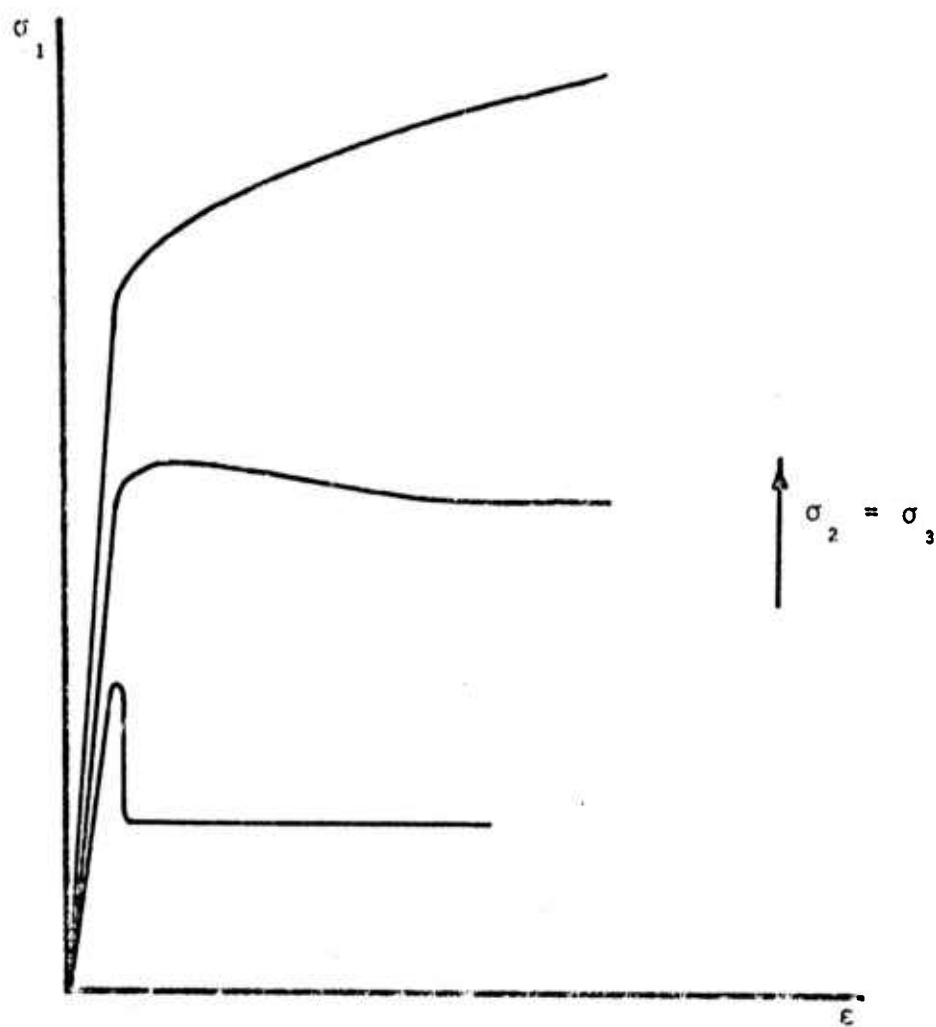


Fig. 6.3--Axial stress-strain curves for varying
confining pressure $\sigma_2 = \sigma_3$.

6.3 TESTS AND DEDUCTIONS

The common laboratory test is triaxial compression of a cylinder with diameter at most a few inches and aspect ratio between 2:1 and 4:1 (Fig. 6.4). Confining pressure is isotropic, $\sigma_2 \equiv \sigma_3$. The two independent stresses σ_1, σ_3 allow fracture and sliding criteria to be interpreted in terms of shear and normal stress on the fracture plane. In principle such data can be fitted to an infinity of criteria involving three independent stresses, for example three stress invariants, and a three-dimensional theory would require additional supporting evidence.

A variety of rocks have been tested^[62 - 67] for fracture of intact material followed by sliding along the fracture plane, and sliding along existing fracture planes, with smooth and rough surfaces. Large displacement sliding over larger areas between rectangular and triangular blocks is also reported.^[66] Recently^[68 - 69] biaxial loading of a slab with cross-section approximately 4×7 inches and an inclined sawcut has been achieved with approximately uniform traction on the fracture surface and with slip displacements up to an inch. Direct measurements of relative displacement parallel and normal to the fracture surface were made.

The direct shear tests on granite and four rock minerals described in [62] were performed at constant slide velocity 0.02 mm/sec, over a normal stress range of 0 to 0.15 kbar and a Centre Line Average (roughness) range of 2.5 to 30×10^{-2} inches. No evidence of intra-granular (plastic) flow was observed in the debris produced by sliding and it was concluded that slip occurs by crushing of asperities (brittle fracture) with possible lift over asperities at low normal stresses. For the rough granite surfaces the data for slip initiation was approximated by

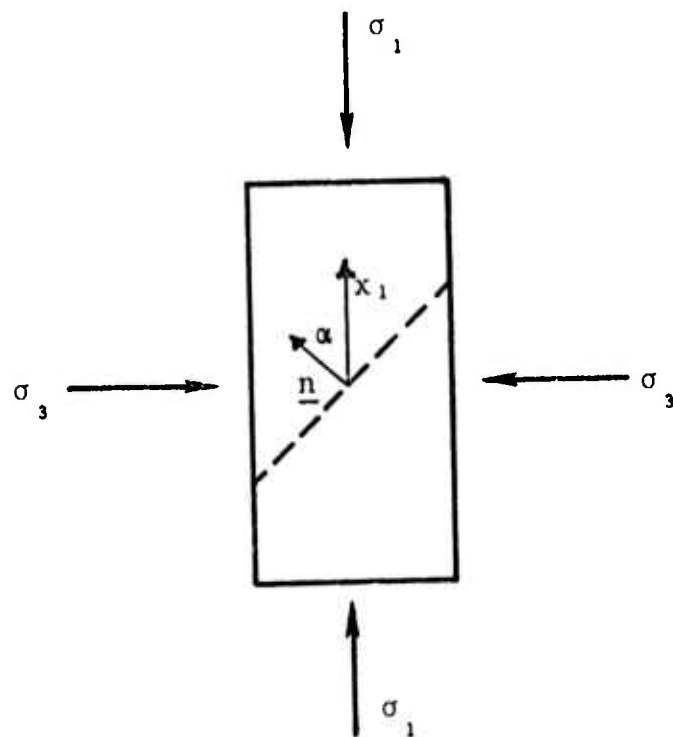


Fig. 6.4--Triaxial compression.

$$\tau_n = 1.3 \sigma_n \quad (0 < \sigma_n \leq 0.06 \text{ kbar}) \quad (6.12)$$

$$\tau_n = 0.03 + 0.8 \sigma_n \quad (0.06 \leq \sigma_n < 0.15 \text{ kbar})$$

implying negligible cohesion τ_s at zero normal stress. Stick-slip (sudden slip with drop in τ_n , stick until τ_n increased to a new critical value) was pronounced for the rougher surfaces.

Triaxial testing of granite with a fully interlocking rough fracture plane under high confining pressure was described in [63]. The inclination of the plane to the major principal stress axis varied from 20° to 35° and the deduced slip criterion was

$$\tau_n = 0.5 + 0.6 \sigma_n \quad (2 \leq \sigma_n \leq 17 \text{ kbar}). \quad (6.13)$$

This relation does not necessarily extrapolate to $\sigma_n = 0$ to imply $\tau_s = 0.5$ kbar, but the slope value $\mu_s = 0.6$ differs from the value 0.8 at the upper end of the range in Eq. (6.12). However, at $\sigma_n = 2$ kbar, $\tau_n/\sigma_n = 0.85$, which suggests a smooth slightly non-linear interpolation between Eqs. (6.12) and (6.13). It was also noted that τ_n/σ_n decreased slightly on critical slip and became effectively constant after 1 cm slip. During sliding the surface went through a rough-smooth-rough sequence.

Effect of machine stiffness and strain rate on the stress drop in stick-slip were investigated for a variety of rocks with smooth and rough joints^[64] and found to be negligible. Stick-slip was absent in highly porous rocks (tuff) and rocks containing calcite and serpentine. The latter are common fillers in naturally occurring joints, as also water, and all these decrease the amplitude of stick-slip significantly from values observed in laboratory

testing. This amplitude reduction has been noted in [54], [67], [69] and [70]. It is also decreased by increase of temperature.

The brittle-ductile transition of a variety of intact rocks was investigated in [65], measured by the normal stress (or confining pressure) at which the stress drop on fracture and initial slip ceases, recall Fig. 6.3. A smooth $\tau_n - \sigma_n$ (or $\tau_n - p$) curve was shown to separate (approximately) domains of brittle and ductile response of the variety of rocks tested. It was also concluded that the friction (slip criterion) was independent of the intermediate principal stress (here $\sigma_2 \equiv \sigma_3 < \sigma_1$ and the situation $\sigma_3 < \sigma_2 < \sigma_1$ is not considered).

A variety of tests on many rock joints are described in Ref. [66] and values of τ_s, μ_s associated with the linear slip criterion of Eq. (6.11) deduced. A range 20 to 1000 psi is reported for τ_s and 0.32 to 0.85 for μ_s . Stick-slip was observed on the smoother surfaces, during initial slip and sometimes after finite displacement which is presumed to smooth out the surface. Slip on inclined intersecting conjugate surfaces was also investigated, and non-symmetric response observed - continuous sliding on one surface and large stick-slip on the other. Here there are complications of non-identical surfaces and non-symmetric geometry and loading - all of which occur in practice.

Tests on ground surfaces of Westerly granite up to normal stresses of 1 kbar^[67] showed that stick-slip was always preceded by a small amount of sliding, suggested as a possible pre-monitoring effect for earthquakes. Measurements of normal displacement across the fracture surface were made to test the "ride over asperities" explanation for this stable sliding, but results indicated that no normal displacement was taking place. A range of 0.4 - 0.5 was observed for τ_n / σ_n at initiation of slip, but after

about 1 cm of sliding, with generation of gouge, a steady frictional behavior at the level 0.5 occurs. The stress drop factor $\Delta\tau_n/\tau_n$ associated with the stick-slip appears to increase with τ_n initially but drops to the level 1 percent to 2 percent with generation of gouge. Tests over the strain rate range 10^{-4} to 10^{-8} /sec implied that τ_n/σ_n increased approximately logarithmically with time of contact (decreased with increase of strain rate).

In the direct shear tests on a number of rocks [55] the dynamic friction τ_n/σ_n for rough surfaces increased with accumulation of gouge during initial stable sliding. Subsequently, stick-slip occurs and the static friction (τ_n/σ_n for initiation of new slip) is time dependent, increasing with the contact time during stick (controlled by the applied loading). Contact times from 1 to 10^5 secs were used, and an approximate law $\mu_s = \mu_0 + A \log_{10} t$ ($t \geq 1$ sec) deduced where here $\mu_s = \tau_n/\sigma_n$. For example, for granite at $\sigma_n = 58$ bars, $\mu_0 = 0.708$, $A = 0.021$; and at 694 bars, $\mu_0 = 0.787$, $A = 0.018$; the increase of μ_s over 10^5 secs is about 0.1

Recently [71] techniques to determine frictional and deformation properties of in situ jointed specimens have been developed and applied to Cedar City Quartz diorite, with surface areas ranging from 22 to 795 square inches. Comparisons are then made with laboratory test data on small samples of the same material. Both initial and residual shear strengths were found to decrease with increasing surface area of the joint, a result suggested to be related to a roughness-contact area properties of natural joints. Above 350 square inches, the residual strength was relatively constant. Both initial and residual friction coefficients decreased with normal stress and slip displacement. In the laboratory tests, the initial coefficient

increased slightly while the residual coefficient decreased slightly with normal stress. It is pointed out that friction is a function of contact area and strength of asperities, and mating of asperities on relatively smooth surfaces can induce higher friction than between rougher surfaces. Also properties of filling material can overshadow normal stress and area effects. Joints dilate at low normal stress during shearing, but not at higher normal stresses (600 to 1500 psi). Properties of jointed and intact specimens are similar before joint shearing for specimens tested, but it was noted that for filled thick joints the filler material properties could have a significant effect on both initial and slip properties. In addition, some tests on multiply jointed specimens were made, parallel and intersecting, as a start to testing "block structures" in natural rocks. Strength was found to be controlled by the joint most "unfavorably" oriented with respect to the load, and slip on the other joints only occurred after the first joint was locked against an adjacent block.

Interpretation of laboratory data from triaxial tests essentially relates mean stresses over the joint surface. Prior to slip, during elastic deformation of the cylinder, stresses may be reasonably uniform away from the ends of the specimen, and mean stress adequately measures local stress over the major part of the joint. The criterion deduced for initiation of slip can therefore be regarded as reasonable local conditions. Once slip is taking place, with shear and normal tractions on the joint satisfying a slip criterion, the stress in the separate elastic sections cannot in general be uniform (the unique uniform stress solution for equilibrium will not satisfy the slip criterion uniformly over the joint), so it is mean stress relations that are determined. When the high accelerations associated

with stick-slip arise, mean stress estimates must take the momentum balance into account, and various assumptions regarding energy partition into work done on asperity crushing (surface energy release), heating, block deformation, are made to calculate velocities. Criterion for continued slip are then less certain than those for initiation, and it is difficult to deduce a "cohesion function" (introduced in the later continuum model) and dependence on slip.

Since the data are generally two-dimensional, effects of a transverse stress in the slip-plane are not observed. At constant confining pressure this varies with the applied side load, and is not varied independently; in plane stress it is zero. Transverse stressing (and straining) could affect roughness and interlock of asperities, and so influence the frictional properties, but there is no quantitative evidence at present. It seems reasonable though to assume that instantaneous slip takes place in the direction of the maximum shear traction, as adopted in the continuum model to be described later.

The real in-situ situation involves rock masses with multiple intersecting fracture planes, creating a block structure. The complex interaction of slips on many planes, particularly intersecting planes involving block interlock, probably causes highly non-uniform redistribution of stress in the intact block material between joints. It is therefore likely that slip mechanisms on single (unconstrained) joints is inadequate to describe the multiple joint and block structure situation, and observations on the response of bodies containing different multiple joint patterns are needed as the basis of a heuristic treatment. This view is taken at Terra-Tek (Salt Lake City, Utah) where they propose such experimental programs on natural rocks, continuing the work reported in [71]. It is also thought that the "interlock resistance" will dominate prior joint

slip, at least for high confining pressure when block offset is small. The most elementary interaction is between the motions on two intersecting cross joints, depending on relative orientation and orientations with respect to principal stresses. Then the effects of two and more joints within each parallel set must be determined, and in particular the sequential behavior of motion on respective joints.

Previous experimental work on block structures is largely concerned with specimens prepared from plaster type materials in order to simulate the slip and fracture response at low stress levels, and to facilitate the preparation of joint surfaces. While care is taken to reproduce qualitatively many of the required rock properties, it is not clear that the overall complex response of jointed natural rock masses is even qualitatively the same. Reference [51] deals with two orthogonal joint sets loaded in plane strain for different ratios of axial load to confining pressure. Failure of the intact blocks and joint slip are both observed. Finite element calculations are compared with data. Constant confining pressure triaxial tests are reported in Ref. 72 for one and two sets of parallel joints at different spacings. Failure of intact material and joint slip are observed, and also dilatancy at low pressures. The failure envelope for the intact material is found to be lower (as measured by applied loads) when joints are present, but undergoing no apparent slip, suggesting that joints are influencing the stress distribution. The strength (of intact material) increases with increase of spacing in each joint configuration. Also the brittle-ductile transition point changes as joint configuration and spacing changes. An extensive program of tests in plane stress is described in Ref. [73]. Axial load is increased by increments of 25 psi, and side load first incremented then held constant.

Various procedures are used to measure strains, and the significant non-uniformity (hence stress concentrations) is demonstrated. Intact and jointed blocks are compared, and joint orientation is varied. Failure of intact blocks, joint slip, and joint dilatation are observed. Block structures containing lined and unlined cylindrical cavities have been tested.^[74] Joint dilatation is important at free boundaries. Generally, joint dilatation is relevant only at low depths when confining pressures are low, or at free boundaries of tunnels, and does not occur at depths when pressures are high. Past methods of block structure and joint simulation have been recently criticized^[75] and an alternative method described. Joint characteristics are discussed and their importance in calculating overall response of a block structure. In particular, linear superposition of "elastic joints" on "elastic blocks" is criticised and the irreversible character of joint deformation is emphasized.

Of great practical importance is the influence of water (and occasionally oil) generally found in porous and cracked rock. In the presence of water at pore pressure p , the failure and slip criteria are found to take the same form provided that stress is replaced by an "effective stress"

$$\langle \sigma \rangle = \sigma - p \quad (6.14)$$

This "conventional" effective stress leaves shear traction on any plane unchanged but subtracts pore pressure from the compressive normal traction. Thus the linear Coulomb slip law in Eq. (6.9) becomes

$$|\tau_n| = \tau_0 + \mu(\sigma_n - p) \quad (6.15)$$

The empirical result Eq. (6.14) is continually verified by experimental observation in regard to failure criteria, and applied over wide ranges of porosity, and porous structure ranging from fine plane cracks to random distribution of holes.

It differs significantly from the effective stress introduced in Section V (and in Ref. [76]) to describe deformation response of saturated porous solids to applied stress, namely,

$$\frac{(\alpha)}{\sigma} e = \frac{(\alpha)}{\sigma} / m^{(\alpha)} \quad (\alpha = 1, 2) \quad (6.16)$$

where $m^{(\alpha)}$ is the scalar factor depending (at least) on the deformation of both solid matrix and fluid, and $\frac{(\alpha)}{\sigma}$ are the partial stresses in the matrix and fluid. When $\frac{(\alpha)}{\sigma} e$ are interpreted as mean stresses (volume averages) in the solid and fluid over a representative element containing many pores, the relation

$$\frac{(\alpha)}{m} = \frac{(\alpha)}{n} \quad (6.17)$$

can be deduced where $\frac{(\alpha)}{n}$ is the volume fraction of solid or fluid respectively in the mixture (this result does not rely on isotropy in any form), so that the porosity (volume fraction of pores or fluid when saturated) is $\frac{(2)}{n} = 1 - \frac{(1)}{n}$. Using Eqs. (6.16) and (6.17), the Coulomb law would become

$$|\tau_n| = \frac{(1)}{n} \tau_0 + \mu \frac{(1)}{\sigma_n} \quad (6.18)$$

or

$$\tau_n = \frac{(1)}{n} \tau_0 + \mu [\sigma_n - (1 - \frac{(1)}{n})p] , \quad (6.19)$$

where τ_n, σ_n are the total stresses given by

$$\sigma \approx \sigma^{(1)} + \sigma^{(2)} \quad (6.20)$$

Equation (6.19) approximates Eq. (6.15) only for very high porosity ($n^{(1)} \ll 1$) and at stress levels for which τ_0 is insignificant. It is not in agreement with failure data for normal porosity ranges, as can be expected since the mean stress interpretation of $\sigma^{(\alpha)}_e$ excludes application to localized phenomena governing failure. The purpose of Eqs. (6.16) and (6.17) is to describe mean stress-deformation response on length scales greater than pore spacing, for which Eq. (6.14) appears to have no basis.

These effective stress measures, and others, are compared and discussed by Garg and Nur.^[77] In particular, the deduction^[78] of a special case for infinitesimal strain of a porous elastic rock is analyzed and shown to be of doubtful validity. An illustration of Eq. (6.14) is given by interpreting failure in terms of minimum circumferential stress at a pore boundary. An infinite slab subjected to uniaxial tension, and containing a transverse cylindrical cavity, has a maximum circumferential tensile stress increased by the pore pressure p in the cavity. Thus, if a compressive stress S can be reached before failure, then this is attained by a boundary load $S-p$. This result is obtained only for a single pore of cylindrical geometry, in plane strain deformation of a linear elastic matrix, and influence of the matrix deformation on pore fluid deformation is neglected.

The explanation offered for Eq. (6.14) in the classical paper by Hubbert and Rubey^[58] is invalid. It is essentially a circular calculation describing the net forces acting on solid and fluid respectively within a body of mixture (the solid matrix is supposed to support normal pressure only, and not shear traction, but this assumption

is irrelevant to the argument). During the calculation an implicit assumption is made regarding the partition of traction between solid and fluid, namely, in the mixture notation of Section V,

$$p^{(1)e} = p^{(2)e} = p, \quad (6.21)$$

that is, effective pressure balance. Here p is total pressure, $p^{(2)e}$ is effective fluid (pore) pressure, $p^{(1)e}$ is matrix effective pressure. Thus $p^{(1)e}$ is actually assured to be the total pressure p - unchanged by the pore pressure - and support for Eq. (6.14) is not clear.

Finally, we conclude with a qualitative proposal made by Dr. J. D. Byerlee in private discussion. The mixture analysis attempts to partition traction between solid and fluid on a fracture plane. Byerlee suggests that the real solution is fluid permeating gaps between mating asperities and thus exerting lateral forces on the asperities which influence their shear and slip. The contribution p in Eq. (6.14) may well be a consequence of such lateral effects.

6.4 BLOCK STRUCTURE AND MOTION

In many applications we are interested in length scales much larger than the block dimensions, which can be inches to several feet. That is, boundary loading may have small gradients over these dimensions, or dominant wave lengths of motion may be much larger. In such situations it is useful to explore a continuum approximation which smoothes out the discontinuous or high gradient relative motion across joints. Within this framework it should be possible to proceed analytically with simple problems and perhaps draw out general features of more complex situations. Furthermore, the continuum equations may lead to more compact numerical solutions than detailed finite difference or finite element code calculations over these larger length scales. They should at least complement and reinforce direct numerical procedures on the gross scale.

First consider the block and joint structure. It is supposed that the rock mass contains one or more sets of regularly spaced parallel joints, with at least two sets if there is a real block structure. Figure 6.5 shows a two-dimensional illustration of joint sets and block structure; sets need not be orthogonal. The orientation of a given set (unit normal vector) is \underline{n} , its spacing is d , and "joint thickness" is δ . Both d and δ may vary between sets, but it is assumed in the continuum approximation that \underline{n} , d , δ for a given set are approximately uniform over a representative region (a few block dimensions) which is small compared with the gross length scale of interest. Joint thickness δ is not a precise parameter, but measures the approximate asperity height (roughness) of the block surfaces or an approximate thickness of filler material. In all situations for which the concept of block and joint is relevant,

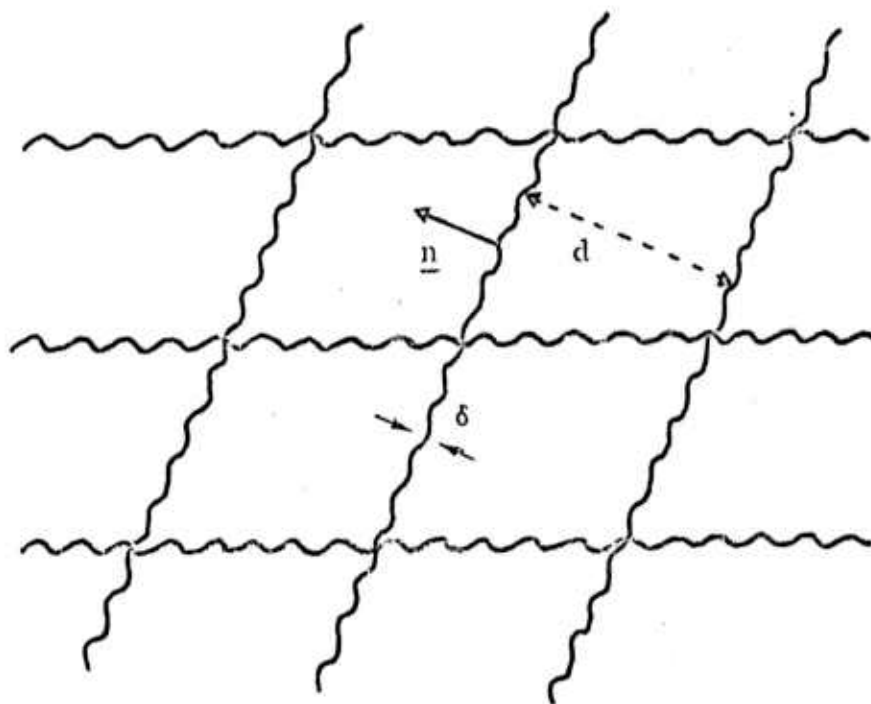


Fig. 6.5--Joint sets and block structure ($\delta \ll d$).

$$\delta \ll d, \quad (6.22)$$

and δ arises in the continuous description only in the sense of Eq. (6.22).

Each block will separately undergo continuous motion (displacement), but in view of the magnitude comparison in Eq. (6.22) the structure of the motion (deformation) within the joint thickness can be neglected and the presence of the joint described by relative velocities (displacements) across the joint regarded as a plane surface (zero thickness). This is also the standard assumption of finite difference and finite element analyses. Across each joint then there are possible discontinuities in the tangential and normal velocities (displacements) of the overall motion. The former define slip at the joint, and the latter dilatation (opening) or contraction. In general the initial confining pressures are sufficiently high that subsequent dilation does not result in actual separation, except perhaps at boundaries of cavities within the rock mass.

Commonly slip will be much more significant than dilation (contraction) — see for example the detailed description of joint types^[79] and illustrative data showing a relative magnitude of 100. In view of this common relative magnitude, and for clarity, our constitutive description will be presented for joint slip alone, assuming that normal displacement is continuous across the joint. Inclusion of dilatancy within the same framework is straightforward but its relevance will depend on availability of good data.

With a single joint set, slip at each joint is in principle unrestricted (by block structure), but in practice will be constrained by surrounding material at joint ends. Furthermore, with more than one joint set, the usual situation,

slip will be restricted by block interlock when joint misalignment arises due to slip on transverse joints. It is convenient then to regard δ as an order of magnitude of an upper bound to the net slip, but this is not an explicit restriction of the theory. If a joint layer were to be considered, then slip of magnitude δ over thickness δ implies a finite shear deformation gradient and distinction between a spatial and material coordinate description. In particular new positions of particles initially opposite across the joint are finitely separated. However, with the relative magnitudes satisfying Eq. (6.22), slip of order δ on the length scale d is small. Furthermore, with this restriction on boundary displacements of separate blocks, deformation and rotation within the blocks is also small and hence overall displacement gradients are small on the length scale d after eliminating any net rigid body motion. Thus over a representative region we can regard the displacement gradients as infinitesimal and identify current and initial positions of all particles. In particular we can evaluate field variables at a single point on the joint to refer to initially opposite particles in the adjacent blocks.

Now consider for clarity a single joint set defined by the parameters $(\underline{n}, d, \delta)$. Effects of other joint sets are given simply by incorporating the analogous joint fields with associated parameters. Let n denote distance along \underline{n} measured from some fixed origin on the negative n -side of all joints, and denote the slip (tangential displacement discontinuity) at a point \underline{x}_j on the joint at distance n_j from the origin by $\underline{U}_j(\underline{x}_j)$. Then at a position \underline{x} in the interior of some block at normal distance n from the origin, the displacement can be expressed in the decomposition

$$\underline{u}(\underline{x}) = \underline{u}^c(\underline{x}) + \sum_j \underline{U}_j(\underline{x}_j) H(n - n_j) \quad (6.23)$$

where $\underline{u}^c(\underline{x})$ is a continuous field and $H(n)$ is the Heaviside step function.

When $\underline{U}_j(\underline{X}_j)$ is non-uniform along the j -joint, then the in-plane displacement gradient, and symmetric-skew decomposition,

$$\nabla_{\underline{n}-j} \underline{U}_j = \underline{E}_j + \underline{\Omega}_j \quad (6.24)$$

define the relative strain \underline{E}_j and rotation $\underline{\Omega}_j$ of elements in adjacent blocks. Both \underline{E}_j and $\underline{\Omega}_j$ are infinitesimal tensors. Thus the strain and rotation at the point \underline{x} in the interior of a block are given by

$$\underline{\tilde{e}}^b(\underline{x}) = \underline{\tilde{e}}^c(\underline{x}) + \sum_j \underline{E}_j(\underline{X}_j) H(n - n_j), \quad (6.25)$$

$$\underline{\tilde{\omega}}^b(\underline{x}) = \underline{\tilde{\omega}}^c(\underline{x}) + \sum_j \underline{\Omega}_j(\underline{X}_j) H(n - n_j).$$

It must be emphasized that the property of infinitesimal displacement on the length scale of joint separation is crucial to the simple additive decompositions in Eq. (6.25). In particular the block strain $\underline{\tilde{e}}^b$ is uncoupled from rotation jumps $\underline{\Omega}_j$ across the joints.

The mechanical response of the intact block material relates the current stress $\underline{\sigma}(\underline{x}, t)$ at an interior point \underline{x} to the block strain history $\underline{\tilde{e}}^b(\underline{x}, t')$, recalling that any net rigid body motion is first eliminated. Thus

$$\underline{\sigma}(\underline{x}, t) = \mathcal{L}[\underline{\tilde{e}}^b(\underline{x}, t'), t' \leq t] \quad (6.26)$$

where \mathcal{L} is the constitutive functional. The common assumption, and a good approximation for many practical applications, is that the blocks have isotropic elastic response, when Eq. (6.26) becomes

$$-\underline{\sigma}(\underline{x}) = 2G\underline{e}^b(\underline{x}) + (K - \frac{2}{3}G) \text{tr} [\underline{e}^b(\underline{x})]\underline{1} \quad (6.27)$$

where K, G are the bulk and shear moduli respectively. This elastic response will be adopted in a later illustration. Time dependent viscoelastic response or rate-independent elastic-plastic response may also be relevant block models, and can be incorporated by appropriate choice of \mathcal{L} .

Note that the usual rock mechanics convention for stress is adopted — principal stress positive in compression — so that the traction on any surface with outward unit normal \underline{n} is

$$\underline{t}_{(\underline{n})} = -\underline{\sigma}\underline{n}. \quad (6.28)$$

In particular the normal and shear tractions are

$$\begin{aligned} \sigma &= -\underline{t}_{(\underline{n})} \cdot \underline{n} = (\underline{\sigma}\underline{n}) \cdot \underline{n} \\ \underline{\tau} &= \underline{t}_{(\underline{n})} + \sigma\underline{n} = (\underline{\sigma}\underline{1} - \underline{\sigma})\underline{n}. \end{aligned} \quad (6.29)$$

For momentum balance σ and $\underline{\tau}$ are continuous across a joint but the in-plane stresses may be discontinuous, and in fact will be discontinuous when there are non-zero relative in-plane strains \underline{E}_j .

It is generally supposed that slip at a joint is initiated when the shear traction magnitude reaches a critical value which depends on the normal traction [44, Chapter 3]. Thus an initial slip criterion is written (see Section 6.2)

$$|\underline{\tau}| = \tau_0 + g(\sigma) \quad (6.30)$$

where $\tau_0 (> 0)$ is the cohesive stress, $g(0) = 0$, and $g'(\sigma) > 0$. That is, the joint will support a shear traction τ_0 at zero normal traction, due to its roughness, and the resistance to slip increases as the joint is compressed. τ_0 may be small and possibly negligible compared with applied stress levels. The common simple model found to be in approximate agreement with many data is the linear Coulomb-Navier law

$$|\underline{\tau}| = \tau_0 + \mu\sigma, \quad (6.31)$$

where $\mu (> 0)$ is called the friction coefficient. This linear law will be adopted in the later illustration.

The criterion in Eq. (6.30) explicitly excludes dependence on the in-plane stresses. It is feasible that the associated in-plane (continuous) block strain prior to slip may influence the "roughness" of the joint and hence the criterion. This is an area for experimental investigation, but at present intuitive theoretical proposals would lack verification (see Section 6.3).

Initial slip is assumed to take place in the direction of the shear traction. Let \underline{v} be the unit in-plane vector such that

$$\underline{\tau} = \tau \underline{v}, \quad \tau = |\underline{\tau}|, \quad \underline{v} \cdot \underline{n} = 0, \quad (6.32)$$

then the slip velocity $\dot{\underline{u}}$ can be expressed

$$\dot{\underline{u}} = \dot{u} \underline{v}, \quad \dot{u} > 0. \quad (6.33)$$

The many accounts of two-dimensional experiments do not comment on the occurrence of any transverse (in-plane) slip,

but do not report its absence. However, the proposed relation in Eq. (6.33) is eminently reasonable.

The ideal-slip theory assumes that the criterion in Eq. (6.30) continues to hold during slip which is governed by the validity inequality in Eq. (6.33). If the loading will not sustain slip in the shear direction, then slip ceases and transverse velocity becomes continuous across the joint. Thus

$$\begin{aligned}\tau &\equiv \tau_0 + g(\sigma), \quad \dot{U} \geq 0, \\ \tau &< \tau_0 + g(\sigma) \quad \dot{U} \equiv 0.\end{aligned}\tag{6.34}$$

Slip is not reversed on unloading but only when the shear traction reaches the critical magnitude in the opposite direction. This is therefore an irreversible mechanism and the overall response of the jointed rock is necessarily inelastic even when the intact block material is elastic. In this ideal slip theory neither \underline{U} nor $\dot{\underline{U}}$ is explicitly determined by the stress, only the direction of slip, and the magnitude is restricted only by kinematic constraints. In practical situations inertia of surrounding material will usually inhibit unbounded slip on a single joint, and in the block structure interlock will be a strong constraint.

Continued sliding on a single joint in triaxial tests at constant confining pressure may occur at (approximately) constant axial stress (the above ideal slip theory), may require increasing axial stress (slip hardening), or may be accompanied by sudden drop of axial stress (brittle response). The latter behavior is not common for very rough surfaces and particularly after gouge has been generated, and for a block structure such sudden slip will be inhibited. Hardening with sliding due to surface change will be much less

significant than increased resistance due to misalignment of the joints (block interlock). While a finite difference or finite element analysis can track the displacements of block corners and incorporate interlock conditions, the subsequent continuum approximation needs to express this requirement in some mean sense.

Resistance to slip in the current shear direction \underline{v} will depend at least on the current slip in the \underline{v} -direction since this measures in some mean sense what further slip in that direction is possible before blocks overlap. The most simple proposal to reflect this idea is that resistance to slip in the \underline{v} -direction depends on a single hardening parameter

$$q = \underline{U} \cdot \underline{v} / \delta \quad (6.35)$$

and in fact increases with positive q . The maximum magnitude of q is $O(1)$ in view of the displacement bound. If q is negative then the slip is back towards a central position which should not be resisted by interlock. Thus we introduce a cohesion function $f(\tau, \sigma)$ such that continued slip requires

$$f(\tau, \sigma) = F(q) \quad (6.36)$$

where

$$F'(q) \begin{cases} > 0, & q \geq 0, \\ \equiv 0, & q < 0. \end{cases} \quad (6.37)$$

Figure 6.6 illustrates such a hardening function $F(q)$, not necessarily asymptotic to $q = 1$ since the "joint thickness" δ is not a precise quantity. In practice we expect that the stress levels as $q \rightarrow 1$ are sufficiently high for the

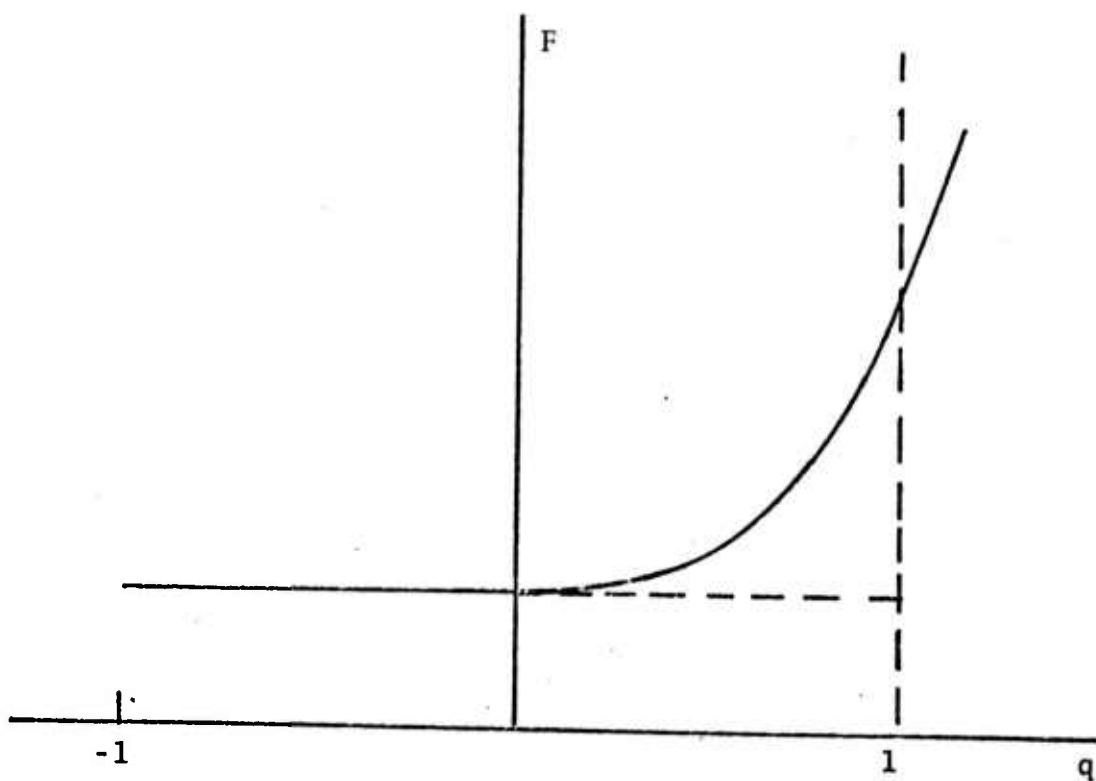


Fig. 6.6--Slip hardening due to block interlock.

present intact block-joint slip theory to fail. The dashed lines illustrate the limit case of ideal slip with total interlock at $q = 1$.

The cohesion function $f(\tau, \sigma)$ defines the current slip criterion and clearly at initial slip ($q = 0$) the criteria expressed in Eqs. (6.30) and (6.36) must coincide. This however does not provide a unique relation between $g(\sigma)$ and $f(\tau, \sigma)$. For example, with the criterion Eq. (6.31), we can choose

$$f(\tau, \sigma) = \tau - \mu\sigma, \quad F(0) = \tau_0, \quad (6.38a)$$

or

$$f(\tau, \sigma) = \frac{\tau - \tau_0}{\sigma}, \quad F(0) = \mu. \quad (6.38b)$$

In the former choice the cohesive stress then becomes the increasing function $F(q)$ while in the latter the friction coefficient became the increasing function $F(q)$. Considerably more evidence from block model experiments will be required to test these simple proposals and select, if possible, appropriate hardening and cohesion functions. The most simple choice for subsequent illustration is the linear function (6.39a); (6.39b) introduces non-linear stress dependence.

It should be noted that the hardening law in Eq. (6.36) is anisotropic, since q depends on the current shear direction \underline{v} in relation to the current slip displacement \underline{U} . Since

$$\underline{U}(t) = \int_0^t \dot{\underline{U}}(t') \underline{v}(t') dt', \quad (6.39)$$

and over a general slip history $\underline{v}(t')$ varies, the direction of $\underline{U}(t)$ is not determined by $\underline{v}(t)$. Differentiating Eq. (6.36):

$$\delta \dot{f} = F'(q) \{ \dot{\underline{U}} + \underline{U} \cdot \dot{\underline{v}} \}, \quad (6.40)$$

and hence for $q \geq 0$,

$$\dot{U} = \frac{\delta f}{F'(q)} - \underline{U} \cdot \dot{\underline{v}}, \quad \geq 0 \quad (6.41)$$

which determines \dot{U} in terms of $\dot{\underline{\tau}}$ and $\dot{\sigma}$ at a given stress state $\underline{\tau}, \sigma$. The validity inequality does not require that the cohesion function f is non-decreasing since $\underline{U} \cdot \dot{\underline{v}}$ may be negative. By Eq. (6.40) the case $\dot{f} < 0$ implies $q < 0$ so that the change of slip direction defined by $\dot{\underline{v}}$ is towards a direction of decreased resistance. For $q < 0$ ideal slip occurs with \dot{U} not determined explicitly by the stress and stress rates, but with the stress criterion identically satisfied:

$$q < 0, \quad f(\underline{\tau}, \sigma) \equiv F(0). \quad (6.42)$$

Thus, in particular, the initiation of reverse slip is not governed by previous hardening in an opposite direction. Further, reverse slip will decrease q and hence lower the resistance to subsequent slip in the positive sense. These are features of the anisotropy of block interlock kinematics.

Finally we can note that the block strain given by Eq. (6.25) incorporates the in-plane gradients of \underline{U} which is governed by the joint slip mechanics entirely independent of the constitutive response of the block material, Eq. (6.26). A strong coupling between joint slip and block response arises in consequence. The case of several parallel joint sets will be described in the continuum approximation.

6.5 CONTINUUM APPROXIMATION

If the length scale of boundary load variation, or dominant wave length of a propagating disturbance, is much longer than the block dimension then we can expect little stress variation over a representative region covering a few block dimensions. In this situation it is reasonable to regard the tractions and relative displacements occurring in a given time interval on r consecutive joints, and over in-plane lengths of order rd , as approximately uniform. In particular, restricting attention to slip at joints, the net slip over r joints is

$$\underline{U} = \sum_{j=1}^r \underline{U}_j(\underline{X}_j) = r \bar{U} \quad (6.43)$$

where \bar{U} is the mean slip over the r joints.

On length scales large compared with rd the actual discontinuities \underline{U}_j and the joint locations will be unimportant, and we are concerned only with the net slip over a representative distance. Thus, we introduce a continuous slip displacement field $\underline{u}^s(\underline{x}, t)$ associated with the joint set of orientation \underline{n} which determines the same net slip. That is,

$$\frac{\partial \underline{u}^s}{\partial \underline{n}} = \frac{r \bar{U}}{rd} = \frac{1}{d} \bar{U}, \quad (6.44)$$

where Eq. (6.44) strictly defines a mean of the normal gradient of \underline{u}^s over the representative distance. However $\partial \underline{u}^s / \partial \underline{n}$ is considered uniform over the representative distance when viewed on our gross length scale. Recall also that initial and current direction of the joint normal are identical on this scale so that the normal derivative is evaluated in the initial configuration.

In the ideal slip theory the slip criterion in Eq. (6.34) applies to the mean stress in the representative region, that is the local stress on the gross scale, with the continuous slip velocity direction given by the shear traction direction, thus

$$\begin{aligned} \tau &\equiv \tau_0 + g(\sigma), \quad \underline{\dot{u}}^S = \dot{u}^S \underline{v}, \quad \frac{\partial \dot{u}^S}{\partial n} \geq 0, \\ \tau &< \tau_0 + g(\sigma), \quad \frac{\partial \dot{u}^S}{\partial n} \equiv 0. \end{aligned} \quad (6.45)$$

For the slip-hardening theory described by Eqs. (6.35) through (6.42) we must first relate the hardening parameter q to the continuous field \underline{u}^S . A mean value of q for the representative region, by Eq. (6.44), is

$$q = \frac{1}{\delta} \underline{U} \cdot \underline{v} = \frac{d}{\delta} \frac{\partial \underline{u}^S}{\partial n} \cdot \underline{v}, \quad (6.46)$$

and the current value of $\partial \underline{u}^S / \partial n$ is given by a time integral of $\partial \dot{\underline{u}}^S / \partial n$ analogous to Eq. (6.39). Hence, during slip with $q \geq 0$, Eq. (6.36) holds and analogous to Eq. (6.41) determines

$$\frac{\partial \dot{\underline{u}}^S}{\partial n} = \frac{\delta \dot{f}}{dF(q)} - \frac{\partial \underline{u}^S}{\partial n} \cdot \underline{\dot{v}}, \quad \geq 0. \quad (6.47)$$

The joint spacing d now enters explicitly, with different values possibly for different joint sets. For $q < 0$ ideal slip occurs with Eq. (6.42) applying and $\partial \dot{\underline{u}}^S / \partial n$ (≥ 0) not explicitly determined by the stress conditions.

With the introduction of the continuous slip field $\underline{u}^S(\underline{x}, t)$, the in-plane strain (and rotation) discontinuities are also replaced by continuous strain (rotation) fields $\underline{e}^S(\underline{x}, t)$, $\underline{\omega}^S(\underline{x}, t)$ determining the net relative strain

(relative rotation) due to joint slip. In particular, by analogy with Eq. (6.44),

$$\frac{\partial \omega^S}{\partial n} = \frac{1}{d} \bar{E} \bar{r} = \nabla_n \left(\frac{1}{d} \bar{U} \right), = \nabla_n \left(\frac{\partial \underline{u}^S}{\partial n} \right). \quad (6.48)$$

Recalling that ∇_n is the in-plane gradient perpendicular to \underline{n} , we have

$$\underline{e}^S(\underline{x}) = \frac{1}{2} \left\{ \nabla_n \underline{u}^S(\underline{x}) + [\nabla_n \underline{u}^S(\underline{x})]^T \right\} \quad (6.49)$$

within an additive symmetric tensor function of the in-plane coordinates. The latter is set to zero since it is only the change of \underline{e}^S along the normal which measures the joint slip contribution to block strain. In fact, it is only the normal derivative $\partial \underline{u}^S / \partial n$ which enters the constitutive equations so that $\underline{u}^S(\underline{x})$ is determined only within an additive in-plane vector function of the in-plane coordinates. Thus, the continuum decomposition

$$\underline{u}(\underline{x}) = \underline{u}^C(\underline{x}) + \underline{u}^S(\underline{x}) \quad (6.50)$$

allows transfer of such vector functions between \underline{u}^C and \underline{u}^S .

The block strain \underline{e}^b is given by

$$\underline{e}^b(\underline{x}) = \underline{e}^C(\underline{x}) + \underline{e}^S(\underline{x}) \quad (6.51)$$

uniquely (unaffected by any such transfer). It must be emphasized that Eq. (6.51) is not a strain decomposition associated with the total displacement decomposition Eq. (6.50) since \underline{e}^S is given by the in-plane gradient only of \underline{u}^C .

When there are several parallel joint sets with normals \underline{n}_k ($k = 1, K$), the displacement decomposition Eq. (6.50) becomes

$$\underline{u}(\underline{x}) = \underline{u}^c(\underline{x}) + \sum_{k=1}^K \underline{u}_k^s(\underline{x}) \quad (6.52)$$

and the block strain Eq. (6.51) becomes

$$\underline{e}^b(\underline{x}) = \underline{e}^c(\underline{x}) + \sum_{k=1}^K \underline{e}_k^s(\underline{x}) \quad (6.53)$$

where

$$\underline{e}_k^s(\underline{x}) = \frac{1}{2} \{ \nabla \underline{n}_k \underline{u}_k^s(\underline{x}) + [\nabla \underline{n}_k \underline{u}_k^s(\underline{x})]^T \} \quad (6.54)$$

Note that the in-plane gradient operator $\nabla \underline{n}_k$ changes with \underline{n}_k . Also joint slip may be governed by different criteria for the different sets, so in general the joint functions in Eq. (6.45) and (6.47) become $g_k(\sigma)$ and $f_k(\tau, \sigma)$, $F_k(q)$ for the \underline{n}_k set. For simplicity common joint functions are adopted in the illustration.

Boundary conditions will be the usual conditions of traction, total displacement (velocity), or appropriate combinations. We have noted that the permitted transfer between \underline{u}^c and \underline{u}^s does not affect $\partial \dot{\underline{u}}^s / \partial n$ nor \underline{e}^b , which are the quantities governed by constitutive laws.

Joint dilation (contraction) described by normal velocity discontinuities across joints may be treated similarly by introducing a continuous dilation displacement field $\underline{u}^d(\underline{x}, t)$ associated with the joint set of orientation \underline{n} , where now \underline{u}^d is parallel to \underline{n} . The normal strain discontinuities across the joints contribute to the block

deformation as do the E_j in Eq. (6.25), and here become a continuous strain field $\tilde{e}^d(\underline{x})$

$$\tilde{e}^d(\underline{x}) = \frac{1}{2} \{ \nabla n \underline{u}^d(\underline{x}) + [\nabla n \underline{u}^d(\underline{x})]^T \} \quad (6.55)$$

which adds to Eq. (6.51). Several joint sets are treated as in the slip case already described. This dilation (contraction) may be a separate property of joint filling material, requiring an independent description, or may be linked directly to slip (dilation accompanying slip at constant normal traction) as described in Ref. [79] when \underline{u}^d is related to \underline{u}^s .

In dynamic situations the particle acceleration is the second derivative of the total displacement $\underline{u}(\underline{x}, t)$, so that momentum balance requires

$$\rho \ddot{\underline{u}} = -\text{div } \underline{\sigma} + \rho \underline{b} \quad (6.56)$$

where ρ is the initial intact material density and \underline{b} is the body force per unit mass (and here gravity effects over extended vertical sections may be relevant).

Within the spirit of the length scale assumptions already made each joint set may have a gradually varying orientation

$$\underline{n} = \underline{n}(\underline{x}) \quad (6.57)$$

where changes of \underline{n} over a few block dimensions are small, but not necessarily over the gross scale. This variation includes non-parallelism and curvature. Similarly non-uniform spacing

$$d = d(\underline{x}) \quad (6.58)$$

is permitted with the same restriction on gradients.

Finally, we mention a recently received manuscript [80] which describes an alternative continuum characterization of jointed rock mass. It is again assumed that there is a representative region of several block dimensions in which overall stress gradients are small and in which the two orthogonal joint sets considered are separately parallel. Staggered joints are allowed and a mean frequency is introduced which reduces to the separation reciprocal for continuous joints. Joints are considered as discontinuity surfaces, but now the discontinuities in tangential and normal displacement are linearly related to the shear and normal tractions respectively, defining two stiffness coefficients. Thus, the concepts of cohesion and irreversible slip (and dilation) are not incorporated. The joints and intact rock blocks are considered as two elastic phases of an overall elastic composite and, following Hill's theory, stress concentration factors for the rock and joint are introduced, first for the rock and one joint set and then regarding this as the matrix phase combined with the second joint set. These concentration factors (ratio of mean joint stress to overall stress) are estimated for different staggered joint geometries in representative rectangular blocks subjected to simple boundary loading, both by analytic approximation and finite element calculations which are in good agreement. The theory does not incorporate the effects of non-uniform displacement discontinuities across the joints on the block deformation.

6.6 BI-AXIAL LOADING

A simple illustration is obtained from uniform bi-axial loading, plane strain or plane stress, of a rectangular mass containing two joint sets symmetric about the principal stress axes, as shown in Fig. 6.7. Uni-axial displacement, $u_2 \equiv 0$, is a particular case. From the uniformity of loading and symmetry of the joint sets the total displacement field with respect to the axes $O_{x_1x_2}$ shown in Fig. 6.7 has the simple form

$$\underline{u} = [u_1(x_1, t), u_2(x_2, t), u_3(x_3, t)] , \quad (6.59)$$

where $u_3 \equiv 0$ in plane strain. If there is only a single joint set with orientation \underline{n} not parallel to one of the principal axes, then once slip occurs the displacement will not have the simple form of Eq. (6.59) and solution is non-trivial. The two joint sets, not necessarily orthogonal, have orientations

$$\underline{n}_1 = (\cos\theta, \sin\theta, 0), \underline{n}_2 = (\cos\theta, -\sin\theta, 0), 0 < \theta < \pi/2. \quad (6.60)$$

For both plane strain and plane stress there are no components of shear traction on the joint planes in the x_3 -direction so all slip must take place in the $O_{x_1x_2}$ plane. No shear traction and hence no slip can occur for $\theta = 0$ or $\pi/2$ since $O_{x_1x_2}$ are principal stress axes. Depending on the slip criterion and relative values of σ_1, σ_2 , there can be ranges of θ for which no slip arises. In particular, isotropic loading $\sigma_1 \equiv \sigma_2$ has zero shear traction (hence no slip) on all planes,

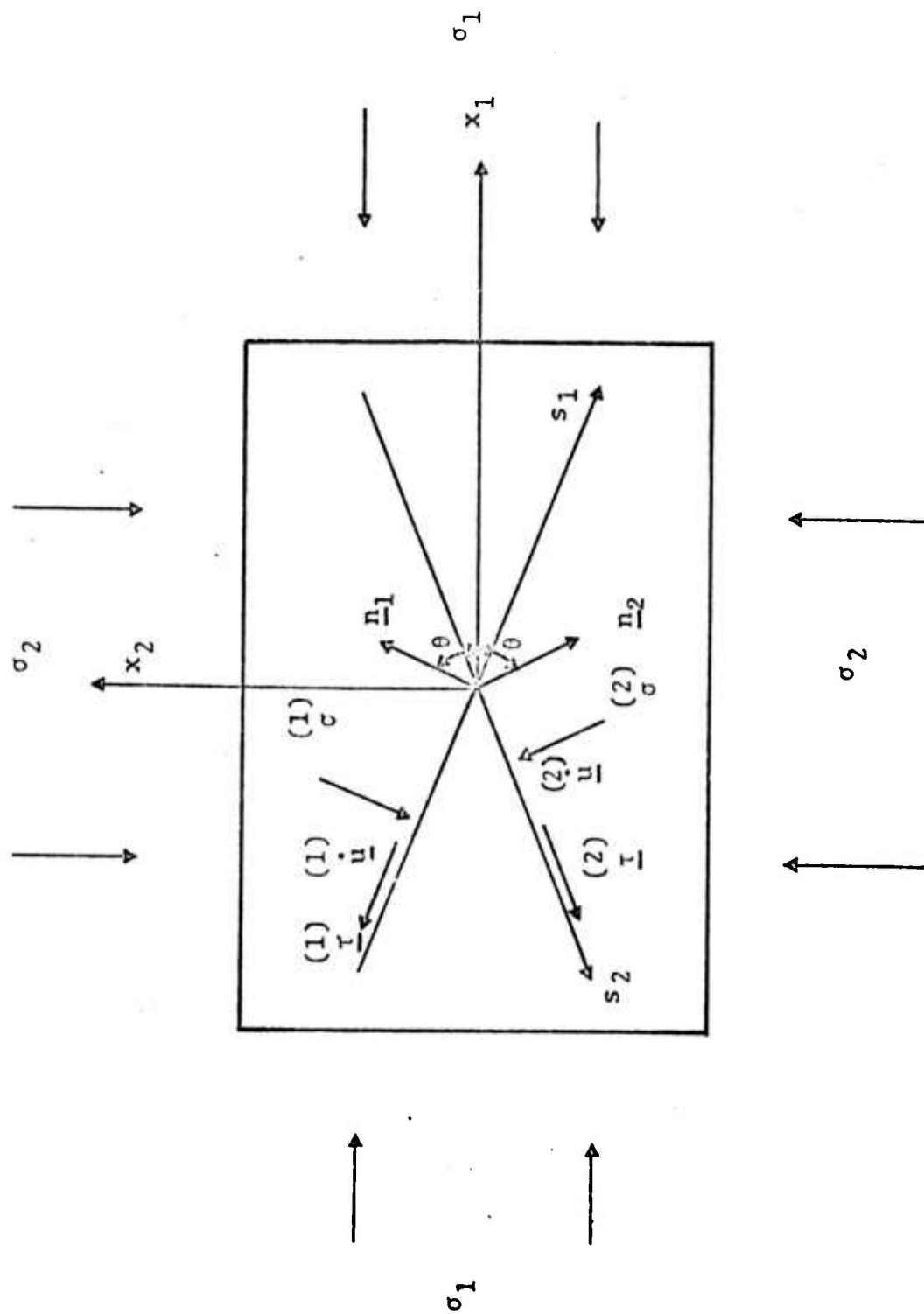


Fig. 6.7--Bi-axial loading for two symmetric joint sets.

For convenience, consider a loading cycle with $\sigma_1 \geq \sigma_2$, then at all stages the shear tractions on the respective joint planes are

$$\begin{aligned} (1) \quad \underline{\tau} &= \tau \underline{v}_1, & \underline{v}_1 &= (-\sin\theta, \cos\theta), \\ (2) \quad \underline{\tau} &= \tau \underline{v}_2, & \underline{v}_2 &= (-\sin\theta, -\cos\theta), \end{aligned} \quad (6.61)$$

$$\tau = \frac{1}{2} (\sigma_1 - \sigma_2) \sin 2\theta, \geq 0,$$

and the normal stresses are

$$\sigma = \sigma^{(1)} = \sigma^{(2)} = \sigma_1 \cos^2 \theta + \sigma_2 \sin^2 \theta, > 0. \quad (6.62)$$

These tractions and the directions of the consequent slip velocity fields (when slip is initiated) $\underline{\dot{u}}^{(1)}, \underline{\dot{u}}^{(2)}$ are shown in Fig. 6.7. Because of the assumed symmetry about the Ox_1 axis we could seek a solution with $\underline{\dot{u}}^{(1)} = \underline{\dot{u}}^{(2)} = \dot{u}^s$, but also, by symmetry about the Ox_2 axis, we could try $\underline{\dot{u}}^{(1)} = -\underline{\dot{u}}^{(2)} = \dot{u}^s$. In fact both these approaches lead to the same total velocity fields (and block deformation), the difference of the two slip fields corresponding to permitted arbitrary fields in $\underline{\dot{u}}^{(1)}$ and $\underline{\dot{u}}^{(2)}$ with respective zero normal gradients. Starting with unrelated fields $\underline{\dot{u}}^{(1)}, \underline{\dot{u}}^{(2)}$ illustrates how the total velocity field is independent of any such symmetry choice.

When slip occurs the velocity fields $\underline{\dot{u}}^{(1)}, \underline{\dot{u}}^{(2)}$ contribute the in-plane strain rates, by Eq. (6.54),

$$\dot{e}_{s_1 s_1}^{(1)} = - \frac{\partial}{\partial s_1} \dot{u}^{(1)}(x_1, x_1, t) = \left(-\sin\theta \frac{\partial}{\partial x_1} + \cos\theta \frac{\partial}{\partial x_2} \right) \dot{u}^{(1)},$$

$$\dot{e}_{s_2 s_2}^{(2)} = \frac{\partial}{\partial s_2} \dot{u}^{(2)}(x_1, x_2, t) = \left(-\sin\theta \frac{\partial}{\partial x_1} - \cos\theta \frac{\partial}{\partial x_2} \right) \dot{u}^{(2)},$$

(6.63)

respectively, with Cartesian components

$$\dot{e}_{11}^{(1)} = \sin^2\theta \left(-\sin\theta \frac{\partial}{\partial x_1} + \cos\theta \frac{\partial}{\partial x_2} \right) \dot{u}^{(1)},$$

$$\dot{e}_{11}^{(2)} = \sin^2\theta \left(-\sin\theta \frac{\partial}{\partial x_1} - \cos\theta \frac{\partial}{\partial x_2} \right) \dot{u}^{(2)},$$

$$\dot{e}_{22}^{(1)} = \cos^2\theta \left(-\sin\theta \frac{\partial}{\partial x_1} + \cos\theta \frac{\partial}{\partial x_2} \right) \dot{u}^{(1)},$$

(6.64)

$$\dot{e}_{22}^{(2)} = \cos^2\theta \left(-\sin\theta \frac{\partial}{\partial x_1} - \cos\theta \frac{\partial}{\partial x_2} \right) \dot{u}^{(2)},$$

$$\dot{e}_{12}^{(1)} = -\sin\theta \cos\theta \left(-\sin\theta \frac{\partial}{\partial x_1} + \cos\theta \frac{\partial}{\partial x_2} \right) \dot{u}^{(1)},$$

$$\dot{e}_{12}^{(2)} = \sin\theta \cos\theta \left(-\sin\theta \frac{\partial}{\partial x_1} - \cos\theta \frac{\partial}{\partial x_2} \right) \dot{u}^{(2)}.$$

The block strain components in Eq. (6.53) are

$$e_{ij}^b = e_{ij}^c + \dot{e}_{ij}^{(1)} + \dot{e}_{ij}^{(2)}, \quad (i, j = 1, 2) \quad (6.65)$$

where

$$e_{ij}^c = \frac{1}{2} \left(\frac{\partial u_i^c}{\partial x_j} + \frac{\partial u_j^c}{\partial x_i} \right), \quad (i, j = 1, 2) \quad (6.66)$$

and

$$e_{13}^b \equiv e_{23}^b \equiv 0, \quad e_{33}^b = e_{33}^c = e_{33}. \quad (6.67)$$

The latter is determined by the intact material properties and plane strain or plane stress condition.

We will consider the case of isotropic elastic blocks with the constitutive law of Eq. (6.27). Since $\sigma_{12} \equiv 0$, then

$$e_{12}^b = e_{12}^c + e_{12}^{(1)} + e_{12}^{(2)} = 0. \quad (6.68)$$

For both plane conditions the principal relations take the form

$$e_{11}^b = e_{11}^c + e_{11}^{(1)} + e_{11}^{(2)} = -A\sigma_1 + B\sigma_2, \quad (6.69)$$

$$e_{22}^b = e_{22}^c + e_{22}^{(1)} + e_{22}^{(2)} = B\sigma_1 - A\sigma_2, \quad (6.70)$$

where

$$\text{plane strain: } A = \frac{K + \frac{4}{3}G}{4G(K + \frac{1}{3}G)} > 0, \quad B = \frac{K - \frac{2}{3}G}{4G(K + \frac{1}{3}G)} > 0, \quad (6.71)$$

$$\text{plane stress: } A = \frac{K + \frac{1}{3}G}{3GK} > 0, \quad B = \frac{K - \frac{2}{3}G}{6GK} > 0. \quad (6.72)$$

The block relations are completed by

$$\text{plane strain: } e_{33} \equiv 0, \quad 2\left(K + \frac{1}{3}G\right)\sigma_3 = \left(K - \frac{2}{3}G\right)(\sigma_1 + \sigma_2), \quad (6.73)$$

$$\text{plane stress: } e_{33} \equiv 0, \quad 6GKe_{33} = \left(K - \frac{2}{3}G\right)(\sigma_1 + \sigma_2). \quad (6.74)$$

The decomposition of Eq. (6.52) for the form of displacement given in Eq. (6.59) yields

$$\dot{u}_1(x_1, t) = \dot{u}_1^c(x_1, x_2, t) - \sin\theta \dot{u}^{(1)}(x_1, x_2, t) - \sin\theta \dot{u}^{(2)}(x_1, x_2, t), \quad (6.75)$$

$$\dot{u}_2(x_2, t) = \dot{u}_2^c(x_1, x_2, t) + \cos\theta \dot{u}^{(1)}(x_1, x_2, t) - \cos\theta \dot{u}^{(2)}(x_1, x_2, t). \quad (6.76)$$

Differentiating \dot{u}_1, \dot{u}_2 with respect to x_2, x_1 , respectively:

$$\frac{\partial \dot{u}_1^c}{\partial x_2} - \sin\theta \frac{\partial \dot{u}^{(1)}}{\partial x_2} - \sin\theta \frac{\partial \dot{u}^{(2)}}{\partial x_2} = 0, \quad (6.77)$$

$$\frac{\partial \dot{u}_2^c}{\partial x_1} + \cos\theta \frac{\partial \dot{u}^{(1)}}{\partial x_1} - \cos\theta \frac{\partial \dot{u}^{(2)}}{\partial x_1} = 0. \quad (6.78)$$

The shear and normal tractions τ, σ are the same on both joint planes at each point \underline{x} , Eqs. (6.61) and (6.62), and to complete the symmetry it is assumed that both joint sets have common spacing d , common cohesion function $f(\tau, \sigma)$, and common hardening function $F(q)$. Then the slip history, and hence q , is identical for both joint sets, and since

$\dot{\underline{v}}_1 = \dot{\underline{v}}_2 = 0$ (reverse slip can be treated separately following the necessary elastic unloading and reverse loading) the slip criterion in Eq. (6.47) gives

$$\frac{\partial \dot{\underline{u}}^{(1)}}{\partial n_1} = \left(\cos \theta \frac{\partial}{\partial x_1} + \sin \theta \frac{\partial}{\partial x_2} \right) \dot{\underline{u}}^{(1)} = \dot{\lambda} , \quad (6.79)$$

$$\frac{\partial \dot{\underline{u}}^{(2)}}{\partial n_2} = \left(\cos \theta \frac{\partial}{\partial x_1} - \sin \theta \frac{\partial}{\partial x_2} \right) \dot{\underline{u}}^{(2)} = \dot{\lambda} . \quad (6.80)$$

For slip-hardening

$$\dot{\lambda} = \frac{\delta \dot{f}}{dF'(q)} \geq 0 , \quad q = \frac{d}{\delta} \frac{\partial \dot{\underline{u}}^{(1)}}{\partial n_1} , \quad (6.81)$$

and for ideal-slip $\dot{\lambda}$ is not related to stress conditions but Eq. (6.81) is replaced by

$$\dot{f} \equiv 0 , \quad \dot{\lambda} \geq 0 . \quad (6.82)$$

In the latter case d does not enter explicitly and need not be common to both joint sets.

Equations (6.68), (6.69), (6.70), (6.77), (6.78), (6.79), (6.80), and (6.81) formally provide eight relations for the two derivatives of each of $\dot{\underline{u}}_1^c, \dot{\underline{u}}_2^c, \dot{\underline{u}}^{(1)}, \dot{\underline{u}}^{(2)}$ in terms of stress rates. For ideal slip, Eq. (6.81) is replaced by an identity in the stress rates together with a required inequality on velocity gradients, and the velocity gradients are not fully determined by stress conditions. During purely elastic deformation of the blocks with no joint slip, $\dot{\underline{u}}^{(1)} = \dot{\underline{u}}^{(2)} = 0$, the total velocity field is continuous and governed by the elastic laws.

From Eqs. (6.77), (6.78), (6.79), (6.80) we find

$$\frac{\partial \dot{u}_1^c}{\partial x_2} = \frac{\partial \dot{u}_2^c}{\partial x_1} = \sin\theta \left(\frac{\partial \dot{u}_1^{(1)}}{\partial x_2} + \frac{\partial \dot{u}_2^{(2)}}{\partial x_2} \right) = -\cos\theta \left(\frac{\partial \dot{u}_1^{(1)}}{\partial x_1} - \frac{\partial \dot{u}_2^{(2)}}{\partial x_1} \right) \quad (6.83)$$

which imply Eqs. (6.77) and (6.78), and make (6.79) and (6.80) equivalent. But also the relations in Eq. (6.83) imply that Eq. (6.68) is satisfied identically, so in fact there are only seven independent relations. However, we require relations only for the total velocity gradients

$$\dot{e}_1 = \frac{\partial \dot{u}_1}{\partial x_1} = \frac{\partial \dot{u}_1^c}{\partial x_1} - \sin\theta \left(\frac{\partial \dot{u}_1^{(1)}}{\partial x_1} + \frac{\partial \dot{u}_2^{(2)}}{\partial x_1} \right), \quad (6.84)$$

$$\dot{e}_2 = \frac{\partial \dot{u}_2}{\partial x_2} = \frac{\partial \dot{u}_2^c}{\partial x_2} + \cos\theta \left(\frac{\partial \dot{u}_1^{(1)}}{\partial x_2} - \frac{\partial \dot{u}_2^{(2)}}{\partial x_2} \right)$$

together with the relative slips measured by the normal gradients, Eqs. (6.79) and (6.80). Eliminating $\partial \dot{u}_1^c / \partial x_1$, $\partial \dot{u}_2^c / \partial x_2$ by the elastic laws, Eqs. (6.69) and (6.70), and in-plane strain rates, Eq. (6.64), we find, using Eqs. (6.79) and (6.80), that

$$\dot{e}_1 = -A\dot{\sigma}_1 + B\dot{\sigma}_2 - \sin 2\theta \dot{\lambda}, \quad (6.85)$$

$$\dot{e}_2 = B\dot{\sigma}_1 - A\dot{\sigma}_2 + \sin 2\theta \dot{\lambda}. \quad (6.86)$$

Finally, for slip-hardening $\dot{\lambda}$ is related to the stress rates and loading history by Eq. (6.81), and for ideal-slip $\dot{\lambda}$ is not so determined but the identity, Eq. (6.82), relating $\dot{\sigma}_1$ and $\dot{\sigma}_2$ holds. In the latter case the lateral loading is fixed by the axial loading and slip criterion, and the slip is unrestricted unless boundary constraints are supplied, as, for

example, in uni-axial motion. Recall that $\dot{\lambda} \equiv 0$ when the stress conditions do not satisfy the slip criterion, and the deformation is purely elastic.

For illustration consider a hardening law, Eq. (6.36), with the simple linear cohesion function, Eq. (6.38):

$$f(\tau, \sigma) = \tau - \mu\sigma = F(q), \quad F(0) = \tau_0. \quad (6.87)$$

During loading with $\sigma_1 \geq \sigma_2$, by Eqs. (6.61) and (6.62),

$$\dot{f} = \alpha \dot{\sigma}_1 - \beta \dot{\sigma}_2, \quad \alpha = \cos^2 \theta (\tan \theta - \mu), \quad \beta = \sin^2 \theta (\cot \theta + \mu), \quad > 0. \quad (6.88)$$

By Eq. (6.31)

$$\dot{\lambda} = \frac{\delta}{d} \dot{q} = \frac{\delta}{d} \frac{\dot{f}}{F'(q)}, \quad = h(q) \dot{f} \quad \text{say}, \quad (6.89)$$

where $h(q) > 0$, approaches zero with full interlock, and increases indefinitely as ideal-slip is approached.

Consider isotropic loading to pressure p followed by further axial loading at constant lateral stress (confining pressure). During the axial loading f increases or decreases from $(\alpha - \beta)p = -\mu p$ as $\alpha \gtrless 0$. Hence for the cohesive stress τ_0 to be reached and slip to occur we require

$$\alpha > 0 \nless \tan \theta > \mu. \quad (6.90)$$

Then the loading $\dot{\sigma}_1 \geq 0$ has three distinct stages:

$$\text{I} \quad 0 \leq \sigma_1 = \sigma_2 \leq p, \quad -\dot{e}_1 = -\dot{e}_2 = (A-B)\dot{\sigma}_1, \quad (6.91)$$

$$\text{II} \quad \sigma_2 \equiv p, \quad -\dot{e}_1 = A\dot{\sigma}_1, \quad \dot{e}_2 = B\dot{\sigma}_1, \quad (6.92)$$

$$\dot{f} = \alpha \dot{\sigma}_1 > 0, \quad -\mu p \leq f \leq \tau_0,$$

$$\text{III} \quad \sigma_2 \equiv p, \quad f \geq \tau_0, \quad \dot{f} = \alpha \dot{\sigma}_1 > 0, \quad \dot{\lambda} = h(q) \dot{f},$$

$$- \dot{e}_1 = [A + \alpha h(q) \sin 2\theta] \quad , \quad (6.93)$$

$$\dot{e}_2 = [B + \alpha h(q) \sin 2\theta] \quad .$$

Since

$$A - B < A < A + \alpha h(q) \sin 2\theta \quad (6.94)$$

the $\sigma_1(-e_1)$ slopes for stages I, II, III, paths OP, PS, SL, in Fig. 6.8, decrease in sequence. If $F'(q)$ is increasing as shown in Fig. 6.6, then $h(q)$ is decreasing with q (and hence with $-e_1$) and the slope of SL increases with $(-e_1)$ as illustrated in Fig. 6.8. As $h \rightarrow 0$ (full interlock) the slope of SL approaches that of PS, the elastic stage II slope, from below, and hence elastic unloading LD (slope $1/A$) always has steeper slope than slip SL. As $h \rightarrow \infty$ (ideal-slip), the slope of SL approaches zero from above.

Slip commences at S where

$$\sigma_1 = \sigma_1^*(p) = \frac{\tau_0 + \beta p}{\alpha} \quad . \quad (6.95)$$

Thus, if $\sigma_1^*(p)$ is determined for a sequence of values p , and if a linear cohesion function f , Eq. (6.87) is appropriate to the gross response, then τ_0/α , β/α can be estimated, and hence μ and τ_0 . Furthermore, the slope of SL determines $h(q)$, and consequently

$$\frac{1}{h(q)} = d \hat{F}' \left(\frac{\partial u^S}{\partial n} \right), \quad \hat{F} \left(\frac{\partial u^S}{\partial n} \right) = F(q). \quad (6.96)$$

A consistent slope should be obtained for varying p if the

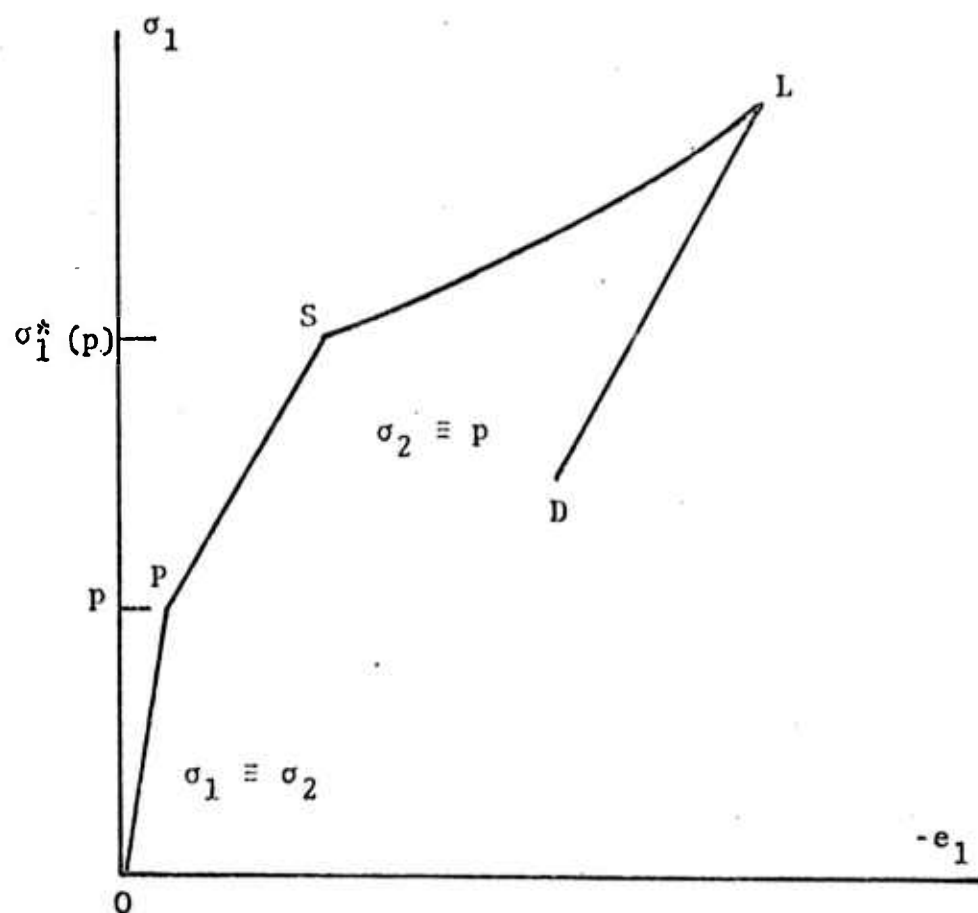


Fig. 6.8--Axial stress-strain path for bi-axial loading.

adopted model is appropriate. Clearly, less restrictive functions f, F can be considered when data inconsistent with this model is obtained.

These results apply to both plane strain and plane stress by appropriate choice of the constants A and B in Eqs. (6.71) and (6.72). The initial slip stress $\sigma_1^*(p)$ depends on the joint orientation θ , through α, β , but is always attained if σ_1 is increased sufficiently when the inequality in Eq. (6.90) holds.

Finally, we describe uni-axial displacement, $u \equiv 0$, for the same model. Setting $\dot{e}_2 \equiv 0$ in Eq. (6.86), together with the plane strain restriction $e_3 \equiv 0$, selecting A and B in Eq. (6.71), gives for elastic changes

$$\dot{\sigma}_1 = -\left(K + \frac{4}{3}G\right)\dot{e}_1, \quad \dot{\sigma}_2 = \frac{K - \frac{2}{3}G}{K + \frac{4}{3}G} \dot{\sigma}_1, \quad = r \dot{\sigma}_1, \quad (6.97)$$

$$\dot{f} = \dot{\sigma}_1 (\alpha - r\beta).$$

For slip to occur with increase of σ_1 we require

$$\alpha - r\beta > 0, \quad (6.98)$$

or equivalently,

$$\frac{\tan\theta(1-r)}{1 + r\tan^2\theta} > \mu, \quad (6.99)$$

which is a stronger requirement than the constant lateral stress condition in Eq. (6.90). Slip is initiated when

$$\sigma_1 = \sigma_1^* = \frac{\tau_a}{\alpha - r\beta}. \quad (6.100)$$

For continued increase of σ_1 slip occurs with

$$\sin 2\theta \dot{\lambda} = -B\dot{\sigma}_1 + A\dot{\sigma}_2 = h(q) \sin 2\theta [\alpha \dot{\sigma}_1 - \beta \dot{\sigma}_2], \quad (6.101)$$

provided that $\dot{\lambda} > 0$. From Eq. (6.101)

$$0 < \frac{\dot{\sigma}_2}{\dot{\sigma}_1} = \frac{B + \alpha h(q) \sin 2\theta}{A + \beta h(q) \sin 2\theta} = \frac{\alpha}{\beta} - \frac{A}{\beta} \left[\frac{\alpha - r\beta}{A + \beta h(q) \sin 2\theta} \right] < \frac{\alpha}{\beta}, \quad (6.102)$$

and

$$h(q) \dot{\lambda} = \dot{\lambda} = Ah(q) \dot{\sigma}_1 \left[\frac{\alpha - r\beta}{A + \beta h(q) \sin 2\theta} \right] > 0. \quad (6.103)$$

Setting

$$s = \frac{A}{\alpha} \left[\frac{\alpha - r\beta}{A + \beta h(q) \sin 2\theta} \right] > 0, \quad (6.104)$$

we have

$$\frac{\dot{\sigma}_2}{\dot{\sigma}_1} = \frac{\alpha}{\beta} (1-s), \quad (6.105)$$

and

$$\alpha s - (\alpha - r\beta) = -\beta h(q) \sin 2\theta (\alpha - r\beta) < 0. \quad (6.106)$$

Then, by Eqs. (6.85), (6.86) and (6.105)

$$-\dot{e}_1 = (A-B) (\dot{\sigma}_1 + \dot{\sigma}_2) = \dot{\sigma}_1 (A-B) \left[1 + \frac{\alpha}{\beta} (1-s) \right], \quad (6.107)$$

or

$$\left[1 + \frac{\alpha}{\beta} (1-s) \right] \dot{\sigma}_1 = -2 \left(K + \frac{1}{3} G \right) \dot{e}_1. \quad (6.108)$$

Since $2\left(K + \frac{1}{3}G\right) = \left(K + \frac{4}{3}G\right)(1+r)$, the ratio of the slip path SL slope to that of the elastic slope, paths OS and LD, shown in Fig. 6.9, is $(1+r)/\left[1 + \frac{\alpha}{\beta}(1-s)\right]$. But

$$(1+r) - \left[1 + \frac{\alpha}{\beta}(1-s)\right] = \frac{1}{\beta}[\alpha s - (\alpha - r\beta)], < 0 \quad (6.109)$$

by Eq. (6.106), so that the SL slope for all q is less than the elastic slope. For $F(q)$ increasing with slip, Eqs. (6.89), (6.104), and (6.108) show that the slope of SL is also increasing.

Now, by Eqs. (6.88) and (6.98),

$$r < \frac{\alpha}{\beta} = 1 - \frac{\mu}{\beta} < 1, \quad (6.110)$$

so the ratio $\dot{\sigma}_2/\dot{\sigma}_1$ may be greater or smaller during slip, Eq. (6.105), than during elastic deformation, Eq. (6.97), depending on the magnitude of s . For $s = 0$, corresponding to ideal slip, Eq. (6.105) yields a greater ratio than Eq. (6.97), and hence after a complete load-unload cycle of σ_1 OSLD in Fig. 6.9, σ_2 is still positive ($>\sigma_1 = 0$) at D, and the direction of the shear stress is opposite to that during the slip loading SL. Reverse slip may possibly occur before complete reduction of σ_1 to zero. The ideal-slip solution is obtained by setting $s = 0$ in Eqs. (6.105) and (6.108) and evaluating $\dot{\lambda}$ by the first relation of Eq. (6.101).

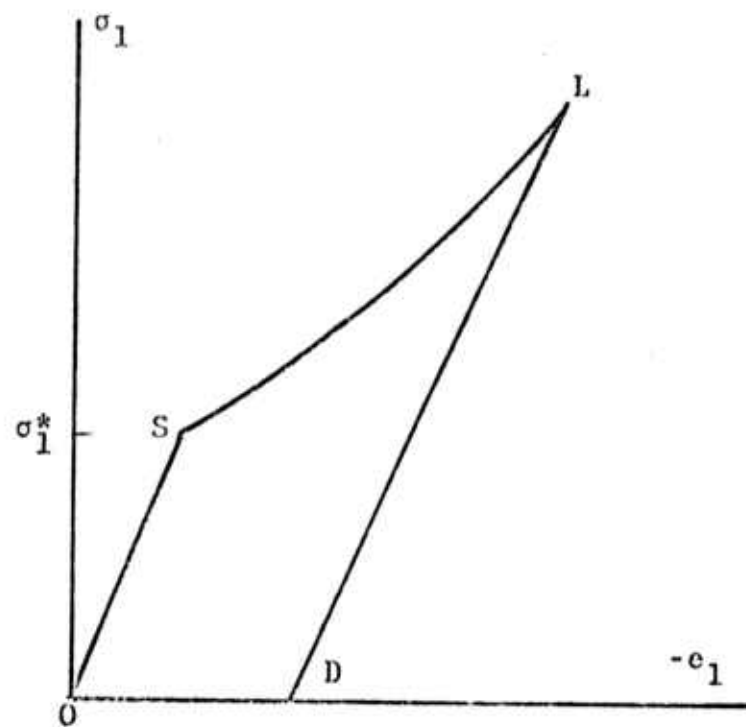


Fig. 6.9--Axial stress-strain path for uniaxial displacement.

VII. FLUID-ROCK INTERACTION NEAR AN INJECTION WELL

7.1 INTRODUCTION

7.1.1 Hydraulically Induced Tensile Cracks

The process of injecting fluid under pressure into the ground alters the tectonic state of stress in the solid material from $\sigma_{ij}^{(0)}$ (tension positive) to some new state $S_{ij} = \sigma_{ij}^{(1)} + \sigma_{ij}^{(0)}$ where $\sigma_{ij}^{(1)}$ is the stress change in the rock due to the injection process. In the near vicinity of an injection site, rock stresses can be sufficiently altered to cause tensile cracks. For the past 25 years, oil companies have been inducing tensile cracks by pumping into oil bearing rock for the purpose of increasing the effective radius of a well. It is not uncommon for these hydraulically induced tensile cracks to arise from pumping pressures significantly less than pressures due to overburden. Hubbert and Willis^[81] attribute this phenomena to the presence of tectonic stresses in horizontal plane which are less compressive than the vertical component of stress due to overburden pressures. As they point out, this appears to be the case in the Gulf Coast area, which is a tectonically relaxed region as evidenced by a history of normal faulting.

The conventional thinking on the subject of hydrofracture is that: (1) the plane of the tensile cracks is oriented normal to the most tensile (least compressive) principal stress, $\sigma_1^{(0)}$, and (2) an overpressure p (pressure in excess of the resident pressure, $p^{(0)}$) equal in magnitude to $\sigma_1^{(0)}$, is required to hold open and extend the cracks. This conceptual model for explaining the behavior of hydraulically induced cracks does not account for (1) the combined geometry of the injection cavity and the crack that is produced, i.e., the influence of $\sigma_{ij}^{(1)}$ for non-penetrating fluids on the tectonic field $\sigma_{ij}^{(0)}$, (2) changes in the rock

stress due to penetration of the injection fluid, and (3) gradients in fluid pressure along the crack – the mechanism by which the crack is eventually arrested. Experience and empirical equations must be heavily relied on to regulate the hydrofracture process since no test-bed computer code is presently available for simulating the development and growth of hydraulically induced cracks. The 2D FRI code, which is used for producing the results of Section 7.4, serves to analyze the state of stress, including the effects of fluid penetration, for an axisymmetric injection system. It appears likely, however, that modeling in 3D geometry will be required to achieve a detailed computer simulation of the hydrofracture process.

7.1.2 Hydraulically Triggered Shear Failure

Fluid injection in the presence of large tectonic stresses $\sigma_{ij}^{(0)}$ with markedly different principal stresses $\sigma_1^{(0)} \gg \sigma_3^{(0)}$, as in an earthquake prone area, can lead to shear failure in addition to the hydraulically induced tensile cracks that emanate from the injection cavity. Whereas, the tensile cracks tend to align normal to the least compressive principal stress $\sigma_1^{(0)}$, shear failures would be expected to occur on planes 30° to 40° from the plane on which $\sigma_1^{(0)}$ acts. As illustrated in the Mohr diagram of Fig. 7.1, shear stresses in the plane of $\sigma_1^{(0)}$ and $\sigma_3^{(0)}$ are the first to come in contact with the shear-failure envelope as the pressure in the pore fluid mounts, i.e., as tensile stresses $\sigma_{ij}^{(1)}$ are induced into the rock matrix by the injection system.

We cite two examples of what appears to be shear failures triggered by fluid injection. The swarm of small earthquakes that occurred near Denver, Colorado during the period 1962 to 1967 were most likely triggered by the

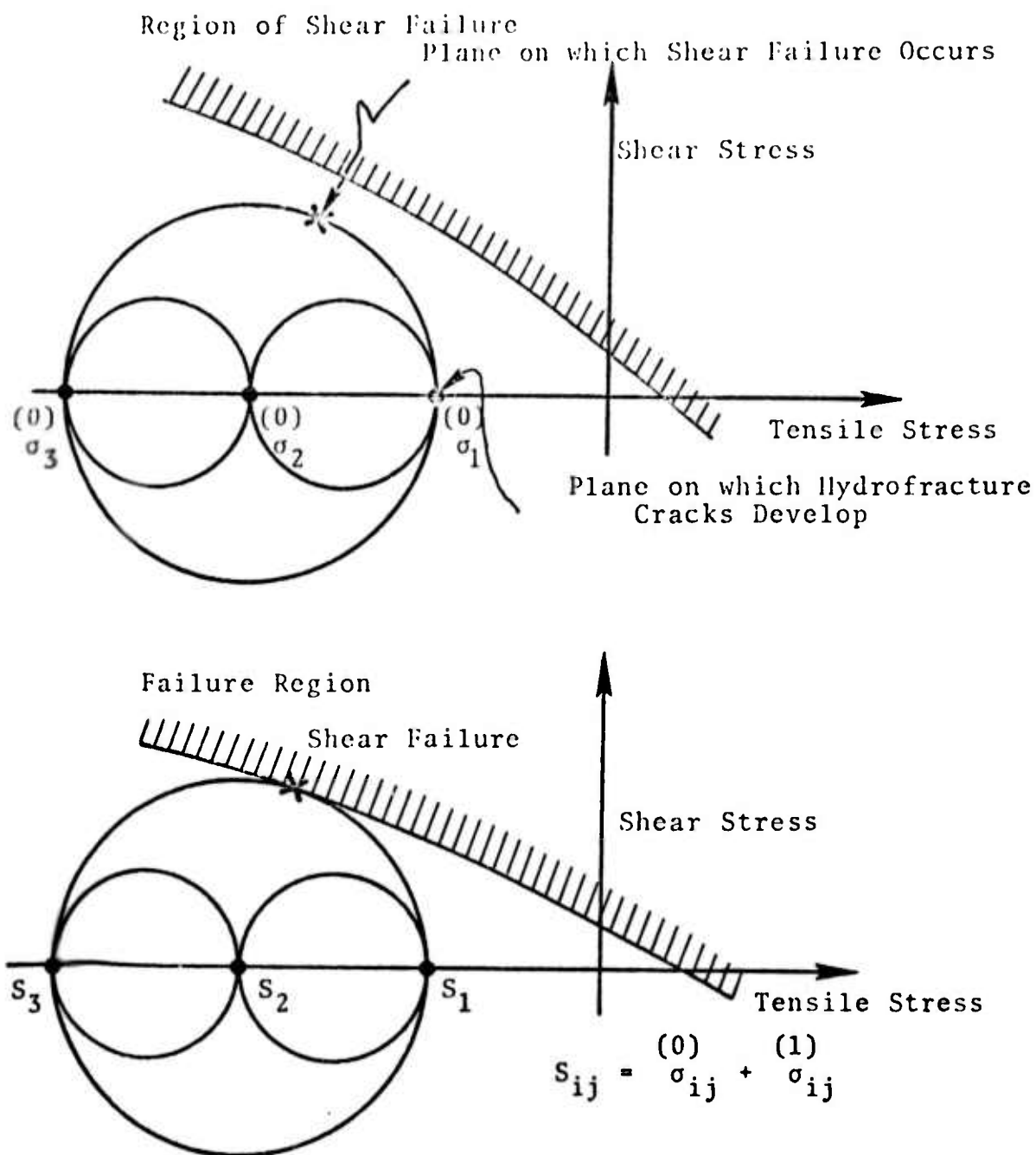


Fig. 7.1--Tectonic state of stress prior to and during fluid injection.

pumping of waste fluids into a 3671-meter disposal well by the Rocky Mountain Arsenal.^[82] More recently, the controlled injection of water into the Rangley Field, Western Colorado has provided USGS researchers data on the potential for triggering small earthquakes by injecting fluid into the ground.^[83,84] In this experimental program, water was injected into the western portion of the Rangley Field, along a previously mapped fault. As the water was driven into the faulted region, small earthquakes began to occur. When the pumping was stopped, the occurrence of earthquakes persisted for a period, then as the fluid pressure diminished by diffusion, the earthquake activity also diminished.

7.1.3 Consolidation Theory

Various theoretical models have been developed for describing the mechanical interactions between the solid and fluid constituents of a saturated porous solid material such as soil or rock. Much of this work has been motivated by structural engineers concerned with the gradual settlement of saturated soils. A simple mechanism to explain this consolidation process was first proposed by Terzaghi.^[85] The next major extension of the theory of consolidation was made by Biot^[86] in which the linear consolidation process was modeled in three spatial dimensions. This formulation, which has extended and refined somewhat since Biot's initial work,^[87] has been proven satisfactory for explaining a variety of experimental results such as the consolidation of a solid sphere of saturated clay,^[88, 89] and the consolidation of a two storied aquifer.^[90]

In Biot's formulation and in all subsequent formulations, we find at least one constitutive constant that serves to account for mechanical interactions between the fluid and the rock. Generally, we find two constants which are operationally defined through explicit laboratory tests.^[86]

Although it is intuitively obvious that the interaction terms must be related to the elastic moduli of the rock grains, we know of no formulation for the quasi-static behavior of an elastic fluid-rock composite that explains the physical processes for the interactions. Such a formulation is needed if we are to provide a mechanism for nonlinear adjustments in the rock grains such as occurs in liquifaction. In Ref. [3] the groundwork for such a formulation was presented using the TINC framework. In the following section, this formulation is extended somewhat so that the mechanical interactions in a fluid-rock composite are developed entirely in terms of the constitutive properties of the rock grains, the porous rock matrix, and the pore fluid; the need for hypothetical interaction coefficients has been eliminated.

7.2 QUASISTATIC THEORY OF FLUID-ROCK COMPOSITE

7.2.1 Simplifying Assumptions

In the subsequent formulation for the mechanical interactions between elastic rock and interspersed compressible pore fluid, we consider only linear behavior. As such, the formulation applies directly to soils or rocks where:

- (1) Strains in the solid material are small compared to unity.
- (2) Stresses in the constituents are linearly related to strains in an isotropic manner.
- (3) Velocities are slowly varying so that inertial forces can be neglected.
- (4) Seepage through the rock is governed by Darcy's law.
- (5) The fluid acts as a single constituent, i.e., no fluid separation occurs. The pores are saturated.

7.2.2 TINC Notation

The TINC framework for composite materials is based on particle stresses and strains, averaged over many particles.^[1,2,3, 77] Consequently, the TINC nomenclature must differ somewhat from that used in conventional consolidation theory.^[86, 87, 88]

Following the TINC notation, we distinguish the individual constituents by a superscripted (α) where, for this development, we will use $\alpha = 1$ to denote the solid constituent and $\alpha = 2$ to denote the pore fluid. Furthermore, we distinguish average particle stress, strain, and density terms by a superscripted e in addition to the superscripted (α) which is used to avoid confusion between average particle field variables and

and corresponding gross field variables for the composite. A subscripted 0 is used to denote initial values. We now define the following terms:

$V^{(\alpha)}$ = volume of constituent (α) excluding the volume occupied by the complementary constituent with

$$V = V^{(1)} + V^{(2)} \quad (7.1)$$

$$n^{(\alpha)} = V^{(\alpha)} / V \quad (7.2)$$

= volume fraction, which, from Eq. (7.1) gives

$$n^{(1)} + n^{(2)} = 1. \quad (7.3)$$

$M^{(\alpha)}$ = mass of constituent (α) , hence

$$M = M^{(1)} + M^{(2)} \quad (7.4)$$

$$\rho^{(\alpha)} e = M^{(\alpha)} / V \quad (7.5)$$

= mass density of particles in constituent (α) , average over many particles.

$$\rho^{(\alpha)} = M^{(\alpha)} / V \quad (7.6)$$

= gross (partial) density of constituent (α) . Combining Eqs. (7.5) and (7.2) with Eq. (7.6) gives

$$\frac{(\alpha)}{\rho} = \frac{(\alpha)}{n} \frac{(\alpha)}{\rho} e \quad (7.7)$$

$\frac{(\alpha)}{u_i}$ = displacement component of a point in constituent (α) from its initial position. From the theory of deformable materials, we have

$$\frac{(\alpha)}{\varepsilon} = \frac{\partial u_i}{\partial x_i} = \frac{\frac{(\alpha)}{\rho}}{\frac{(\alpha)}{\rho}} - 1 \quad (7.8)$$

= gross (partial) volumetric strain of constituent (α) .

$$\frac{(\alpha)}{\varepsilon} e = \frac{\frac{(\alpha)}{\rho} e}{\frac{(\alpha)}{\rho} e} - 1 \quad (7.9)$$

= volumetric strain of the particles in constituent (α) averaged over many particles. From Eqs. (7.8), (7.9), and (7.7) we relate volumetric particle strain to volumetric gross strain.

$$\frac{(\alpha)}{\varepsilon} e = \frac{\frac{(\alpha)}{n}}{\frac{(\alpha)}{n_0}} \left(1 + \frac{(\alpha)}{\varepsilon} \right) - 1 \quad (7.10)$$

$\frac{(\alpha)}{\sigma_{ij}}$ = gross (partial) stress, i.e., the force component in constituent (α) per unit area of composite.

$$\frac{(\alpha)}{\sigma_{ij}} e = \frac{1}{\frac{(\alpha)}{n}} \frac{(\alpha)}{\sigma_{ij}} \quad (7.11)$$

= particle stress in constituent (α) averaged over many particles.

7.2.3 Constitutive Equations

We relate average particle stress to average particle strain using Hooke's law for a linearly elastic isotropic material

$$\sigma_{ij}^{(\alpha)e} = 2 \mu^{(\alpha)e} \left(\epsilon_{ij}^{(\alpha)e} - \frac{1}{3} \delta_{ij} \epsilon^{(\alpha)e} \right) + K^{(\alpha)e} \delta_{ij} \epsilon^{(\alpha)e} \quad (7.12)$$

where $\mu^{(\alpha)e}$ is the shear modulus of the particle material and $K^{(\alpha)e}$ is the bulk modulus of the particle material. We assume that equivoluminal strains in the rock matrix give rise to no changes in the pore volume. With this assumption we decouple shearing modes in the rock matrix from the state of stress and strain in the pore fluid and write

$$\sigma_{ij}^{(1)} - \delta_{ij} \sigma^{(1)} = 2 \mu^{(1)} \left(\epsilon_{ij}^{(1)} - \frac{1}{3} \delta_{ij} \epsilon^{(1)} \right) \quad (7.13)$$

where $\mu^{(1)}$ is the shear modulus of the porous rock matrix and $\sigma^{(1)} = \frac{1}{3} \sigma_{ij}^{(1)} \delta_{ij}$ is the dilatational stress in the rock matrix.

More generally we denote dilatational particle stress by

$$\sigma^{(\alpha)e} = \frac{1}{3} \sigma_{ij}^{(\alpha)e} \delta_{ij} \quad (7.14)$$

and gross dilatational stress by

$$\sigma^{(\alpha)} = \frac{1}{3} \sigma_{ij}^{(\alpha)} \delta_{ij} \quad (7.15)$$

Isolating the dilatational component of Eq. (7.12), we get

$$\binom{(\alpha)}{\sigma} e = \binom{(\alpha)}{K} e \binom{(\alpha)}{\epsilon} e . \quad (7.16)$$

Relating effective particle stress to gross stress by Eq. (7.11) and effective particle strain to gross strain by Eq. (7.10) gives

$$\begin{aligned} \binom{(\alpha)}{\sigma} &= \binom{(\alpha)}{n} \binom{(\alpha)}{K} e \binom{(\alpha)}{\epsilon} e \\ &= \binom{(\alpha)}{n} \binom{(\alpha)}{K} e \left[\frac{\binom{(\alpha)}{n}}{\binom{(\alpha)}{n_0}} \left(1 + \binom{(\alpha)}{\epsilon} \right) - 1 \right] \end{aligned} \quad (7.17)$$

The dilatational stress components $\binom{(1)}{\sigma}$ and $\binom{(2)}{\sigma}$ given by this expression are differentiated with respect to $\binom{(1)}{\epsilon}$ and $\binom{(2)}{\epsilon}$ to determine linear stress-strain coefficients in the expression

$$\begin{aligned} \begin{Bmatrix} \binom{(1)}{\sigma} \\ \binom{(2)}{\sigma} \end{Bmatrix} &= \begin{bmatrix} C_{11} & C_{12} \\ C_{21} & C_{22} \end{bmatrix} \begin{Bmatrix} \binom{(1)}{\epsilon} \\ \binom{(2)}{\epsilon} \end{Bmatrix} \end{aligned} \quad (7.18)$$

where

$$C_{11} = \frac{\partial \binom{(1)}{\sigma}}{\partial \binom{(1)}{\epsilon}} = \binom{(1)}{K} e \left(\frac{\binom{(1)}{n}}{n_0} + \frac{\partial \binom{(1)}{n}}{\partial \binom{(1)}{\epsilon}} \right) + O(\epsilon)$$

$$C_{12} = \frac{\partial \binom{(1)}{\sigma}}{\partial \binom{(2)}{\epsilon}} = \binom{(1)}{K} e \frac{\partial \binom{(1)}{n}}{\partial \binom{(2)}{\epsilon}} + O(\epsilon)$$

$$C_{21} = \frac{\partial \sigma^{(2)}}{\partial \epsilon^{(1)}} = \frac{(2)}{K} e \frac{\partial n^{(2)}}{\partial \epsilon^{(1)}} + O(\epsilon) = - \frac{(2)}{K} e \frac{\partial n^{(1)}}{\partial \epsilon^{(1)}} + O(\epsilon)$$

$$C_{22} = \frac{\partial \sigma^{(2)}}{\partial \epsilon^{(2)}} = \frac{(2)}{K} e \left(\frac{(2)}{n_0} + \frac{\partial n^{(2)}}{\partial \epsilon^{(2)}} \right) + O(\epsilon) = \frac{(2)}{K} e \left(1 - \frac{(1)}{n_0} - \frac{\partial n^{(1)}}{\partial \epsilon^{(2)}} \right) + O(\epsilon)$$

using the fact that $n^{(2)} = 1 - n^{(1)}$ from Eq. (7.3). Being consistent with our restriction to linear strain theory, we will neglect the higher order terms, $O(\epsilon) \ll 1$.

In order to obtain results that are independent of loading path, we apply Betti's reciprocal theorem to write^[60]

$$C_{12} = C_{21}$$

or

$$\frac{(1)}{K} e \frac{\partial n^{(1)}}{\partial \epsilon^{(2)}} = + \frac{(2)}{K} e \frac{\partial n^{(2)}}{\partial \epsilon^{(1)}} = - \frac{(2)}{K} e \frac{\partial n^{(1)}}{\partial \epsilon^{(1)}} \quad (7.19)$$

Equation (7.18) is inverted to obtain strain-stress constitutive relations

$$\begin{Bmatrix} \epsilon^{(1)} \\ \epsilon^{(2)} \end{Bmatrix} = \begin{bmatrix} D_{11} & D_{12} \\ D_{21} & D_{22} \end{bmatrix} \begin{Bmatrix} \sigma^{(1)} \\ \sigma^{(2)} \end{Bmatrix} \quad (7.20)$$

where

$$\begin{aligned}
D_{11} &= \frac{\left(1 - n_0^{(1)} - \frac{\partial n^{(1)}}{\partial \epsilon^{(2)}}\right)}{\frac{\partial n^{(1)}}{\partial \epsilon^{(1)}}} D_{12} \\
D_{12} = D_{21} &= \frac{\frac{\partial n^{(1)}}{\partial \epsilon^{(2)}}}{K^{(2)} e_{n_0^{(1)}} \left[1 - n_0^{(1)} - \frac{\partial n^{(1)}}{\partial \epsilon^{(2)}} + \left(\frac{1 - n_0^{(1)}}{n_0^{(1)}}\right) \frac{\partial n^{(1)}}{\partial \epsilon^{(1)}}\right]} \\
&= - \frac{\frac{\partial n^{(1)}}{\partial \epsilon^{(1)}}}{K^{(1)} e_{n_0^{(1)}} \left[1 - n_0^{(1)} - \frac{\partial n^{(1)}}{\partial \epsilon^{(2)}} + \left(\frac{1 - n_0^{(1)}}{n_0^{(1)}}\right) \frac{\partial n^{(1)}}{\partial \epsilon^{(1)}}\right]} \\
D_{22} &= - \frac{\left(n_0^{(1)} + \frac{\partial n^{(1)}}{\partial \epsilon^{(1)}}\right)}{\frac{\partial n^{(1)}}{\partial \epsilon^{(2)}}} D_{12}
\end{aligned}$$

At this point we still have the single interaction constant of the material $\frac{\partial n^{(1)}}{\partial \epsilon^{(1)}} = - \left(\frac{K^{(1)} e_{n_0^{(1)}}}{K^{(2)} e_{n_0^{(1)}}}\right) \frac{\partial n^{(1)}}{\partial \epsilon^{(2)}}$. However, we note that the bulk modulus of the porous rock matrix (measured with $\sigma^{(2)} = 0$) is simply the inverse of D_{11} in Eq. (7.20)

$$K^{(1)} = \frac{1}{D_{11}} \quad (7.21)$$

which we then use to eliminate the remaining interaction constant to obtain

$$\frac{\partial \left(\frac{n^{(1)}}{(1)} \right)}{\partial \epsilon} = - \left(1 - \frac{n^{(1)}}{n_0} \right) \left[\frac{\left(\frac{K^{(2)}}{(1)} \right)_e}{\frac{n_0^{(1)}}{K} - \frac{(1)}{K}} + \frac{\left(1 - \frac{n^{(1)}}{n_0} \right)}{\frac{(1)}{K} - \frac{(1)}{K}} \right] \quad (7.22)$$

and

$$\begin{aligned} \frac{\partial \left(\frac{n^{(1)}}{(2)} \right)}{\partial \epsilon} &= - \frac{\left(\frac{K^{(2)}}{(1)} \right)_e}{K} \frac{\partial \left(\frac{n^{(1)}}{(1)} \right)}{\partial \epsilon} \\ &= + \left(1 - \frac{n^{(1)}}{n_0} \right) \left[1 + \frac{\left(1 - \frac{n^{(1)}}{n_0} \right) \left(\frac{K^{(1)}}{(1)} \right)_e / \left(\frac{K^{(2)}}{(1)} \right)_e}{\frac{n_0^{(1)}}{K} - \frac{(1)}{K}} \right] \end{aligned} \quad (7.23)$$

We now have the elastic constants for a fluid-rock composite expressed in terms of physical material properties: porosity $\left(\frac{n^{(1)}}{n_0} \right)$, bulk modulus of the pore fluid $\left(\frac{K^{(2)}}{(1)} \right)_e$, bulk modulus of the rock grains $\left(\frac{K^{(1)}}{(1)} \right)_e$, bulk modulus of the rock matrix $\left(\frac{K^{(1)}}{(1)} \right)$, and shear modulus of the rock matrix $\left(\frac{\mu^{(1)}}{(1)} \right)$. The need for operationally defined interaction constants has been eliminated. If we were to substitute the terms $\frac{\partial \left(\frac{n^{(1)}}{(1)} \right)}{\partial \epsilon}$ and $\frac{\partial \left(\frac{n^{(1)}}{(2)} \right)}{\partial \epsilon}$ from Eqs. (7.22) and (7.23), respectively, into the stress-strain and the stress-strain equations, Eqs. (7.18) and (7.20), respectively, the resulting expressions would become rather complex. We avoid this by introducing two terms from consolidation theory

$$a = \frac{1}{\left(1 - \frac{n^{(1)}}{n_0} \right)} \left[1 - \frac{\left(\frac{K^{(1)}}{(1)} \right)_e}{\frac{(1)}{K}} \right] \quad (7.24)$$

$$M = \frac{1 - n_0^{(1)}}{\frac{(2)}{K} e + (a - 1) / \frac{(1)}{K} e} \quad (7.25)$$

where a is the constant α , α , and $1 + Q/R$ in References [91], [86], and [87], respectively; and M is the constant M , Q , and R in References [91], [86], and [87], respectively.

Thus, we have developed the "interaction" constants of consolidation theory in terms of the physical constants of the constituents. This fact makes it possible to place bounds on the terms a and M . First we note that when a porous rock is loaded, only a portion of the volumetric strain $\epsilon^{(1)}$ is transmitted to the rock grains, i.e., $|\epsilon^{(1)}| \leq |\epsilon^{(1)}|$. Using this inequality in Eq. (7.17), we find that $\frac{(1)}{n_0} \frac{(1)}{K} e \geq \frac{(1)}{K}$, consequently

$$0 \leq \frac{\frac{(1)}{K}}{\frac{(1)}{K} e} \leq n_0^{(1)} \quad (7.26)$$

Substituting these bounds into the expression above for a and M gives

$$1 \leq a \leq \frac{1}{\left(1 - n_0^{(1)}\right)} \quad (7.27)$$

$$0 \leq \frac{\frac{(2)}{K} e \left(1 - n_0^{(1)}\right)}{\frac{(1)}{n_0} \frac{(2)}{K} e} \leq M \leq \left(1 - n_0^{(1)}\right) \frac{(2)}{K} e \quad (7.28)$$

$$1 + \frac{0}{\left(1 - n_0^{(1)}\right) \frac{(1)}{K} e}$$

For sand and silt materials, $\frac{(1)}{K} / \frac{(1)}{K} e \rightarrow 0$,

$$a \rightarrow \frac{1}{1 - \frac{(1)}{n_0}}, \text{ and } M \rightarrow \frac{\frac{(2)}{K} e \left(1 - \frac{(1)}{n_0}\right)}{1 + \frac{\frac{(1)(2)}{n K} e}{1 - \left(\frac{(1)}{n_0}\right) \frac{(1)}{K} e}}; \text{ whereas for}$$

$$\text{crystalline rock, } K / K^e \rightarrow \frac{(1)}{n_0}, a \rightarrow 1, \text{ and } M \rightarrow \left(1 - \frac{(1)}{n_0}\right) \frac{(2)}{K} e.$$

To complete the development of the stress-strain relations for the fluid rock composite, we replace $\partial \frac{(1)}{n} / \partial \epsilon^{(1)}$ and $\partial \frac{(1)}{n} / \partial \epsilon^{(2)}$ in Eq. (7.20) using Eqs. (7.22), (7.23), (7.24), and (7.25) to obtain

$$\begin{Bmatrix} \frac{(1)}{\epsilon} \\ \frac{(2)}{\epsilon} \end{Bmatrix} = \frac{1}{\frac{(1)}{K}} \begin{bmatrix} 1 & -(a-1) \\ -(a-1) & (a-1)^2 + \frac{K}{M} \end{bmatrix} \begin{Bmatrix} \frac{(1)}{\sigma} \\ \frac{(2)}{\sigma} \end{Bmatrix} \quad (7.29)$$

Similarly, we obtain the stress-strain relations from Eq. (7.18)

$$\begin{Bmatrix} \frac{(1)}{\sigma} \\ \frac{(2)}{\sigma} \end{Bmatrix} = M \begin{bmatrix} (a-1)^2 + \frac{(1)}{K} / M & (a-1) \\ (a-1) & 1 \end{bmatrix} \begin{Bmatrix} \frac{(1)}{\epsilon} \\ \frac{(2)}{\epsilon} \end{Bmatrix} \quad (7.30)$$

The stress in the rock matrix, when we include the shear components, becomes

$$\sigma_{ij}^{(1)} = 2 \mu \frac{(1)}{\epsilon_{ij}} + \left[\frac{(1)}{K} - \frac{2}{3} \mu \frac{(1)}{\epsilon} + (a-1)^2 M \right] \delta_{ij} \epsilon^{(1)} + (a-1) M \delta_{ij} \epsilon^{(2)}. \quad (7.31)$$

or alternately

$$\sigma_{ij}^{(1)} = 2 \mu^{(1)} \epsilon_{ij}^{(1)} + \left(K^{(1)} - \frac{2}{3} \mu^{(1)} \right) \delta_{ij} \epsilon^{(1)} + (a - 1) \delta_{ij} \sigma^{(2)} \quad (7.32)$$

7.2.4 Conservation of Momentum

Conservation of momentum in the fluid-rock composite is expressed

$$\rho^{(\alpha)} \left(\frac{\partial v_i^{(\alpha)}}{\partial t} + v_j^{(\alpha)} \frac{\partial v_i^{(\alpha)}}{\partial x_j} \right) = \frac{\partial \sigma_{ij}^{(\alpha)}}{\partial x_j} + \rho^{(\alpha)} f_i^{(\alpha)} + \rho^{(\alpha)} \beta_i^{(\alpha)} \quad (7.33)$$

where $v_i^{(\alpha)} = \frac{\partial u_i^{(\alpha)}}{\partial t}$, $f_i^{(\alpha)}$ is the body force per unit of composite mass that results from gravitational forces, $\beta_i^{(\alpha)}$ is the body force per unit of composite mass that results from drag forces due to differential movement between constituents. According to Darcy's law

$$\rho \beta_i^{(1)} = - \rho \beta_i^{(2)} = \frac{1}{k^*} \left(v_i^{(2)} - v_i^{(1)} \right) \quad (7.34)$$

where

$$k^* = \frac{k}{n^{(2)} \gamma_e^{(2)}} \quad (7.35)$$

Here k represents the permeability of the rock matrix to the pore fluid (units of velocity) and $\gamma_e^{(2)} = \rho^{(2)} g$ is the weight density of the pore fluid. The permeability is related to physical properties of the solid and fluid by

$$k = \frac{\bar{K} \gamma_e^{(2)}}{\mu^{(2)}}$$

in which $\mu^{(2)}$ is the absolute viscosity of the fluid and \bar{K} is a physical coefficient of permeability $\bar{K} = \kappa D^2$, D being

the effective diameter of the pores and κ a quantity without dimensions depending only on the geometry of the pores.

Conservation of momentum for the fluid-rock composite is expressed by combining Eq. (7.33) with $\alpha = 1$ and $\alpha = 2$ thereby cancelling the interconstituent drag terms $\rho \beta_i^{(\alpha)}$

$$\frac{\partial \sigma_{ij}^{(1)}}{\partial x_j} + \frac{\partial \sigma_{ij}^{(2)}}{\partial x_i} + \rho f_i = \rho^{(1)} \left(\frac{\partial v_i^{(1)}}{\partial t} + v_j^{(1)} \frac{\partial v_i^{(1)}}{\partial x_j} \right) + \rho^{(2)} \left(\frac{\partial v_i^{(2)}}{\partial t} + v_j^{(2)} \frac{\partial v_i^{(2)}}{\partial x_j} \right) \quad (7.36)$$

Incidentally, we note that for the special case of waves propagating through a fluid-rock composite in which fluid seepage is negligible ($k^* \rightarrow 0$) then $v_i = v_i^{(1)} = v_i^{(2)}$ and Eq. (7.36) reduces to

$$\frac{\partial \tau_{ij}}{\partial x_j} + \rho f_i = \left(\rho \frac{\partial v_i}{\partial t} + v_j \frac{\partial v_i}{\partial x_j} \right) \quad (7.37)$$

where $\tau_{ij} = \sigma_{ij}^{(1)} + \delta_{ij} \sigma^{(2)}$ is the gross composite stress. The constitutive equation for this special case is given by

$$\tau_{ij} = 2\mu \epsilon_{ij} + \left(K - \frac{2}{3} \mu + a^2 M \right) \delta_{ij} \epsilon \quad (7.38)$$

This expression is obtained by combining Eqs. (7.14) and (7.30) with $\epsilon_{ij} = \epsilon_{ij}^{(1)} = \epsilon_{ij}^{(2)}$.

For the purpose of investigating the state of stress near an injection well, we include seepage effects. However, we will work on a time scale in which inertial forces may be neglected so that Eq. (7.36) reduces to

$$\frac{\partial \sigma_{ij}^{(1)}}{\partial x_j} + \frac{\partial \sigma_{ij}^{(2)}}{\partial x_i} + \rho f_i = 0 \quad (7.39)$$

The constitutive equations for the rock matrix from Eq. (7.32) are introduced to give

$$2 \mu^{(1)} \frac{\partial \epsilon_{ij}^{(1)}}{\partial x_j^2} + \left(K^{(1)} - \frac{2}{3} \mu^{(1)} \right) \frac{\partial \epsilon^{(1)}}{\partial x_i} + a \frac{\partial \sigma^{(2)}}{\partial x_i} + \rho f_i = 0 \quad (7.40)$$

or in terms of the displacement field for the rock matrix

$$\mu^{(1)} \frac{\partial^2 u_i^{(1)}}{\partial x_j^2} + \left(K^{(1)} + \frac{1}{3} \mu^{(1)} \right) \frac{\partial^2 u_j^{(1)}}{\partial x_i \partial x_j} + a \frac{\partial \sigma^{(2)}}{\partial x_i} + \rho f_i = 0 \quad (7.41)$$

The above three equations describe equilibrium in the fluid-rock composite.

Seepage equations for the fluid constituent are obtained by substituting $\rho \beta_i^{(2)}$ from Eq. (7.34) into the momentum equation, Eq. (7.33), with $\alpha = 2$

$$\frac{\partial \sigma^{(2)}}{\partial x_i} + \rho f_i^{(2)} = \frac{1}{k^*} \left(v_i^{(2)} - v_i^{(1)} \right) \quad (7.42)$$

where we have again neglected inertial effects. We take the divergence of the above expression to obtain a single scalar equation for describing fluid seepage

$$\frac{k^*}{(2)_e} \frac{\partial^2 \sigma^{(2)}}{\partial x_i \partial x_j} + \rho \frac{k^*}{(2)_e} \frac{\partial f_i^{(2)}}{\partial x_i} = \frac{\partial \epsilon^{(2)}}{\partial t} - \frac{\partial \epsilon^{(1)}}{\partial t} \quad (7.43)$$

We substitute for $\epsilon^{(2)}$ in terms of $\epsilon^{(1)}$ and $\sigma^{(2)}$ from Eq. (7.30) to obtain

$$k^* \frac{\partial^2 \sigma^{(2)}}{\partial x_i \partial x_i} + k^* \frac{\partial f_i^{(2)}}{\partial x_i} = -a \frac{\partial \epsilon^{(1)}}{\partial t} + \frac{1}{M} \frac{\partial \sigma^{(2)}}{\partial t} \quad (7.44)$$

the conventional seepage equation that appears in consolidation theory.

7.2.5 Finite Element Formulation

The interacting set of equations that describe seepage of compressible fluid in an elastic rock matrix, Eqs. (7.41) and (7.44), are solved numerically using the finite element method. The numerical scheme is developed from the following virtual work expression

$$\begin{aligned} \int_V & \left[E_{ijkl}^{(1)} \frac{\partial u_i^{(1)}}{\partial x_k} \frac{\partial \delta u_j^{(1)}}{\partial x_l} + a \sigma^{(2)} \frac{\partial \delta u_i^{(1)}}{\partial x_i} - \rho f_i^{(1)} \delta u_i^{(1)} \right. \\ & - k^* \frac{\partial \sigma^{(2)}}{\partial x_i} \frac{\partial \delta \sigma^{(2)}}{\partial x_i} - \frac{1}{M} \frac{\partial \sigma^{(2)}}{\partial t} \delta \sigma^{(2)} \\ & \left. + a \frac{\partial \epsilon^{(1)}}{\partial t} \delta \sigma^{(2)} + \rho k^* \frac{\partial f_i^{(2)}}{\partial x_i} \right] dv \\ & - \int_{S_\sigma} \left(\sigma_{ij}^{(1)} n_j + a \sigma^{(2)} n_i \right) \delta u_i^{(1)} ds \\ & + \int_{S_q} k^* \frac{\partial \sigma^{(2)}}{\partial x_i} n_i \delta \sigma^{(2)} ds = 0 \quad (7.45) \end{aligned}$$

where n_i is the i^{th} component of the unit outward normal vector and

$$E_{ikjl} = \left(\binom{(1)}{K} - \frac{2}{3} \binom{(1)}{\mu} \right) \delta_{ik} \delta_{jl} + \binom{(1)}{\mu} \delta_{ij} \delta_{kl} + \binom{(1)}{\mu} \delta_{il} \delta_{kj} \quad (7.46)$$

for isotropic material. The volume V is bounded by the closed surface $S = S_u + S_\sigma = S_p + S_q$. On S_u , displacements of the rock matrix are specified ($\binom{(1)}{u}_i = \text{data}$) and virtual displacements are constrained to zero ($\delta \binom{(1)}{u}_i = 0$). On $S_\sigma = S - S_u$, surface tractions acting on the fluid-rock composite are specified ($\binom{(1)}{\sigma}_{ij} n_j + a \binom{(2)}{\sigma} n_i = \text{data}$). On S_p , dilatational stresses in the fluid are specified ($\binom{(2)}{\sigma} = \text{data}$) and virtual stresses in the fluid are constrained to zero ($\delta \binom{(2)}{\sigma} = 0$). On $S_q = S - S_p$, volumetric flow rates per unit normal area are specified ($k^* \binom{(2)}{\sigma} / \partial x_i n_i = \text{data}$). The virtual work expression above is an equivalent to the description of the fluid-rock composite given by Eqs. (7.41) and (7.44) with the boundary conditions described above.

Following conventional finite element procedures, the dependent variables $\binom{(1)}{u}_i$ and $\binom{(2)}{\sigma}$ are expressed with the region of each element by spatial interpolation functions

$$\binom{(1)}{u}_i(\underline{x}, t) \cong \langle \phi(\underline{x}) \rangle \{ U_i(t) \} \quad (7.47)$$

and

$$\binom{(2)}{\sigma}(\underline{x}, t) \cong \langle \phi(\underline{x}) \rangle \{ \pi(t) \} \quad (7.48)$$

where the symbols $\langle \rangle$ and $\{ \}$ denote row and column matrices, respectively, of order $N = \text{total number of nodes in the discrete system}$. The terms $\{ U_i(t) \}$ and $\{ \pi(t) \}$ are

column listings of nodal displacements of the rock matrix and fluid stress, respectively.

The spatial approximations expressed above are then substituted in the virtual work equation, Eq. (7.45) and the nodal values of displacement and fluid stress are factored out of the integral expressions to obtain

$$\begin{aligned}
 - \{\delta U_i\}^T & \left([K_{ij}] \{U_j(t)\} + [C_i] \{\pi(t)\} - \{F_i(t)\} \right) \\
 \{\delta \pi\} & = \left([C_i]^T \{\dot{U}_i(t)\} - [H] \{\pi(t)\} - [E] \{\dot{\pi}(t)\} + \{Q(t)\} \right) = 0
 \end{aligned}
 \tag{7.49}$$

where

$$[K_{ij}] = \sum_e \int_{V^e} E_{ijkl} \left\langle \frac{\partial \phi}{\partial x_k} \right\rangle^T \left\langle \frac{\partial \phi}{\partial x_l} \right\rangle dv$$

$$[C_i] = \sum_e \int_{V^e} a \left\langle \frac{\partial \phi}{\partial x_i} \right\rangle^T \langle \phi \rangle dv$$

$$[H] = \sum_e \int_{V^e} k^* \left\langle \frac{\partial \phi}{\partial x_k} \right\rangle \left\langle \frac{\partial \phi}{\partial x_k} \right\rangle dv$$

$$[E] = \sum_e \int_{V^e} \frac{1}{M} \langle \phi \rangle^T \langle \phi \rangle dv$$

$$\begin{aligned}
 \{F_i(t)\} & = \sum_e \int_{V^e} \rho f_i(t) \langle \phi \rangle^T dv \\
 & + \sum_e \int_{S_\sigma^e} \left(\sigma_{ij}^{(1)} n_j + a \sigma_i^{(2)} n_i \right) \langle \phi \rangle^T ds
 \end{aligned}$$

$$\{Q(t)\} = \sum_e \int_{V^e} k^* \rho \frac{\partial f_i^{(2)}}{\partial x_i} \langle \phi \rangle^T dv + \sum_e \int_{s_q^e} k^* \frac{\partial \sigma}{\partial x_i} n_i \langle \phi \rangle ds$$

Since the nodal variations δU_i and $\delta \pi$ are arbitrary, Eq. (7.49) becomes

$$[K_{ij}] \{U_j(t)\} + [C_i] \{\pi(t)\} = \{F_i(t)\} \quad (7.50)$$

$$[C_j]^T \{U_j(t)\} - [H] \{\pi(t)\} - [E] \{\dot{\pi}(t)\} = -\{Q(t)\} \quad (7.51)$$

The original FRI code was developed for performing the indicated calculations and stepping the solutions in time.^[3] In this code, fluid stress is advanced in time using Eq. (7.51). The fluid stress at the advanced time is then introduced into Eq. (7.50) to update displacement, strain, and stress in the rock matrix. The time rate of displacement in the rock matrix is then used in Eq. (7.51) to affect further changes in the fluid stress.

In the present version of FRI (FRI2) an implicit time stepping scheme is developed for the combined set of equations by assuming linear variations in the dependent variables $\{U_i(t)\}$ and $\{\pi(t)\}$ over the time interval Δt . Equation (7.51) is then integrated from $t - \Delta t$ to t to obtain

$$[C_j]^T \{U_j(t) - U_j(t - \Delta t)\} - \frac{\Delta t}{2} [H] \{\pi(t) + \pi(t - \Delta t)\} - [E] \cdot \{\pi(t) - \pi(t - \Delta t)\} = \frac{\Delta t}{2} \{Q(t) + Q(t - \Delta t)\} \quad (7.52)$$

We now combine Eqs. (7.50) and (7.52) into a single matrix equation and collect terms involving the advanced time t to obtain

$$\begin{bmatrix} [K_{ij}] & [C_i] \\ [C_j]^T & -[E] - \frac{\Delta t}{2} [H] \end{bmatrix} \begin{Bmatrix} \{U_j(t)\} \\ \{\pi(t)\} \end{Bmatrix} = \\
 \begin{bmatrix} 0 & 0 \\ [C_j]^T & -[E] + \frac{\Delta t}{2} [H] \end{bmatrix} \begin{Bmatrix} \{U_j(t-\Delta t)\} \\ \pi(t-\Delta t) \end{Bmatrix} + \begin{Bmatrix} \{F_i(t)\} \\ -\frac{\Delta t}{2} \{Q(t) + Q(t-\Delta t)\} \end{Bmatrix} \quad (7.53)$$

It is this equation that is solved to advance the interactive calculations in time, one solution of the equation per time step. A 2D (plane strain or axisymmetric) finite element program, which was originally developed by Ghabousi and Wilson^[91] has been extensively modified at S³ to form the FRI2 code.

7.3 NUMERICAL RESULTS

7.3.1 Test Calculations

In order to develop confidence in the computing procedure, a number of test calculations have been performed:

1. Simple compression of the rock matrix with $a = 0$ to remove the influence of fluid from the equilibrium equations, Eq. (7.41).
2. One-dimensional diffusion with $a = 0$ to remove the influence that the rate of dilation in rock has on the seepage equation, Eq. (7.44).
3. One-dimensional consolidation under a uniform load with $a = 0$ and $a = 1$. [3]
4. Injection of fluid at a constant overpressure into a spherically symmetric injection well with $a = 1$.

The test calculations with $a = 0$ are not intended to simulate a physical problem but rather to compare numerical results with analytic solutions. After some effort, suitable accuracy has been achieved in all of the test calculations with the exception of the time varying behavior at very early times. For these cases, the numerical results match analytic solutions only after the fluid pressure has diffused sufficiently for the piecewise linear spatial approximation (linear variations within each element) used in FRI2 to represent the spatial variations with reasonable accuracy. From this point on, until a steady condition was reached, the numerical results match the analytic results to within about 2 percent of the peak values for rock stress, rock displacement, and fluid pressure.

7.3.2 Spherically Symmetric Injection Cavity

As the result of the number of terms that influence the quasistatic behavior of a fluid-rock composite, the mechanisms that govern a numerical simulation are sometimes difficult to isolate. The existence of an analytic solution to an injection well with fluid penetration is useful for gaining these needed insights, even though many of the physical complexities are necessarily missing from the analytic treatment. Frazier^[3] has obtained solutions for the special case of injection into a spherical cavity in a homogeneous porous material. We present these solutions here in order to form a basis for extracting information from numerical calculations involving more complex injection systems.

Injection into a cavity of radius r_0 is accomplished by stepping the fluid pressure in the injection cavity from the resident pressure $p_{(0)}$ to an elevated pressure $p_{(0)} + p_0$, illustrated in Fig. 7.2. The interactive equations governing equilibrium in the composite, Eq. (7.40), and the seepage of fluid, Eq. (7.44), are satisfied simultaneously by the following expressions: The overpressure in the pore fluid, as a function of the distance r from the center of the injection cavity and the dimensionless time τ , is given by

$$p(r, \tau) = - \frac{\sigma^{(2)}(r, \tau)}{\left(1 - \frac{\sigma^{(1)}}{n_0}\right)} \quad (7.54)$$

$$= \frac{r_0}{r} p_0 \left[1 - \operatorname{erf} \left(\frac{r/r_0 - 1}{2\sqrt{\tau}} \right) \right] \quad (7.55)$$

The stresses in the rock matrix are altered by the presence of the injection system according to

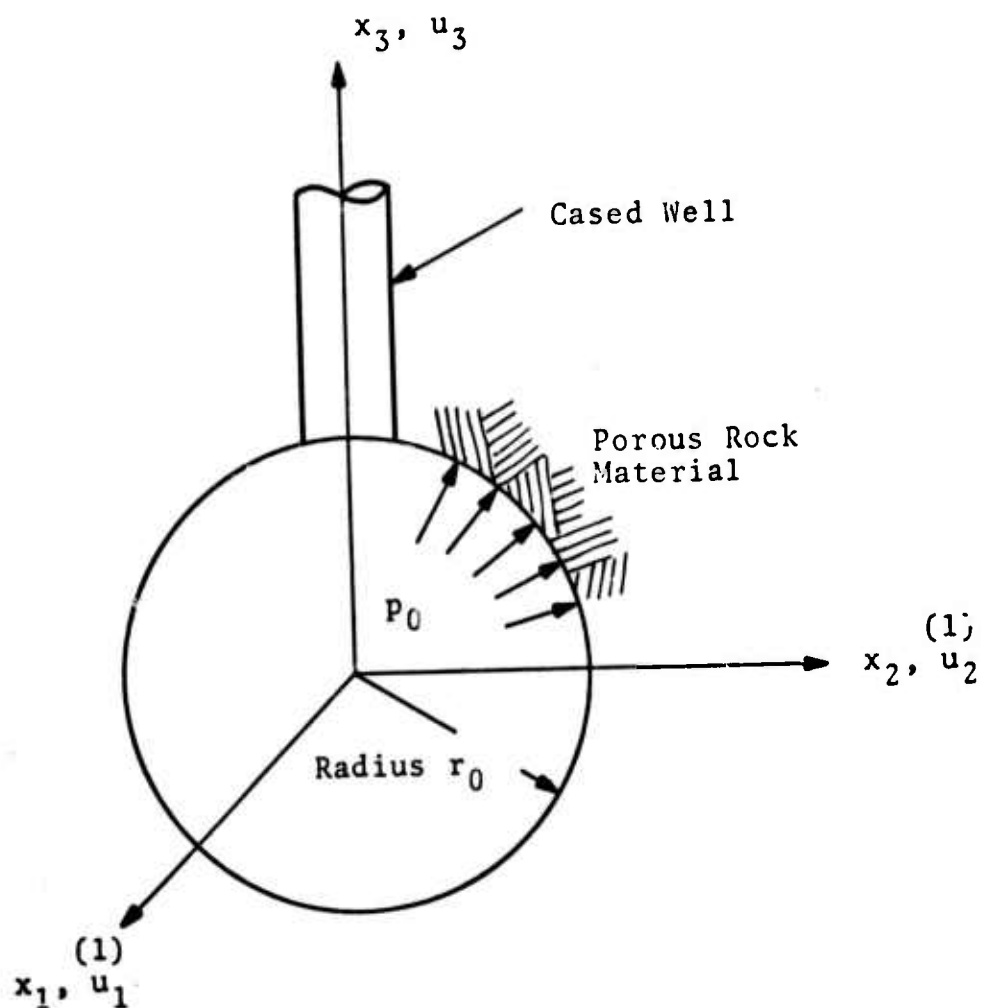


Fig. 7.2--Spherically symmetric fluid injection system. The overpressure p_0 is introduced in the cavity at the initial time and then held at this level.

$$\begin{aligned} \sigma_{ij}^{(1)}(\underline{x}, t) = & -\frac{p_0}{2} (r_0/r)^3 \left(\frac{3}{r^2} x_i x_j - \delta_{ij} \right) \\ & + \frac{(2)}{n_0 p_0} \left(\frac{r_0}{r} \right) \left[1 - \operatorname{erf} \left(\frac{r/r_0 - 1}{2\sqrt{\tau}} \right) \right] \delta_{ij} \end{aligned} \quad (7.56)$$

In the above expressions, the dimensionless time is given by

$$\tau = \frac{t}{T} \quad (7.57)$$

where

$$T = \frac{r_0^2}{k^*} \left(\frac{1}{M} + \frac{a^2}{(1)} \right). \quad (7.58)$$

For injection of water into competent rock with 10 percent porosity, we get $T = 5.1 \times 10^2$ sec using the physical parameters $(1)_K^e = 111$ kbars, $(1)_K^e = 100$ kbars ($a = 1$), $(2)_K^e = 20$ kbars ($M = 2$ kbars), $k = 10^{-7}$ cm/sec, $(2)_Y^e = 10^3$ dynes/cm ($k^* = 10^{-8}$ cm⁴/dyne-sec) and $r_0 = 100$ cm. [92]

At the other extreme, when we consider in injection into a sedimentary deposit with 40 percent porosity, we get $T = 0.56$ sec using physical parameters $(1)_K^e = 100$ kbars, $(1)_K^e = 20$ kbars ($a = 2.0$), $(2)_K^e = 20$ kbars ($M = 6.67$ kbars), $k = 10^{-3}$ cm/sec, $(2)_Y^e = 10^3$ dynes/cm³ ($k^* = 6.25 \times 10^{-6}$ cm⁴/dyne-sec), and $r_0 = 100$ cm. Pore pressure as a function of radius is presented in Fig. 7.3 at various values of dimensionless time. Pore pressures, obtained numerically using the FRI code, are also presented.

We make the following observations pertaining to these results:

1. The permeability (k) and the elastic constants $(2)_K^e$, $(1)_K^e$, and $(1)_K^e$ influences only the time rate of seepage; these material properties do

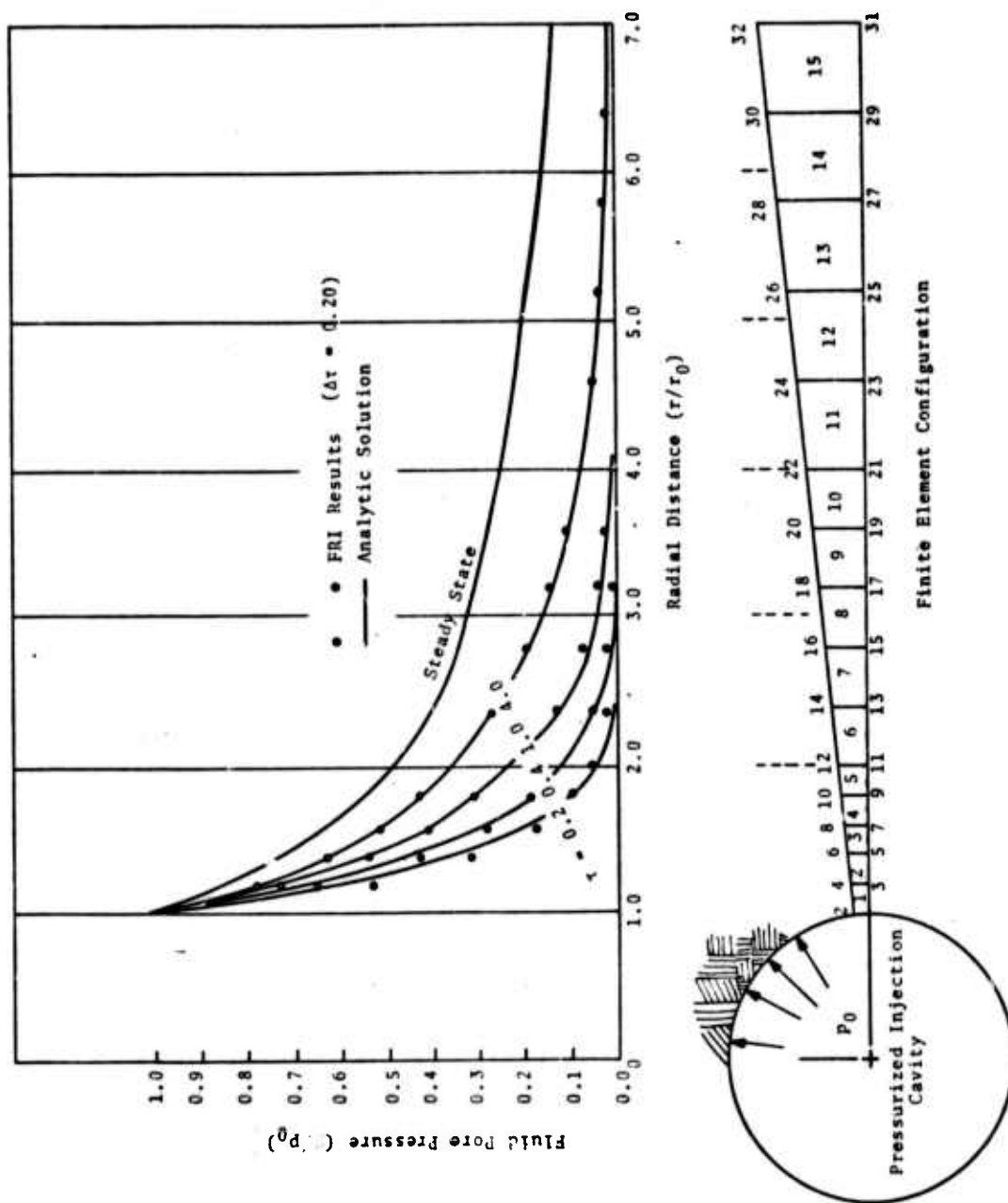


Fig. 7.3--Overpressure generated by a spherically symmetric fluid injection system.

not influence the stresses in the linearly elastic, spherically symmetric injection well. Increases in k , $k^{(2)}_e$, $k^{(1)}_e/k^{(1)}$, and $1/n^{(2)}_0$ increase the time rate of seepage.

2. The shear stress in the rock matrix is time invariant.
3. The tensile stresses that are induced into the rock matrix by the injection system increase linearly with increasing porosity, $n^{(2)}_0$.
4. At late times, the fluid pressure and the tensile rock stress introduced by the injection system die out as the inverse of the distance from the injection cavity; whereas, the rock stresses induced by non-penetrating fluid ($k = 0$ or $\tau = 0$) die out as the third power of the inverse of the distance from the injection cavity.
5. At ten cavity radii, the pore pressure and the rock stress reach half of their steady-state (ultimate) values for $\tau = 8$ or 10^4 sec for competent rock ($T = 500$ sec) and 10 sec for sedimentary material ($T = 0.5$ sec).

In general, half the steady-state stress change is reached when

$$\tau = \left(\frac{r}{r_0} - 1 \right)^2$$

i.e., when

$$t = \frac{1}{k^*} \left(\frac{1}{M} + \frac{a^2}{(I)K} \right) r^2 - r_0^2. \quad (7.59)$$

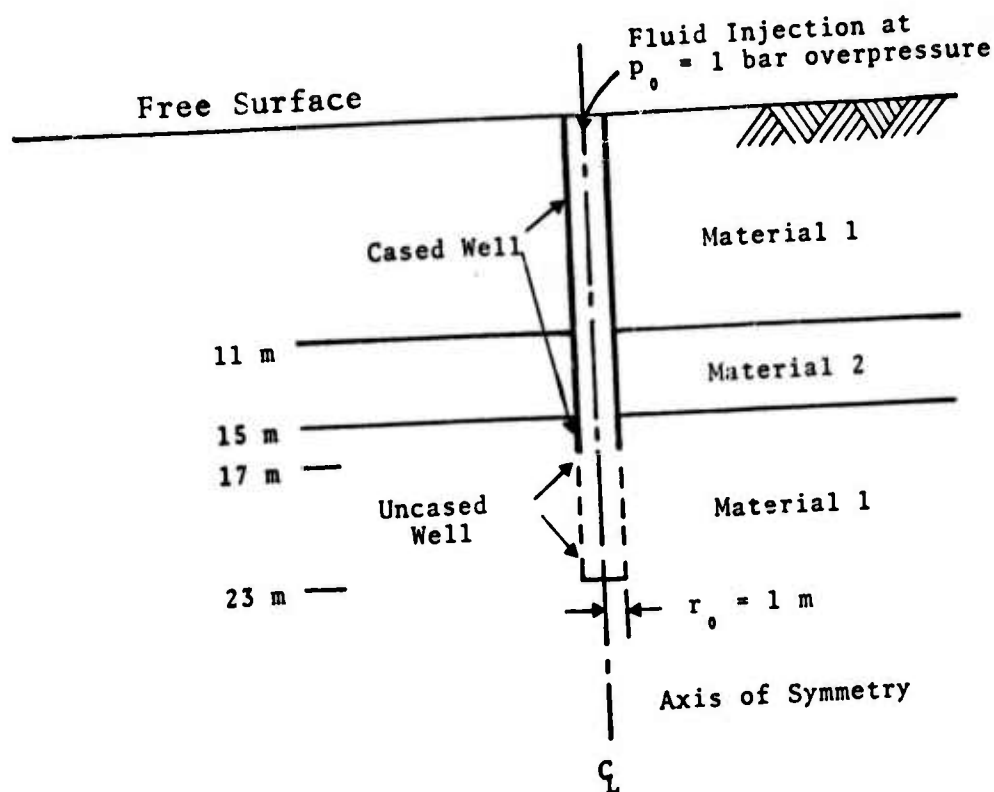
6. The principal stresses in the rock matrix generated by the fluid injection align radial and tangential to the injection cavity with the tangential stress (hoop stress) adjacent to the cavity being the most tensile. Consequently, hydraulically induced cracks will align normal to the least compressive tectonic stress.

7.3.3 Shallow Injection Well

The FRI code is used to investigate the fluid pressure and rock stress produced by injecting water into a cylindrical well near the free surface. Injection occurs at a mean depth of 20 meters over a vertical extent of 6 meters. The injection well is illustrated in Fig. 7.4. A set of three complete calculations are made to examine how the injection process is influenced by presence of the free surface and a nearby layer with contrasting permeability. The material properties, typical of a shallow sedimentary deposit, are also presented in Fig. 7.4.

We note that a rather large radius (1.0 m) is used for injection. The analytic solutions of the previous section for injection into a spherical cavity indicate that the cavity radius strongly influences the rate at which fluid pressures spread into the surrounding media, Eq. (7.55). For the cylindrical injection cavity of Fig. 7.4, the influence of cavity radius will be somewhat less than for the spherical cavity.

The shallow injection system is modeled numerically with an axisymmetric grid consisting of 10 elements in the



Material 1

$$^{(1)}K = 10 \text{ kbars}, \quad ^{(1)}\nu = 1/3, \quad ^{(2)}n_0 = 0.4, \quad a = 1, \quad M \rightarrow \infty$$

$$k = 1.85 \times 10^{-6} \text{ cm/sec}$$

Material 2

$$^{(1)}K = 10 \text{ kbars}, \quad ^{(1)}\nu = 1/3, \quad ^{(2)}n_0 = 0.4, \quad a = 1, \quad M \rightarrow \infty$$

$$\text{Problem 1: } k = 1.85 \times 10^{-6} \text{ cm/sec}$$

$$\text{Problem 2: } k = 18.5 \times 10^{-6} \text{ cm/sec}$$

$$\text{Problem 3: } k = 0.185 \times 10^{-6} \text{ cm/sec}$$

Fig. 7.4--Fluid injection into a shallow surface layer, here $^{(1)}\nu$ is Poisson's ratio for the rock matrix.

radial dimension. The finite element grid, which is presented in Fig. 7.5, is bounded from below by impervious, rigid rock and bounded at large radius (61 m) by a highly pervious, smooth, rigid wall. The upper surface is traction free with no resistance to fluid flow. Injection takes place over a vertical extent of 6 meters in a 1-meter cylindrical well. Injection is accomplished by stepping the pressure in the injection zone to 1.0 kbar and holding it at this level.

Computed rock displacement, gross (partial) fluid stress, maximum gross rock stress, and gross rock deviatoric stress are presented in Figs. 7.6, 7.7, 7.8, and 7.9, respectively, for a homogeneous surface layer. The spherically symmetric time constant, T of Eq. (7.58), using the properties of the surface layer and a cavity radius of 1.0 meter is 10^{-3} days. Using Eq. (7.59), we would estimate that the pore pressure would reach half of its steady state value in 0.5 days at a distance of 20 meters. In Fig. 7.7 we see that this estimate is probably within a factor of two for points below the level of the injection; however, points near the free surface approach a steady-state condition somewhat more rapidly. A steady-state condition is essentially reached throughout the grid in one day. From the rock displacement plots of Figs. 7.6, we see that the presence of the free surface has negligible influence for $t < 0.01$ days. At this point the rock mass overlying the injection zone heaves vertically, and the outer fluid stress contour begins to parallel the free surface indicating fluid escaping at the free surfaces.

The fluid and rock stress contours near the injection zone, Figs. 7.7, 7.8, and 7.9, are vertically elongated due to the six to one, length to radius, geometry of the injection zone. At intermediate distances, however, the

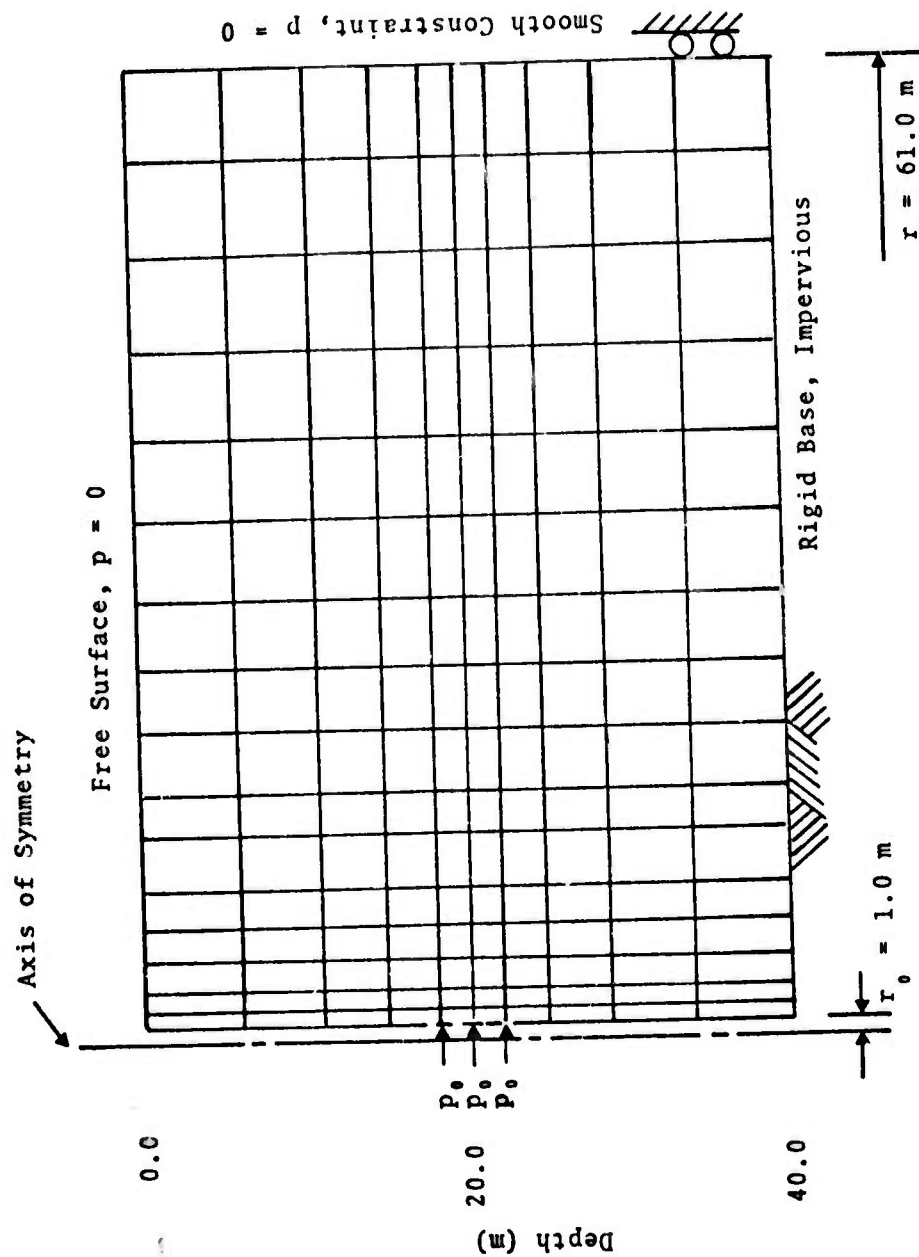


Fig. 7.5--Finite element representation, shallow injection well.

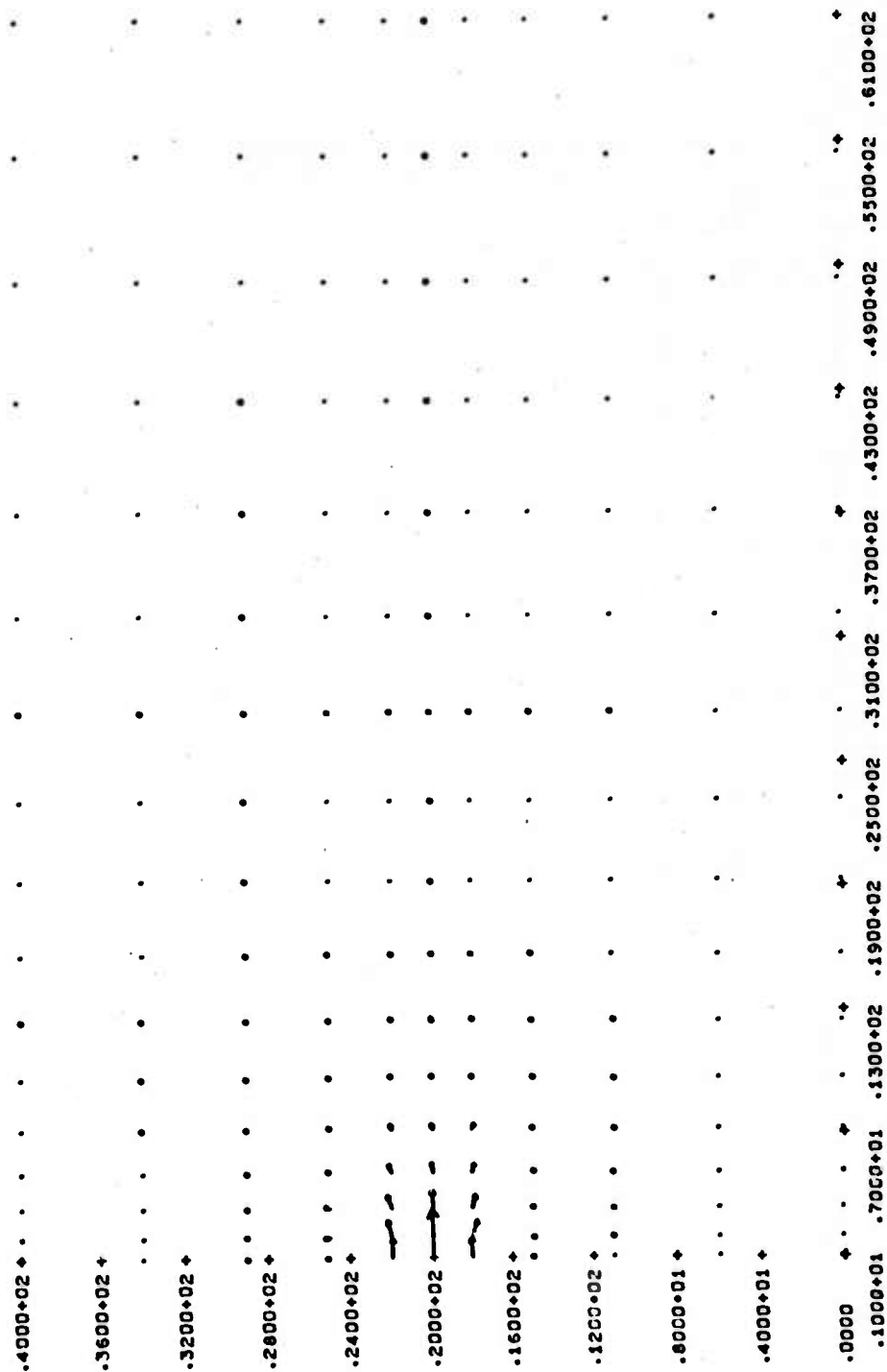


Fig. 7.6(a) -- Displacements in the rock, homogeneous surface layer, $t = 0.001$ day,
maximum vector = 0.122 mm.

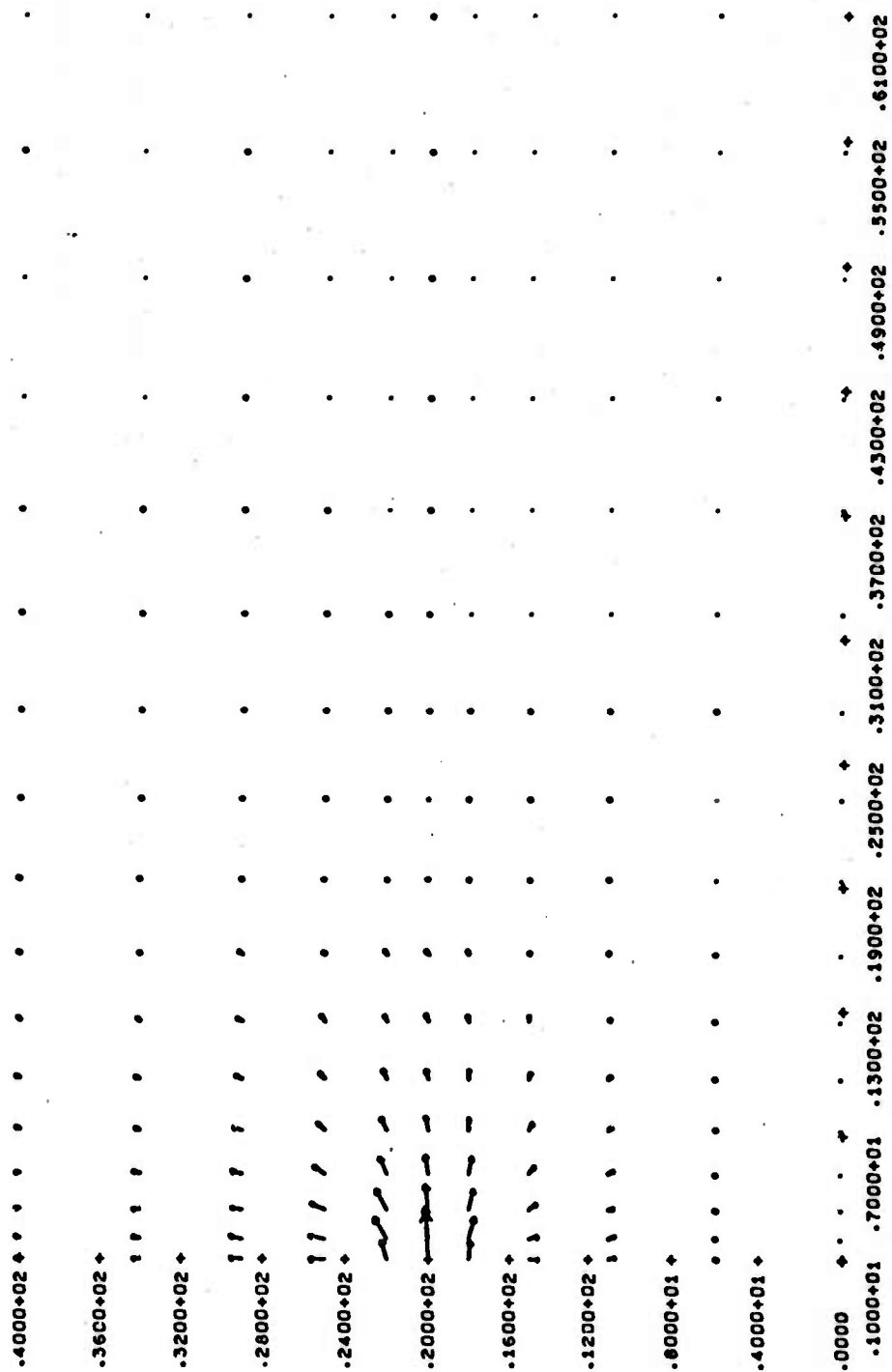


Fig. 7.6(b) -- Displacements in the rock, homogeneous surface layer, $t = 0.01$ day,
maximum displacement = 0.120 mm.

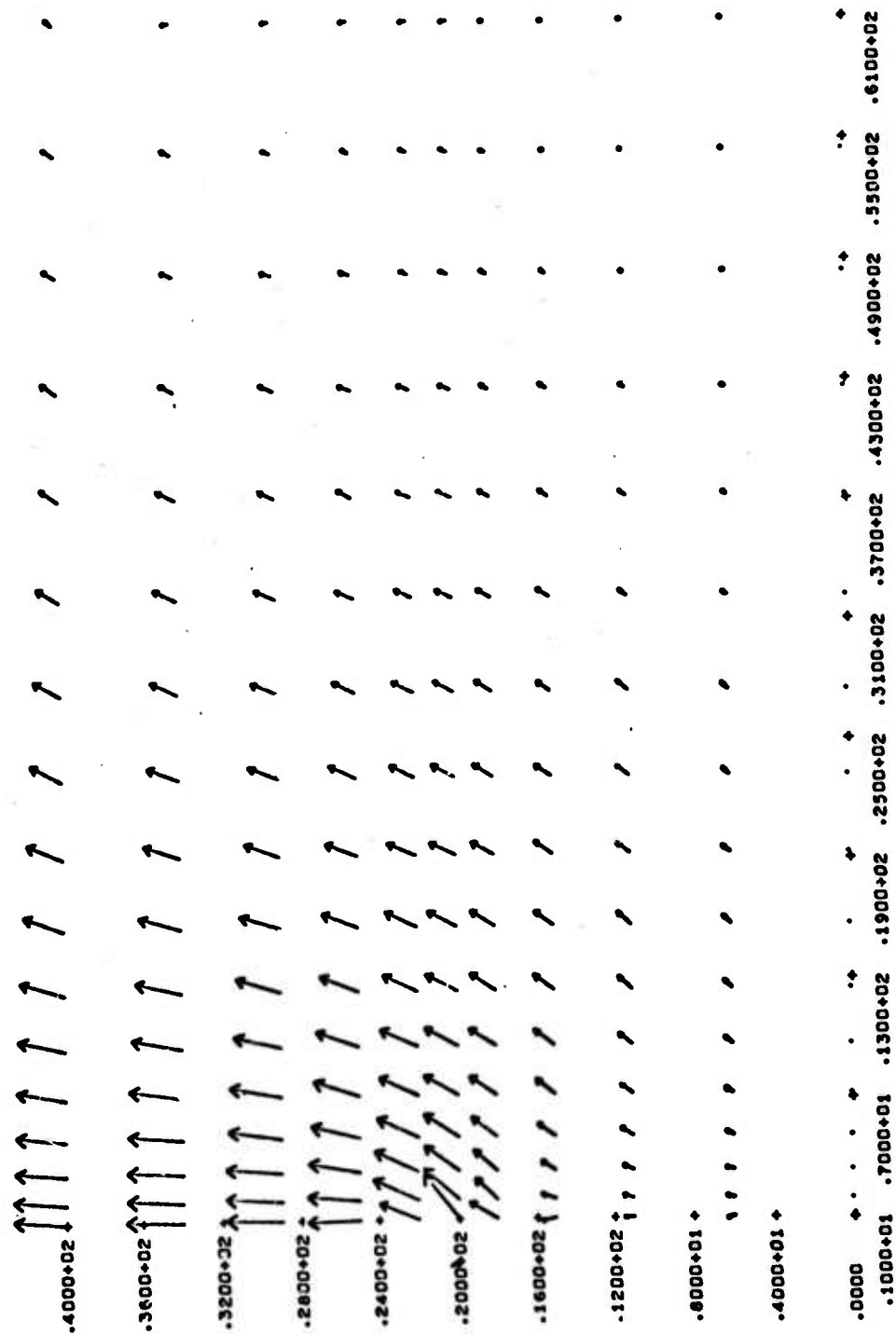


Fig. 7.6(d)--Displacements in the rock, homogeneous surface layer, $t = 1.0$ day, maximum displacement = 0.152 mm.

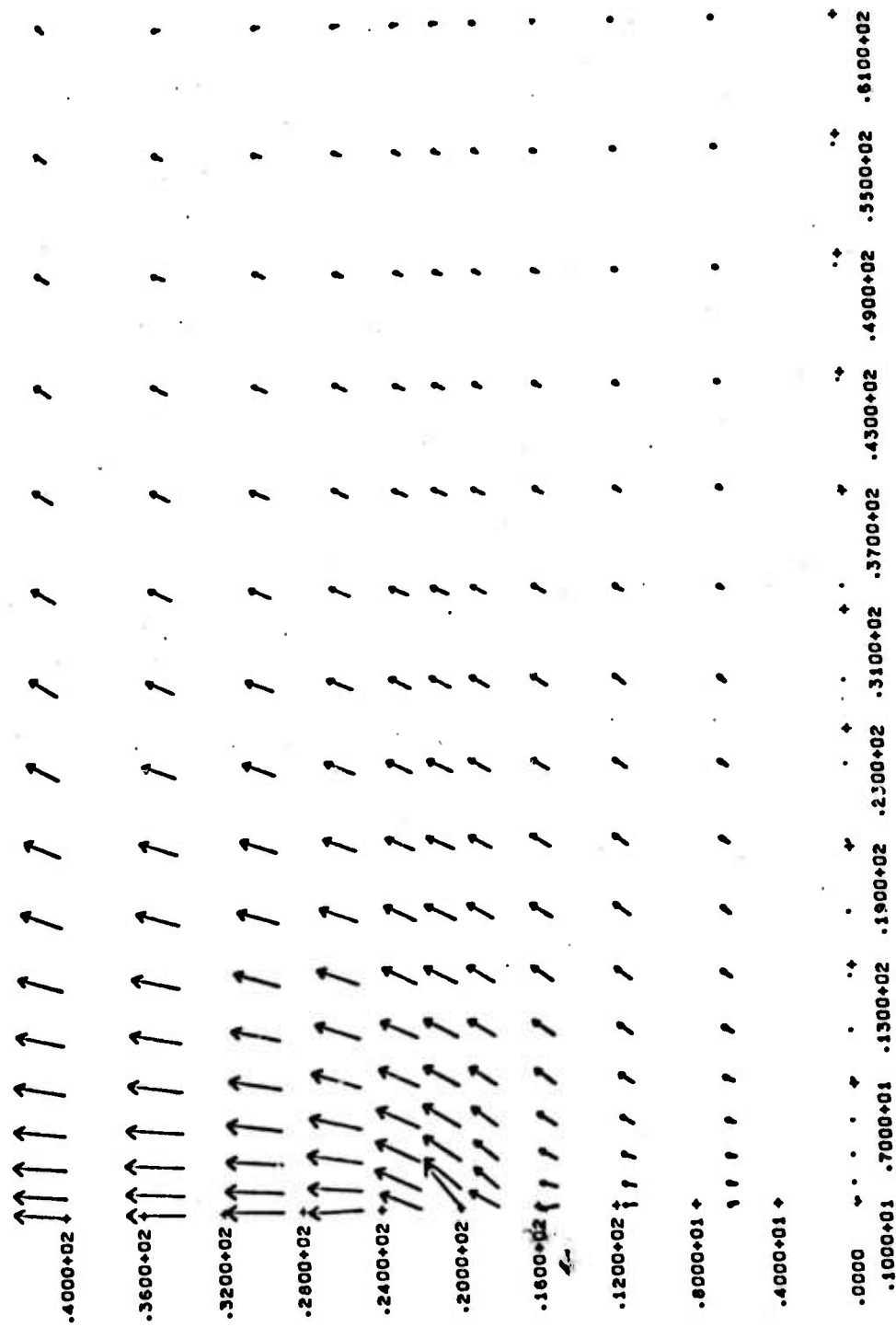


Fig. 7.6(e) -- Displacements in the rock, homogeneous surface layer, $t = 10$ days,
maximum displacement = 0.155 mm.

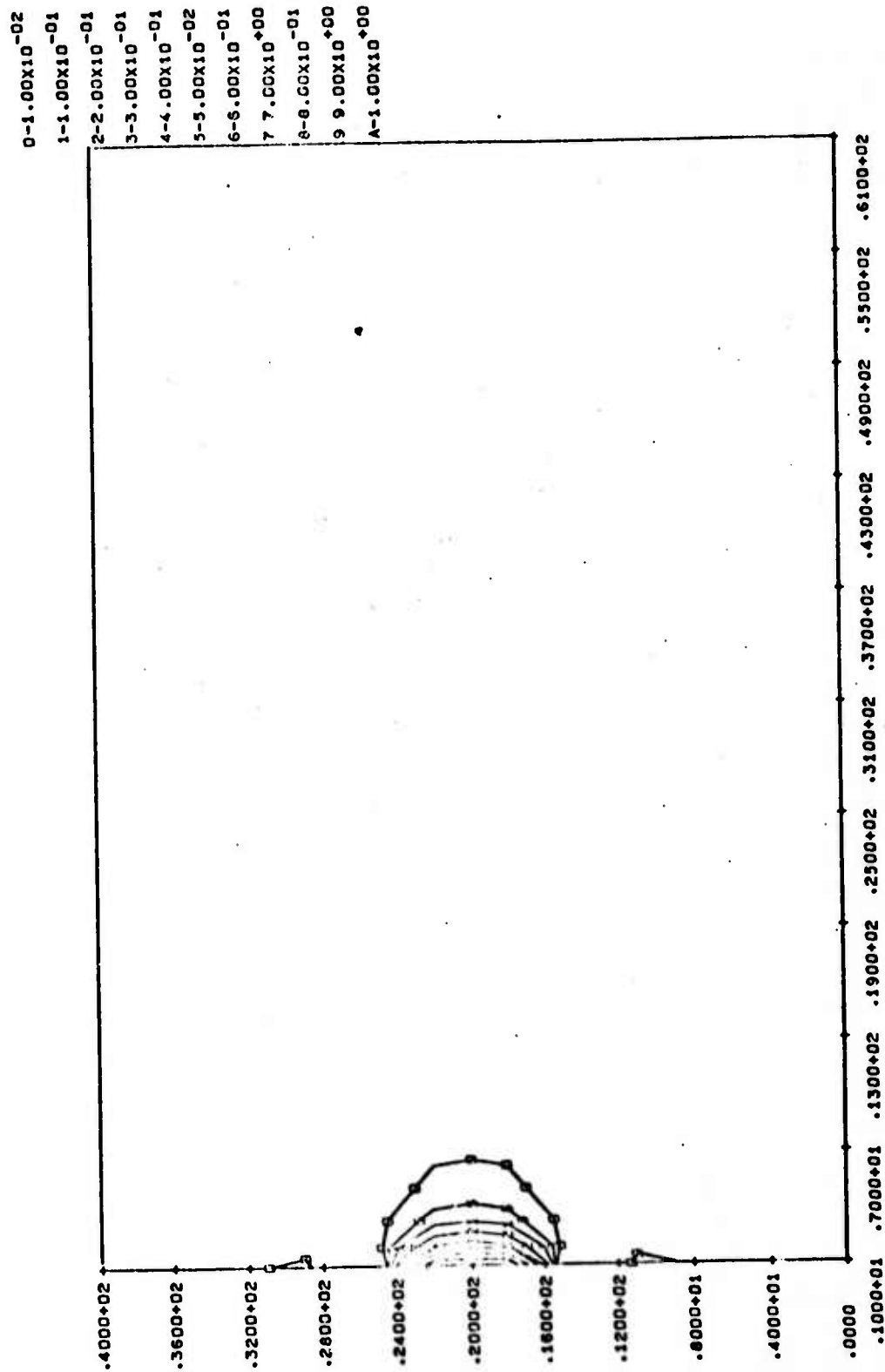


Fig. 7.7(a) -- Gross fluid stress $\sigma^{(2)} = -n_0 p$ (bars, homogeneous surface layer, $t = 0.001$ day.

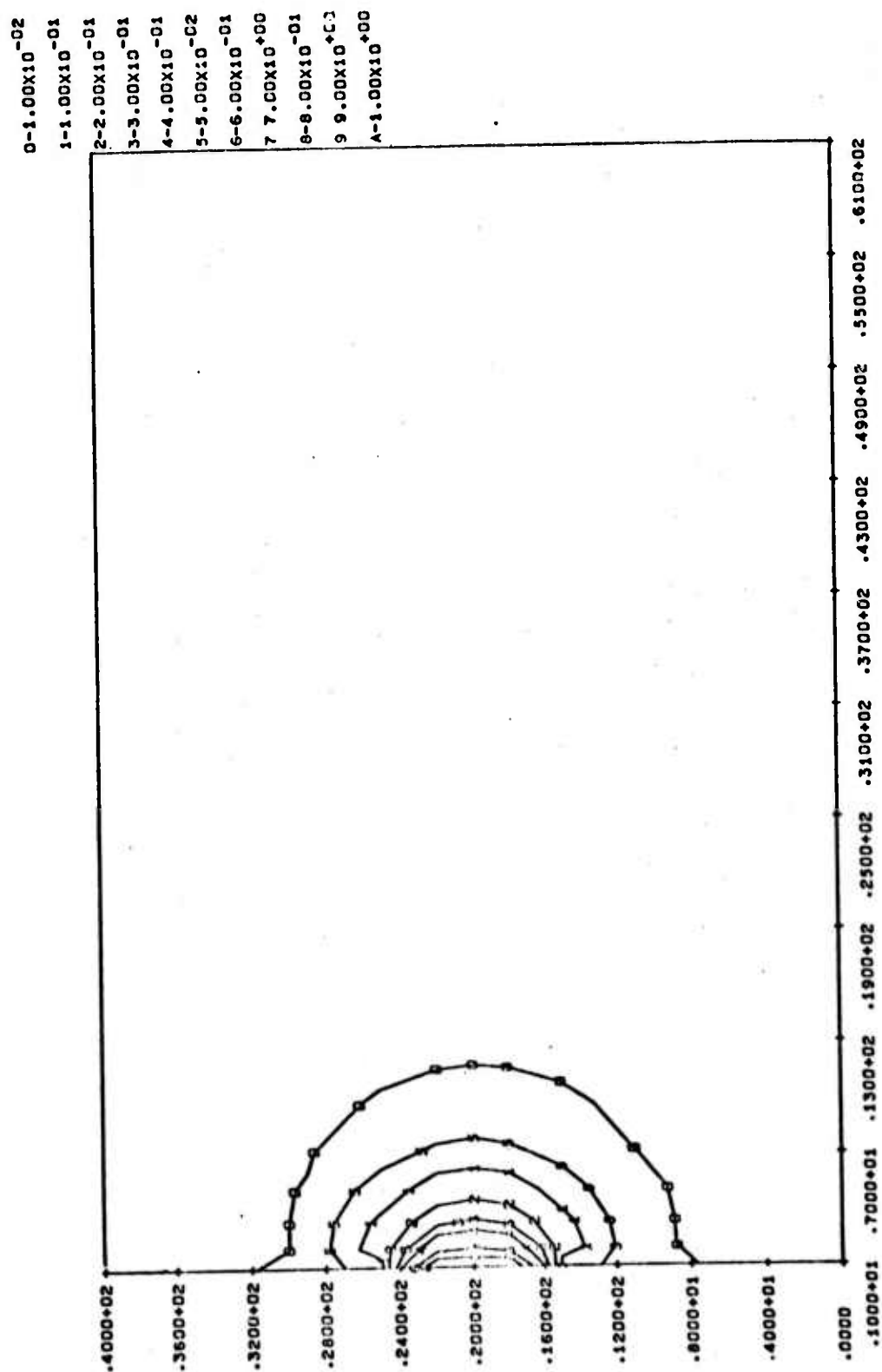


Fig. 7.7(b) -- Gross fluid stress $\sigma = -n_0 p$ (bars), homogeneous surface layer, $t = 0.01$ day.

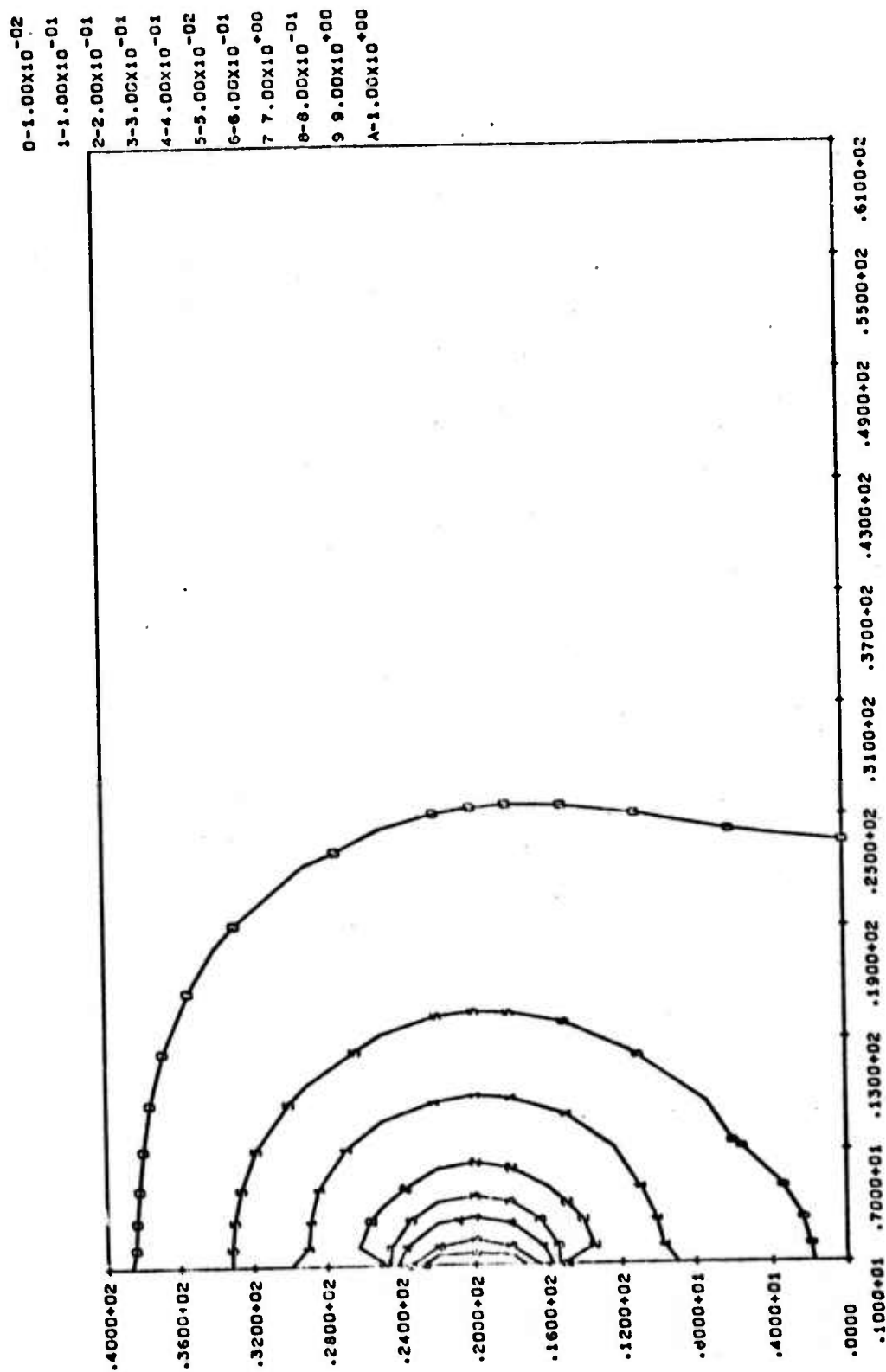


Fig. 7.7(c) -- Gross fluid stress $\sigma^{(2)} = -n_0 p$ (bars), homogeneous surface layer, $t = 0.1$ day.

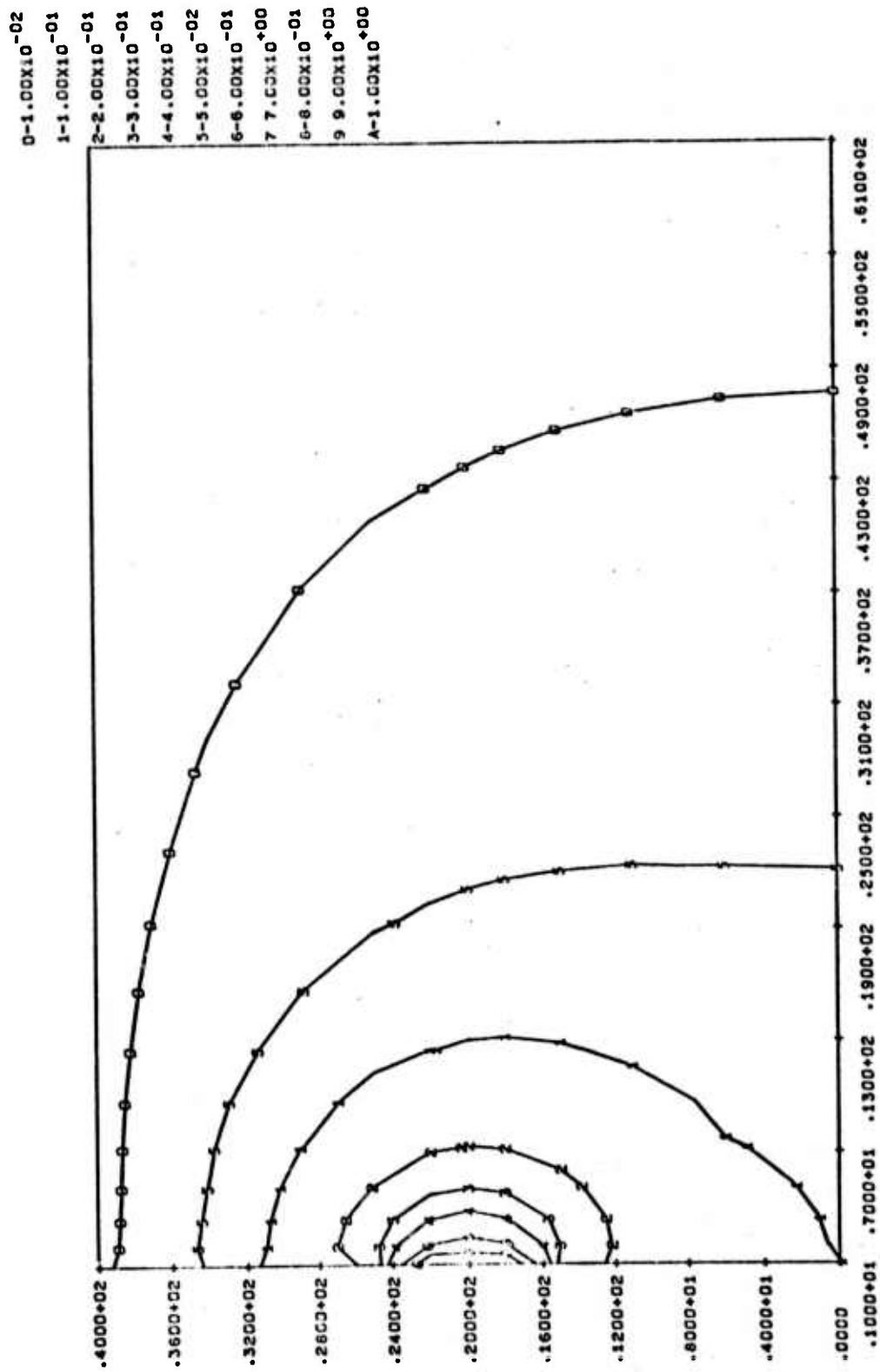


Fig. 7.7(d) -- Gross fluid stress σ (2) = $n_0 p$ (bars), homogeneous surface layer,
 $t = 1.0$ day.

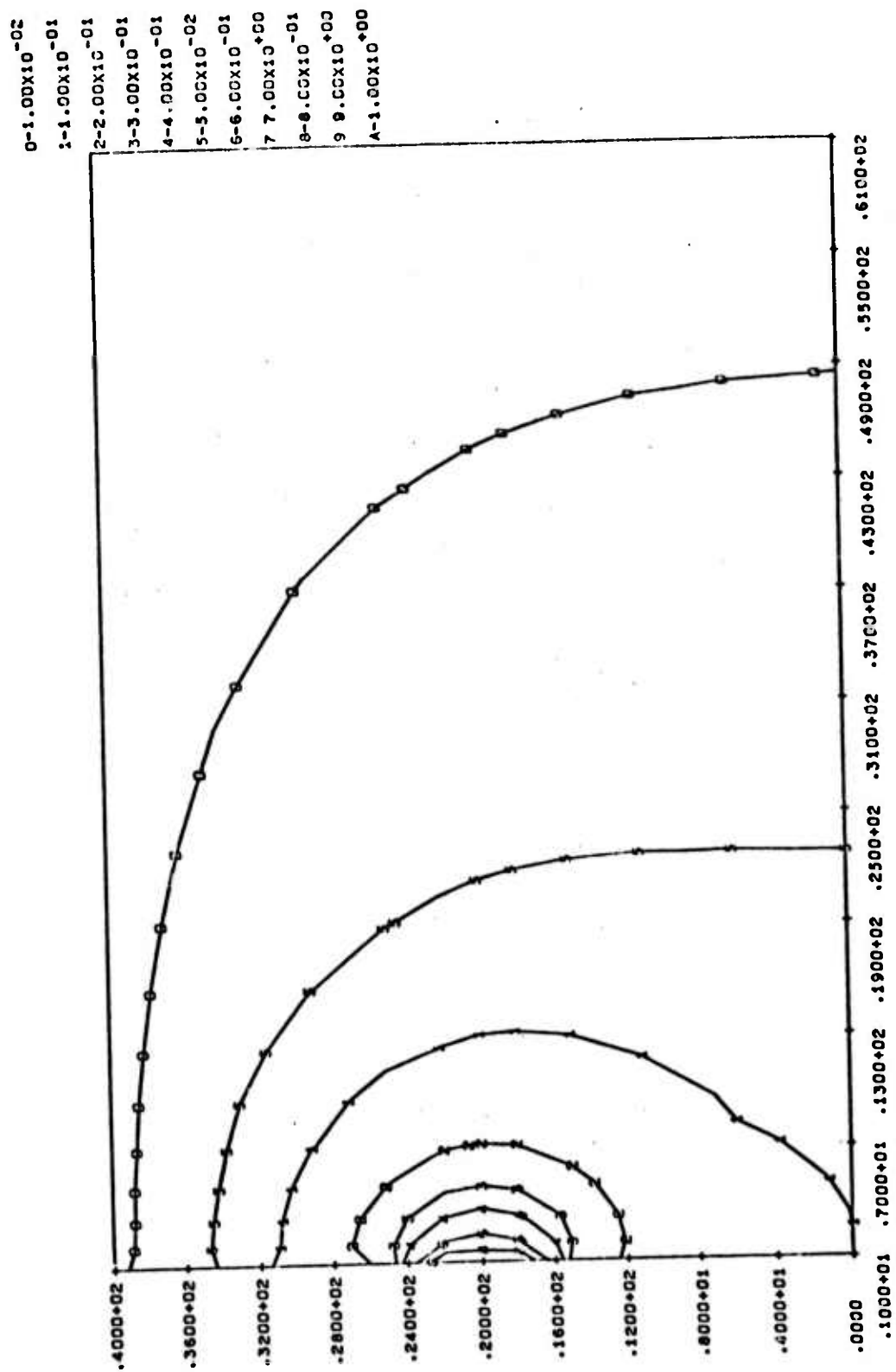


Fig. 7.7(e) -- Gross fluid stress σ (2) = - $n_0 p$ (bars), homogeneous surface layer, $t = 10.0$ days.

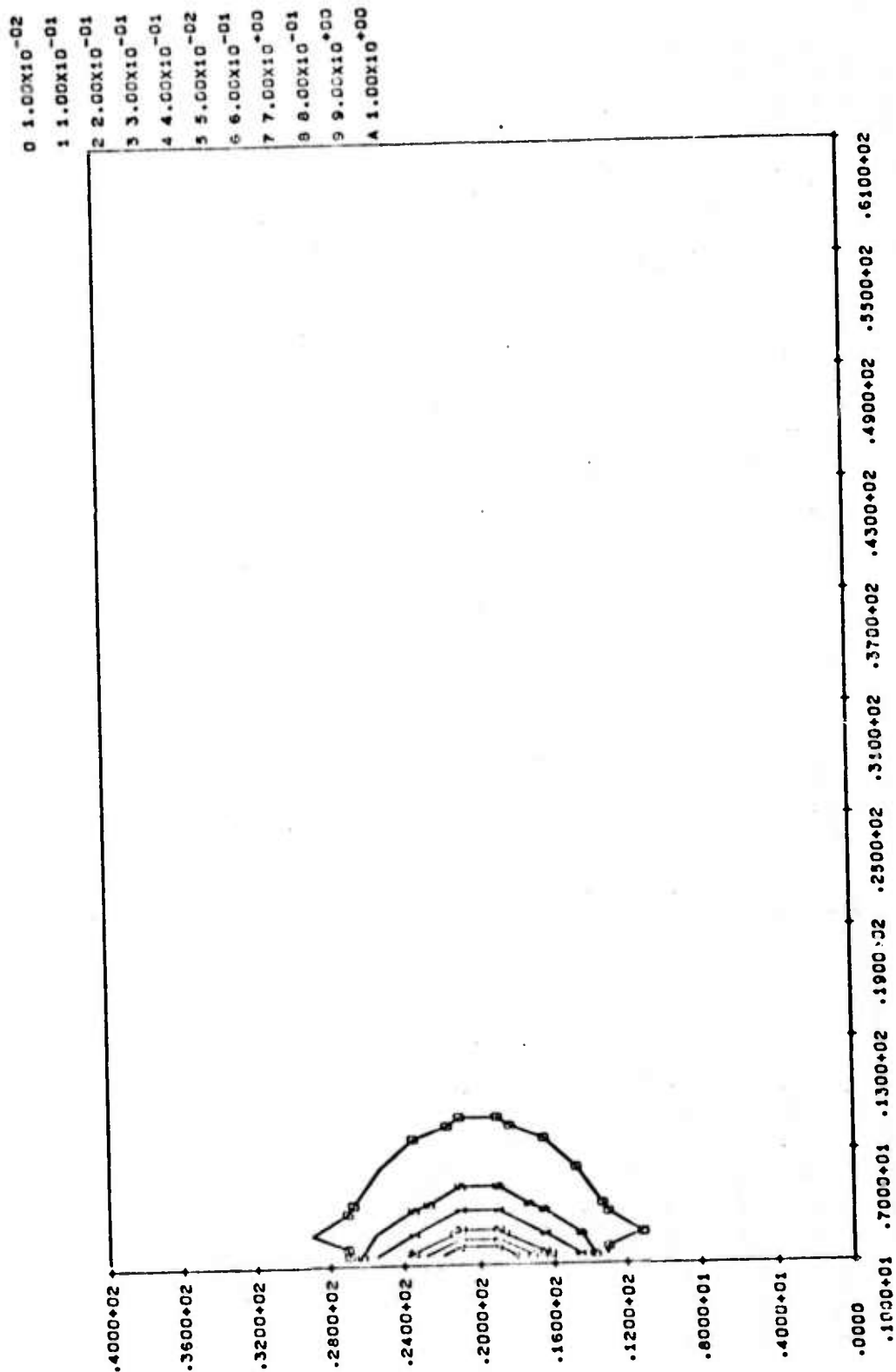


Fig. 7.8(a) -- Most tensile principal gross rock stress (bars), homogeneous surface layer, $t = 0.001$ day.

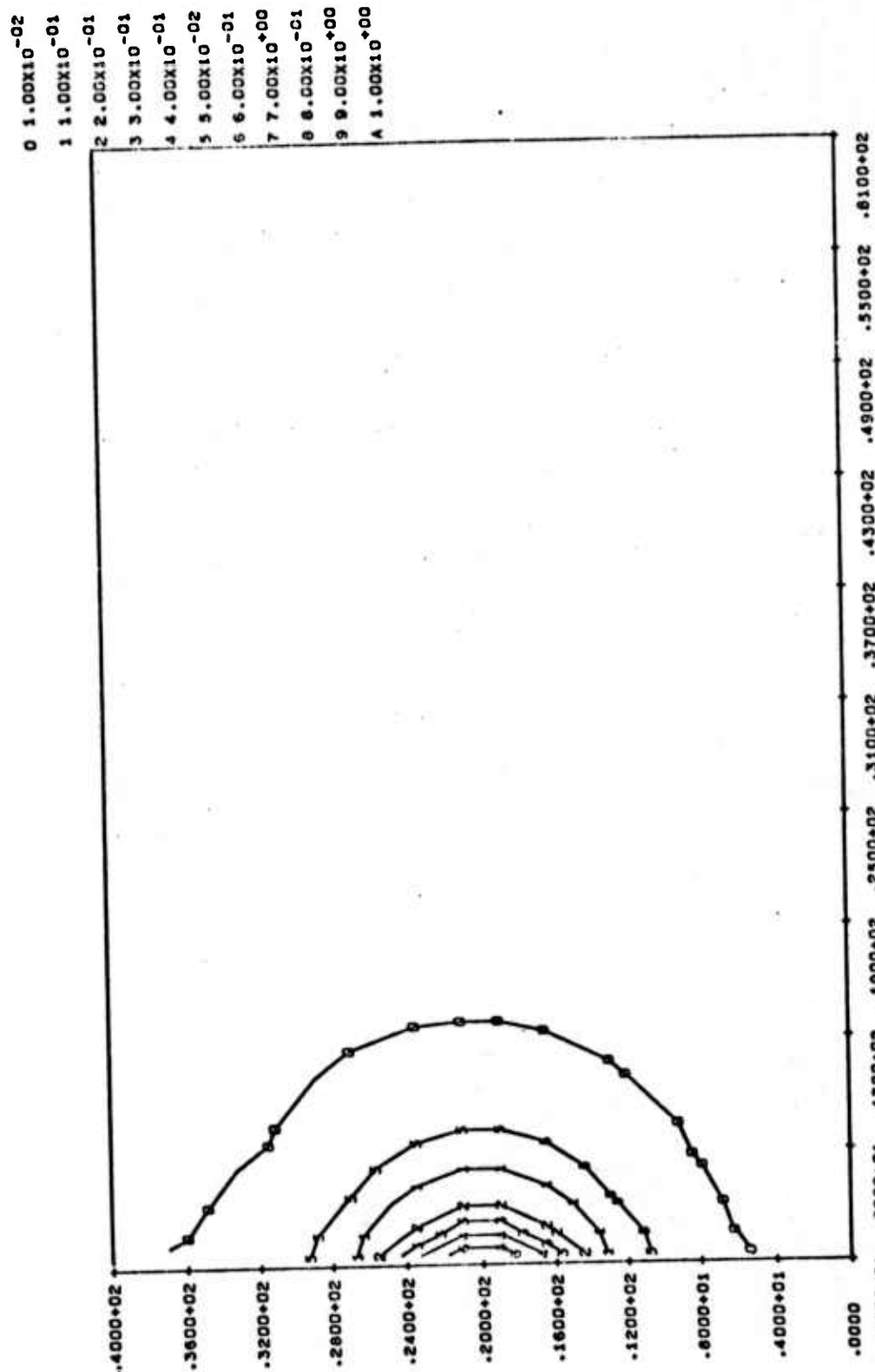


Fig. 7.8(b) -- Most tensile principal gross rock stress (bars), homogeneous surface layer, $t = 0.01$ day.

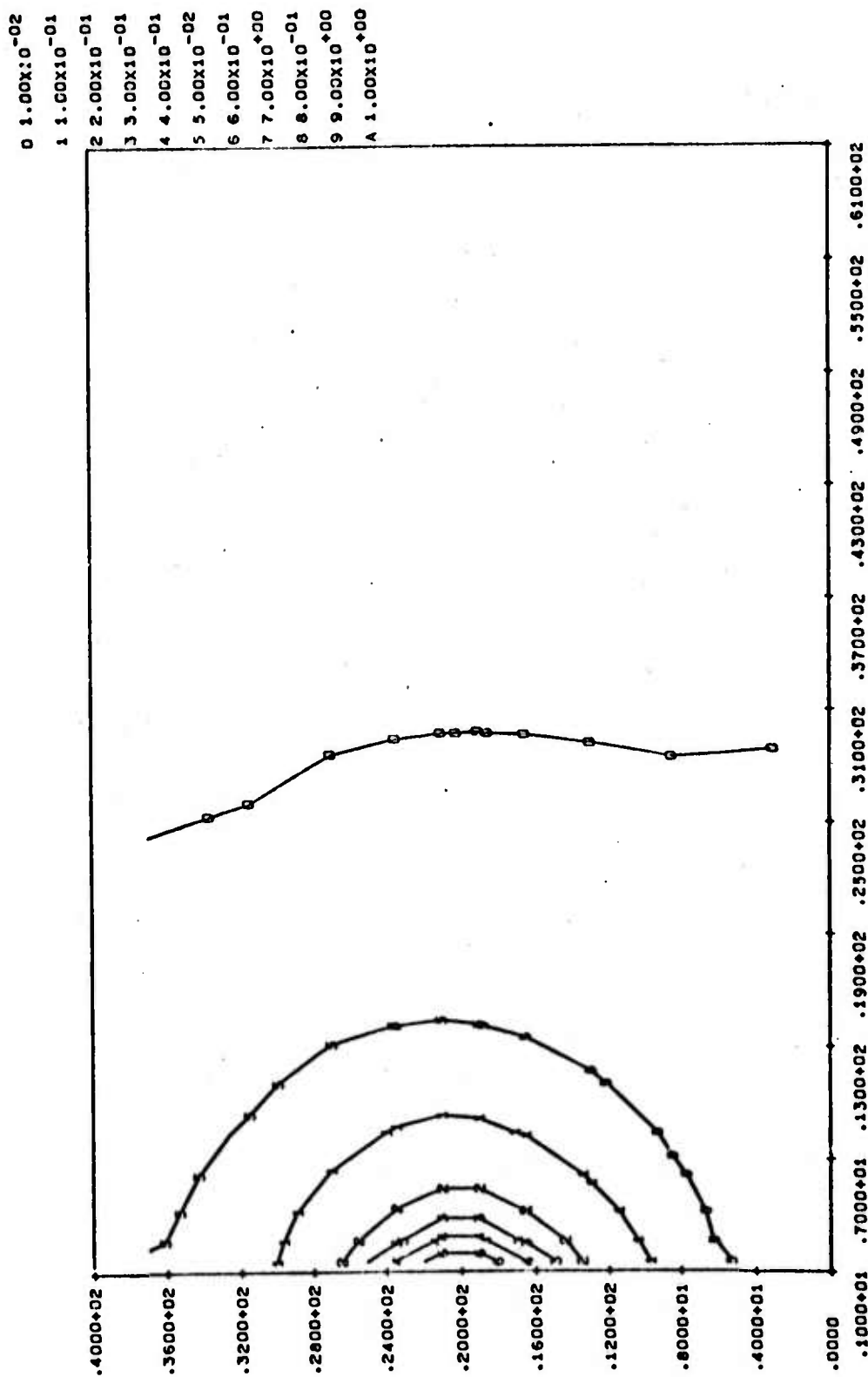


Fig. 7.8(c) -- Most tensile principal gross rock stress (bars), homogeneous surface layer, $t = 0.1$ day.

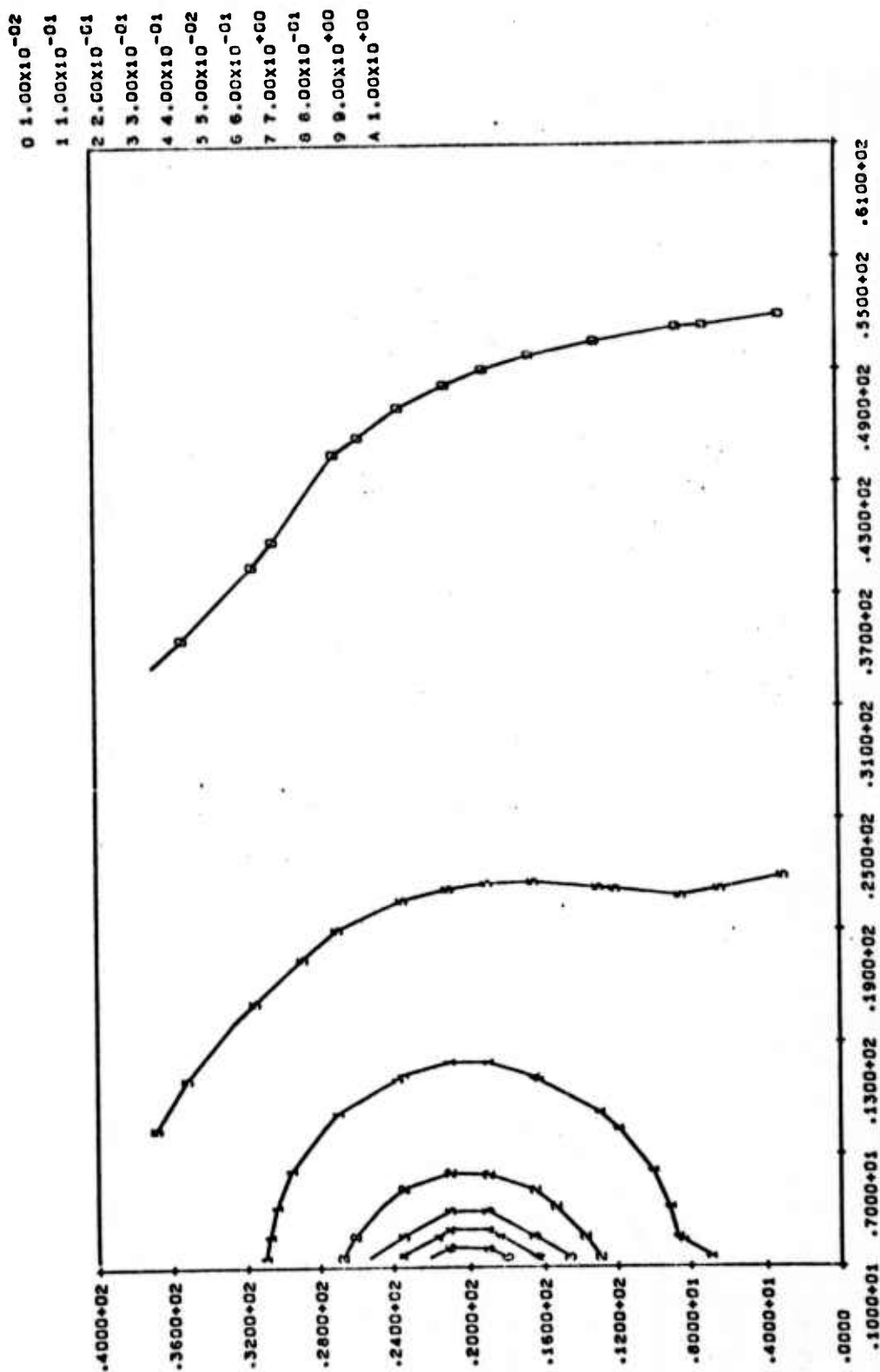


Fig. 7.8(d) -- Most tensile principal gross rock stress (bars), homogeneous surface layer, $t = 1.0$ day.

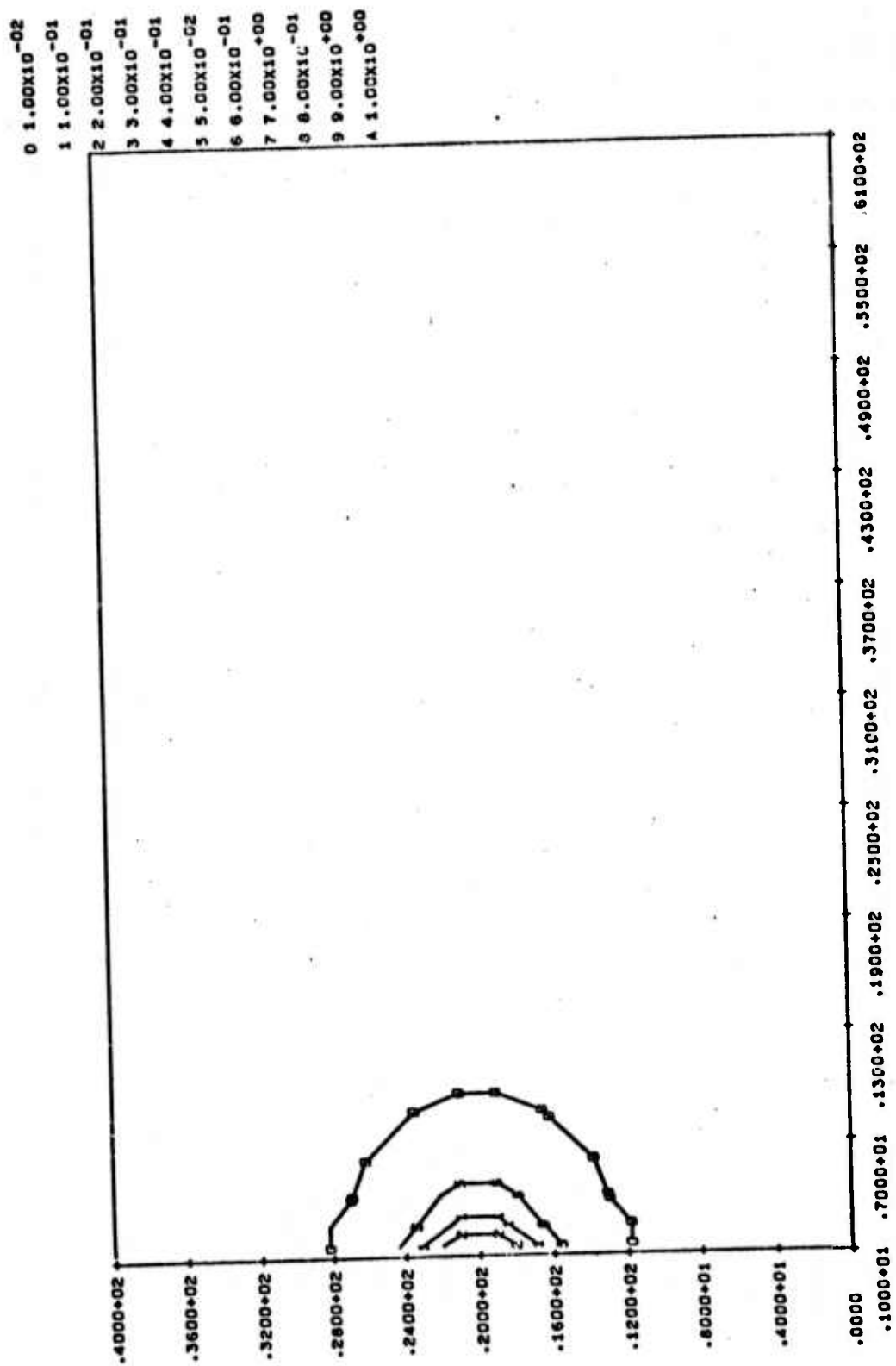


Fig. 7.9(a) -- Gross deviatoric rock stress (bars), homogeneous surface layer,
 $t = 0.001$ day.

0 1.00X10⁻⁰²
 1 1.00X10⁻⁰¹
 2 2.00X10⁻⁰¹
 3 3.00X10⁻⁰¹
 4 4.00X10⁻⁰¹
 5 5.00X10⁻⁰²
 6 6.00X10⁻⁰¹
 7 7.00X10⁻⁰⁰
 8 8.00X10⁻⁰¹
 9 9.00X10⁻⁰⁰
 A 1.00X10⁻⁰⁰

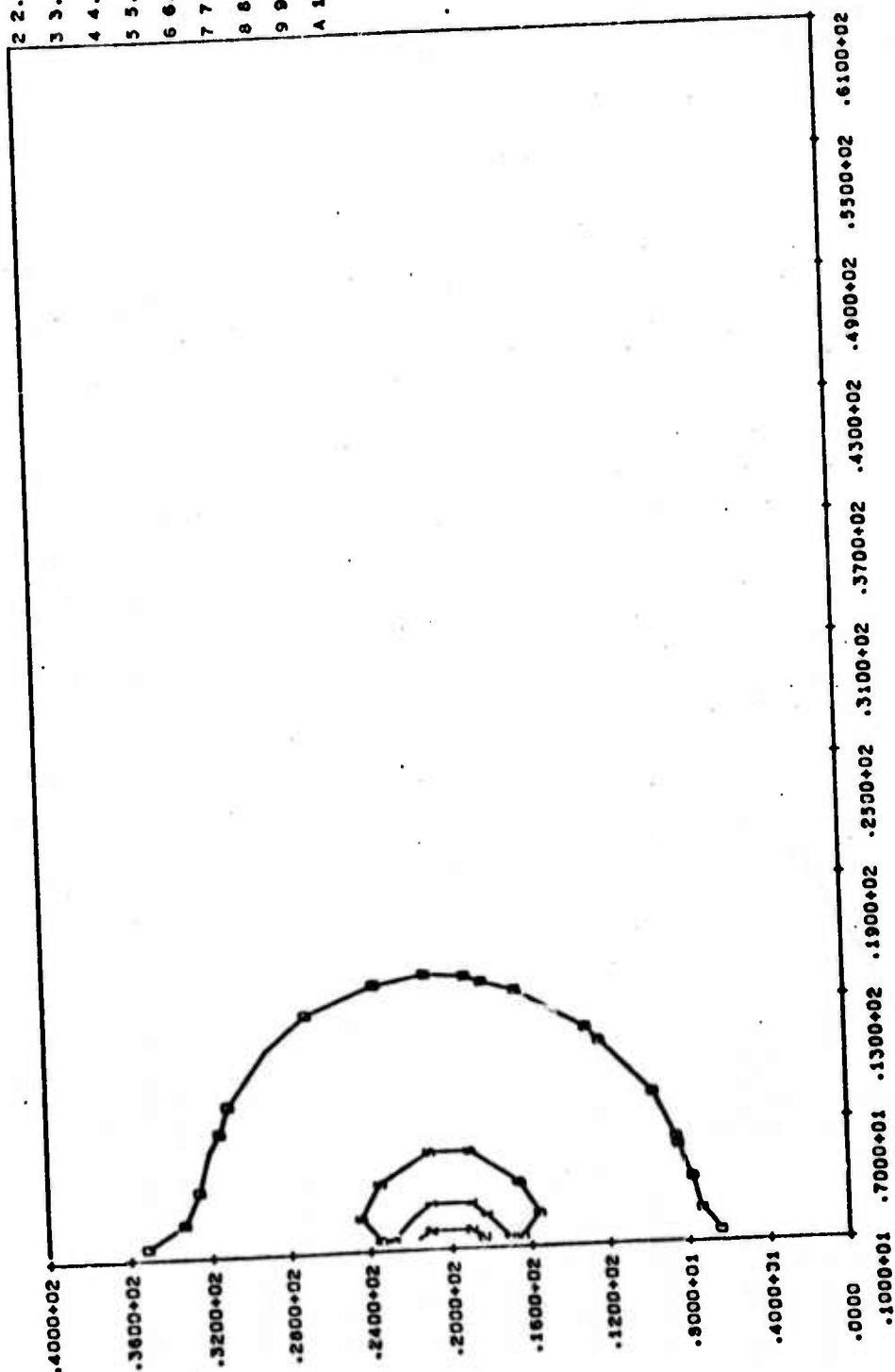


Fig. 7.9(b) -- Gross deviatoric rock stress (bars), homogeneous surface layer, $t = 0.01$ day.

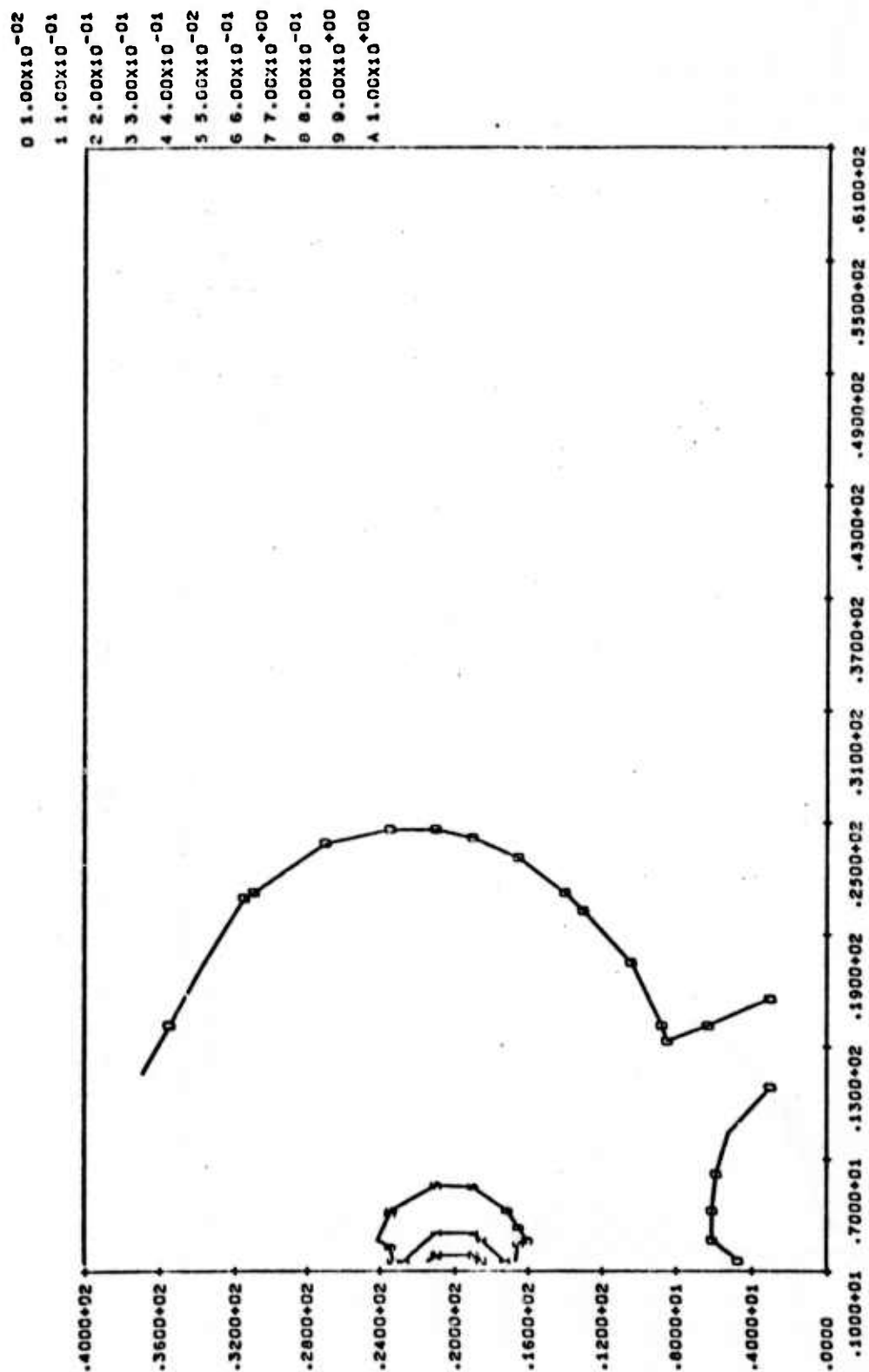


Fig. 7.9(c)---Gross deviatoric rock stress (bars), homogeneous surface layer, $t = 0.1$ day.

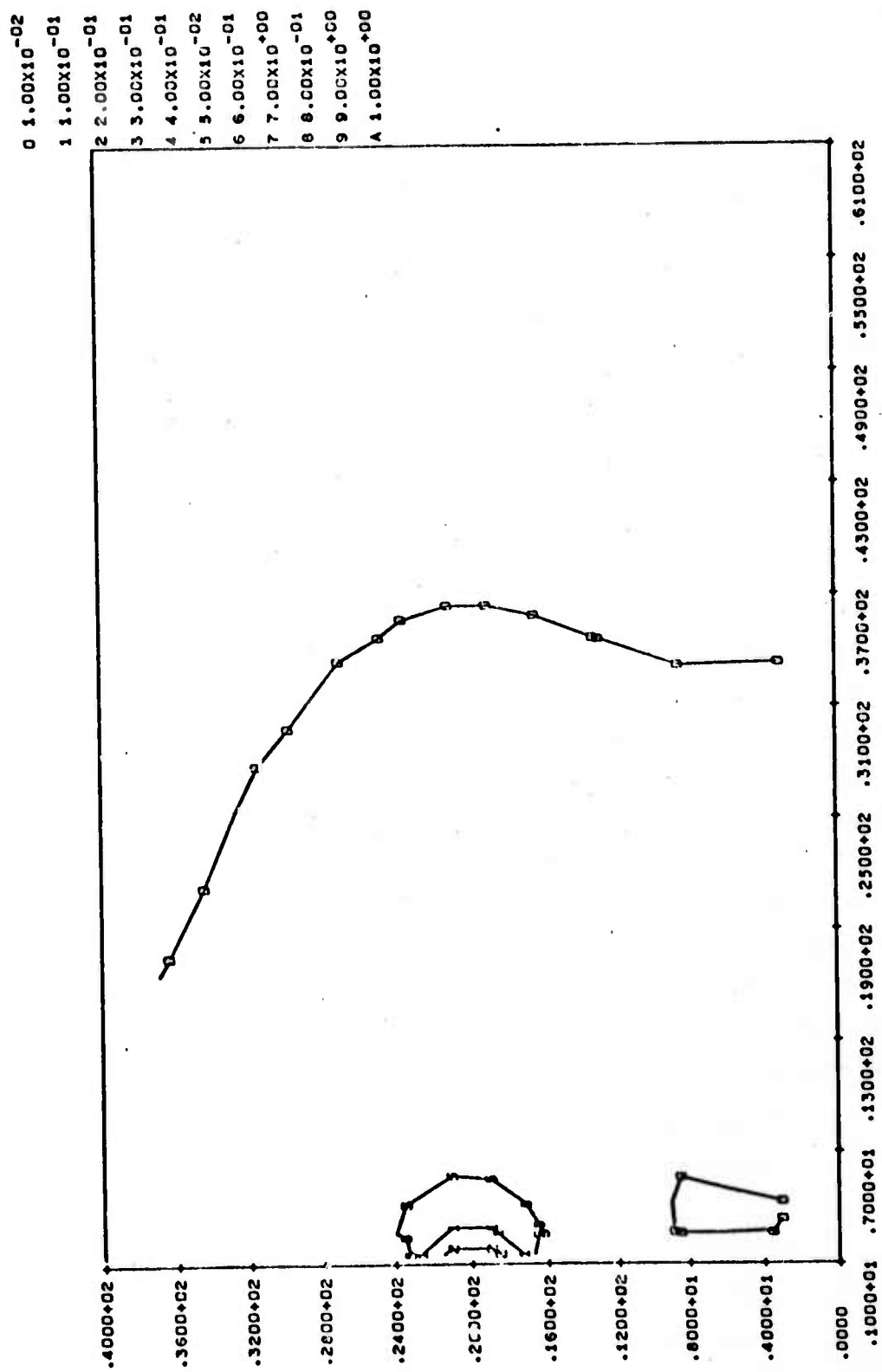


Fig. 7.9(d) -- Gross deviatoric rock stress (bars), homogeneous surface layer, $t = 1.0$ day.

contours become nearly circular, characteristic of a spherical injection well. At greater distances, the free surface and the impervious, rigid base distort the contours. It is interesting to note, however, that the steady-state fluid stress and maximum rock stress fall off very nearly as the inverse of the distance from the injection well in the horizontal plane of injection, just as in the spherically symmetric injection system. Finally, we note that deviatoric stresses below 0.05 bars do not remain invariant with time. The rigid base condition significantly influences the very low deviatoric stresses as the steady-state condition is reached $t \geq 0.1$ days.

Similar graphical form, although less detailed, is used for presenting the results of injection into an identical environment with the exception of a narrow zone (4 meters thick) of material just above the injection site with an order of magnitude higher permeability. The computed displacements, fluid stress, maximum rock stress, and deviatoric stress for this layered region are presented in Figs. 7.10, 7.11, 7.12, and 7.13, respectively. In Figs. 7.14 through 7.17, we present results for the same overlying layer with an order of magnitude lower permeability than the remaining material. From these three sets of calculations – the homogeneous surface layer, the overlying high permeability layer, and the overlying low permeability layer – we have made the following observations:

1. Stresses are generated in rock mass near the injection well, even before seepage begins. Because the vertical dimension of the injection cavity is greater than the horizontal dimension, the circumferential stress produced by the non-penetrating fluid pressure is the most tensile principal stress. In a shear-free tectonic

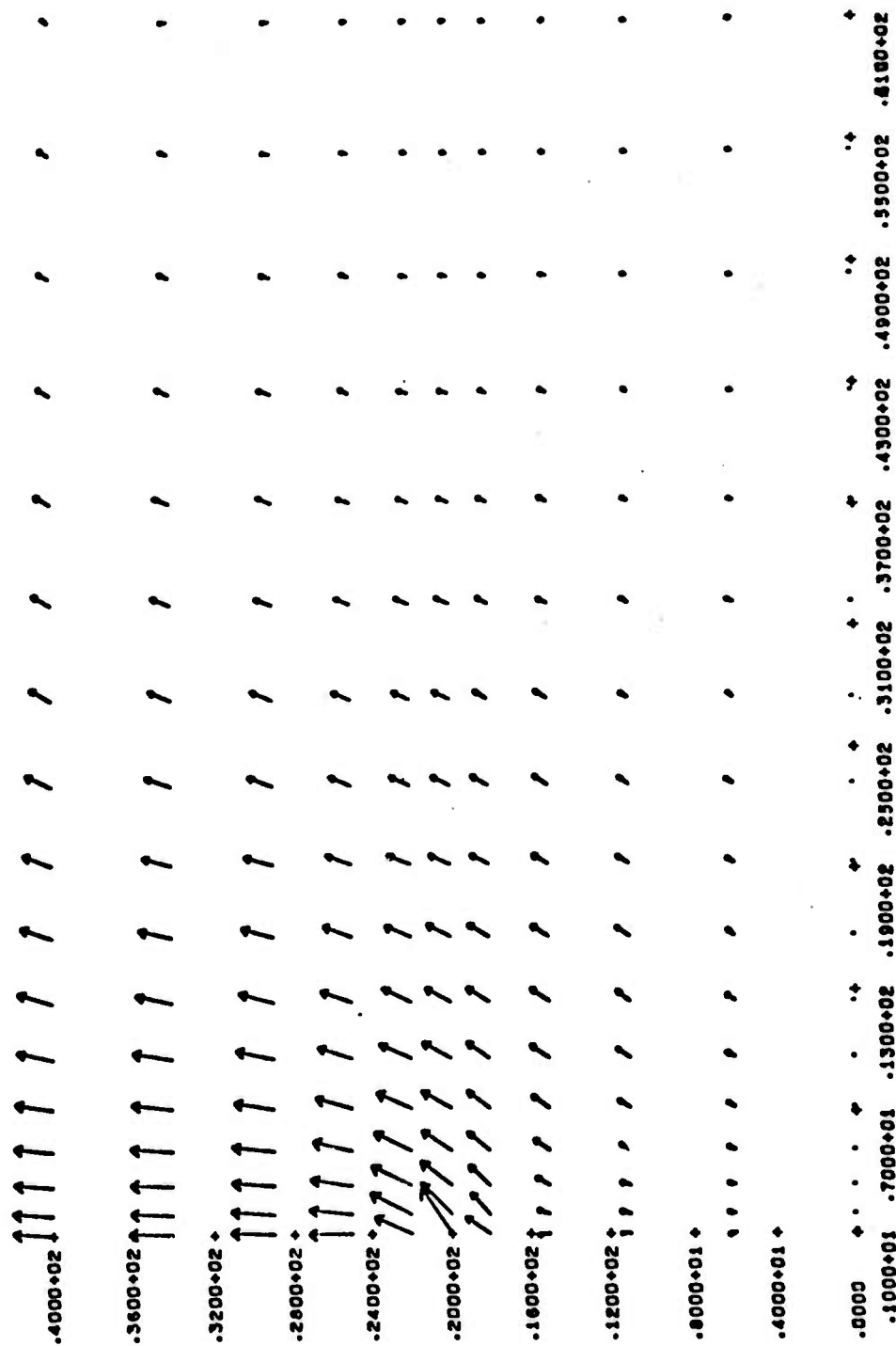


Fig. 7.10--Displacements in the rock, overlying high permeability layer,
 $t = 10$. days (steady state), maximum displacement = 0.118 mm.

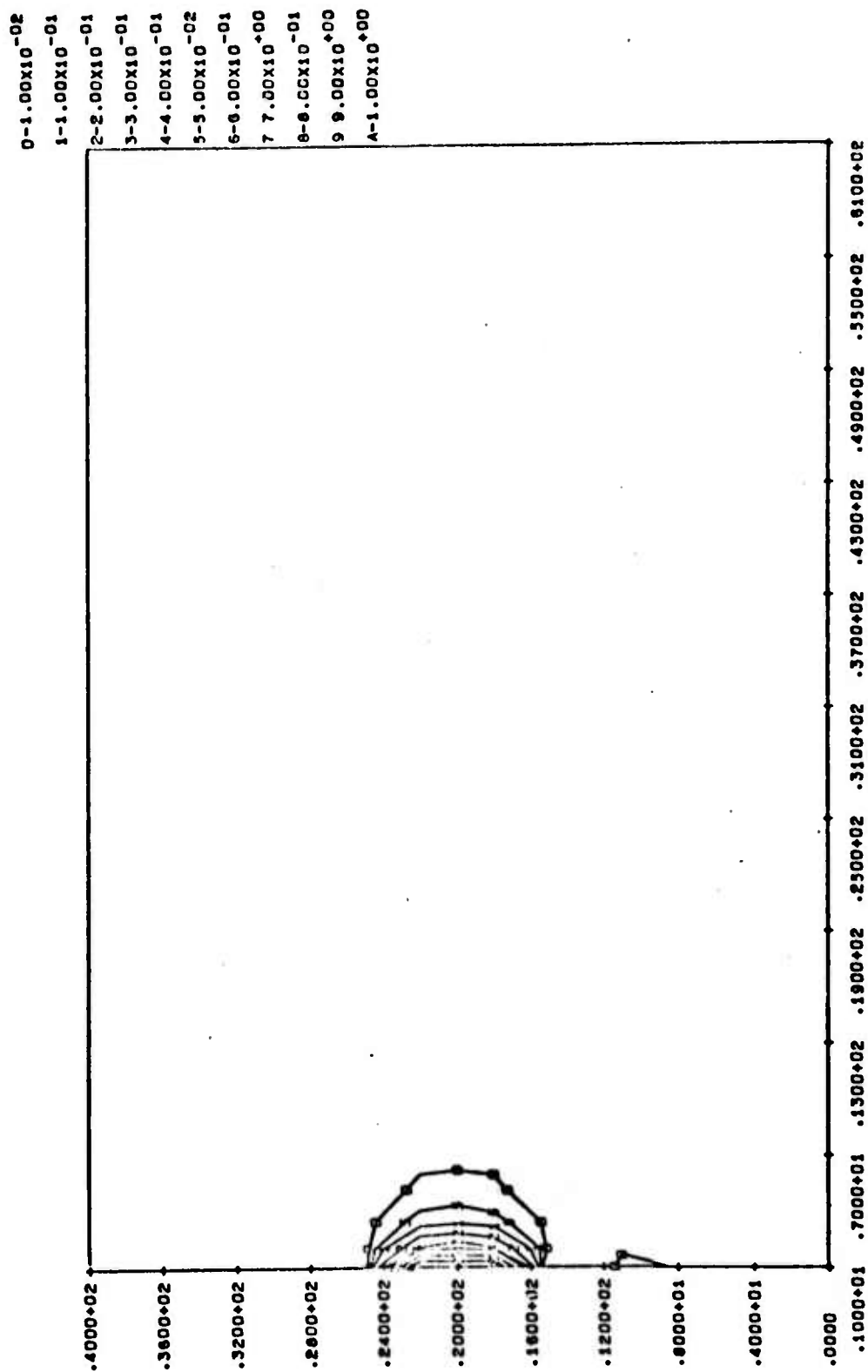


Fig. 7.11(a) -- Gross fluid stress $\sigma = -n p$ (bars), overlying high permeability layer, $t = 0.001$ day.

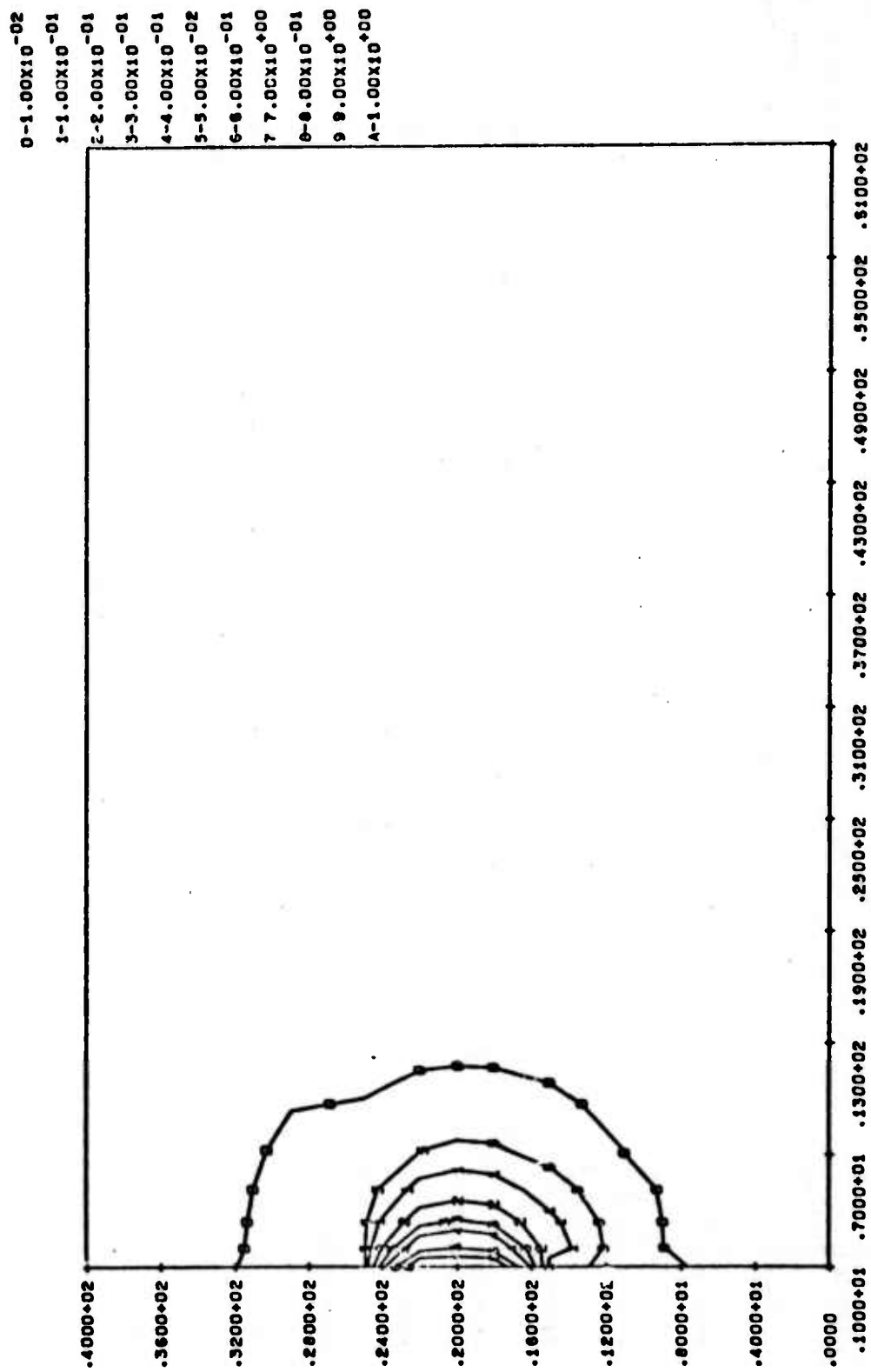


Fig. 7.11(b) -- Gross fluid stress σ = - n p (bars) overlying high permeability layer, $t = 0.01$ days.

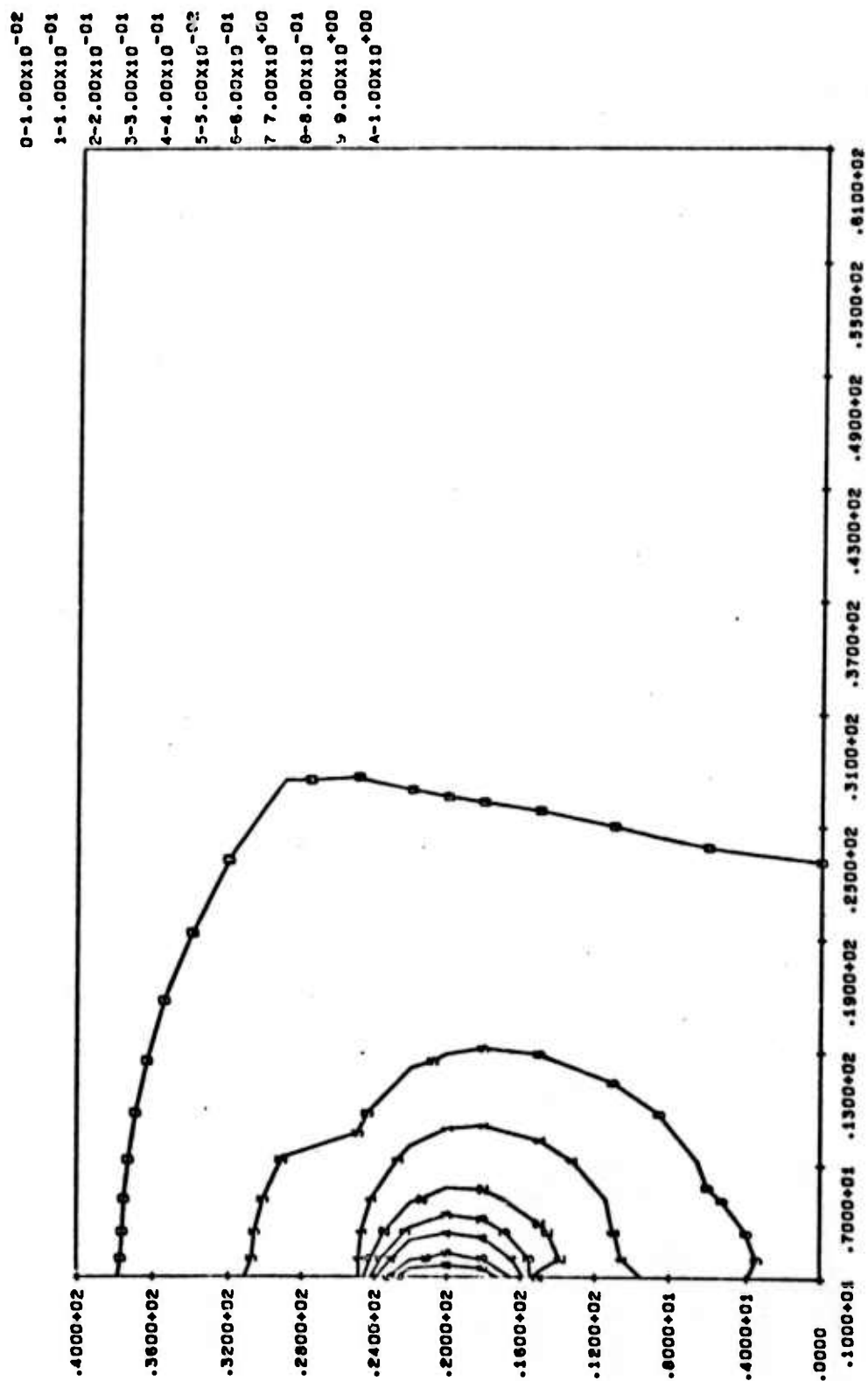


Fig. 7.11(c) -- Gross fluid stress $\sigma^{(2)} = -n_0 p$ (bars), overlying high permeability layer, $t = 0.1$ day.

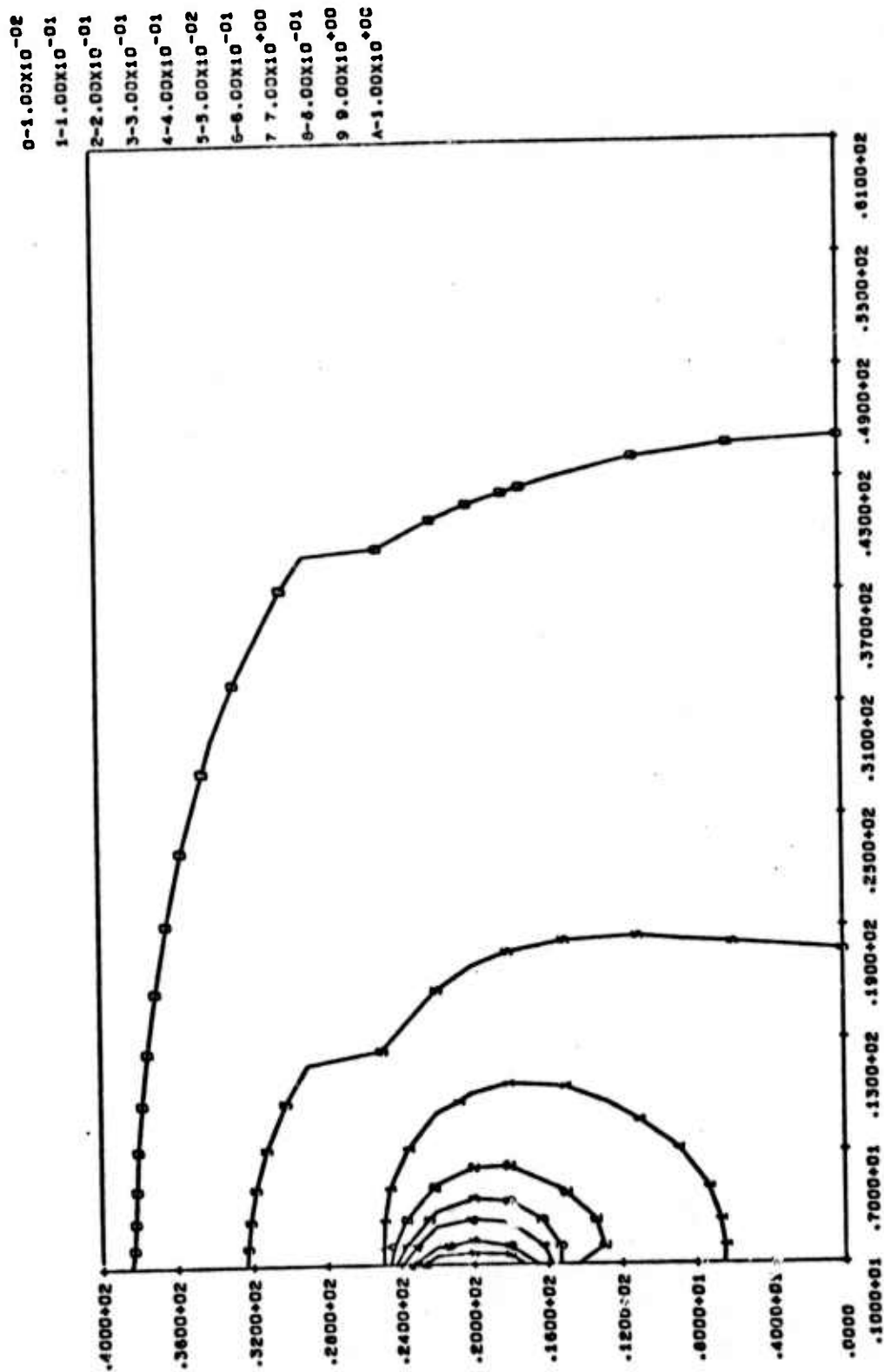


Fig. 7.11(d) -- Gross fluid stress σ (bars), overlying high permeability layer, $t = 1.0$ days.

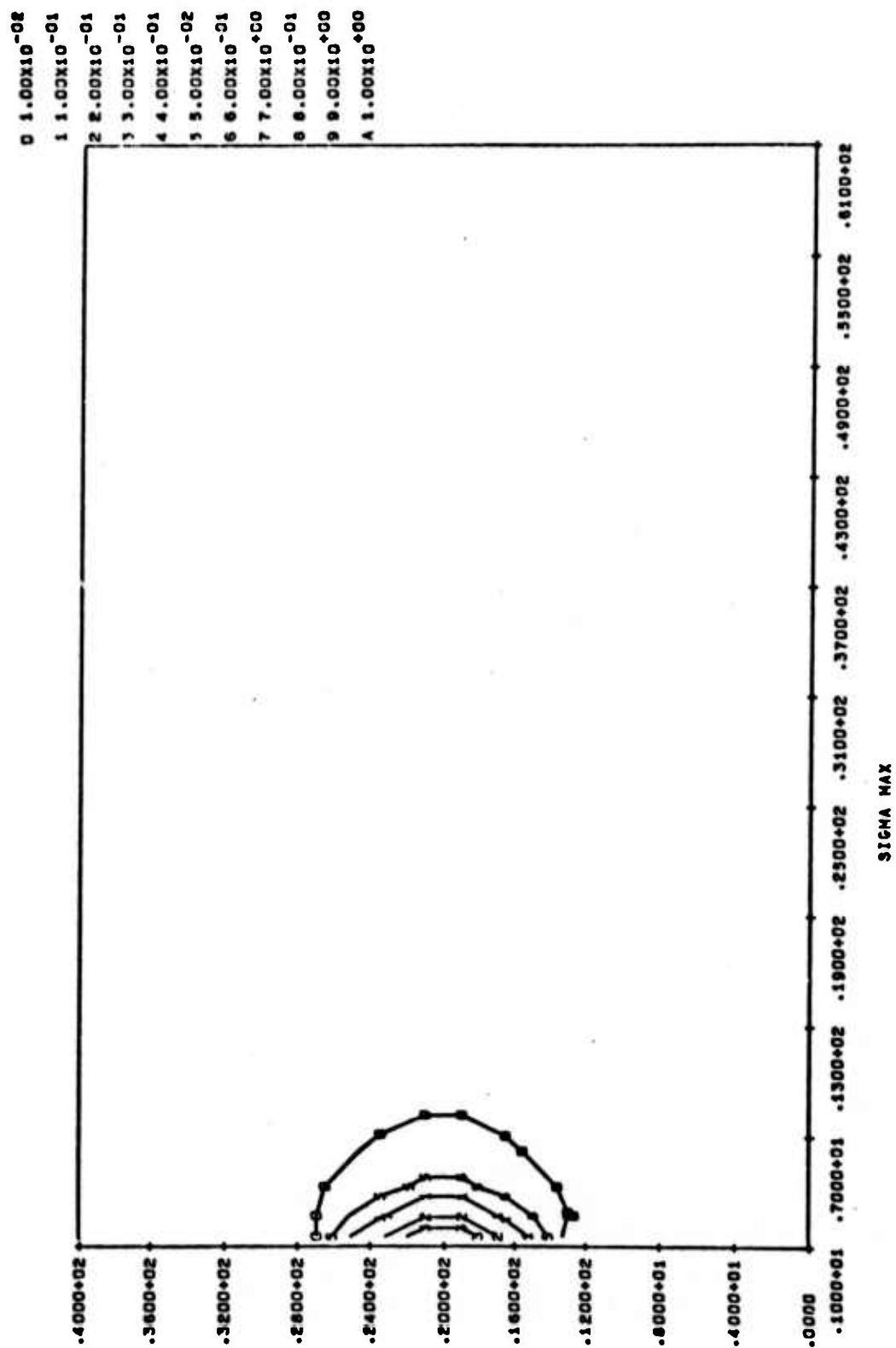


Fig. 7.12(a) -- Most tensile principal gross rock stress (bars), overlying high permeability layer, $t = 0.001$ day.

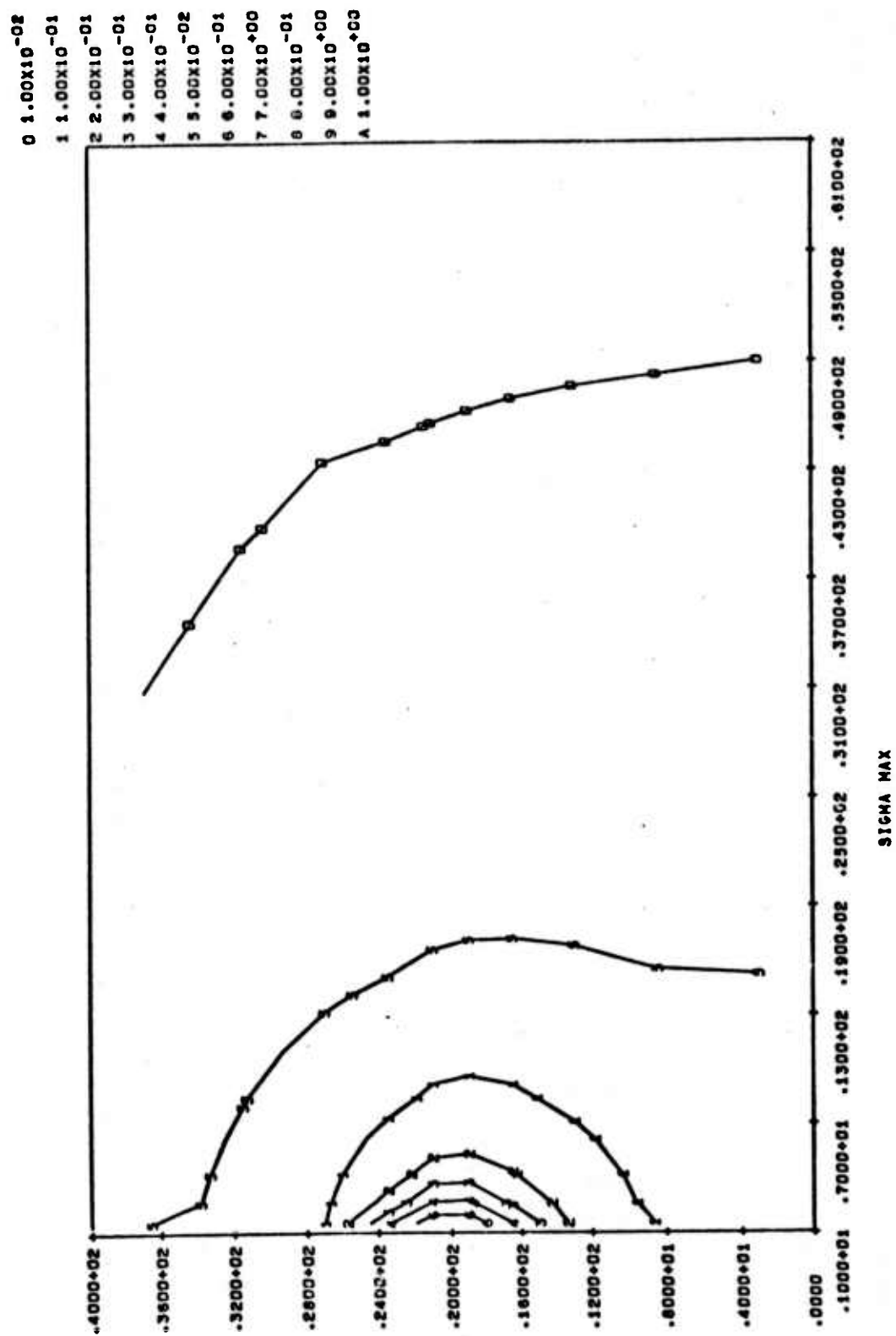


Fig. 7.12(b) -- Most tensile principal gross rock stress (bars), overlying high permeability layer, $t = 1.0$ day.

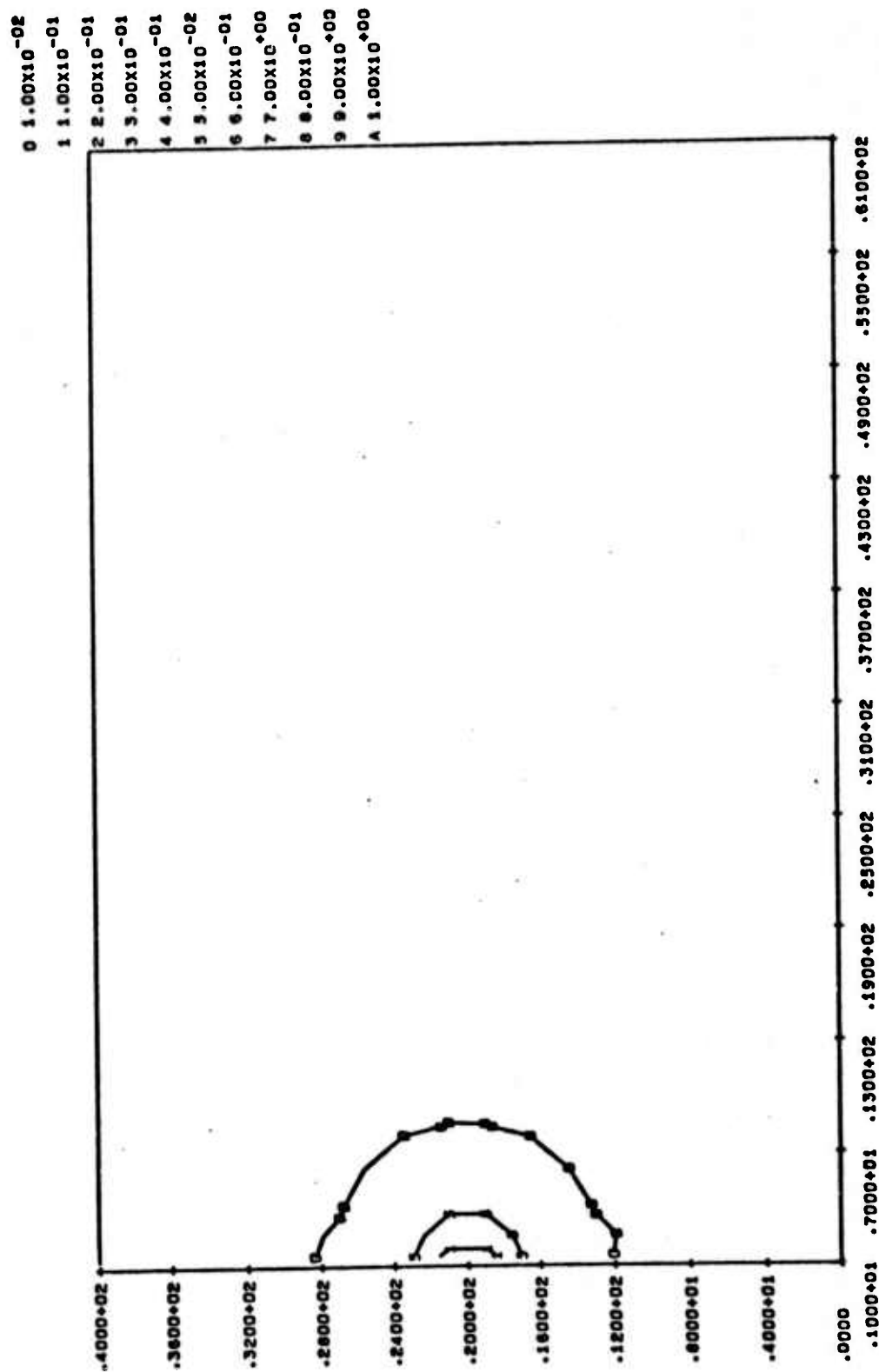


Fig. 7.13(a)---Gross deviatoric rock stress (bars), homogeneous surface layer,
 $t = 0.001$ day.

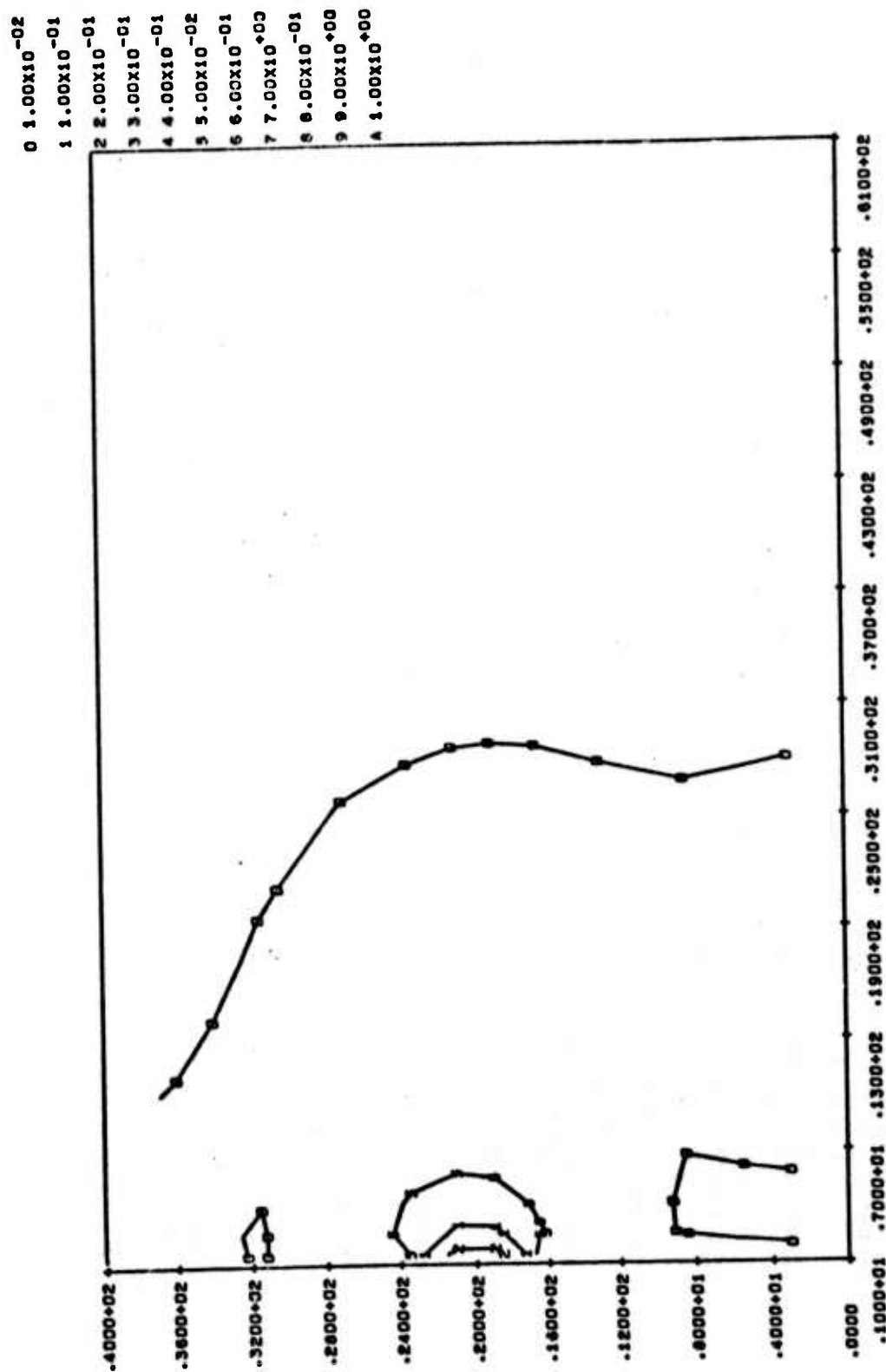


Fig. 7.13(b) -- Gross deviatoric rock stress (bars), homogeneous surface layer,
 $t = 1.0$ day.

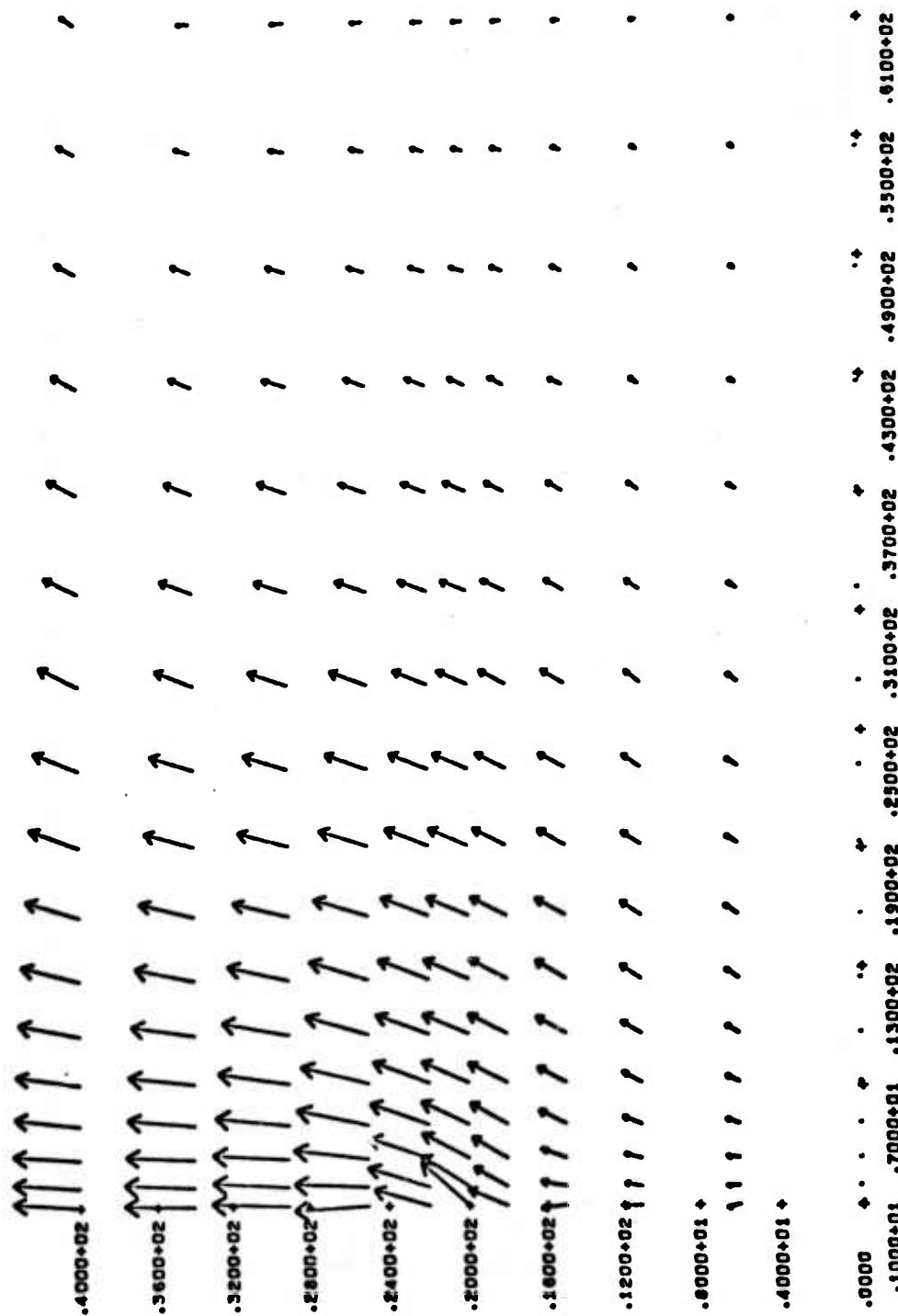


Fig. 7.14--Displacements in the rock, overlying low permeability layer, $t = 10$ days (steady state), maximum displacement = 0.215 mm.

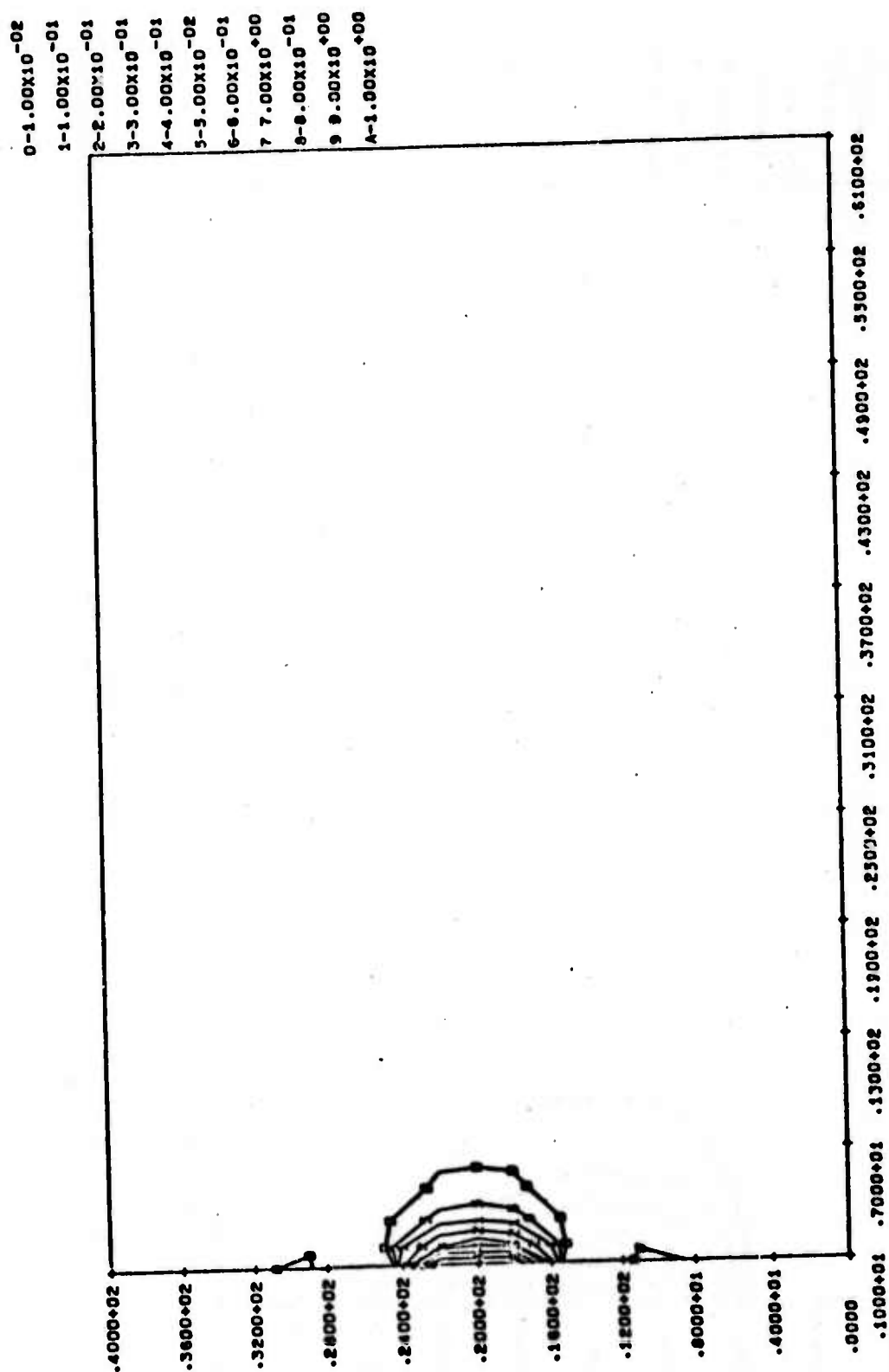


Fig. 7.15(a) -- Gross fluid stress $\sigma^{(2)} = -n_p^{(2)}$ (bars), overlying low permeability layer, $t = 0.001$ day.

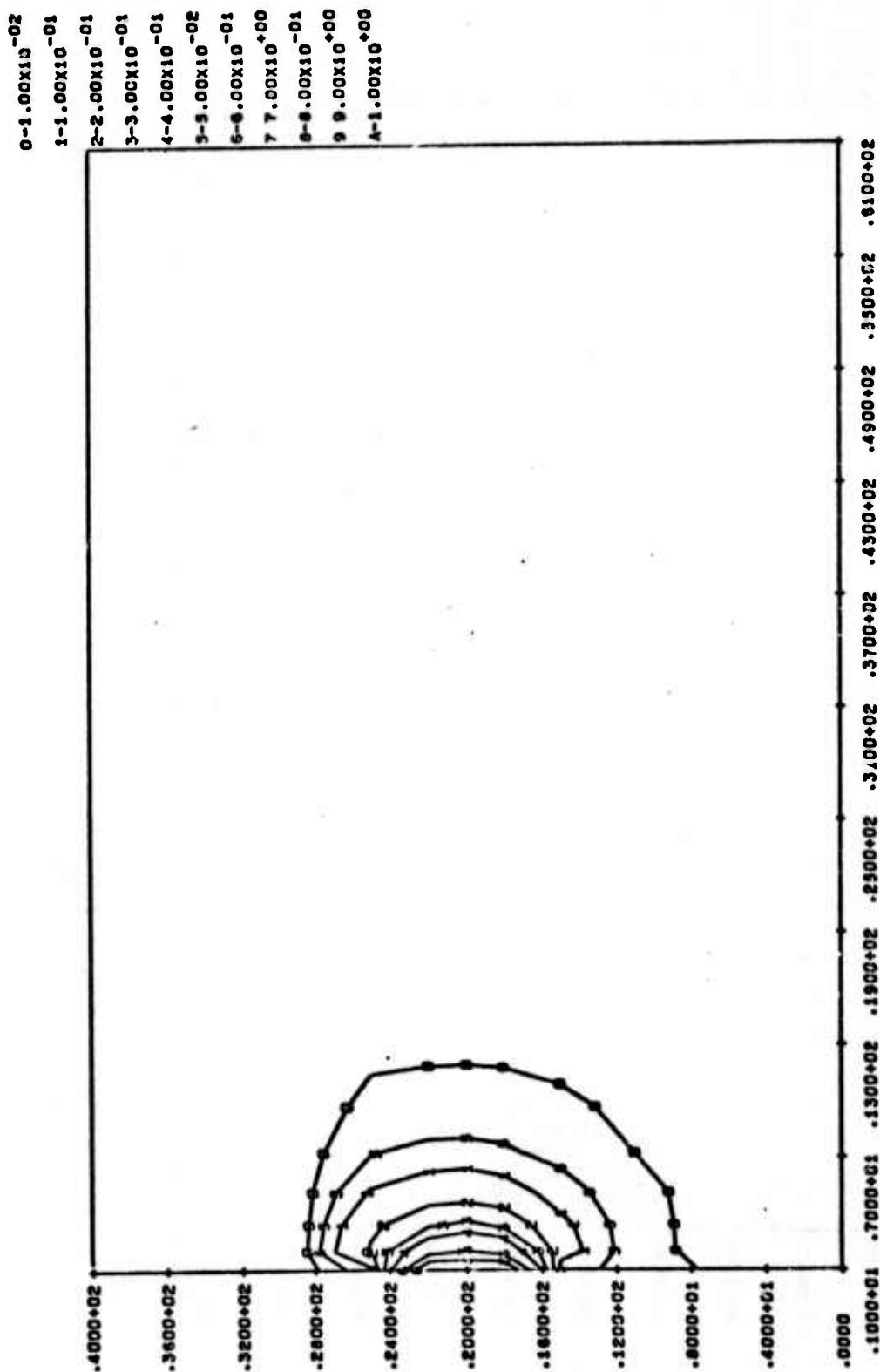


Fig. 7.15(b) -- Gross fluid stress $\sigma^{(2)} = -n_0 p^{(2)}$ (bars), overlying low permeability layer, $t = 0.01$ day.

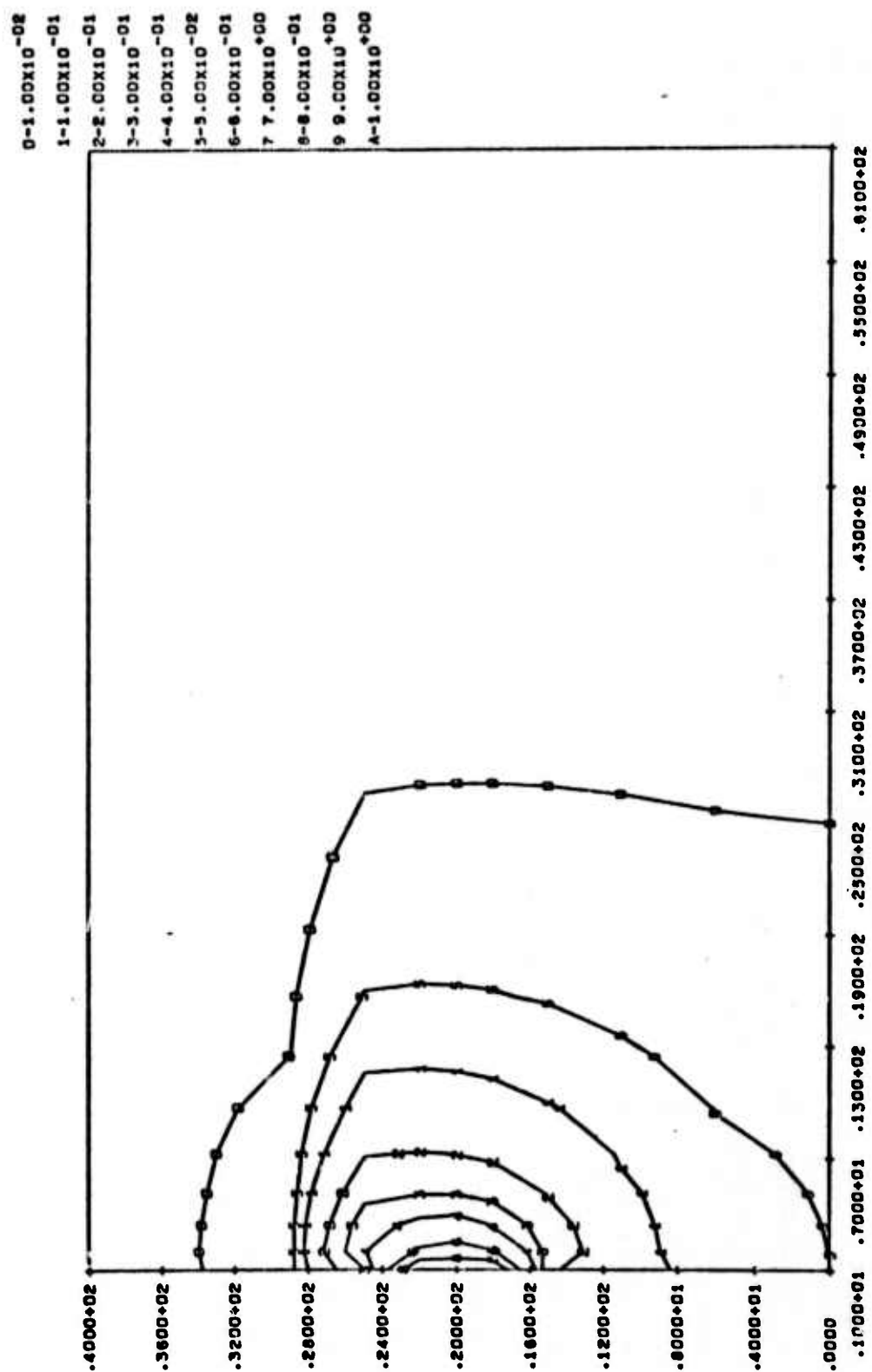


Fig. 7.15(c) -- Gross fluid stress σ (2) = $-n_0 p$ (bars), overlying low permeability layer, $t = 0.1$ day.

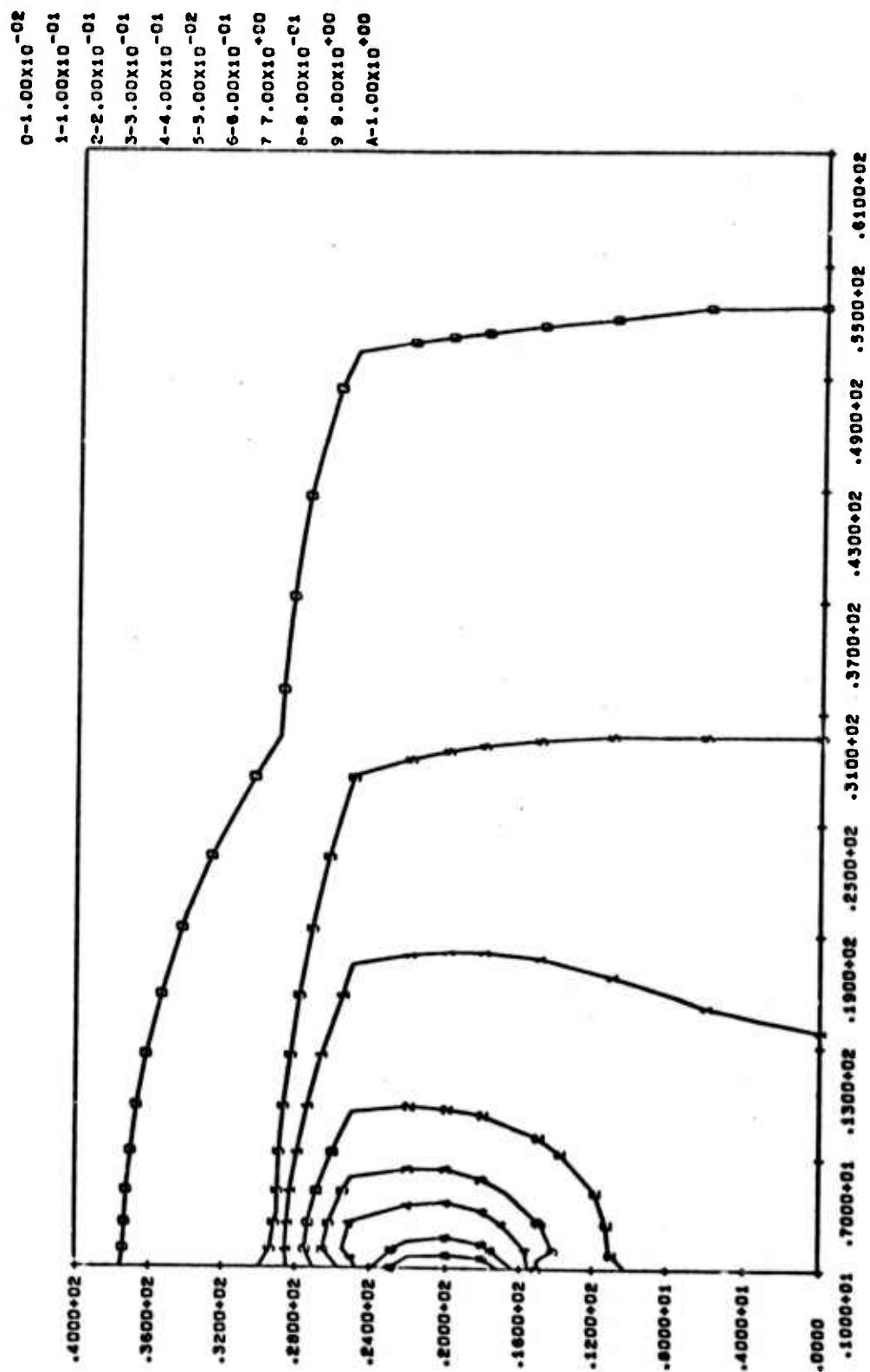


Fig. 7.15(d) -- Gross fluid stress $\sigma^{(2)} = -n_p$ (bars), overlying low permeability layer, $t = 1.0$ days.

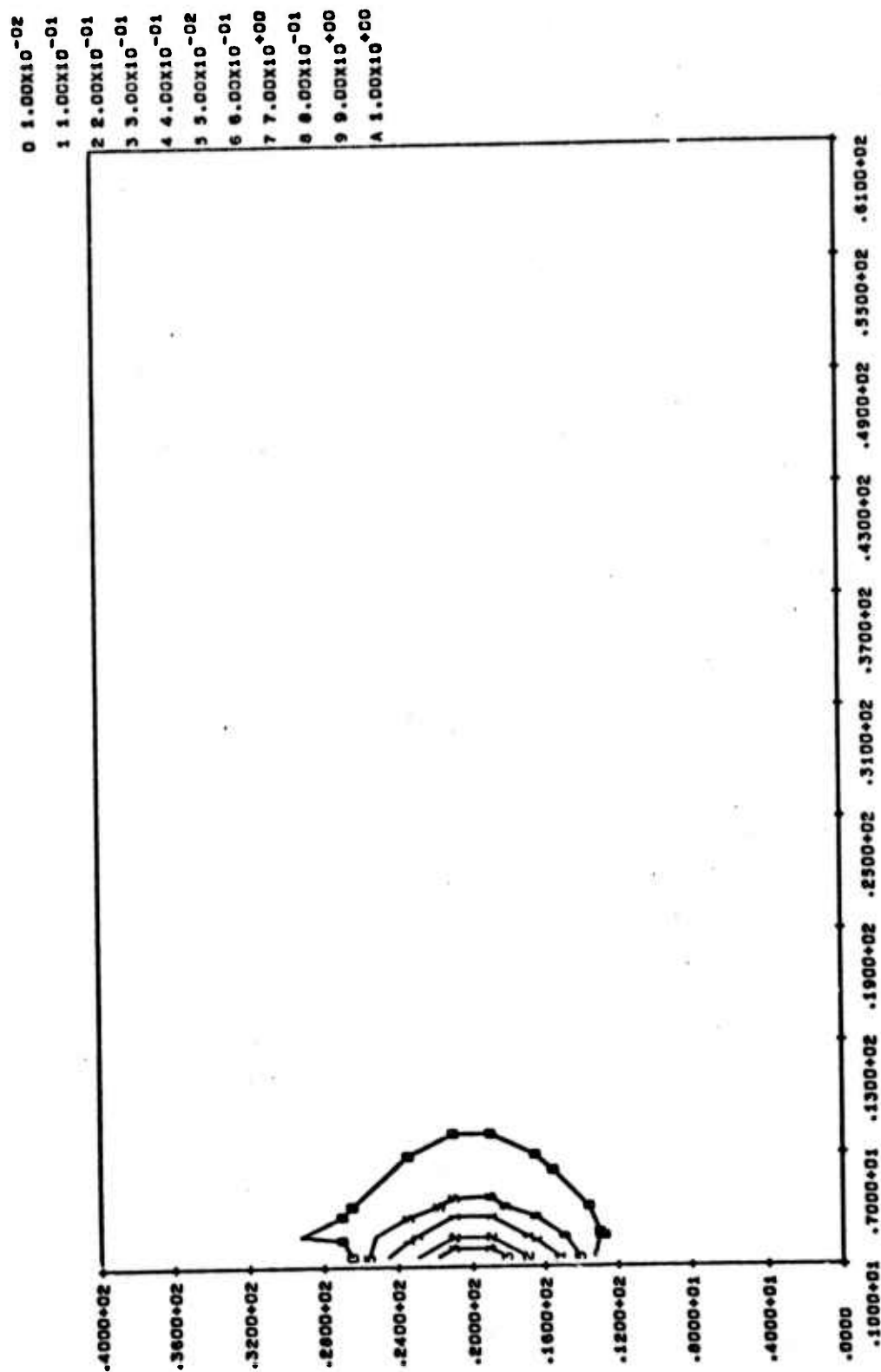


Fig. 7.16(a) -- Most tensile principal gross rock stress (bars), overlying low permeability layer, $t = 0.001$ day.

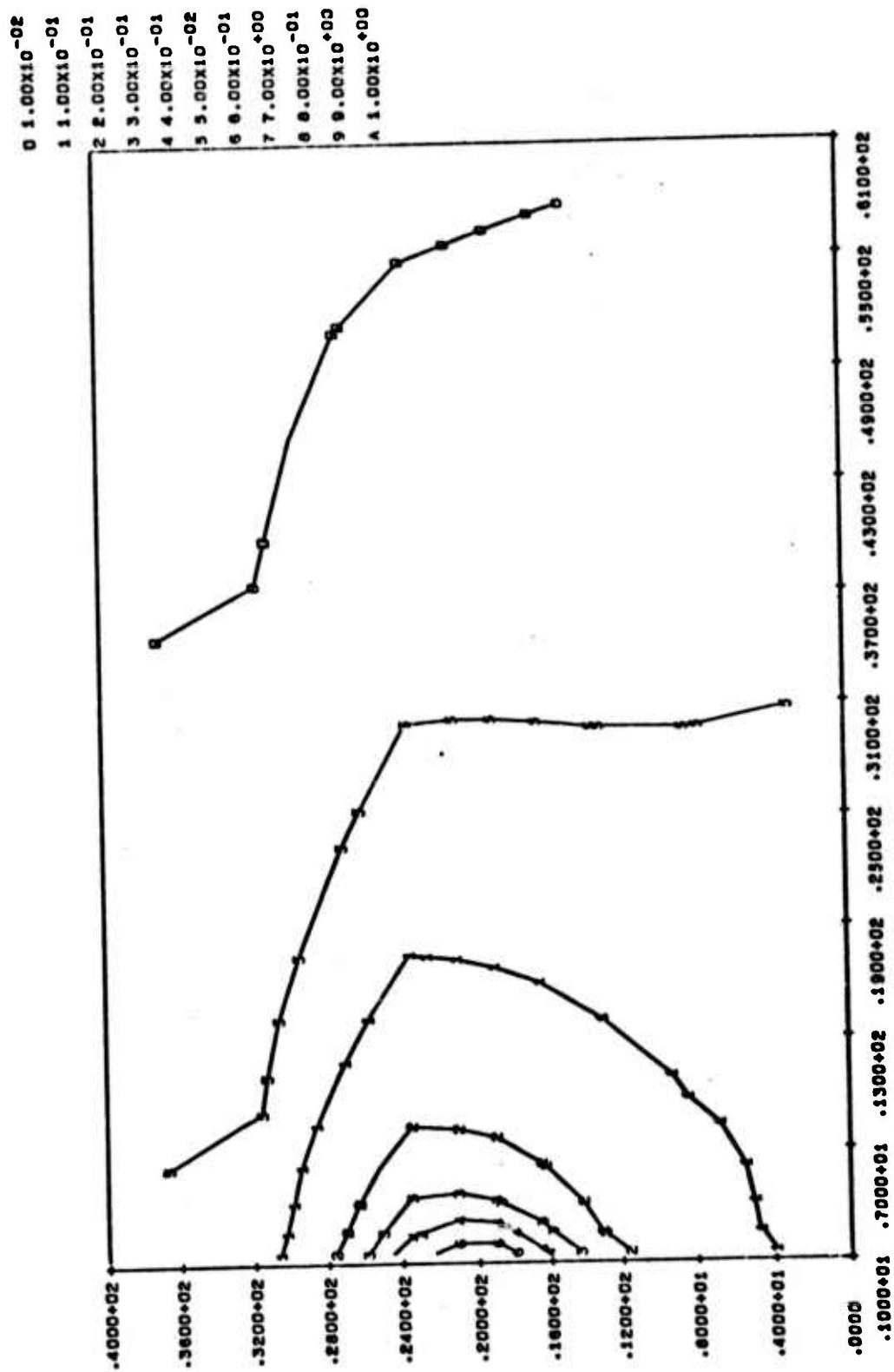


Fig. 7.16(b) -- Most tensile principal gross rock stress (bars), overlying low permeability layer, $t = 1.0$ day.

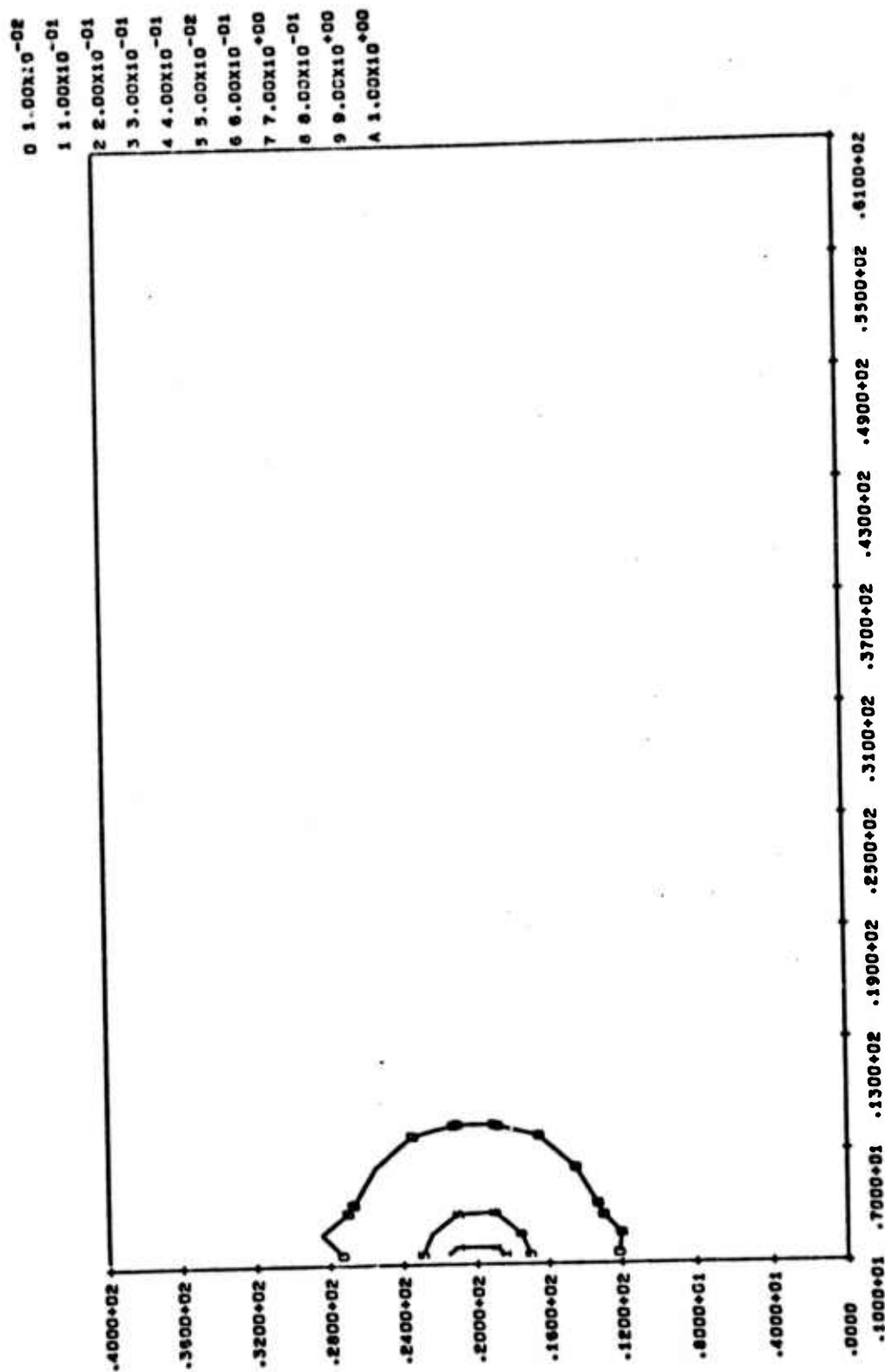


Fig. 7.17 (a) --Gross deviatoric stress (bars), overlying low permeability layer,
 $t = 0.001$ day.

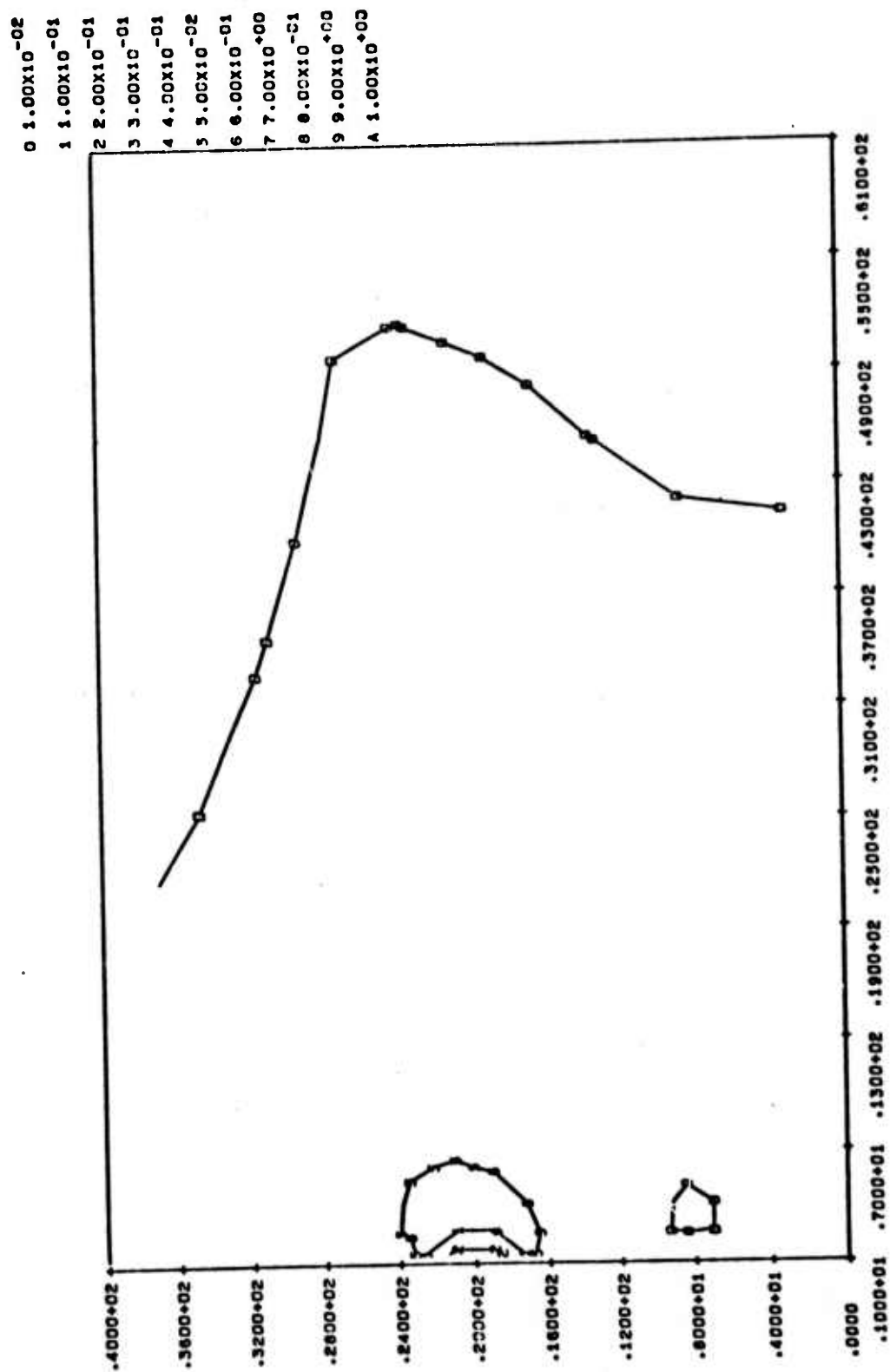


Fig. 7.17(b)--Gross deviatoric rock stress (bars), overlying low permeability layer, $t = 1.0$ day.

condition, hydraulically induced cracks would be initiated in the vertical plane. In the more common state of unequal tectonic principal stresses, the hydraulically induced cracks would likely orient normal to the least compressive principal stress quite near to the well.

2. After the seepage progresses for some time, $t > 0.01$ days, the maximum principal rock stress is essentially vertical everywhere except very near the zone of injection. The vertical orientation is attributed to the presence of the free surface. The overlying low permeability layer gives rise to nearly twice the tensile stress produced with the overlying high permeability layer. In general, the presence of a highly permeable zone tends to reduce the fluid pressure and rock stress in the region between the point of injection and the permeable zone. Conversely, the presence of a nearly impervious zone tends to cause fluid pressures to mount thereby increasing the tensile stress introduced into the rock. The increase in vertical stress is accompanied by an increase in the vertical displacements in the rock as compared to the case with higher overlying permeability.
3. Deviatoric stresses vary only slightly as seepage progresses.
4. At early times, before the presence of non-homogeneous structure influences the seepage, seepage rates can be estimated from the spherically symmetric injection well results

of Section 7.3.2. This would probably not be the case for a more elongated injection cavity. The presence of the free surface shortens the time it takes to reach steady-state conditions at large distances from the injection site.

7.4 SUMMARY AND CONCLUSIONS

Volumetric changes in the pores of fluid saturated rock give rise to mechanical interactions between the pore fluid and rock material. Starting with the stress-strain behavior of the particles, using the TINC framework, the mechanism for these interactions has been formulated. The result is a linear theory for describing the state of stress and strain in both the rock and the fluid constituent. The resulting equations have been reduced to the form that appears in consolidation theory. In so doing, the interaction constants of consolidation theory become defined in terms of material parameters thereby eliminating the need for hypothetical interaction constants.

Assuming Darcian flow through the pores, the equations that govern the seepage of fluid through an elastic material are presented both in differential form and in integral form. The integral form, which appears as a virtual work equation, is used to develop a finite element scheme for treating interactive seepage. The 2D FRI2 code is based on this development. The 2D finite element code is designed to model irregular geometry and material heterogeneities using an implicit time stepping algorithm.

After testing the code on numerous problems for which exact solutions could be obtained, FRI2 was used to simulate the injection of water into a shallow sedimentary deposit. The permeability of an overlying layer was varied to determine its influence on the injection system. Based on these conditions, the following conclusions can be drawn:

1. The deviatoric stress produced by an injection well tend to be very localized and nearly time invariant. Consequently, we conclude that alterations in the deviatoric stress in the vicinity of an injection well will have no

significant effect on the triggering of shear failures. It will be the tensile alterations in the rock stress produced by fluid injection that pose the greatest threat for triggering an earthquake.

2. The shape of an injection cavity can strongly influence the state of stress in the rock adjacent to the injection site. It appears that cracks at the boundary of the cavity can be initiated with an injection over pressure less than the minimum compressive tectonic stress. It is unlikely, however, that these cracks could be extended beyond a couple of cavity dimensions with a fluid overpressure less than the minimum compressive tectonic stress.
3. The presence of a highly permeable zone near an injection site tends to reduce the fluid pressure and the induced tensile rock stress in the direction of permeable zone. An impermeable zone near an injection site has the opposite effect and therefore would be more conducive to triggering an earthquake.

VIII. DISCUSSION

The work completed during the course of this contract provides the basis for more realistic ground motion predictions in the nonlinear region near a buried nuclear explosion. Such techniques are required to evaluate the effects of the siting medium on the signal transmitted into the more distant elastic region. This primary purpose of the program has been realized and in a companion program Cherry, et al. [4] merged the shock code techniques with seismic code techniques to calculate the effect of the siting medium on the signal radiated to teleseismic distances. The techniques are also being used to generate equivalent source functions in a systematic study of the effect of siting conditions on strong seismic motions that form a potential hazard to surface structures located approximately a hundred kilometers from the source. [16]

The applications of the improved ground motion predictive techniques, however, are much broader than the calculation of equivalent seismic source functions. For example, one possible method for designing a defense system to survive a massive nuclear test is to employ structures in cavities buried deeply enough to withstand a direct hit from a credible threat. A predictive understanding of the energy coupling processes, stress wave propagation effects, and the failure modes of the geologic media in the vicinity of the cavity are all required in order to develop a design methodology for hardened underground structures subjected to nuclear-weapon-induced ground shock. Some implications of the results of the present study to the evaluation of sites for a hardened structure may be indicated.

A series of parameter calculation using TAMEOS subroutine have indicated air-filled porosity (void volume) to be an important property governing stress attenuation

in spherical configurations, [3] in agreement with earlier conclusions by Bjork [9] and Cherry and Peterson. [88] The nitromethane tests described in Section 2.2 confirmed this and reinforced our confidence in TAMEOS for generating equations of state in partially saturated geologic materials. This suggests the possibility of an optimum attenuating surface layer overlaying a stronger deep layer for the actual underground structure. For example, an alluvium layer with large void volume overlaying a competent hard rock formation may be superior to a site in which the hard rock extends to the surface. Such a layer will attenuate the pulse from a surface burst and increase its rise time. The vaporization of pore water in the near surface material after shock processing, however, will increase the momentum contained in the material thrown backward during the cratering process. [94] A corresponding increase in the momentum initially carried downward towards the buried structure may be expected. The TAMEOS subroutine could be a useful tool in assessing these counteracting effects if used for different rock-water-void mixes in detailed calculations. Although such an investigation is outside the scope of this program, the planar 1D SKIPPER calculations in Section 2.3 indicate that explicit treatment of pore water vaporization must be included when calculating the ground shock transmitted from a surface burst to a buried structure.

An optimum site may be selected to include geologic layers with large mismatch in their stress wave propagation characteristics. If granitic layers are involved at stress levels above 70 kbars a two-phase equation of state (Section III) should be employed since the associated energy absorption reduces the energy available to propagate the pulse to greater depths. TAMEOS could be used to generate equations of state for any weaker sedimentary layers. Different plasticity models (Section IV) may well be required to

adequately calculate the transmission of the pulse through the various layers between the surface and the buried structure.

Ground motion data from underground nuclear explosions and high explosive simulation tests (e.g., Project STARMET, Ref. [95,96]) demonstrate that late time motions were strongly influenced by the preexisting joints. Although the available data base is restricted to ground shock phenomena pertinent to near surface structures, similar anisotropic effects are likely in the case of jointed media, even at great depths. The model of regularly jointed media presented in Section VI provides a framework for including planes of weakness and block motion in a continuum code for calculating gross ground motion effects.

The POROUS code for computing ground motion effects within the framework of the Theory of Interacting Continua has now reached the stage of development where it can be used for predictive calculations (Section V). Its ability to treat relative motion between the rock and water components in highly permeable wet aggregate media, such as saturated sands and corals, suggests application of POROUS for calculations in support of the PACE program. Its ability to explicitly monitor the pore water pressure in a wet competent medium suggests a parametric study of the implications to ground motion of the effective stress law of rock mechanics which has evolved from laboratory triaxial tests on cylindrical specimens under quasistatic loading conditions.

IX. REFERENCES

1. Riney, T. D., S. K. Garg, J. W. Kirsch, L. W. Morland, and C. R. Hastings, "Stress Wave Effects in Inhomogeneous and Porous Earth Materials," Systems, Science and Software Report 3SR-267, Defense Atomic Support Agency Report DASA-2498, March 31, 1970.
2. Riney, T. D., S. K. Garg, J. W. Kirsch, C. R. Hastings, and K. G. Hamilton, "Wave Propagation in Geologic Composites," Systems, Science and Software Report 3SR-648, Defense Atomic Support Agency Report, March 15, 1971.
3. Riney, T. D., J. K. Dienes, G. A. Frazier, S. K. Garg, J. W. Kirsch, D. H. Brownell, and A. J. Good, "Ground Motion Models and Computer Techniques," Formal Report under Contract No. DASA 01-69-C-0159(P00003), S³ Report 3SR-1071, April 1972.
4. Cherry, J. T., C. B. Archambeau, G. A. Frazier, A. J. Good, K. G. Hamilton, and D. G. Harkrider, "The Teleseismic Radiation Field from Explosions: Dependence of Seismic Amplitudes upon Properties of Materials in the Source Region," Final Report under Contract No. DASA 01-71-C-0156, Systems, Science and Software Report SSS-R-72-1193, July 1972.
5. Gurtman, G. A., A. H. Nayfeh, and G. A. Hegemier, "A Continuum Theory Applied to Wave Propagation in Structural Composite Materials," Air Force Weapons Laboratory Technical Report No. AFWL TR-71-167, May 1972.
6. Gurtman, G. A., A. H. Nayfeh, G. A. Hegemier, E. W. Sims, and D. H. Brownell, "A Continuum Theory Applied to Wave Propagation in Three-Dimensional Reinforced Composites," Systems, Science and Software Report SSS-R-72-1462, February 1973.
7. Gaffney, E. S., "Shock Propagation in Middle Gust Materials," Bimonthly Progress Report, Systems, Science and Software, January 1973.
8. Green, S. J., R. M. Griffin, A. D. Black, S. W. Butters, S. W. Duncan, H. R. Pratt, and K. B. Watson, "High Pressure Properties of Several Nevada Test Site Tuffs," Terra Tek Report TR 71-30, August 1971.

9. Bjork, R. L., "Computed Response of the Hudson Moon H.E. Experiment," Topical Report under Contract No. DASA 01-69-C-0146, Systems, Science and Software Report 3SIR-976, February 1972.
10. Riney, T. D., letters transmitted to C. B. McFarland on May 8 and May 9, 1972.
11. Bjork, R. L., and M. L. Gittings, "Wave Generation by Shallow Underwater Explosions," Systems, Science and Software Report 3SR-1008, December 1972.
12. Herrmann, W., "Constitutive Equation for the Dynamic Compaction of Ductile Porous Materials," J. Appl. Phys. 40 (6), pp. 2490-2499 (1969).
13. Stephens, D. R., H. C. Heard, and R. N. Schock, "High-Pressure Mechanical Properties of Tuff from the Diamond Dust Site," Lawrence Livermore Laboratory Report UCRL-50858, April 1970.
14. Lee, E. L., H. C. Hornig, and J. W. Kury, "Adiabatic Expansion of High Explosive Detonation Products," Lawrence Livermore Laboratory Report UCRL-50422, May 1968.
15. Green, S. J., personal communication.
16. Cherry, J. T., A. J. Good, and K. G. Hamilton, "Near Field Source Calculations for Seismic Predictions," Systems, Science and Software Report SSS-R-73-1605, April 5, 1973.
17. McQueen, R. G., S. P. Marsh, and J. N. Fritz, "Hugoniot Equation of State of Twelve Rocks," J. Geophys. Res., 72, p. 4999 (1967).
18. Birch, F., "The Velocity of Compressional Waves in Rocks to 10 Kilobars, 1," J. Geophys. Res. 65, p. 1083 (1960).
19. Simmons, G., "Velocity of Shear Waves in Rocks to 10 Kilobars, 1," J. Geophys. Res. 69, p. 1123 (1964).
20. Ahrens, T. J., "Evaluation of Equation of State Data," DASA 2359, January 1970.
21. Stephens, D. R., "The Hydrostatic Compression of Eight Rocks," J. Geophys. Res. 69, p. 2967 (1964).

22. Davies, G. F., and D. L. Anderson, "Revised Shock-Wave Equations of State for High-Pressure Phases or Rocks and Minerals," J. Geophys. Res. 76, p. 2617 (1971).
23. Ahrens, T. J., "High Temperature and High Pressure Equations of State," DNA 2838F, April 1972.
24. Akimoto, S., and Y. Syono, "Coessite-Stishovite Transition," J. Geophys. Res. 74, p. 1653 (1969).
25. Horie, Y., Washington State University Shock Dynamics Laboratory Report, WSU-SDL 66-02, July 1966.
26. Johnson, J. N., "Considerations for the Calculation of Shock-Induced Phase Transformations in Solids," SC-RR-72-0626, September 1972.
27. Allen, R. T., "Equation of State of Rocks and Minerals," General Atomic Report GAMD-7834, March 1967.
28. Sedgwick, R. T., and D. A. Wolfgang, "CRAM, A Two-Dimensional Lagrangian Code for Elastic-Plastic-Hydrodynamic Material Behavior," General Electric Company, 69SD1002, February 1969.
29. Wilkins, M. L., "Calculation of Elastic-Plastic Flow," Methods in Computational Physics, 3, pp. 221-263 (1964).
30. Herrmann, W., P. Holzhauser, and R. J. Thompson, "WONDY, A Computer Program for Calculating Problems of Motion in One Dimension," Sandia Laboratories, SC-RR-66-601, February 1967.
31. Cherry, J. T., "A Simple Computational Procedure for Determining the Flow Rule Multiplier," Systems, Science and Software internal communication, May 8, 1972.
32. Sandler, I., and F. L. DiMaggio, "Material Models for Rocks," Defense Nuclear Agency Report DASA-2595, October 1970.
33. Dienes, J. K., "Hardening Models for Granite at High Pressures," Systems, Science and Software Report 3SR-881, January 21, 1972.
34. Swanson, S. R., "Development of Constitutive Equations for Rocks," Ph.D. Dissertation, University of Utah, 1969.

35. Werth, G. C., and R. F. Herbst, "Comparison of Amplitudes of Seismic Waves from Nuclear Explosions in Four Mediums," J. Geophys. Res., 68, (5), March 1963.
36. Carroll, M., and A. C. Holt, "Suggested Modification of the P- α Model for Porous Materials," J. Appl. Phys., 43 (2), pp. 759-761 (1972).
37. von Mises, R., "Mechanik der Plastischen Formanderung von Kristallen," ZAMM 8, pp. 161-185 (1928).
38. Roark, R. J., Formulas for Stress and Strain, McGraw-Hill Book Company, 1965.
39. Hashin, Z., "The Elastic Moduli of Heterogeneous Materials," J. Appl. Mech., 29, pp. 143-150, (1962).
40. Prager, W., "The Theory of Plasticity: A Survey of Recent Achievements," Proc. Instn. Mech. Engrs., 169, pp. 41-57 (1955).
41. Drucker, D. C., "A More Fundamental Approach to Plastic Stress Strain Relations," Proc. 1st U. S. Natl. Congress Appl. Mech., pp. 487-491, 1951.
42. Sandler, I. S., J. P. Wright, and M. L. Baron, "Data Report - Pretest Ground Motion Calculations for the Mixed Company Event of the Middle North Series," Paul Weidlinger Report, October 1972.
43. Biot, M. A., "Theory of Propagation of Elastic Waves in a Fluid Saturated Porous Solid, I. Low-frequency Range," J. Acoust. Soc. Am., 28, p. 168 (1956).
44. Jaeger, J. C., and N. G. W. Cook, Fundamentals of Rock Mechanics, Methuen, 1969.
45. Jaeger, J. C., "Behavior of Closely Jointed Rock," Chapter 4, Rock Mechanics, 11th Symposium (Berkeley), Ed. Somerton, W. H., Port City Press, 1969.
46. Rosenblatt, M., and K. N. Kregenhagen, "Free Field Motions in Jointed Media," Shock Hydrodynamics, Inc. Report DNA 2769F, 1971.
47. Wilson, C. R., and P. A. Witherspoon, "An Investigation of Laminar Flow in Fractured Porous Rocks," Dep. Civ. Eng., Berkeley Pub. 70-6, 1970.

48. Abbott, P. A., and E. H. Wang, "Dynamic Two-Dimensional Continuum Model for Orthogonal Cracked Rock," AFWL Report WCL-TN-70-020, 1970.
49. Perloff, W. H., "Strain Distribution Around Underground Openings," Purdue Technical Report 7 (Jointed Systems), 1972.
50. Fairhurst, C., J. A. Hudson, B. Singh, and C. R. Nelson, "Mechanical Properties of Rock Masses," Minnesota Report USBMR H0101610, 1971.
51. John, K. W., "Strength and Deformability of Regularly Jointed Rocks," Chapter 5, Rock Mechanics, 11th Symposium (Berkeley), Ed. Sommertcn, W. H., Port City Press, 1969.
52. Goodman, R. E., and J. Dabojs, "Static and Dynamic Analysis of Rock Bolt Support," Berkeley Technical Report 6, DACA 45-67-C-0015, 1971.
53. Rouvra, A de, R. E. Goodman, K. Drozd, and F. Heuze, "Analysis and Model Studies of Underground Openings in Jointed Rock," Berkeley Technical Report 7, DACA 45-69-C0038, 1971.
54. Dudley, P. P., and R. E. Riecker, Penrose Conference on Fracture Mechanics and Earthquake Source Mechanisms, 1972.
55. Dieterich, J. H., "Time-Dependent Friction in Rocks," J. Geophys. Res., 77 (22), pp. 3690 (1972).
56. Price, N. J., "Laws of Rock Behavior in the Earth's Crust," Chapter 1, Rock Mechanics, 11th Symposium (Berkeley), Ed. Somertcn, W. H., Port City Press, 1969.
57. Obert, L., and W. I. Duvall, Rock Mechanics and the Design of Structures in Rocks, Wiley, 1967.
58. Hubbert, M. K., and W. W. Rubey, "Role of Fluid-Filled Porous Solids and its Application to Overthrusting Faulting," Bull. Geol. Soc. Amer. 70, p. 115, (1959), and 71, p. 617 (1960).
59. McKay, M. W., R. R. Shadel, R. P. Swift, and C. Young, Physics International Report DASA 01-69-C-0071, (2525), 1970.

60. Sokolnikoff, I. S., Mathematical Theory of Elasticity, McGraw-Hill, Second Edition, 1956.
61. Brace, W. F., and J. D. Byerlee, "Stick-Slip as a Mechanism for Earthquakes," Science, 153, (3739), p. 990, (1966).
62. Byerlee, J. D., "Theory of Friction Based on Brittle Fracture," J. Appl. Phys. 38, p. 2928 (1967).
63. Byerlee, J. D., "Frictional Characteristics of Granite under High Confining Pressure," J. Geophys. Res. 72, p. 3639 (1967).
64. Byerlee, J. D., and W. F. Brace, "Stick-Slip, Stable Sliding, and Earthquakes--Effect of Rock Type, Pressure, Strain Rate, and Stiffness," J. Geophys. Res. 73, p. 6031 (1968).
65. Byerlee, J. D., "Brittle-Ductile Transition in Rocks," J. Geophys. Res. 73, p. 4741 (1968).
66. Jaeger, J. C., and K. J. Rosengren, "Friction and Sliding of Joints," Proc. Aust. Inst. Met. No. 229, p. 93, 1969.
67. Byerlee, J. D., "Static and Kinetic Friction of Granite at High Normal Stress," Int. J. Rock Mech. Sci. 7, p. 577 (1970).
68. Johnson, T., F. T. Wu, and C. H. Scholz, "Source Parameters for Stick-Slip and for Earthquakes," Science, 179, p. 278, January 1973.
69. Scholz, C., P. Molnar, and T. Johnson, "Detailed Studies of Frictional Sliding of Granite and Implications for the Earthquake Mechanism," manuscript submitted to J. Geophys. Res., 1972.
70. Drennon, C. B., and R. L. Handy, "Stick-Slip of Lightly Loaded Limestone," Iowa State University Eng. Res. Inst. DASA 01-69-C-0148, DNA 2839F.
71. Pratt, H. R., A. D. Black, and F. J. Bonney, "Frictional Properties of Cedar City Quartz Dionite," Terra Tek Report, AFWL-TR-72-122.
72. Einstein, H. H., R. A. Nelson, R. W. Bruhn, and R. C. Hirschfield, "Model Studies of Jointed Rock Behavior," Chapter 6 of Rock Mechanics, 11th Symposium (Berkeley) Ed. Somerton, W. H., Port City Press, 1969.

73. Rosenblad, J. L., "Geomechanical Model Study of the Failure Modes of Jointed Rock Masses," Technical Report MRDL 1-71, Omaha, 1971.
74. Hendron, A. J., P. Engeling, and A. K. Aiyer, "Geomechanical Model Study of the Behavior of Underground Openings in Rock Subjected to Static Loads," U. S. Army Eng. Waterways Experimental Station Report N-69-1, 1972.
75. Barton, N. R., "A Model Study of Rock-Joint Deformation," Int. Journal Rock Mech. Mining Sci. 9, p. 579, (1972).
76. Morland, L. W., "A Simple Constitutive Theory for a Fluid Saturated Porous Solid," J. Geophys. Res. 77, p. 890 (1972).
77. Garg, S. K., and A. Nur, "Effective Stress Laws for Deformation and Fracture of Fluid Saturated Porous Rocks," manuscript submitted to J. Geophys. Res., 1973.
78. Nur, A., and J. D. Byerlee, "An Exact Effective Stress Law for Elastic Deformation of Rock with Fluids," J. Geophys. Res. 76, p. 6414 (1971).
79. Goodman, R. E., and J. Dubois, "Duplication of Dilatancy in Analysis of Jointed Rocks," J. Soil Mech., Found. Div., (ASCE), 98, p. 399 (1972).
80. Singh, B., "Continuum Characterization of Jointed Rock Masses, Part I -- The Constitutive Equations," University of Minnesota manuscript, 1972.
81. Hubbert, M. K. and David G. Willis, "Mechanics of Hydraulic Fracturing," Trans. AIME, 21, pp. 153-166, (1957).
82. Healy, J. H., W. W. Rubey, D. T. Griggs, and C. B. Raleigh, "The Denver Earthquakes," Science, 161, pp. 1301-1310 (1968).
83. Raleigh, C. B., "Rangley, Colorado," Presentation at the Penrose Conference, Snowmass at Aspen, Colorado, September 1971.
84. Healy, J. H., "Rangley Microearthquakes," Presentation at the Penrose Conference, Snowmass at Aspen, Colorado, September 1971.

85. Terzaghi, K., "Principle of Soil Mechanics," Engr. News Record, 1925, a series of articles.
86. Biot, M. A., "General Theory of Three-Dimensional Consolidation," J. Appl. Phys., 12, pp. 155-164
87. Biot, M. A., "Theory of Elasticity and Consolidation for a Porous Anisotropic Solid," J. of Appl. Phys., 22 (1), pp. 182-185, (1955).
88. Gibson, R. E., K. Knight, and P. W. Taylor, "A Critical Experiment to Examine Theories of Three-Dimensional Consolidations," Proc. European Conf. Soil Mech. and Found. Eng., Wiesbaden, Vol. 1, pp. 69-76.
89. Verruijt, A., Discussion, Proc. 6th International Conf. Soil Mech. and Found. Eng., Montreal, Vol. 3, pp. 401-402, 1965.
91. Ghaboussi, J. and E. L. Wilson, "Flow of Compressible Fluid in Porous Elastic Media," SESM Report No. 71-12, University of California at Berkeley, 1971.
92. Stagg, K. G., and O. C. Zienkiewicz, Rock Mechanics in Engineering Practice, John Wiley and Sons, 1968.
93. Cherry, J. T. and F. L. Peterson, "Numerical Simulation of Stress Wave Propagation from Underground Nuclear Explosions," Proc. of Symposium on Engineering with Nuclear Explosions, Las Vegas, January 14-16, 1970.
94. Butkovich, T. R., "Influence of Water in Rocks on Effects of Underground Nuclear Explosions," J. Geophys. Res., 76, p. 1993, 1971.
95. Blowin, S. E., and J. V. Kaiser, "Project STARMET--Ground Motion Data," AFWL-TR-72-68, Vol. I, June 1972.
96. Shunk, R. A., "Project STARMET - Use of Strain Cylinders in Rock Stress Instrumentation," AFWL-TR-72-68, Vol. II, June 1972.

DISTRIBUTION LIST

DEPARTMENT OF DEFENSE

Assistant to the Secretary of Defense
Atomic Energy
ATTN: Document Control

Director
Defense Advanced Research Projects Agency
ATTN: NMRO (2 copies)
ATTN: PMO (3 copies)

Defense Civil Preparedness Agency
ATTN: Staff Director, RE(SR),
Mr. George N. Sisson

Director
Defense Communications Agency
ATTN: Code 930

Defense Documentation Center
ATTN: TC

Director
Defense Intelligence Agency
ATTN: DI-7D, Phys. Vul. Div.,
Mr. Edward O'Farrell
ATTN: DT-2, Weapons and Systems Div.

Director
Defense Nuclear Agency
ATTN: STSP
ATTN: APSI (Archives)
ATTN: DLST
ATTN: SPSS
ATTN: APTL, Technical Library (2 copies)

Director of Defense Research
& Engineering
ATTN: Dep. Dir. (Info & Space Systems)
ATTN: Dep Dir. (Strategic Systems)
ATTN: Assistant Dir. (Strategic
Weapons

Commander
Field Command
Defense Nuclear Agency
ATTN: Technical Library, FCSD-A4
ATTN: FCTA-C
ATTN: FCWD-C

Commandant
Industrial College of the Armed Forces
ATTN: Document Control

Director
Joint Strategic Target Planning Staff
ATTN: JLTW

Chief
Livermore Division, Field Command DNA
ATTN: FCTA-D
ATTN: Document Control (2 copies)

Commandant
National War College
ATTN: NWCLB-CR

Director
Weapons Systems Evaluation Group, ODR&E
ATTN: Capt. Donald E. McCoy, USN

DEPARTMENT OF THE ARMY

Director
Advanced Ballistic Missile Defense Agency
ATTN: CRDABM-NE, LTC James H. Sloan

Assistant Chief of Staff for Force
Development
Department of the Army
ATTN: Director of Chemical and
Nuclear Operations

Chief of Engineers
Department of the Army
ATTN: ENGMC-ED
ATTN: ENGME-RD
ATTN: ENGMC
ATTN: ENGME-S

Chief of Research and Development
Department of the Army
ATTN: NCB Division
ATTN: Dr. Valentine E. Zadnik

Chief
Engineer Strategic Studies Group
ATTN: Mr. E. H. Underwood

Director
Explosive Excavation Research Laboratory
ATTN: Document Control

Commander
Harry Diamond Laboratories
ATTN: AMXDO-NP

Safeguard System Manager
Safeguard System Office
ATTN: Dr. C. C. Old

Commander
U.S. Army Aberdeen Research and
Development Center
ATTN: Document Control (2 copies)

Commander
U. S. Army Engineer Center
ATTN: ATSEN-SY-L

Project Engineer
U. S. Army Engineer District, Huntsville
ATTN: HNDSE-R, Mr. Michael M. Dembo

Division Engineer
U. S. Army Engineer District, Missouri
River
ATTN: MRDED-G, Mr. Lloyd B. Underwood,
Geologist

Division Engineer
U. S. Army Engineer District, Ohio River
ATTN: Document Control

District Engineer
U.S. Army Engineer District, Omaha
Corps of Engineers

Director
U. S. Army Engineer Waterways
Experiment Station
ATTN: Dr. Guy Jackson
ATTN: Library Branch

Commander
U. S. Army Materiel Command
ATTN: AMCRD-BN (2 copies)

Commander
U. S. Army Mobility Equipment R and D
Center

Commander
U. S. Army Nuclear Agency
ATTN: CDINS-E

Commandant
U. S. Army War College
ATTN: Library

DEPARTMENT OF THE NAVY

Chief of Naval Operations
Navy Department
ATTN: OP-985
ATTN: OP-03EG

Chief of Naval Research
Department of the Navy

Commanding Officer
Naval Civil Engineering Laboratory
ATTN: Mr. J. Allgood
ATTN: Code L31

Commander
Naval Facilities Engineering Command
Command Headquarters
ATTN: Code 04B, Kmr. William J. Bobisch
ATTN: Code 03A, Mr. Stanley Rockefeller

Commander
Naval Ordnance Laboratory
ATTN: Code 242, Mr. Irving Kabik
ATTN: Code 243, Mr. Frederick J. Gleason
ATTN: Code 240, Mr. C. J. Aronson
ATTN: Code 121, Navy Nuclear Programs
Office

Commander
Naval Ordnance Systems Command
ATTN: ORD-91313, Library

Superintendent
Naval Postgraduate School
ATTN: Code 2124, Technical Reports
Librarian

Director
Naval Research Laboratory
ATTN: Code 1065, Classified
Material Control Branch

Commanding Officer
Naval School
ATTN: Document Control

Commander
Naval Ship Engineering Center
ATTN: Document Control

Commander
Naval Ship Research and Development
Center
ATTN: Code L42,3, Library

President
Naval War College
ATTN: Document Control

Commander
Naval Weapons Center

Director
Strategic Systems Project Office
ATTN: SP-272, CDR Robert J. Stinner,
Section Head

DEPARTMENT OF THE AIR FORCE

Commander
Aerospace Defense Command
ATTN: XPDW, Advanced Planning Division
ATTN: XP, DCS/Plans

A.F. Armament Laboratory, AFSC
ATTN: ADLRW, Mr. W. H. Dittrich

A.F. Cambridge Research Laboratories,
AFSC
ATTN: LWV, Dr. Ker Thompson

A. F. Weapons Laboratory, AFSC
ATTN: Maj. George Bulin
ATTN: Dev, Dr. M. A. Plamondon
ATTN: DE-1
ATTN: Mr. J. Bratton
ATTN: DOGL, Technical Library
ATTN: DE
ATTN: Robert Henny
ATTN: Robert Port
ATTN: Dr. E. Zwayer

Headquarters
Air Force Systems Command

Commander
Armament Development & Test Center
ATTN: ADBRL-2

Chief of Staff
U. S. Air Force
ATTN: INATA (Dissemination Request
Research Branch)
ATTN: RDPM (Missile Sys. Div., Dir.
of Dev. & Acq.)
ATTN: PRE (Director of Civil
Engineering
ATTN: RDQPN (S/V & Nuclear Programs
Division)

Commander
Rome Air Development Center, AFSC
ATTN: EMREC, Mr. R. W. Mair
ATTN: EMTLD, Documents Library

Space and Missile Systems Organization
ATTN: RNS
ATTN: SYSN
ATTN: XRTB
ATTN: CCD

Space and Missile Systems Organization,
AFSC
ATTN: MMN, Engineering Division
ATTN: MMH, Hard Rock Silo Development

Commander
Strategic Air Command
ATTN: XPFS
ATTN: OAI

ATOMIC ENERGY COMMISSION

Los Alamos Scientific Laboratory
ATTN: Document Control for Mr. Robert
McQueen
ATTN: Document Control for Dr. Al Davis
ATTN: Document Control for Report
Library
ATTN: Document Control for Dr. William
E. Ogle

Sandia Laboratories
Livermore Laboratory
ATTN: Dr. Les Hill, Material Division

Sandia Laboratories
ATTN: Doc. Control for Org 9100,
Dr. Byron Murphey
ATTN: Doc. Control for Dr. M.L. Merritt
(2 copies)
ATTN: Doc. Control for Dr. Walter
Herrmann

U. S. Atomic Energy Commission
Albuquerque Operations Office
ATTN: Document Control

U. S. Atomic Energy Commission
Nevada Operations Office
ATTN: Document Control for Technical
Library
ATTN: Mr. R. Thalgott

U. S. Atomic Energy Commission
Division of Headquarters Services
ATTN: Doc. Control for Classified
Tech. Info. Serv.
ATTN: Doc. Control for Classified
Tech. Library

University of California
Lawrence Livermore Laboratory
Library, Bldg. 50, Room 134

University of California
Lawrence Livermore Laboratory
Technical Information Division
ATTN: J. R. Hearst, L-41
ATTN: Dr. Robert Schock
ATTN: D. M. Norris, L-90
ATTN: Dr. J. Coruthers L-18
ATTN: Jack Kahn
ATTN: Dr. Richard G. Dong L-424
ATTN: Douglas Stephens, L-437,
Chemistry Dept.
ATTN: Ted Butkovich
ATTN: Dr. Howard Rodean

OTHER GOVERNMENT

Bureau of Mines
Twin Cities Research Center
ATTN: Dr. T. C. Atchison
ATTN: Dr. T. Ricketts

Department of the Interior
Bureau of Mines
ATTN: Dr. Leonard A. Obert

Department of the Interior
Bureau of Mines
ATTN: Dr. James J. Scott

Department of the Interior
U. S. Geological Survey
ATTN: Dr. John H. Healy
ATTN: Dr. Cecil B. Raleigh,
Earthquake Res. Ctr.

DEPARTMENT OF DEFENSE CONTRACTORS

Aerospace Corporation
ATTN: Dr. Prem N. Mathur
ATTN: Technical Information Services
(2 copies)

Agbabian Associates
ATTN: Document Control
ATTN: J. Isenberg

Analytic Services, Inc.
ATTN: George Hesselbacher

Applied Theory, Inc.
ATTN: Security Officer (2 copies)

AVCO
ATTN: Research Library, A830,
Room 2201

Battelle Memorial Institute
ATTN: Mr. R. W. Klingesmith

Bell Telephone Laboratories, Inc.
ATTN: J. P. White, Room 3F223

Boeing Company
ATTN: Mr. John Blaylock
ATTN: Dr. R. Hager

Braddock, Dunn & McDonald, Inc.
ATTN: A. Lavagnino

Braddock, Dunn & McDonald, Inc.
ATTN: Mr. Richard Hensley

Brown Engineering Company, Inc.
ATTN: J. Cahoon

University of California at San Diego
ATTN: Dr. Manual Rotenberg,
Title Code 3215

California Institute of Technology
ATTN: Dr. Thomas J. Ahrens

California, Berkeley Campus,
University of
ATTN: W. Goldsmith, Dept. of Mech. Eng.

Calspan Corporation
ATTN: Burt Changers, Tech. Division

Environmental Research Corporation
ATTN: Dr. W. W. Hays, Technical
Director

General American Transportation
Corporation
ATTN: Dr. Marion J. Balcerzak,
Technical Director
ATTN: Dr. G. L. Neidhardt, Manager
of Engineering

General Electric Company
ATTN: Dr. M. H. Bortner, Space Sci. Lab.

General Electric Company
TEMPO-Center for Advanced Studies
ATTN: DASIA

General Research Corporation
ATTN: Dr. Giles F. Crimi

General Research Corporation
ATTN: Tech. Info. Office for
Mr. Benjamin Alexander

Gulf Oil Corporation
Manager, Security Branch
ATTN: For GGA

IIT Research Institute
ATTN: Dr. Madan M. Singh, Manager
ATTN: Dr. R. E. Welch
ATTN: Technical Library
ATTN: Mr. Milton R. Johnson

Illinois, University of
ATTN: Dr. Nathan M. Newmark

Institute for Defense Analyses
ATTN: Technical Information Office

Iowa State University of Science and Technology ATTN: Dr. Richard L. Handy	Southwest Research Institute ATTN: A. B. Wenzel
J. L. Merritt Consulting and Special Engineering Services, Inc.	Stanford Research Institute ATTN: Dr. Carl Peterson ATTN: Dr. Douglas D. Leough
Kaman Sciences Corporation ATTN: Mr. Paul A. Ellis	Systems, Science and Software, Inc. ATTN: Dr. Donald R. Grine ATTN: Mr. R. Bjork ATTN: Dr. Ted Cherry ATTN: Doc. Control, Sec. Off. ATTN: Dr. D. Riney ATTN: Dr. Kedar D. Pyatt ATTN: Dr. John M. Walsh
Lockheed Missiles and Space Company ATTN: Dr. Roland E. Meyerott, Dept. 50-01, Bldg. 201	
Lockheed Missiles and Space Company, Inc.	Terra Tek, Inc. ATTN: Dr. A. H. Jones ATTN: Mr. Sidney J. Green
Massachusetts Institute of Technology ATTN: Prof. William F. Brace	Tetra Tech. Inc. ATTN: Dr. Li-San Hwang
Mitre Corporation ATTN: Document Control	Texas A&M University System ATTN: Dr. John Handin, Director
Nathan M. Newmark	TRW Systems Group San Bernardino Operations
University of New Mexico ATTN: Dr. G. E. Triandafalidis	TRW Systems Group ATTN: Dr. Robert L. Johnson ATTN: Mr. H. Jerry Carpenter (R-1, Room 2211) ATTN: Dr. Benjamin Sussholtz ATTN: Dr. Pravin Bhutta ATTN: Dr. Peter K. Kai, R1/2178
Physics International Company ATTN: Doc. Control for Mr. Dennis Orphal ATTN: Doc. Control for Mr. Fred M. Sauer ATTN: Doc. Control for Mr. M. McKay (2 cc) ATTN: Doc. Control for Dr. Charles Godfrey ATTN: Doc. Control for Dr. D. B. Maxwell ATTN: Doc. Control for Dr. Robert Swift	Universal Analytics, Inc. ATTN: Dr. E. I. Field
Purdue University ATTN: Mr. William R. Judd	URS Research Company
R&D Associates ATTN: Dr. C. P. Knowles ATTN: Dr. Henry Cooper ATTN: Mr. William B. Wright ATTN: Dr. Albert Latter ATTN: Dr. Harold L. Brode	Washington State University ATTN: Dr. George Duval
The Rand Corporation ATTN: Dr. C. C. Mow	Paul Weidlinger, Consulting Engineer ATTN: Dr. Melvin L. Baron
Research Analysis Corporation ATTN: Documents Library	
Science Applications, Inc. ATTN: Mr. Michael McKay	
Science Applications, Inc. ATTN: Dr. John Mansfield ATTN: Dr. William M. Layson	
Shock Hydrodynamics, Inc. Division of Whittaker Corporation ATTN: Dr. L. Zeronow	